

The behaviour of gas-emitting particles in fluidised beds

Zachariah William Michael Bond

Department of Chemical Engineering and Biotechnology
University of Cambridge

This thesis is submitted for the degree of

Doctor of Philosophy

Declaration

This thesis is the result of my own work and includes nothing which is the outcome of work done in collaboration except as declared in the Preface and specified in the text. I further state that no substantial part of my thesis has already been submitted, or, is being concurrently submitted for any such degree, diploma, or other qualification at the University of Cambridge or any other University or similar institution except as declared in the Preface and specified in the text. It does not exceed the prescribed word limit for the relevant Degree Committee.

Zachariah Bond

Summary

The behaviour of gas-emitting particles in fluidised beds

Zachariah William Michael Bond

This dissertation concerns solid spheres, with diameters $\sim 6 - 10$ mm, densities between $\sim 700 - 1500$ kg m⁻³ and emitting gas at various peripheral velocities, U_d , and their tendency to float or sink when introduced into gas-fluidised beds of Geldart Group B particles. This is relevant, for example, to the fluidised bed combustion of biomass, and the apparent tendency of the fuel to devolatilise predominantly near the upper surface of the bed with the attendant undesirable complications of unconverted volatile matter (VM) entering the freeboard.

Inert spheres (*viz.* where $U_d = 0$) in a bubbling fluidised bed can sink, even if less dense than the fluidised medium, owing to the additional weight of bed particles which tend to settle on top of them forming a defluidised hood. A 2-D fluidised bed, at room temperature, was used to investigate the structure of the fluidised bed in the vicinity of a cylinder emitting gas, as a mimic of a 3-D system. It was found that if U_d is more than 0.7, then the gas emitted can fluidise the bed particles in the entire defluidised hood. Consequently, it was inferred for a 3-D system that gas-emitting spheres are not burdened by a defluidised hood and will rise to the surface more rapidly than inert spheres, which are burdened.

The hypothesis that a gas-emitting sphere forms a pocket of high pressure around its underside sufficient to enable it to hover above the surface of the fluidised bed, was investigated, in a mechanism akin to the Leidenfrost effect exhibited by liquid drops on a hot plate. Experimentation showed that this hypothesis could be rejected. In fact, by observing the structure of the bed and measuring the pressure around a gas-emitting cylinder close to the surface of a 2-D fluidised bed, it was found that the emission of gas from a freely-floating sphere decreases the net upthrust of the bed on its underside thereby causing the sphere to sink lower into the bed than buoyancy alone would suggest. However, it was also discovered that the emission of gas from a sphere sunk deep within a fluidised bed caused the net upthrust from the bed to increase, causing the sphere to rise more rapidly to the surface than an inert sphere. This suggests that there exists a stable depth at which gas-emitting spheres reach dynamic

equilibrium just beneath the surface of the bed where the bed's upthrust matches the weight of the sphere. An interesting aside of investigating the Leidenfrost mechanism was that, as far as Geldart Group B solids are concerned, experiments showed the two-phase theory of fluidisation holds exactly.

To simulate spheres of devolatilising biomass, spheres of dry ice, sublimating in a hot fluidised bed were used, because dry ice emits a single, readily detectable gas. The spheres of dry ice were, however, much denser than any biomass fuel and so only segregated once the rate of sublimation was very high. The external heat transfer coefficient for the spheres of dry ice was measured at a variety of bed temperatures and bed particle sizes. Unlike inert particles, gas emitted by the dry ice particles caused the heat transfer coefficient to a) decrease as the bed material size was decreased and b) decrease as the bed temperature increased. For the first time, a heat transfer model, which accounted for the change in structure of the bed material near the gas-emitting particle, was developed to predict the rate of gas emitted from the dry ice particles and gave good agreement with the experimental results.

A novel method for finding the peripheral velocity of VM, emitted by spheres of biomass during devolatilisation in a fluidised bed, was developed and validated experimentally. The mean molar mass and composition of the VM was measured, with the result that measuring the concentration of the combustion products of the VM alone could be used to find the molar flowrate of the VM. Using this method, values of U_d , for spheres of beech, devolatilising in a hot fluidised bed, were measured and, simultaneously, the depth of the spheres in the bed was determined using X-radiography. The simultaneous measurements of gas velocity and depth allowed the behaviour of freely floating, devolatilising spheres to be compared with the calculations obtained with the 2-D fluidised bed. The spheres of beech remained just beneath the surface of the bed throughout devolatilisation and were less influenced by the mixing motions of the bed than inert spheres, even when the fluidisation velocity was increased. The devolatilising beech behaved much as anticipated by the results of the 2-D bed experiments.

Tentatively, a dimensionless plot was made which, brings the variables U_d , the incipient fluidisation velocity U_{mf} , the densities of the gas-emitting particles and the bed material, and the depth at which a particle will neither rise nor sink in the bed, together. The plot shows under what conditions a gas-emitting particle is likely to have a sinking or rising tendency in a

fluidised bed. The plot is a tool for predicting if segregation of a particular fuel particle is likely to occur in any bubbling fluidised bed.

Overall, this dissertation concludes that the emission of VM from a devolatilising particle of biomass not only draws the particle to the surface of the bed but acts to keep it there, even at low rates of gas emission. To eliminate the segregation of biomass during combustion in a bubbling fluidised bed, the biomass must be denser than the emulsion phase of the fluidised bed and the velocity of VM leaving the biomass must be as low as possible. An impracticable degree of pre-processing of the biomass would be required to achieve these conditions.

I would like to dedicate this thesis to the memory of Uncle Eric Robinson. I have attempted to carry his enthusiastic, yet pragmatic approach to life and, above all, his senses of humour and humility into my work and only regret that I could not share the outcome with him.

Acknowledgements

I wish to acknowledge the support of my supervisors, Prof. John Dennis and Dr. Ewa Marek. The project could not have been completed without their attention to detail, rigour and high standards for written work. I also thank Dr. Stuart Scott for being my advisor and Prof. Allan Hayhurst who has provided much help and insight. I thank the EPSRC for funding the project.

The latter parts of this dissertation would not have been possible without the help and collaboration of the fluidisation group at University College London. I would like to thank Dr. Massimiliano Materazzi, Dr. Domenico Macri and, in particular, Stefano Iannello for their expertise in X-radiography and help to complete the experiments under difficult circumstances.

The combustion, latterly the energy, reactions and carriers group, have formed an invaluable network of discussion and collaboration, so I would like to thank: Dr. Mauro Malizia, Dr. Herme G. Baldoví, Dr. Michael Sargent, Dr. Ross Hubble, Dr. Peng Dai, Dr. Martin Chan, Dr. Matthias Schnellman, Dr. Paul Hodgson, Clayton Rabideau, Sam Gabra, Kenny Kwong and Alexander Harrison in addition to members of Dr. Scott's group in the Engineering Department.

I would like to thank, for their wise words of advice and support: Dr. Patrick Barrie, Dr Laura Torrente Murciano, Dr. Ljiljana Fruk, Prof. Róisín Owens, Dr. Jethro Akroyd, Dr. Sarah Rough and Bob Skelton.

Within the department many staff have helped me to complete my research safely. I would like to thank Christopher Bawden, Pete Claxton and Dr. Simon Butler, Phil Salway and Sharada Crowe for their capable help with anything and everything I threw their way. I must thank the talented workshop staff for whom no job was too obscure and the I.T. department for their endless expertise at fixing the many faults which I seem to have a knack for inducing in computers.

My time in Cambridge would have been very much fewer memorable without the excellent wipers of CUTwC. I may not have climbed very far through the rantings but I have enjoyed every nurdle and boondock along the way.

A special mention must go to Dr. Rich Roebuck for his advice, support and friendship, and for several vanloads of compost. Without Rich's steering, advice and astute admissions choices I would literally not be where I am today.

To Tony Martin and David Mordecai. Thank you for inspiring and teaching me so much, not just the practical engineering skills I have used to fabricobble my experimental equipment together with but for teaching me how to have fun working in a team and to motivate others.

To my family and friends: I would like to extend a vast thank you for putting up with me and for helping me through to the end of this project with most of my sanity intact. I will endeavour to be slightly less boring from now on.

To my Nanny and Popi: Thank you for supporting me throughout this project, for taking so much interest in the goings on at the University and for keeping me so thoroughly well supplied with fruit cake.

To Mum, Prof. Emma Bond. Quite how you did your PhD part time, in less time than me, whilst raising a family of 5 children and working, I will never understand. Thank you for inspiring me and for your unfaltering belief in me and this project even at times when I doubted that it would ever be completed.

Finally, to my partner and best friend, Isabel. Thank you for understanding me better than I understand myself and for being unbelievably patient. Thank you for picking me up when I was down, reminding me to eat and pushing me to get on with it. Now this thesis has been written I am looking forward to writing the next chapter of our lives, together.

Contents

Declaration.....	ii
Summary.....	iii
Acknowledgements.....	vii
Contents.....	ix
Chapter 1 Introduction.....	1
1.1 Background.....	1
1.1.1 The need for biomass energy with carbon capture and storage.....	1
1.1.2 Chemical Looping Combustion.....	2
1.1.3 Biomass in a bubbling fluidised bed.....	4
1.2 Segregation of fuel particles in gas-fluidised beds.....	5
1.2.1 Consequences of the segregation of fuel particles for fluidised beds.....	7
1.3 Mechanistic studies on the effect of the emission of gas from a particle of biomass on the segregation of the particle.....	9
1.4 Heat transfer from bed to fuel particles.....	10
1.5 Methods of limiting segregation of fuel particles during devolatilisation.....	11
1.6 Objectives of the work described in this dissertation.....	12
1.7 Structure of dissertation.....	13
Chapter 2 Materials and Experimental Methods.....	15
2.1 Bed materials.....	16
2.2. Buoyancy of inert spheres at room temperature.....	19
2.3 2-D fluidised bed experiments.....	21
2.4 Spheres which release gas on introduction to a fluidised bed.....	25
2.4.1 Dry ice.....	25
2.4.2 Spheres of beech wood.....	26
2.5. Fluidised bed experiments on large spheres of alumina or dry ice at elevated temperatures.....	28
2.5.1 Apparatus.....	28
2.5.2 Materials.....	30
2.6. Fluidised bed experiments on the devolatilization of large spheres of beech wood at elevated temperatures.....	34

2.6.3 Transient heating rate of beech particles in a fluidised bed	34
2.7. Rate of emission and composition of the volatile matter	35
2.7.1 Apparatus	35
2.7.2 Methodology.....	39
2.8. Fluidised bed experiments on devolatilization and combustion of beech employing X- radiography	40
2.8.1 Apparatus	40
2.8.2 Methodology.....	42
Chapter 3 The consequences of the defluidised hood on the buoyancy of both inert and gas-producing particles	45
3.1 Introduction.....	45
3.2 Buoyancy of large particles at the surface of fluidised beds	45
3.2.1 Buoyancy of plastic spheres at room temperature	48
3.1.2 Parallel sided defluidised hood.....	51
3.2.3 Tapered defluidised hood	55
3.2.4 The size of the defluidised hood near the surface of the bed	60
3.3 The disruption of the defluidised hood by the emission of gas from the surface of a submerged object	65
3.3.1 Fluidisation of the defluidised hood by ingress of gas from an associated spherical object.....	69
3.4 The maintenance of an elevated fluidised cap of particles owing to the emission of gas from the surface of a buoyant object.....	75
Conclusions	81
Chapter 4 Levitation of devolatilising particles in fluidised beds	84
4.1 Introduction.....	84
4.2 Fluidised bed “Leidenfrost” hypothesis	85
4.2.1 Buoyancy of a sphere assuming the pressure distribution in the fluidised bed is unchanged by the presence of the sphere.	97
4.3 Experimental validation of the fluidised bed Leidenfrost effect	99
4.4 Analysis of the structure of the fluidised bed beneath a gas-emitting cylinder	102
4.4.1 Experiment	102
4.4.2 Analysis.....	105
4.4.3 Results	108

4.7 Conclusions.....	115
Chapter 5 The sublimation of spheres of dry ice in fluidised beds	116
5.1 Method.....	117
5.2 The velocity ratio	120
5.3 Total time for sublimation	123
5.4 Circulation of inert and dry ice spheres.....	125
5.5 Experimental measurement of the heat transfer coefficient	128
5.5.1 Calculation of the heat transfer coefficient	128
5.5.2 Results	129
5.5.3 Discussion	131
5.5.4 Modifications to a steady state heat transfer model using experimental observations.	134
5.5.5 Assessing the steady state assumption	140
5.6 Conclusions.....	142
Chapter 6 Devolatilisation of spheres of beech wood	143
6.1 Analysis of the volatile matter	143
6.1.1 Method	144
6.1.2 Validation using the sublimation of dry ice	147
6.1.3 Results for the devolatilisation of beech spheres.....	150
6.2 The velocity of the volatile matter emitted from beech spheres floating freely in a bed fluidised by air	155
6.2.1 Method	156
6.2.2 The rate of emission of volatile matter	159
6.3 Measurement of the draught of freely floating beech spheres.....	167
6.3.1 Comparing the floating behaviour of inert particles at ambient temperature with particles emitting gas at 600°C.....	169
6.3.2 Experiments at 500 and 600°C	171
6.3.3 Discussion	176
6.4 Conclusions.....	184
Chapter 7 Conclusions.....	186
Chapter 8 Further Work.....	193
References	197
Nomenclature.....	204

Appendices	207
A 2.1 Analysis of the size distribution of bed particles	207
A 2.2 Deconvolution	208
A 2.3 Image processing	210
Appendix 3: Defluidised Hoods	213
A 3.1. Maximum height of a conical defluidised hood on top of a sphere.	213
A 3.2 Ratio between the volume of a conical pile of bed material above a sphere and the sphere itself.....	214
A 3.3 Volume of the fluidised cap.	215
A 3.3.1 Cylindrical Geometry.....	215
A 3.3.2 Spherical Geometry.....	217
Appendix 4: A Model for a Floating Particle Assuming a Leidenfrost Mechanism	218
A 4.1. Derivation of cylindrical stream function solution for $\delta = 1$	218
A 4.2. Parameters used for analysis of a gas-emitting sphere in a porous medium in Comsol	224
Appendix 5: A Model for Heat transfer to a Particle Emitting Gas.....	226
A 5.1 Modified Agarwal (1991) heat transfer model.....	226
A 5.1.1 Particle convective heat transfer coefficients.	226
A 5.1.2 Gas convective heat transfer coefficient	230
A 5.1.3 Radiative heat transfer.....	232
A 5.1.4 Weighting	233
Appendix 6: Combustion.....	235
A 6.1 Stoichiometric flowrate calculations for combustion of volatile matter for section 6.1.1.....	235
A 6.2 Stoichiometric flowrate calculations for Section 6.2.1.....	236

Chapter 1 Introduction

1.1 Background

1.1.1 The need for biomass energy with carbon capture and storage

The global average temperature is predicted to rise by between 2.8 and 4.6°C from pre-industrial levels by 2100 (IPCC, 2021), owing to the unchecked emission of anthropogenic CO₂ and other greenhouse gases. The accompanying environmental consequences will be severe. The Paris agreement has been signed by 195 countries pledging to reduce their greenhouse gas emissions to limit the global average temperature rise to be less than 2°C (UNFCCC, 2015). Fuss *et al.* (2014) outlined cost-effective options to avoid exceeding this temperature rise by reducing the net emission of CO₂. They demonstrated that most scenarios include the combustion of biomass-derived fuels, and capturing and storing the CO₂, so-called bio-energy with carbon capture and storage (BECCS). On the basis that the production of biomass does not result in net CO₂ emissions to the atmosphere, the capture of the CO₂ from the combustion of biomass and its sequestration in the Earth should give an overall removal of CO₂ from the atmosphere. There are, of course, major assumptions, for example, that the production of the biomass does not use substantial amounts of fossil fuel and does not release the CO₂ already sequestered in the land. Fajardy and MacDowell (2017) performed life cycle assessments for possible BECCS plants and concluded that, although the amount of time before the process became a net remover of CO₂ was sensitive to the emissions arising from fertilising, irrigating, harvesting, crushing and transporting the crop, BECCS was a dependable option for the permanent removal of CO₂ from the atmosphere. Fuss *et al.* (2014) asserted that, for any comprehensive CO₂ removal strategy to be deployed, the cost of emitting CO₂ to atmosphere and, therefore, the reward for negative emissions, must rise as part of a global regulatory framework, not currently extant. Consequently, at the time of writing no large scale BECCS schemes are in operation.

To implement BECCS requires co-operation amongst many industries and disciplines, because the core steps in the BECCS process are as follows:

1. The growth and harvesting of woody fuel crops or the utilisation of bio-derived waste products such as agricultural residues.
2. The biomass fuel must be transported to the site of utilisation; this often involves drying and pelletisation prior to the transport, to increase the energy density of the fuel and decrease the environmental impact of shipment.
3. Combustion or gasification of the biomass in combination with a carbon capture scheme to remove the CO₂ from the exhaust gas produced in the process. The main aim of the thermal treatment is to extract useful energy or chemical feedstocks from the fuel.
4. The captured CO₂ stream is compressed and delivered to a burial site before long-term sequestration within deep geological formations.

The feasibility of steps 1, 2 and 4 are beyond the scope of this work, which focuses on step 3 where biomass is combusted or gasified in preparation for carbon capture and storage.

A techno-economic assessment comparing four possible BECCs schemes was performed by Bhave *et al.* (2017). The four schemes investigated were: (i) capture of CO₂ by dissolution using amines from the flue gases from conventional pulverised fuel (pf) boilers burning biomass, (ii) pf boilers using biomass with the oxidant being a mixture of CO₂ and O₂, the latter produced by the liquefaction of air, (iii) gasification of biomass in a mixture of O₂ and steam, followed by removal of the CO₂ by physical absorption from the synthesis gas and subsequent combustion of the synthesis gas in a combined cycle gas turbine with air and (iv) chemical looping combustion (CLC) of biomass. Bhave *et al.* (2017) estimated that CLC with biomass feedstocks gave the lowest cost of CO₂ captured, with the lowest capital cost of implementation and resulted in the lowest costs of electricity. However, it was acknowledged that chemical looping combustion had a lower Technology Readiness Level than the other technologies investigated and that there were fewer than 10 pilot plants with, at most 3 MW_{th} capacity. Therefore, the estimates of cost for chemical looping combustion of biomass carried a large amount of uncertainty.

1.1.2 Chemical Looping Combustion

The overall scheme for chemical looping combustion of a gaseous fuel is shown in Fig. 1.1. A fuel is oxidised in a fluidised bed “fuel reactor” using particles of a solid metal oxide, *MeO*, termed an “oxygen carrier”:



The exhaust from the fuel reactor is largely CO₂ and steam. The reduced oxygen carrier is transferred to the “air reactor” where it is oxidised:

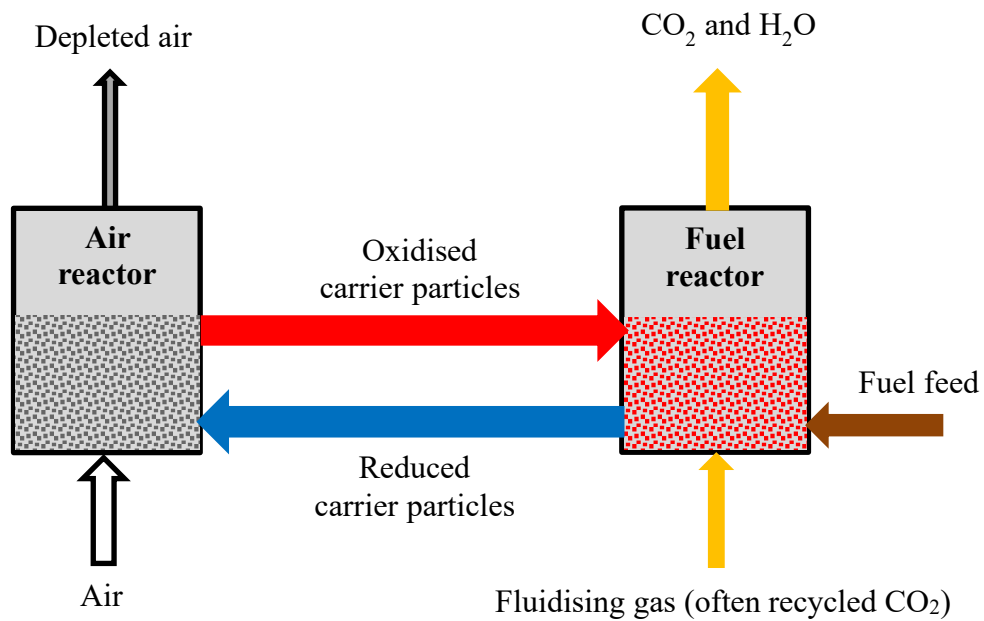
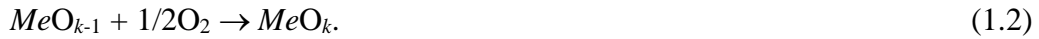


Fig. 1.1. Schematic diagram of chemical looping principles showing how the separation between the fuel and the air is maintained and, consequently, the exhaust gas from the fuel reactor contains no nitrogen.

Overall, the fuel has been combusted with the same heat evolved as for conventional combustion in air; however, the atmospheric N₂ and the CO₂ product are kept inherently separate. Consequently, a major cost associated with CO₂ capture, the separation of CO₂ from the exhaust gases, is avoided. The above introduction to CLC has been made using the assumption that the fuel is gaseous. Chemical Looping Combustion requires good contact between the fluid and the solid phases and therefore an added complication arises when combusting solid fuels because transfer of oxygen from a solid oxide to the solid fuel by particle contact will be impractically slow. This can be circumvented by either gasifying the solid fuel *in situ* and reacting the gases with the bed solids or by employing metal oxides which release gaseous oxygen.

Chemical looping can also be used to partially oxidise a solid fuel to produce synthesis gas in a process known as Chemical Looping Gasification (CLG). Both CLC and CLG are usually performed in bubbling fluidised beds where the solid fuel is introduced into a dense fluidised phase. The bed material is transported pneumatically, between the air and fuel reactors (Grace and Lim, 2013).

1.1.3 Biomass in a bubbling fluidised bed

When introduced into a bubbling fluidised bed at temperatures exceeding about 700 K, a particle of biomass undergoes four successive transformations, which can overlap, thus:

1. Heating and drying

Moisture trapped in the porous structure of the biomass particle is driven off. In fluidised beds the drying process usually occurs rapidly and near the point of fuel injection to the bed.

2. Devolatilisation

As the particle is heated further, volatile matter (VM) is given off. Biomass typically contains a very high proportion of VM which is quickly given off at this stage and can account for more than 70% of the fuel's heating value (Chirone *et al.*, 2004). The released VM comprises a mixture of gaseous compounds resulting from the thermal decomposition of the fuel. The mixture is difficult to characterise owing to its complexity, as discussed by Li and Suzuki (2009). As this step occurs, the structure of the particle becomes more porous.

During devolatilisation, the emission of gas can be so vigorous that the oxidant gas present in the reactor is prevented from contact with the fuel particle and, consequently, devolatilisation occurs in the absence of oxygen, even if the fluidising gas contains oxygen.

3. Char combustion or gasification

Once the VM has been driven off, a highly porous structure of carbon and inorganic elements, known as char, remains. Combustion or gasification of the char is slow, compared to devolatilisation (Nilsson *et al.*, 2011); however, rates of conversion vary greatly depending on the fuel. The location of the char within the bed depends on its density and size relative to the bed material. The char can break down by attrition towards the end of this step.

4. Ash circulation and attrition

After char gasification or combustion, the ash remains, comprised of the majority of the inorganic elements from the parent fuel. The physical properties of the ash vary greatly depending on the properties of the parent fuel and the bed temperature. If the ash is friable, very fine particles of ash will be produced which will be eluted alongside fine particles of char. If the bed is operating near the ash fusion temperature, the ash can soften and begin to clump bed particles together, causing significant operational difficulties. A purge is required within the system to remove the ash from circulation to avoid issues associated with a large ash inventory such as agglomeration of the bed material.

Consequently, during thermal treatment in a fluidised bed, a particle of biomass undergoes significant changes. The difference in mass and size of the particle between the original biomass and the subsequent char can result in different mixing or segregating behaviour at the different stages of conversion in fluidised beds (Scala and Solimene, 2013). Drying and devolatilising particles are referred to in this dissertation as “gas-emitting” particles as distinct from those which do not emit gas or, “inert” particles.

1.2 Segregation of fuel particles in gas-fluidised beds

Bubbling fluidised beds handling solid fuels do not require the fuel to be reduced to as small a particle size as for pulverised fuel combustion, resulting in a saving in energy required to grind or mill the fuel. Hurskainen and Vainikka (2016) commented that, for a bed of 1 mm diameter particles, the fuel particles can be as much as 80 mm in diameter for bubbling fluidised bed combustion. The particles of fuel are therefore significantly larger than the bed particles and, in the case of biomass, are typically less dense than the particulate phase. Consequently, a fluidised bed fed with biomass is typically described as a “jetsam-rich” bed. The terms “flotsam” and “jetsam”¹ have been used widely in the literature to describe particles with a

¹ The terms “jetsam” and “flotsam” have been used extensively in the literature to describe particles with a tendency to sink and float, respectively. Referring to the original and legal definitions of jetsam and flotsam, both refer to floating objects. Therefore, “flotsam and lagan” or “flotsam and derelict” would be more correct, if less conventional terminology to refer to particles which float and sink in fluidised beds.

tendency to float or sink in a fluidised bed, respectively. However, these terms can only be used to describe the behaviour of a particle when related to another *i.e.* a flotsam particle in one fluidised bed may behave as a jetsam particle in another.

Nienow *et al.* (1978) formed an empirical correlation, which stated that when the proportion of flotsam particles was small and they were much larger than the bed particles, the depth to which the flotsam particles would sink into the bed was a function only of $(U-U_{mf})^{0.5}$. The insensitivity of the segregation of flotsam particles to differences in density was supported by Hoffmann *et al.* (1993) in their model. Nienow and Chiba (1985) asserted that large inert particles, of similar density to the bed particles, should sink back into the bed due to the folding, bubbling flow pattern associated with fluidised bed mixing. A great many experimental studies have been carried out to determine the extent of segregation of biomass fuels in fluidised beds at room temperature, *e.g.* Zhang *et al.* (2009), Szücs and Szentannai (2019), Cluet *et al.* (2015), Fotovat *et al.* (2013), and Emiola-Sadiq *et al.* (2021). Such studies fail to recreate accurately the evolution of gas from the biomass particles, or the change in density of such particles during devolatilisation. Scala and Solimene (2013) stated that the segregation characteristics of a devolatilising particle can be quite different to an equivalent particle, which is not emitting gas.

Prins *et al.* (1989), Bruni *et al.* (2002), Madrali *et al.* (1991), Urciuolo *et al.* (2012) and Ruoppolo *et al.* (2021), amongst others, carried out experiments with a range of solid fuels in bubbling fluidised beds at elevated temperatures and observed that the particles of fuel floated on the surface of the fluidised bed during devolatilisation. Solimene *et al.* (2003) stated that this behaviour occurs even at fluidising velocities substantially higher than that required to fluidise the bed incipiently. Further to this, Cook *et al.* (2003) observed that, once a particle of bituminous coal had finished devolatilising, during which it had floated on the top of the bed, it sank and circulated around the bed as a particle of char. Bituminous coal has a higher density than most biomass fuels but such an observation indicates that the emission of gas is sufficient to increase the buoyancy of a particle which would, otherwise, sink into the bed. Similarly, Yang *et al.* (2020) found that particles of compressed rice husk, despite having a density of around 1600 kg m^{-3} , still spent 20%, rising to 50% of its time at the surface of a fluidised bed with a density of the emulsion phase of around 1450 kg m^{-3} . Biomass fuels mostly have a higher proportion of VM than bituminous coal and so any such increase in buoyancy on account of the emission of VM is likely to be more pronounced for biomass than for the coal. Prins *et al.*

(1989) also found that once devolatilisation had finished, newly-formed char particles quickly became well mixed in the bed.

It is preferable for a fuel to be well distributed throughout a fluidised bed as the tendency for biomass fuels to accumulate at the surface of fluidised beds during devolatilisation has been found to complicate the utilisation of biomass in CLC systems.

1.2.1 Consequences of the segregation of fuel particles for fluidised beds

Owing to the tendency for solid fuels with a high proportion of VM to remain close to the surface of the bed during devolatilisation, a large proportion of the VM given off by the fuel is emitted into the freeboard, rather than percolating through the fluidised bed material. The evolution of a large proportion of the fuel's heating value as VM in the freeboard, causes operational difficulties for a range of fluidised bed applications.

Fluidised bed combustion

One of the benefits of fluidised bed combustion is that the combustion can occur at reduced temperatures and produce lower concentrations of NO_x compared with pulverised fuel combustion. If VM is emitted directly into the freeboard, it will combust there and lead to unwanted elevated temperature of freeboard gases promoting NO_x formation. A further benefit of a bubbling fluidised bed is the good heat transfer coefficients. If a large proportion of the heating value of the fuel is evolved in the freeboard this advantage is negated and can result in the bed temperature dropping and extinction of the process (Scala & Chirone, 2004).

Fluidised bed gasification

Fluidised bed gasification of biomass and waste feedstocks can provide a competitive means of generating bio-hydrogen, or synthesis gas and providing a solution for waste disposal (Amaya-Santos *et al.*, 2021). The segregation of the feedstock particles during devolatilisation can lead to a high load of VM in the product gas, which requires separation downstream of the reactor (Scala and Solimene, 2013). The product gas from the fluidised bed gasification of biomass contains ~10 g m⁻³ (STP) VM according to Milne *et al.* (1998), although this varies greatly depending upon the process conditions and biomass feedstock. VM present in the product gas, even in small quantities, will limit the utility of the gas: Milne *et al.* (1998) tabulated the tolerances of downstream equipment and concluded that the VM concentration

in the fuel gas should not exceed 0.5 mg m^{-3} (STP) if used in a direct-fired gas turbine: fuel cells require even tighter tolerances on VM. Some successful means of cleaning up syngas have been demonstrated, for example, Materazzi *et al.* (2019) handled the heavy burden of VM from the fluidised bed gasification of refuse derived fuel by using a downstream plasma converter to produce a stream of clean syngas.

Chemical Looping Combustion

If the VM is emitted by particles of biomass residing at the surface of the bed it enters the freeboard directly and must be combusted downstream of the fluidised bed so that the product gas meets the requirements for sequestration of the CO_2 . This is achieved in a step called oxygen polishing, which Lyngfelt *et al.* (2019) concluded was one of the major additional operating costs associated with CLC compared with a circulating fluidised bed boiler. Lyngfelt and Leckner (2015) suggested that oxygen polishing might add 6.5 €/tonne to a total cost of 20 €/tonne of CO_2 captured to the operating cost. In fact, oxygen polishing is so important to the economics of CLC that the oxygen demand has become an important means of comparing the performance of CLC pilot plants. Adánez and Abad (2019) and, Mendiara *et al.*, (2013) found that the chemical looping combustion of biomass required a higher oxygen demand than that of coal.

If the concentration of unburnt VM in the product gas can be reduced to a small amount, for example by using a second fuel reactor to bring the VM into close contact with more bed material, as investigated by Gayán *et al.* (2013), the subsequent small proportion of unburnt volatiles could be condensed from the exhaust stream, thus omitting the need for an oxygen polishing step. Additional fluidised beds add complexity to the management of the inventory of bed materials between the beds. To that end, Devi *et al.* (2003) asserted that it is desirable to utilise primary methods for reducing VM loads in the gasification itself rather than secondary methods, *viz.* downstream clean-up of the gas. In the case of fluidised bed gasification, Bridgwater (1994) asserted that the amount of tar in the product gas could be greatly reduced by ensuring that the fuel particles remained submerged. Therefore, the mode of segregation during devolatilisation of particles of biomass was studied to understand how to minimise devolatilisation directly to the freeboard such that secondary cleaning of the product gas could be reduced.

1.3 Mechanistic studies on the effect of the emission of gas from a particle of biomass on the segregation of the particle

Currently, the only segregation mechanism in aggregatively fluidised beds to receive major attention in the literature is that resulting from the motion of bubbles. The VM produced by a biomass particle deep within a fluidised bed pushes the bed material away and forms a bubble. Fiorentino *et al.* (1997 a) and Bruni *et al.* (2002) investigated how the bubble of VM can lift the fuel particle towards the surface of the bed. They found that, typically, as bubbles rise in fluidised beds, they cause a column of bed material to be lifted through the bed behind them in what is known as a wake. If the biomass particles are carried atop this wake all the way to the surface of the bed, it is known as “single bubble segregation” (SBS). In “multiple bubble segregation” (MBS), the biomass detaches from the bubbles it forms so travels to the surface in a series of steps behind a string of bubbles. Rees (2005) investigated a possible criterion for the change between SBS and MBS for a devolatilising particle of sewage sludge in a bed of silica sand, predicting that for SBS the particle should be entirely supported by the pressure of the gas percolating through the wake material at the base of the bubble. Rees (2005) showed experimentally that, when the rate of gas production exceeded a critical value depending on the fluidisation conditions, then SBS was more likely to occur than MBS, and consequently that the particle would rise very quickly to the surface of the bed.

The behaviour of the biomass particles once they reach the surface of the bed is undocumented. It is unknown currently if biomass particles sink into the bed a short distance before rising again *via* one of the bubble segregation mechanisms or if they remain so close to the surface that a bubble cannot form around them. The observations of Prins *et al.* (1989), Bruni *et al.* (2002), Madrali *et al.* (1991), Urciuolo *et al.* (2012), Cooke *et al.* (2003) and Ruoppolo *et al.* (2021) that particles float at the surface of fluidised beds during devolatilisation may suggest that there could be further phenomena caused by the emission of gas from the fuel particles which keep them at the surface.

1.4 Heat transfer from bed to fuel particles

The work of Fiorentino *et al.* (1997 a), Rees (2005), and Bruni *et al.* (2002) showed that the gas evolved from a devolatilising wood particle in fluidised beds pushes the bed particles away from the wood particle. Cui and Grace (2007) pointed out that characterising the hydrodynamic interaction between the biomass particles and the bed particles, and how this changed with bed temperature, was a key area in which more research was required. The rate of devolatilisation depends on both internal and external heat transfer. Gomez-Barea *et al.* (2010) and Kersten *et al.* (2005) stated that the effect of the heat transfer coefficient for particles of biomass of diameter larger than 5 mm on the conversion time can be as high as 20%. Hence, a poor estimate of the heat transfer coefficient can have an impact on the accuracy of studies which model the conversion time and rate of evolution of VM of biomass particles in fluidised beds.

Heat transfer from a bubbling fluidised bed to inert objects, which are free to move and are larger than the bed particles, has been studied in detail as a means of determining the rate of heat transfer to char particles as they react. Agarwal (1991) created a model for the heat transfer coefficient which accounted for the proportion of time which a sphere, circulating in a fluidised bed, spent traveling upwards in the bubble phase. Parmar and Hayhurst (2002) developed the ideas of Agarwal (1991) by providing expressions for some of the terms which were left as fitted parameters. Parmar and Hayhurst's (2002) model also used multiple heat transfer coefficients in parallel: the gas convective, particle convective and radiative heat transfer coefficients. They argued that all components are significant for fluidised beds of particles of diameter larger than 500 μm , at temperatures exceeding 600°C. For the particle convective component of the heat transfer coefficient it was assumed that a fixed proportion of the heat transfer surface was covered by bed particles and depended only on the voidage at incipient fluidisation. As the fraction of a biomass particle's surface which is covered by bed particles during devolatilisation was shown by Bruni *et al.* (2002) to be significantly lower, because the VM pushes the bed particles away from the fuel particle, the results for the heat transfer coefficient obtained by correlations intended for inert particles will probably be overestimates.

Scott *et al.* (2004) determined the external coefficients of heat transfer between fluidised beds of particles of various sizes at room temperature and particles of dry ice and compared them with experiments using bronze spheres attached to thin flexible thermocouples. A correction was made to account for the transpiration effect of the CO₂ gas emitted by the particle, but

close agreement in the values of heat transfer coefficient between the dry ice and the bronze spheres showed that the fundamental mechanisms for heat transfer were largely unaltered by the emission of gas in their experiments. Hence, it was concluded that the structure of the fluidised bed around the dry ice was similar to that around the bronze spheres. The ratio of the velocity of gas emitted at the surface of the particle, U_d , to the incipient fluidising velocity, U_{mf} , was relatively low ~ 0.025 and so their approach needs to be examined further for the higher rates of gas emission occurring during devolatilisation.

As the rate of heat transfer between the hot fluidised bed and particles of biomass influences the rate of devolatilisation, and the rate of devolatilisation alters the interaction between the biomass particles and the bed material, a study of the hydrodynamic effects of the emission of gas on the bed particles would not be complete without considering the heat transfer coefficient.

1.5 Methods of limiting segregation of fuel particles during devolatilisation

As summarised above, it is desirable to improve the distribution of fuel particles in fluidised beds during devolatilisation to improve the conversion of the VM without resorting to additional downstream processes.

The injection of the fuel deep under the bed, rather than down on to the surface of the fluidised bed, has only a limited effect on reducing the emission of unreacted VM to the freeboard, because devolatilising particles rise rapidly to the surface owing to bubble uplift mechanisms, studied by Fiorentino *et al.* (1997 a) and Bruni *et al.* (2002) and others. Fiorentino *et al.* (1997 b) found that devolatilisation of a 0.5 cm diameter piece of the wood *Robinia pseudoacaci* at 850°C lasted 40 s, but the particles only took 2% of this time to rise from the injection point to the surface of their bed. By altering the bed properties, such as bed particle diameter and bed height, the upward velocity of the particles could be reduced. Rees *et al.* (2006) found that, by increasing the velocity of gas passing through the bed to induce slugging, a devolatilising fuel pellet rose far more slowly than in a bubbling bed and that devolatilisation could be completed before the surface was reached. Slugging beds, however, have been notoriously difficult to scale up from the pilot plant scale to larger sizes (Knowlton, 2013).

An alternative approach is to design structures which prevent the biomass fuel from reaching the surface, either by slowing its rising velocity down or by increasing the path length for the biomass to take using baffles as employed by Patil *et al.* (2007). Li *et al.* (2021) described a “volatiles distributor”, a structure allowing a pocket of gas to form deep within the fluidised bed, into which the biomass particles can be fed. The volatiles are subsequently mixed with the fluidising gas and re-distributed into the bed material above. Once the biomass has finished devolatilising the resultant char is free to mix into the bed material. Such structures represent a greater level of complexity in the construction, operation and maintenance of a fluidised bed as any submerged structure will be susceptible to abrasion from the bed material. It may, therefore, be preferable to find operating conditions under which segregation of biomass does not occur. This approach was used by Żukowski and Berkowicz (2019) who used a very low-density bed material, cenospheres, to improve the axial distribution of paraffin wax during combustion in a bubbling fluidised bed combustor.

1.6 Objectives of the work described in this dissertation

The overall aim of this dissertation is to investigate how the VM, which is rapidly emitted by particles of biomass during devolatilisation, interacts with the fluidised material around it. The aim of the work is to determine if, and how, that interaction changes a) the tendency of the biomass particles to segregate axially in a fluidised bed, and b) the heat transfer coefficient between the bed and the particles. The research has been conducted with the intention of exploring means of improving the contact between the VM and the bed material and, thus, improving the performance of fluidised bed processes involving biomass. The specific objectives for this dissertation arise from the literature discussed in Sections 1.2 – 1.5:

1. To determine if biomass particles rise to the surface of the bed *via* one of the bubble segregation mechanisms and then sink down into the bed to particular depths before rising up again in a cycle or if they remain so close to the surface of the bed that a bubble cannot form around them.
2. To determine the means by which a particle of biomass can float at the surface of the fluidised bed during devolatilisation, where an inert particle of equivalent size and density would be expected to sink.

3. To determine the effect of the rate of gas emission on the structure of the bed around a gas-emitting particle and segregation.
4. To determine if changes to the structure of the fluidised bed close to a gas-emitting particle should be accounted for in heat transfer models.

1.7 Structure of dissertation

The work to explore the above objectives is described in the proceeding chapters. In brief: Chapter 2 outlines the materials and experimental methods, which are used throughout the remainder of this dissertation.

In Chapter 3, the structure of the fluidised bed above a gas-emitting particle was investigated both when the particle is deep within the bed and when it is close to the surface of the bed. The interaction between the bed material above the particle and the gas being emitted by the particle has also been studied.

Chapter 4 investigated the hypothesis that the emission of gas increases the buoyancy of a gas-emitting particle at the surface of a fluidised bed by examining the pressure distribution in the fluidised material around it, first analytically, then experimentally. Observations were made of the structure of the bed material underneath a gas-emitting particle with a high speed camera.

In Chapter 5, experiments are described where spheres of dry ice were used to simulate a devolatilising particle of fuel, free to circulate in a hot fluidised bed. Their behaviour at the surface of a fluidised bed under a variety of conditions was observed and the rate of emission of gas was measured and compared with the predications of Chapters 3 and 4. The experiments with dry ice were also used to calculate the heat transfer coefficient between the dry ice and the fluidised bed. The resulting values of heat transfer coefficient were compared with the predictions from the literature.

In Chapter 6 a new technique was developed to allow the molar rate of production of VM from biomass to be calculated from measurements of CO₂ and CO in the off gas from a fluidised bed combustor. The technique was used to find the rate of gas emission of spheres of beech wood in a large fluidised bed at elevated temperatures. Additionally, the position of spheres of beech wood, during devolatilisation, was observed using X-radiography. The two simultaneous measurements allowed the theory developed in Chapters 3 and 4 to be applied and examined in the context of a real biomass and fluidised bed system. The applicability and validity of the

theory of Chapters 3 and 4 was then examined in a wider context to allow a series of criteria to be developed to determine whether a gas-emitting particle is likely to sink or float in a fluidised bed. The criteria were then used to determine if any practical conditions exist under which particles of biomass can be induced to mix well in a fluidised bed during devolatilisation.

Chapter 2 Materials and Experimental Methods

This Chapter is structured as follows.

Section 2.1 covers the properties of the particulate solids used as bed materials throughout the study.

Section 2.2 describes the properties of inert spheres used in the experiments in Chapter 3 to determine their tendency to sink or float in a fluidised bed.

Section 2.3 describes the design and use of a room temperature, pseudo-2-D bed built to investigate how the fluidised medium interacts with a large particle, which, in turn, is emitting gas into the fluidised bed. These experiments provided insight into the validity of the theory developed in Chapters 3 and 4.

Section 2.4 describes the properties of the gas-emitting spheres studied for their tendency to float when introduced to a fluidised bed.

Section 2.5 details the experimental work undertaken to determine (i) whether or not the emission of gas by a solid fuel particle increases its apparent buoyancy, and (ii) the extent to which the emission of gas contributes to the segregation of devolatilising fuel particles. In addition to investigating circulation, the experimental work of Section 2.5 was also used to investigate the external heat transfer coefficient from the fluidised bed to the devolatilising particles which is discussed in Chapter 5.

The rate at which the centre of spheres of beech heat up, once plunged into a hot fluidised bed, was determined by means of the experiment described in Section 2.6.

Section 2.7 describes apparatus to determine the composition of the gas that a sphere of biomass emits as it heats up. The experiment was designed in order that the velocity of the gas, as it leaves the devolatilising beech sphere, could be estimated in the experiments described in Section 2.8 and used in Chapter 6.

The use of a fluidised bed, much larger than those used in Sections 2.5 to 2.7, equipped with an X-ray imaging device is explained in Section 2.8. The X-ray images allowed the vertical position of the beech spheres in a fluidised bed to be found. Gas analysis was performed

simultaneously so that the rate of devolatilisation could be compared with the vertical position of the devolatilising sphere.

2.1 Bed materials

A variety of Geldart Group B bed materials was used. All materials were graded into size fractions, by passing through a series of sieves using a sieve shaker. A sample of each size fraction was analysed with a Morphologi G3 Microscope (Automated Particle Size Characterisation System) to obtain the mean circle equivalent diameter.

The values of voidage for each bed material in its settled state were obtained by pouring a known mass of particles into a vertical tube provided with a gas distributor at its lower end. With no gas flowing through the tube, and at ambient conditions, the vertical distance between the distributor and the top surface of the bed was measured at four locations around the perimeter of the bed and the average was taken. The bulk density of the untapped material was calculated. Using known values of particle density, the voidage of the untapped packed bed was therefore found. Air was then metered into each bed of particles. The air flowrate was adjusted until the bed of particles was incipiently fluidised, as described below. The height of the bed was again measured allowing the voidage of the incipiently fluidised bed to be determined. The results are summarised in Table 2.1.

Table 2.1. Properties of fluidised bed materials.

Material	Sieve size / μm	Mean Circle Equivalent diameter. / μm	Particle density / kg m^{-3}	Voidage of untapped packed bed	Voidage of incipiently fluidised bed
Silica Sand (David Ball Group, Fraction C)	600-750		2680	0.37	0.42
	425 - 600	637			
	355-425	512			
	200-355	432			
	180 - 200	262		0.43	0.46
Porous gamma alumina (Puralox NWA-155, Sasol Germany GmbH)	355-425	440	1430 ¹	0.45	0.48
	200-355	292			
	150-200	207			
Porous gamma alumina particles doped with iron oxide.	200 -355		1682 ²	0.45	0.48
Alpha alumina	425 - 600		3950	0.49	0.5

¹calculated from the porosity, 0.55, (Schnellmann, 2018) and the skeletal density, 3180 kg m^{-3} . (Dudák *et al.*, 2014)

² 15 wt% loading onto particles of 1430 kg m^{-3} (Schnellmann, 2018)

The molar flowrate of gas was measured using a calibrated, variable-area flow meter. The gas was assumed to be ideal and, in experiments at elevated temperatures, was assumed to have reached bed temperature at the end of a short “entry region” just above the distributor. The area of the distributor was measured so that the volumetric flowrate of gas at the distributor could be used to calculate the superficial velocity. A stainless steel 3 mm diameter tube was lowered into the fluidised bed until its lower end rested on the distributor, as shown in Fig. 2.1.

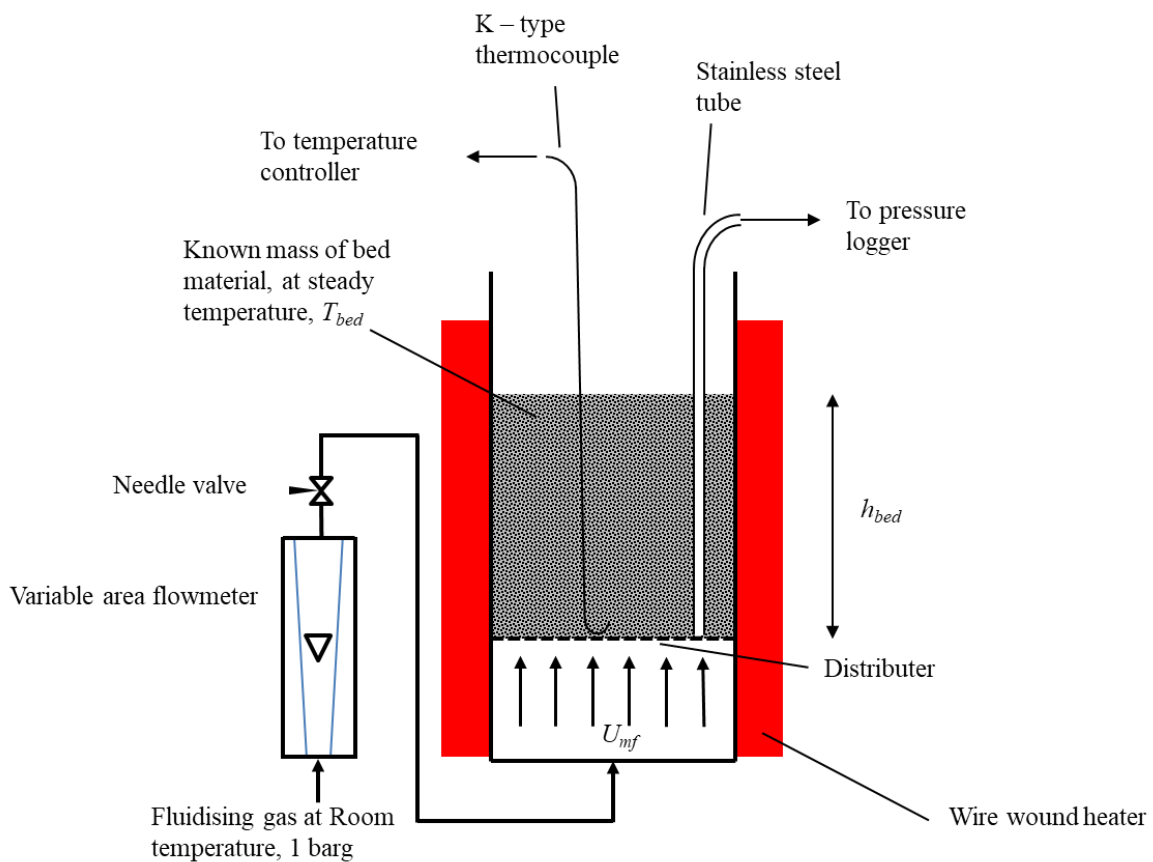


Fig. 2.1. Example experimental set up for determining the incipient fluidising velocity, U_{mf} , using a known mass of bed material. A calibrated variable area flowmeter is used to measure the molar flowrate of gas at 1 barg, room temperature, flowing into the bed. A needle valve controls the flowrate. The bed is assumed to be at a uniform temperature T_{bed} which is controlled using a thermocouple and heater. A stainless-steel tube inserted from the top of the bed allows the gas pressure at the distributor to be measured.

The upper end of the stainless-steel tube was connected *via* a silicone rubber tube to a pressure logger. For each bed temperature and bed material used throughout this dissertation, U_{mf} was found by measuring the pressure at the distributor at a range of values of U/U_{mf} , progressing

from high to low values. The intersection between the lines of best fit for each linear region in the resultant graph gave the value of U_{mf} as demonstrated in Fig. 2.2. The incipient fluidisation velocity was measured for each bed material for each bed temperature investigated and in every size of fluidised bed used throughout this work. Hence, no specific bed diameter has been provided in the following description of the apparatus. The large number of times U_{mf} was measured prevents the inclusion of the results of U_{mf} in this section. The pressure gradient in an incipiently fluidised bed should be equal to the weight of the bed material divided by the area of the bed. This separate calculation was used to validate the pressure at which U_{mf} was recorded.

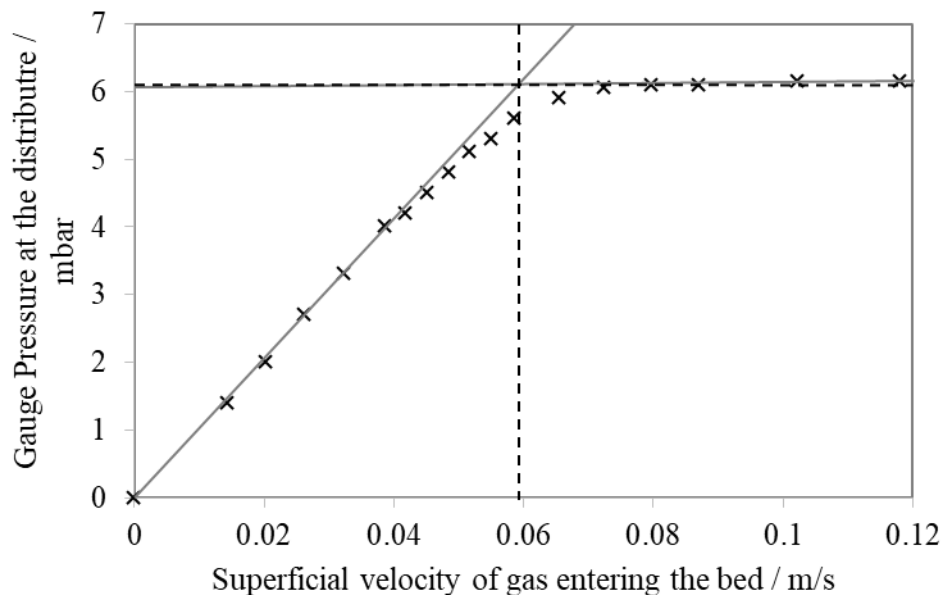


Fig. 2.2. Gauge pressure, measured at the distributor of a fluidised bed of doped porous alumina particles in the 2-D bed described in Section 2.3, at room temperature. The incipient fluidising velocity is given by the intersection between the lines of best fit (—) for measurements when the bed was well fluidised and when the bed was not fluidised. This intersection (vertical broken line) also intersects with the pressure required to just support the weight of the whole bed (horizontal broken line).

2.2. Buoyancy of inert spheres at room temperature

To study inert² spheres of various densities, hollow polypropylene spheres, nominally 0.02 m diameter, were sawn open along their diametral seam. Pieces of steel were glued into the base of the cavity of one of the hemispheres before the hemispheres were re-bonded together with cyanoacrylate adhesive. Each sphere was measured with digital callipers across three axes and weighed such that its density could be determined. The densities of the range of spheres produced are given in Table 2.2.

Table 2.2. The diameters and densities of plastic spheres produced for buoyancy experiments.

Diameter / m	Density / kg m⁻³
0.0197	375
0.0197	569
0.0195	634
0.0197	681
0.0197	691
0.0197	844
0.0197	1031
0.0196	1110
0.0196	1166
0.0197	1310
0.0197	1380

The rising or sinking behaviour of the spheres was studied in beds of various particles, incipiently fluidised by air at room temperature and atmospheric pressure, contained within a 0.0295 m i.d. quartz tube and supported by a quartz frit distributor. Millimetre gradations were added to the outside of the tube. Digital photographs were taken from a camera positioned 1 m away from the bed adjusted such that the lens was level with the surface of the bed. From the photographs the vertical distance from the surface of the bed to the uppermost point on the sphere was measured.

In Chapter 3, the effect of defluidised hoods is explored where the bed material above the spheres can become defluidised and rest on top of the spheres. To investigate this, the spheres were pushed further into the bed to find the depth at which enough bed material had defluidised above them to cause the sphere to sink to the distributor. The diameter of the bed used was only

² Here, an inert sphere is one which does not emit any gas.

1.5 times larger than the diameter of the spheres. The small size of the bed, relative to the size of the sphere, was necessary to allow spheres beneath the surface of the bed to be located and observed from the side of the bed, as shown in Fig. 2.3.



Fig. 2.3. A large void, visible, at the side of a fluidised bed, of 0.03 m dia. The void, highlighted in red, is caused by a large, submerged sphere which has come to equilibrium beneath the surface of the bed.

The depth of buried spheres was measured by inserting a thin piece of wire from the top of the bed, moving it slowly towards the submerged sphere until the sphere was observed to be pushed downwards by the wire. The length of wire submerged was measured to find the distance between the top of the sphere and the surface of the bed. The motion up and down the bed of the spheres was likely to have been impeded as the spheres were two thirds the diameter of the bed. Nevertheless, the spheres were still able to reach a steady position within the bed, given sufficient time. Given that the experiment was devised only to find the steady state depth of the spheres, rather than rise velocities, the results were not affected unduly by the narrowness of the bed.

2.3 2-D fluidised bed experiments

A pseudo 2-D fluidised bed apparatus was arranged to study the pressure field around a single, porous, horizontal cylinder held stationary in a fluidised bed. Various flowrates of air could be passed from the inside to the outside of the cylinder, thus mimicking a large, devolatilising particle to some degree.

The 2-D fluidised bed, rectangular in cross-section (5.5 mm × 100 mm) was constructed from two sheets of clear, colourless acrylic as shown in Fig. 2.4. A 6 mm thick strip of Vyon[®] D porous plastic material was sandwiched horizontally between the front and back walls of the bed, 40 mm from the base to form a gas distributor, above which the fluidised material was supported. Air was supplied to the plenum chamber below the distributor *via* a tapped hole in the rear wall. To simulate a cylindrical fuel particle emitting gas, a cylinder of Vyon[®] D (5.5mm thick, 12 mm external diameter) was formed and inserted between the front and rear walls of the bed with its centre 70 mm above the distributor. A 3 mm diameter hole was drilled through the centre of this cylinder and a hole was drilled and tapped in the acrylic wall behind the cylinder. Air was supplied through these holes such that the air could percolate radially from the cylinder. In the rear face of the fluidised bed an array of M4 threaded holes were provided for pressure tapings.

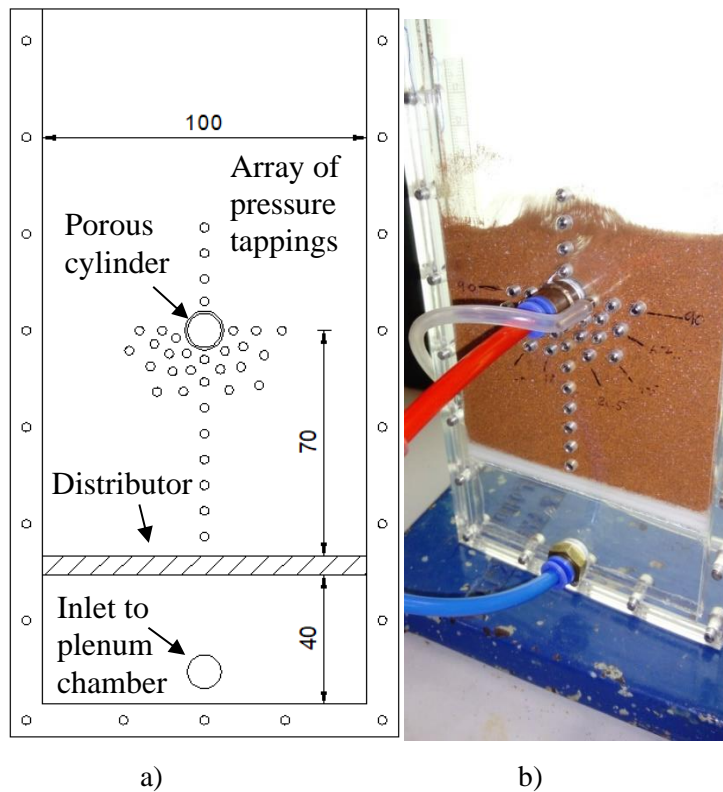


Fig. 2.4 a) Drawing of the front wall of the 2-D bed showing distributor (hatched), inlet to plenum chamber, position of the porous 12 mm cylinder, overall width and the array of pressure tappings.
 b) Photograph of 2-D bed apparatus in operation. Here the bed is filled to above the level of the porous cylinder.

To assemble the fluidised bed the two acrylic walls were bolted together separated by a 5.5 mm thick, U-shaped acrylic spacer: the cylinder and distributor were bonded to both walls using clear silicone sealant to ensure there was no bypassing of gas around these. The assembly was filled with water and air supplied to the cylinder, bubbles were observed emerging uniformly from the surface of the cylinder with no directional preference.

Porous γ -alumina particles (Puralox NWa-155, Sasol Germany GmbH) were impregnated with iron oxide (15 wt%) as described by Schnellmann (2018) such that the particles had a density of 1680 kg m^{-3} . The loading of iron oxide was necessary to permit room temperature fluidisation for long periods of time as without the iron oxide, fluidised beds of silica and alumina particles at room temperature were found to rapidly de-fluidise owing to static electrical effects.

The $\text{Fe}_2\text{O}_3\text{-Al}_2\text{O}_3$ particles were sieved to yield particles of sieve size between 200 and 355 μm , which fluidise as Geldart Group B material. The incipient fluidisation velocity for this material at room temperature was found to be 0.059 m s^{-1} . The $\text{Fe}_2\text{O}_3\text{-Al}_2\text{O}_3$ particles were dark red. A small quantity of bright white γ -alumina particles, containing no iron oxide, were added to the bed and these can clearly be seen as the bright specks shown in Fig. 2.5. The contrast between the white and the dark-red impregnated particles allowed particle image velocimetry to be undertaken.

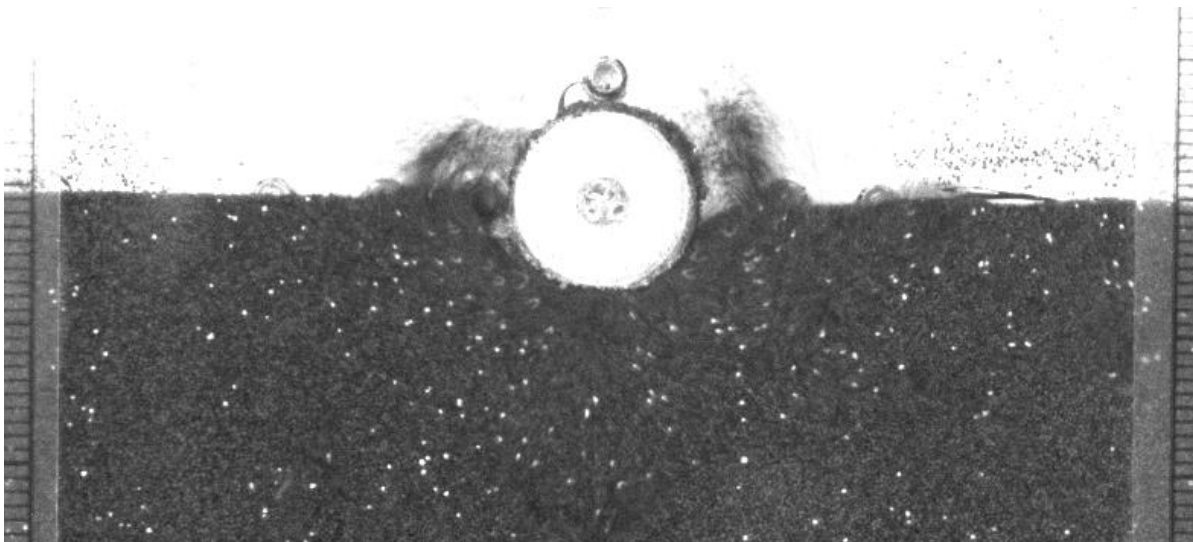


Fig. 2.5. Example of a grey scale image showing the mixture of bed materials – the bright white particles are un-doped γ -alumina, the dark grey particles are impregnated with 15 wt% iron oxide. The white circle is an end on view of the porous cylinder. In this example $\delta = 1$, $U = U_{mf}$ and $U_d = 2U_{mf}$.

In an experiment, the apparatus was filled, whilst at the fluidising velocity of interest, with this mixture of particles to a given bed height. The ratio, $\delta (= h/a)$, was defined as the vertical distance between the surface of the bed and the bottom of the porous cylinder, h , divided by the radius of the cylinder, a . In practice, values of h of 67, 70, 75, and 101 mm were used, giving values of δ of 0.5, 1, 1.8, and 6.2, where $\delta = 1$ describes a cylinder which is semi-submerged, and $\delta = 2$ describes a cylinder which is just completely submerged.

The supply of gas to both the distributor and the porous cylinder was controlled using needle valves. The flow rate was set using variable area flow meters, calibrated using a bubble film flow meter. Nitrogen was supplied to the distributor at superficial velocities of 0, 0.5, 1 and 2

and 4 times U_{mf} . Air was supplied to the porous cylinder at velocities of between 0 and 4 times U_{mf} (measured at the surface of the cylinder).

A pressure probe was turned from brass with 6 mm length of M4 thread at one end and a 2 mm dia. hole drilled axially through it. When screwed into the side of the 2-D fluidised bed the end of the pressure probe was flush with the inner wall of the bed and so measured static gas pressure. The other end of the probe was machined to be a tight sliding fit into 3 mm o.d. flexible silicone tubing. The tubing was attached in turn to an AMS 5915 pressure sensor mounted in communication with an Arduino, which logged the signal from the sensor every 0.1s. Each measurement was made for 30 seconds over which the mean pressure was calculated.

The array of M4 holes, into which the pressure probe was screwed, were plugged with 6 mm long grub screws so that, when screwed in, the grub screws were flush with the inside of the bed wall. To change the position of the pressure probe, the fluidising gas was switched off and the whole bed was laid horizontally with the wall with the pressure tappings uppermost. The probe and a grub screw could then be switched without losing any bed material.

Greyscale photographs, an example of which is shown in Fig. 2.5, were taken of the bed with a QImaging QICam camera at an acquisition rate of approximately 37 frames s^{-1} using StreamPix ver 3.16.5 software. The camera was aligned perpendicular to, and level with, the surface of the fluidised bed.

PIVlab (William Thielicke, 2020) was used to analyse the photographs. Ensemble analysis was used to obtain the 2-D velocity vector field for each experiment and to generate the time averaged streamlines. A time-averaged image for each experiment was formed by calculating the mean intensity for each pixel position in the set of photographs recorded over 30 s to show the structure of the bed around the cylinder.

In addition to photographs illuminated from the front that gave a high contrast between the red and white particles, as shown in Fig. 2.5, a further, backlit, set of photographs was taken. The back lighting gave a better contrast between the emulsion phase and the bubbles in the bed.

For a limited number of experiments, additional observations of the 2-D bed were made using a QImaging QICAM Fast 1394, monochrome 12 bit camera at 150 frames s^{-1} , processed with

StreamPix 3.18.2 by Norpix in order to observe the rapid changes of the structure of fluidised medium close to the gas-emitting porous cylinder.

2.4 Spheres which release gas on introduction to a fluidised bed

2.4.1 Dry ice

Spheres of dry ice were used as a model for devolatilising particles. They were formed immediately prior to each experiment using an aluminium press. Dry ice pellets, of 9 mm diameter, supplied by BOC, were placed between the inside faces of the press. As the sides of the press were brought smartly together, the aluminium rapidly conducted heat towards the dry ice wherever the dry ice was in contact with the press. Mating pairs of hemispherical divots formed spheres of dry ice, available when the press was opened. Each sphere was removed quickly from the mould using bamboo forceps, the points of which were kept cool in the box of dry ice, and dropped immediately into the fluidised bed.

The repeatability of the sphere production process was evaluated by making 10 spheres, each 8 mm diameter, and weighing each immediately after it was produced. The highest settled value was read from the scales (the mass, of course, dropped as the balance pan of the scales conducted heat towards the dry ice sphere causing a high rate of sublimation of the dry ice). The mean mass of the 10 spheres was 0.35 g with a standard deviation of 0.015 g. Assuming the density of the dry ice to be 1562 kg m^{-3} (Wittemann, 2003), the diameter of the spheres when weighed was 7.5 mm.

During the experiments in Chapter 5, 6 mm particles were used as it was found that it was easier to produce these reliably. Assuming the spheres had zero porosity and were pure CO_2 this gives 0.0041 ± 0.00015 moles of CO_2 per experiment.

In Chapter 6, 8 mm particles were used. Assuming the spheres had zero porosity and were pure CO_2 , the mean mass of a sphere gives 0.0080 ± 0.0003 moles of CO_2 per experiment.

Experiments were limited to the 12 hours immediately following a fresh delivery of dry ice as it was found that whilst in storage the dry ice rapidly became contaminated with water ice and became brittle and difficult to form into spheres.

2.4.2 Spheres of beech wood.

European beech, *Fagus sylvatica*, was chosen as a model biomass as it is readily available in dowel form and has a relatively high density of approximately 700 kg m^{-3} compared to many other, readily-available types of wood. It was found to have a high resistance to the abrasion of a fluidised bed.

Spheres of beech of nominally 10 mm diameter from a proprietary source (Tischlerschuppen, Neunkirchen-Seelscheid, Germany) were purchased. The mass and diameter of each was measured prior to each experiment.

To determine the density difference between a beech sphere and the char produced from it following devolatilisation, individual spheres of beech were dropped into a bed of silica sand fluidised by N_2 at 600°C and allowed to circulate freely. Once devolatilisation had finished, the char was removed using a small stainless-steel mesh net. The char was held near the top of the freeboard of the reactor and allowed to cool in the stream of N_2 to avoid the char combusting as it was removed from the reactor. Once cool, the diameter and mass of the char particle was measured, with results given in Table 2.3. The change in mass of the particles during devolatilisation was more consistent than the change in volume, which appeared to be a loose function of the initial size of the particle.

The 10 mm diameter spheres of beech, devolatilised at 600°C , remained broadly spherical although most had a crack running along the direction of the grain through the middle of the particle and this crack become more pronounced as the char cooled to room temperature. In most cases the char particle subsequently broke cleanly into two hemispheres on handling.

Table 2.3. Change in density of 10 mm beech spheres following pyrolysis in a fluidised bed of silica sand at 600°C. Included for comparison is the mean change in density of two 6 mm diameter beech particles as prepared in Section 2.3.2 and a 10 mm particle containing a piece of lead as used in Section 2.8.

	Initial dia. / mm	Final dia. / mm	Initial mass / g	Final mass / g	Initial density/ kg m ⁻³	Final density/ kg m ⁻³	% change in nominal volume	% change in mass	% change in density
1	10.17	8.08	0.3729	0.0502	677	182	49.8	86.5	73.2
2	10.13	8.20	0.3868	0.0522	711	181	47.0	86.5	74.6
3	10.14	8.31	0.4044	0.0650	740	216	45.0	83.9	70.8
4	9.85	8.10	0.3574	0.0517	715	186	44.4	85.5	74.0
5	10.27	8.07	0.4243	0.0666	747	242	51.6	84.3	67.6
Mean	10.11	8.15	0.3892	0.0571	718	201	47.6	85.4	72.0
Sphere with lead (with lead removed) ¹	9.82	8.15	0.4046 (0.352)	0.059	817 (710)	197	42.7	86.2 (84.2)	75.9 (72.3)

¹ As used in Section 2.8.

The char particles formed at 600°C were approximately spherical. Later in the experiments particles of lead were inserted into the spheres of beech to change the density and to allow the particles to be tracked using X-radiography as discussed in Section 2.8. The presence of a piece of lead inserted into a sphere of beech appeared to not influence the structure of the resulting char significantly.

Beech dust was generated from a 10 mm beech sphere with a clean file. This and a fine powder produced from beech char produced at 600°C were sent for CHN analysis at the Department of Chemistry, University of Cambridge, returning the compositions shown in Table 2.4

Table 2.4. Composition of beech wood and beech char produced at 600°C.

Component	Beech wood composition wt% (Demirbaş, 1997)	Beech wood composition wt% (Wang <i>et al.</i> , 2005)	Beech wood composition wt% Present study	Beech char (pyrolysis in a fluidised bed at 600°C) composition wt%
Carbon	49.5	48.42	45.9	80.1
Hydrogen	6.2	6.01	6.02	2.46
Nitrogen	0.4	0.15	0.00	0.00
Ash	1.4	-	0.47	3.20
Oxygen	41.2	45.42 (balance)	47.61 (balance)	14.24

Individually, a finely ground sample of beech and its char were heated at 5°C min⁻¹ to 900°C in a thermogravimetric analyser (Mettler Toledo DSC 1), TGA, under a stream of N₂ to obtain the ash content as shown in the fourth row of Table 2.4. The oxygen content was estimated by assuming that it made up the rest of the mass of the beech and the char and the resultant composition compared well with that found by Demirbaş (1997) and Wang *et al.* (2005) for beech wood.

2.5. Fluidised bed experiments on large spheres of alumina or dry ice at elevated temperatures

2.5.1 Apparatus

The fluidised bed apparatus consisted of a quartz tube, 0.03 m internal diameter, provided with a quartz frit as a distributor, mounted within an electric tube furnace. The pressure drop over the distributor was typically 0.5 times that across the bed at experimental conditions, thereby ensuring even fluidisation. The fluidised bed was supplied with N₂ at a variety of flowrates provided by variable area flow meters calibrated using a soap film flow meter. A QImaging QICAM digital camera was used to photograph the surface of the bed at approximately 24 frames s⁻¹ by means of a mirror mounted above the bed thus allowing the camera to be mounted well out of the stream of hot gases as shown in Fig. 2.6. A ring lamp was mounted over the quartz tube and ensured uniform illumination of the surface of the bed. An example image is shown in Fig. 2.7, which shows a 3 mm diameter sphere of porous alumina, doped with iron oxide, clearly visible at the surface of the bed of fluidised silica sand particles.

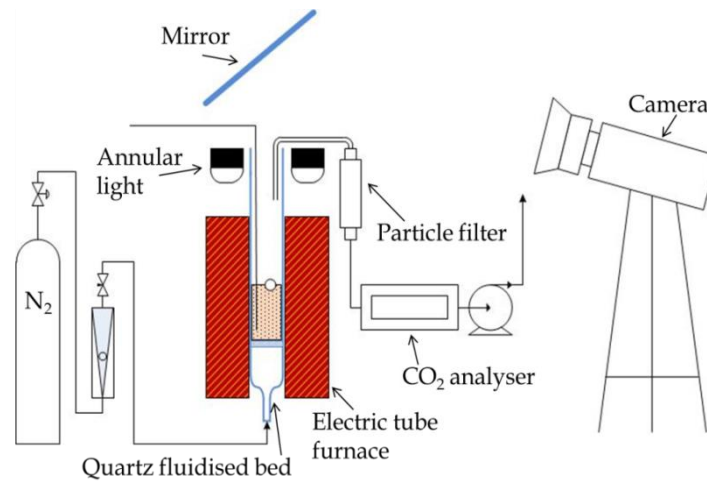


Fig. 2.6. Schematic diagram of the quartz fluidised bed reactor (i.d. 0.03 m) and camera apparatus used.

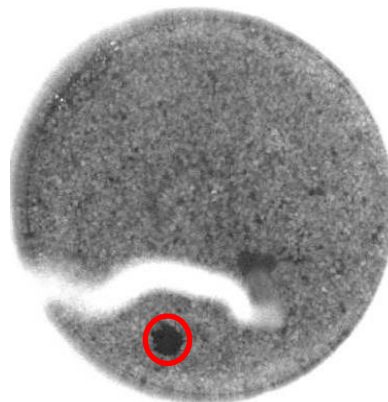


Fig. 2.7. An example image showing the view of the 0.03 m diameter fluidised bed from the top. Visible are the fluidised silica sand particles (grey), the thermocouple extending from the top down into the bed (white), and a single 3 mm diameter particle of porous alumina doped with iron oxide (black, circled in red).

2.5.2 Materials

2.5.2.1 Fluidising Medium

Sieved silica sand (David Ball Group, Fraction C) of fractions 425-600, 355–425 and 200-355 μm were used.

2.5.2.2 Large, inert particles

To study floating behaviour, large particles were made with a variety of densities by taking single spheres of porous γ -alumina of 3 mm diameter, impregnating them with a given quantity of iron nitrate solution and then calcining them at 550°C to form Fe_2O_3 . The spheres originally had a density of 1100 kg m^{-3} and after successive impregnations with iron oxide a range of densities were achieved from 1100 kg m^{-3} to 1500 kg m^{-3} . In a typical experiment, a single doped particle was dropped into a bed of 50 g of silica sand, fluidised at 2, 3 or 4 U/U_{mf} at bed temperatures of 150 to 850°C . The proportion of time that the sphere spent at the surface of the bed was observed. It was necessary to determine the length of time observations needed to be made if a time-averaged behaviour was to be reliably recorded. To find this shortest reliable length of time, observations were made of a 3 mm dia. sphere with a density of 1163 kgm^{-3} as it circulated in a bed of 200-355 μm silica sand particles, fluidised by N_2 at 600°C at $U/U_{mf} = 2$ and 4 for 300 s. The mean proportion of time for which the particle had been visible, since the start of the experiment, was calculated for every frame. Naturally, near the start of the experiment when a particle was visible at the surface each frame contributed greatly to increasing the mean value, as shown in Fig. 2.8. However, after 180 s the mean value stopped changing significantly and settled to fluctuating closely around a single value. Hence, for all further experiments on the circulation of large particles used in this section of work only 180 s of footage was recorded for analysis, assuming that the error introduced to the measurement by the chaotic nature of the fluidised bed was not a function also of the size or density of the spheres which were being observed.

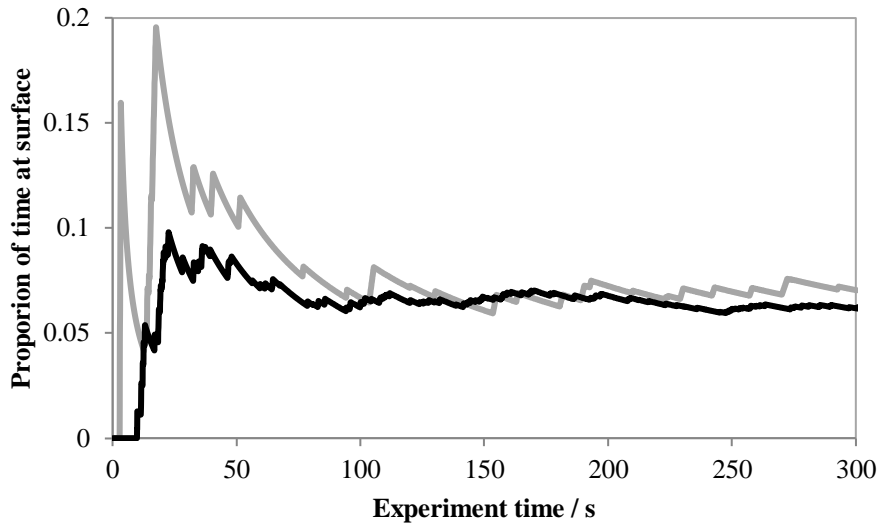


Fig. 2.8. The proportion of time, updated every frame, a 3 mm sphere was visible at the surface of a fluidised bed of silica at 600°C at $U/U_{mf} = 2$ (—) and $U/U_{mf} = 4$ (---).

2.5.2.3 Large particles producing gas: dry ice

Dry ice spheres were prepared as discussed in Section 2.3.1. Immediately following the production of a sphere of dry ice, it was dropped into the fluidised described in Section 2.5.1. The off gas was sampled from the freeboard at a rate of 0.1 L minute⁻¹ (room temperature and pressure) by a pump, passed through a tube of calcium chloride, and subsequently fed through a non-dispersive infra-red (NDIR) analyser (ABB EL3020) before exhausting to local extraction. The voltage produced by the analyser was recorded with time at a frequency of 10 Hz and was linearly proportional to the concentration of CO₂. The analyser was calibrated by using a certified mixture of CO₂ and N₂ (BOC).

The sampling line was modelled as a well-mixed tank in series with a plug flow vessel, such that a characteristic mixing time and delay time could be found by analysing the recorded response to step changes in CO₂ concentration. Assuming that the sampling line was a series of mixed tanks in series with a plug flow vessel did not improve the outcome of deconvolution appreciably and made the deconvolution process more sensitive to noise in the raw signal. By measuring the mixing time, the CO₂ concentration recorded during experiments could then be deconvolved to account for the mixing in the sample line and analyser according to the procedure set out by Scott (2004) and described further in Appendix 2.2.

The characterisation of the sampling line and analyser was undertaken by effecting a step change in CO₂ concentration at the tip of the sampling probe. The response was measured and

an exponential decay was fitted using least squares regression. The mean values from at least three step changes in each direction were taken. The mixing time varied from 1 to 4 seconds across the range of experimental conditions, so a mixing time was determined for each set of conditions which was investigated.

Additionally, step changes in the flow rate of CO₂ were also investigated with the sampling probe inserted at different heights in the fluidised bed and with the source of CO₂ either at the bottom, middle or on the surface of the bed. It was found that the mixing between the source of the CO₂ and the sensor were independent of height at which the CO₂ was released within the bed as shown in Fig. 2.9. a) This was an important result as the dry-ice particles move vertically within the bed over time. If the position in the bed had had a significant effect on the delay in the sampled signal then it would have been impossible to account for mixing and to find the true flowrate at which the particles emitted CO₂ during the experiments.

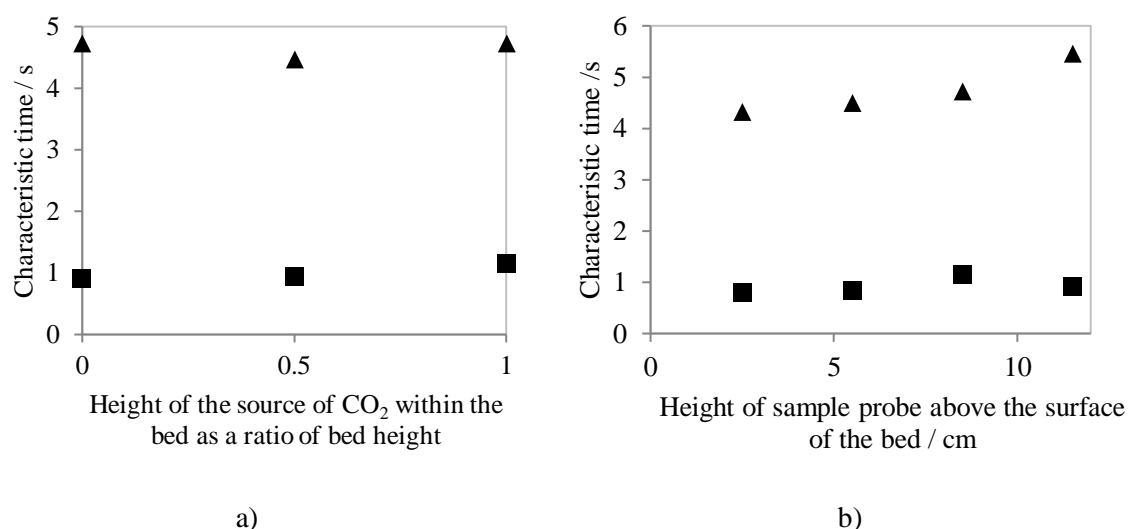


Fig. 2.9. a) The characteristic mixing (■) and delay (▲) times for signal of the analyser for step changes in CO₂ as the position of the source of CO₂ was varied axially in the freeboard of the bed. b) The characteristic mixing (■) and delay (▲) times for signal of the analyser for step changes in CO₂ as the position of the sampling probe was varied.

By varying the height of the sample probe above the bed, the distance between the bed and the sampling probe varied only the delay time as shown in Fig. 2.9 b). The delay in the signal was constant for each experiment and was later eliminated in the data analysis. As the mixing time was independent of the position of the sample probe above the bed the position of the sample probe was not considered important in the experimental set up. The sample probe was positioned far enough down into the freeboard of the reactor to avoid air from the laboratory being drawn in through the top of the freeboard of the reactor.

As in Section 2.5 the surface of the bed was photographed from above. As seen in Fig. 2.10 the view of the bed surface was obscured not only by the thermocouple but also by the sample probe.

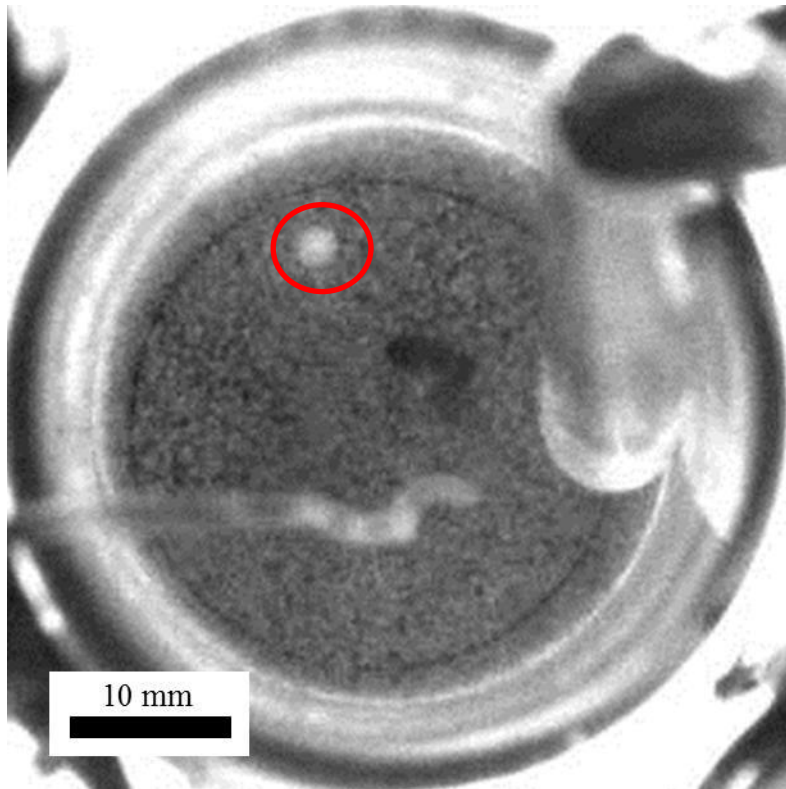


Fig. 2.10 Photograph of the bed surface clearly showing the sample probe (right), the thermocouple (centre to centre left), and a sphere of dry ice (circled, top left).

Observations of the bright white dry ice against the grey background of the sand bed were recorded such that the length of time that a particle visited the surface, the length of time between the particle's visits to the surface and the proportion of time the particle spent at the surface could be found. In analysing the frames, if a dry ice particle was seen, it was assumed to be present for the entire duration of the frame. The particle of dry ice became more difficult to discern from the bed particles as it approached the size of the latter, resulting in fewer observations at that stage. As noted above, the view of the top of the bed was partly obscured by the sampling probe and by the thermocouple. The thermocouple covered an area of no more than 5% of the bed and rarely obscured a particle. The end of the sample probe presented more

of an issue, although it was found that the dry ice particle could still be detected even when directly beneath the probe, owing to the particle's reflection in the sides of the quartz tube.

From the measured CO₂ concentration, the molar flow rate of CO₂ released from the dry ice particles as a function of time was found. The conversion of the solid dry ice to CO₂ throughout each experiment was calculated, and, from the conversion, the radius of the dry ice spheres, assuming they remained spherical and of constant density.

The conversion, at which the particles appeared at the surface, apparition frequency, total surface dwell time, and the velocity of gas at the periphery of the particle, U_d , were calculated by synchronising the observations of the bed surface with the gas sampling. By setting the time during each experiment to zero at the point at which the particle was first introduced to the bed, and at the point at which the measured CO₂ concentration first rose above the noise, any lag in the gas sampling line was eliminated.

2.6. Fluidised bed experiments on the devolatilization of large spheres of beech wood at elevated temperatures

2.6.3 Transient heating rate of beech particles in a fluidised bed

Spheres of beech of ~10 mm diameter were measured using digital callipers along three axes and weighed after a small hole had been drilled into the particle as far as its centre (in the direction of the grain) using a 31 gauge hypodermic needle. A thermocouple, 0.25 mm diameter, was inserted into the hole such that the tip was near to the centre of the particle. The thermocouple and particle, as well as a bare thermocouple, were dropped into the bed described in Section 2.6.1, fluidised by N₂ at 600°C at $U/U_{mf} = 3$, and the temperature response was measured. Figure 2.11 shows the response of two, replicated experiments, indicating a high level of reproducibility.

Additionally, a 10 mm diameter sphere of beech was dropped into a bed fluidised by air at 600°C and the temperature at its centre measured. This particle had a very similar heat up curve to the particles heated in N₂, as shown in Fig. 2.11, until around 55 s, at which point the char

started to combust causing an additional heating effect which took the temperature at the centre of the particle well above the temperature of the surrounding fluidised bed.

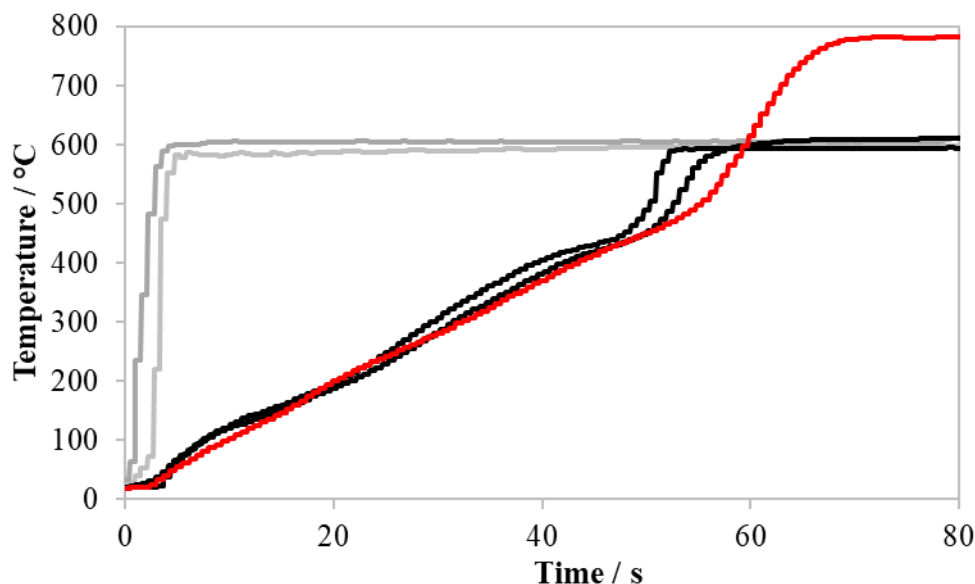


Fig. 2.11. Shown in grey are the temperatures measured by thermocouple inserted into the fluidised bed. In black are the temperatures measured at the centre of a 10 mm dia. devolatilising sphere of beech wood in a bed fluidised by nitrogen. In red is the temperature measured at the centre of a 10 mm dia. devolatilising sphere of beech wood in a bed fluidised by air at $U/U_{mf} = 3$.

2.7. Rate of emission and composition of the volatile matter

It was desired to measure the molar flowrate of volatile matter (VM) emitted by spheres of wood as they heated up and devolatilised in a fluidised bed. Spheres of a single type of wood, beech, was used of 10 mm dia., as described in Section 2.3.3.

2.7.1 Apparatus

It was necessary to find the average molecular mass and chemical formula of the many species which comprised the VM evolved during the devolatilisation. To do so, a device was designed to measure simultaneously both the molar flowrate of VM emitted from the surface of a sphere of beech during devolatilisation and the molar flowrate of the principal products of combustion of the VM. By comparing the molar flowrate of the VM to the molar flowrate of the combustion products, the mean molar mass of the VM could be calculated. The device, shown in Fig. 2.12 performed a variety of functions in that it:

1. measured the molar flowrate of VM released by a sphere of beech in bed fluidised by N_2 beneath it,
2. added air, above the baffle to the mixture of N_2 and VM,
3. ignited the gas mixture in the freeboard, and
4. measured the concentration of CO, CO_2 and CH_4 following the combustion of the VM.

The molar flowrate of the VM was measured by constraining the VM and the fluidising gas to flow through a narrow annulus between a circular baffle and the walls of the freeboard of the fluidised bed reactor. The VM increased the velocity of gas around the baffle and, hence, increased the pressure drop measured over the baffle. The internal diameter of the, nominally 0.03 m, quartz tube was slightly irregular along its length, the exact dimensions of the tube at the intended location of the baffle were unknown. The change in dimensions of the baffle and quartz tube due to thermal expansion were also unknown. To overcome this, five baffles were manufactured from mild steel and the baffle which was the tightest free sliding fit into quartz tube, at $600^\circ C$, which happened to be 29.35 mm dia. baffle, was used.

The close-fitting baffle was suspended from a 3 mm i.d. stainless tube and was positioned 0.07 m above the surface of the bed. The static gauge pressure beneath the baffle was measured *via* the stainless-steel tube, and the measurements were recorded by an Amsys AMS 5915-0010 pressure sensor in communication with an Arduino. The baffle gave a linear relationship between measured pressure drop and molar flowrate of gas at $600^\circ C$ when the flowrate around it was varied between $0.0005 \text{ mol s}^{-1}$ and 0.004 mol s^{-1} . The pressure sensor responded quickly to disturbances in the flowrate and, as such, no deconvolution of the signal was required. A step change response is shown for the pressure sensor in Fig. 2.13.

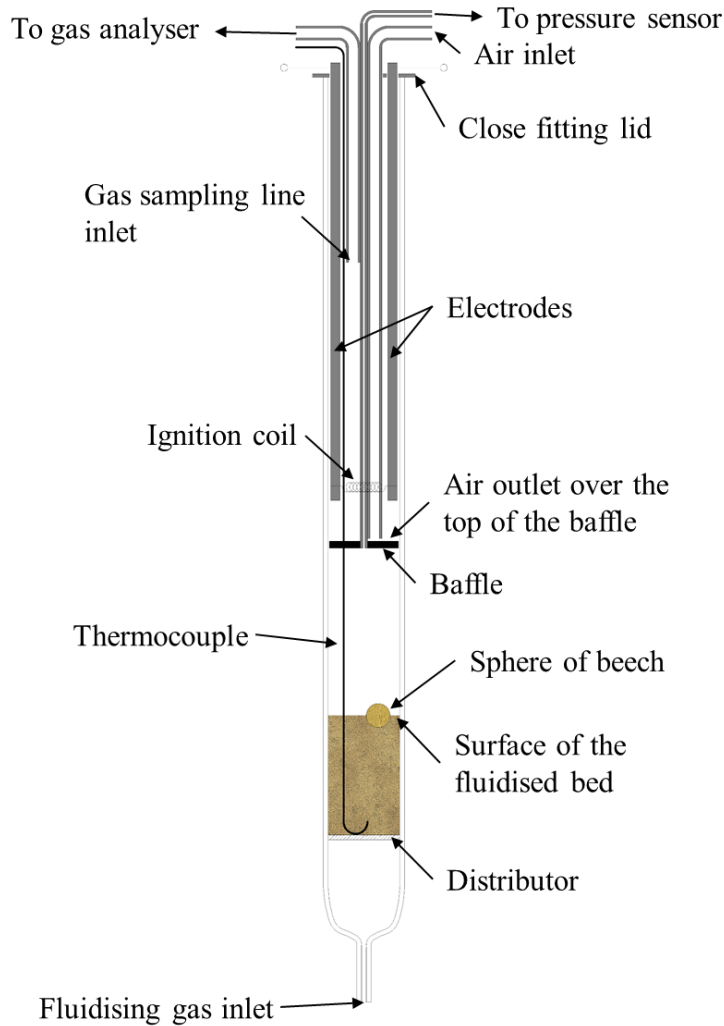


Fig. 2.12. The arrangement of the baffle probe within a quartz tube, above the fluidised bed.

Air was introduced to the freeboard at a rate of $2.7 \times 10^{-5} \text{ mol s}^{-1}$, just above the baffle, to allow the VM to combust. The air feed was arranged to impinge on the top of the baffle and flow out radially into the stream of VM and nitrogen flowing around the baffle to ensure good mixing of the gases. The baffle prevented oxygen ingress to the fluidised bed, and as the bed was fluidised by N_2 , the VM could not combust before the baffle. The CO_2 concentration was observed to fall to zero following the combustion of the VM which indicated that O_2 was being prevented from reaching the char.



Fig. 2.13. The pressure difference recorded by the pressure sensor while a step change in the flow rate of gas past the baffle was introduced at 1069 s.

An incandescent wire, heated by electrical resistance, was provided above the baffle to ignite the mixture of air and fuel. For this, 15V and 3A were used with a coil of 0.25 mm diameter stainless steel wire, which incandesced and ignited the VM. The wire was wound around a 3 mm pipe 30 times to form the coil, two 6 mm stainless pipes formed the electrodes which carried the current from the top of the freeboard, down to just above the baffle inside the reactor.

Through a sample probe, 0.1 L min^{-1} of gas (as measured at room temperature and pressure) was removed from the freeboard and passed through a tube packed with calcium chloride before being fed into the ABB analyser as described in Section 2.5.2.3 to measure the concentration of CO, CO₂ and CH₄ in the freeboard gases. The calcium chloride protected the ABB analyser from damage from particles and condensable components of the sample stream, water from combustion and any unreacted VM.

A steel lid for the quartz tube reactor was fabricated to fit around the pipes and electrodes at the top of the reactor. The lid reduced the intake of air from the laboratory, which, otherwise, diluted the freeboard gas. The concentrations of CO₂ and CO were used to calculate the molar flowrate of VM produced.

2.7.2 Methodology

First, to validate the experimental technique, dry ice was sublimated in the fluidised bed and the agreement between the flow rate of CO₂ from the concentration sensing sampling line and flow rate of CO₂ from the pressure sensing was determined. This is discussed in greater detail in Section 6.1.2.

Once the experimental technique had been validated, experiments proceeded as follows. The bed was fluidised with N₂ at 600°C, $U/U_{mf} = 1.5$. The baffle probe shown in Fig. 2.12 was removed from the quartz tube. Prior to the experiment, a 10 mm dia. sphere of beech wood was cooled in dry ice for at least 10 minutes to maximise the time between dropping the sphere into the bed and the onset of emission of VM. The delay was necessary to allow for the baffle arrangement shown in Fig. 2.12 to be reinserted after the fuel was dropped into the bed.

It was found that the success of the experiment depended on ensuring a self-sustaining combustion of the VM by means of the ignition coil. Ignition coils were, however, short lived and frequently burnt out before this was achieved and many experiments went literally up in smoke. Once the beech had finished devolatilising, which took around 60 s, the fluidising gas was switched from nitrogen to air to combust the char particle.

The char particles took around 6 minutes to combust. Following this, the gases were switched to the condition at the start of the experiment. Then, CO₂ was added to the air feed above the baffle *via* a three-way valve to create a step change in CO₂ concentration starting just above the baffle. After 120 s, the CO₂ was stopped to give a step decrease in CO₂ concentration. The analyser's response to these step changes was used to determine the characteristic mixing time of the sampling line for deconvolution of the measurements taken during devolatilisation. After the CO₂ concentration changes, the flowrate of N₂ to the fluidised bed was varied and the pressure corresponding to each flowrate was measured to obtain a pressure *vs* flowrate curve. This was performed for every experiment because the position of the baffle changed slightly from experiment to experiment; hence, the pressure drop characteristic of the baffle was slightly different for each experiment. The pressure *vs.* flowrate characteristic was then used to determine the molar flowrate of gas past the baffle during the devolatilisation. In doing so the assumption was made that the discharge coefficient for the annular gap remained unaffected by the change in gas composition between a mixture of N₂ and VM, and pure N₂ as used in the

calibration. The sensitivity of the apparatus to the change in density of the gas passing the annular orifice is investigated in Sections 6.1.2 and 6.1.3.

2.8. Fluidised bed experiments on devolatilization and combustion of beech employing X-radiography

2.8.1 Apparatus

The apparatus was located at the Department of Chemical Engineering, University College London (UCL). The equipment and technique have been described by Lettieri and Yates (2013) and Lettieri (1999) and the fluidised bed into which the particles were dropped by Bruni *et al.* (2002). The X-ray equipment was operated by Stefano Iannello at University College London.

Briefly, the fluidised bed consisted of an Inconel tube with 3 mm wall thickness, 146 mm i.d. and 1 m long. This was mounted fine stainless-steel distributor, with pore size of 20 μ m, atop a heated wind-box packed with 20 mm diameter ceramic beads. The heating elements, shown in Fig. 2.14, were arranged vertically around the outside of the Inconel tube and each element was encased in ceramic beads. The array of heating elements was arranged such that a gap was left on both sides of the reactor to leave an unobscured window for X-ray imaging. Compressed air was used to fluidise the bed of silica sand particles of 262 μ m mean circle equivalent diameter at velocities of 1.4, 2.1 and 2.8 times U_{mf} .

The X-ray apparatus could capture images for only 1 minute at a time to avoid overheating. After this, it had to be reset and further imaging could only be taken after a pause of 20 s. Thus, it was impossible to capture, in one continuous take, the entire life cycle of a combusting biomass particle.

The 10 mm spheres of beech were prepared with a 4.5 mm deep hole made using a 2 mm drill parallel to the direction of the grain. A small amount of lead was hammered into the blind holes in the spheres of wood. The addition of lead was used to vary the density of the wood particles. It also allowed the position of the wood particles to be determined as lead is a strong absorber of X-rays and appears very dark in the images compared to the surrounding bed material.

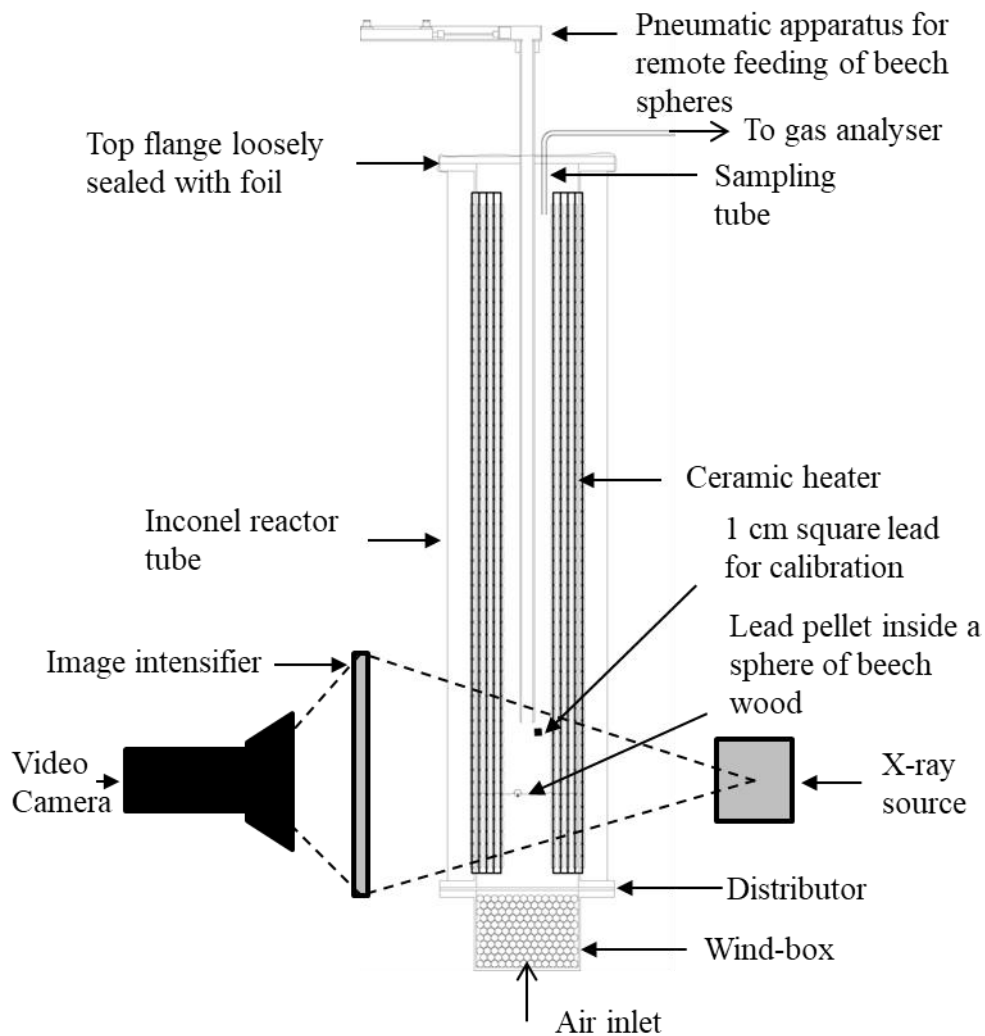


Fig. 2.14. Large electrically heated fluidised bed. The vertical array of heating wires is surrounded by ceramic beads, the wires are arranged to leave a window of 8 cm width for X-ray imaging. The insulation around the Inconel tube and heater has not been included for clarity.

A pneumatically-operated dropper was used to enable wood particles to be introduced to the fluidised bed remotely. This was important because the room containing the apparatus had to be evacuated by personnel when the X-ray equipment was in operation. The device consisted of a pneumatic cylinder, which pushed the particle towards a drop tube mounted centrally above the fluidised bed. The stainless-steel drop tube extended down to 0.01 m above the bed's surface.

Simultaneously with the capture of X-ray images, a sample of the gas flowing through the freeboard of the reactor was fed to two analysers in parallel. A Cambridge Sensotec analyser

handled 0.4 L min^{-1} (room temperature and pressure) and recorded the concentrations of CO_2 and CO . A SprintIR-R CO_2 sensor took 0.1 L min^{-1} (room temperature and pressure) and recorded only the CO_2 concentration. A stainless-steel probe was used to introduce a flow of CO_2 on to the surface of the bed and manual valves were used to admit step changes in the flow rate. The response of the analysers to these step changes in CO_2 concentration was recorded. As in Sections 2.6 and 2.7, the sampling lines were approximated as a PFR in series with a CSTR – hence, a first order exponential lag response was expected. Using a minimisation of residuals, a best fit exponential curve was found for the analysers' responses to a step change in CO_2 concentration at each reactor condition used. The speed of gas through the freeboard varied with temperature and U/U_{mf} , hence, the response time of the sampling line was expected also to change.

The sample line with the Cambridge Sensotec analyser had a mean response time of 40 s and the step change responses were not a good fit to a first order decay curve. Thus, the data from the Cambridge analyser could not be deconvolved using the method described by Scott (2004), because the mixing could not be modelled with just a CSTR and PFR in series. Therefore, the results obtained were only used to check the overall carbon balance for each experiment and to determine find if any CO or CH_4 were being produced. However, for the Sprint IR-R CO_2 sensor, the step response to CO_2 concentration was a good approximation to a first order decay and the mixing time varied between 15 and 4 s depending on the flowrate of the fluidising gas. The data from the Sprint IR-R was deconvolved as described by Scott (2004). In practice, negligible concentrations of CO or CH_4 were detected by the Cambridge Sensotec analyser so the rate of emission of gas from the particle was calculated using solely the CO_2 concentration trace recorded by the Sprint IR-R.

2.8.2 Methodology

The method used to process the images captured by the X-ray equipment is described in more detail in Appendix 2.3. In short, the image processing improved the contrast and removed distortion in the images to allow the lead particle inside the spheres of beech to be accurately located. A reference object of known size in each image was used to calibrate for distances in the images. The surface of the bed was automatically located in each image; however, as a result of the X-ray equipment producing a divergent beam of X-rays, two distinct surfaces, one above the other, could be found in each image as shown in Fig. 2.15. The edge of the surface

of the bed closest to the source of X-rays appeared higher than the edge of the surface of the bed furthest from the source. The upper boundary was taken as the reference during the image processing as this had the greater contrast and half the distance between the two edges was subtracted from its position to give the vertical height in the centre of the bed in each image.

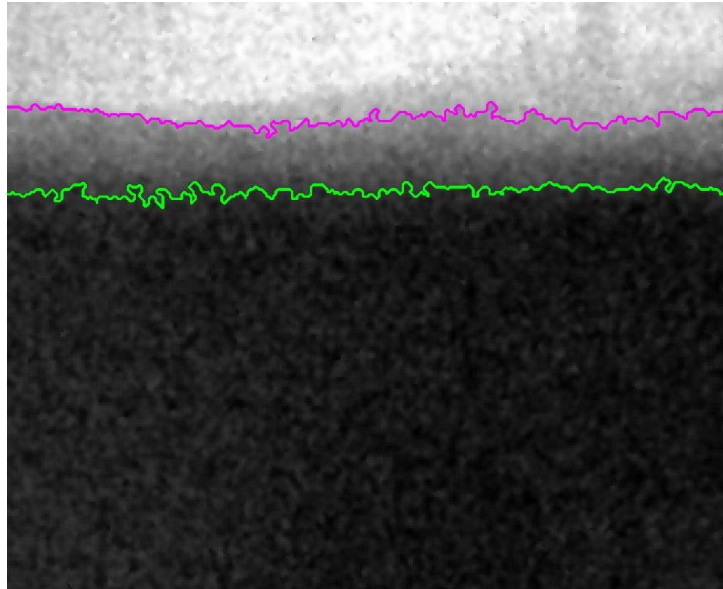


Fig. 2.15. The near (green) and far (magenta) edges of the bed surface as found by the Matlab function “imbinarize” using a threshold value of 0.2 and 0.6, respectively. The apparent vertical distance between these two boundaries was 4 mm.

Once the position of the lead particle was identified, if, indeed it was within the field of view of the camera, the co-ordinates within the image frame, which described the position of the lowest part of the lead particle were recorded. Using the particle’s x -co-ordinate the corresponding y -co-ordinate of the surface of the bed vertically above the lead particle was found. The vertical distance between the y co-ordinate of the bottom of the particle and that of the surface of the bed immediately above the bottom of the particle was calculated wherever the particle of lead was visible. Hence, the depth of the particle relative to the local surface was found for every image. Each measurement carried an uncertainty of ± 2 mm as the radial position of the particle within the bed in the direction of the camera-source axis was unknown.

When the velocity of gas through the bed was greater than U_{mf} the biomass particles were flung left and right by bubbles rising to the surface of the bed. At times, the biomass particles moved

beyond the window of visibility for the X-ray apparatus, hence there were lengthy gaps in the recordings of position of the particles.

Over the course of the 60 s of X-ray image capture, producing ~ 2000 frames, the lead usually remained inside the particle. However, in most cases, it was observed that by the end of each experiment the lead had substantially reduced in size, indicating that the wood particle had heated up beyond the melting temperature of the lead. The lead must have been able to wick away through the bed material gradually. Figure 3.13 shows that the middle of a beech particle, introduced to a fluidised bed at 600°C, will reach the melting temperature of lead, 328°C, after approximately 35 s. The retention of the lead in the biomass particles is dealt with in more detail in Chapter 6. For the first half of each experiment any mass lost by the beech could be solely attributed to devolatilisation, after this, the loss of lead from the particle would also have contributed.

Chapter 3 The consequences of the defluidised hood on the buoyancy of both inert and gas-producing particles

3.1 Introduction

This chapter investigates the steady state behaviour of inert spheres floating in a bubbling fluidised bed. A key difference between the buoyancy of solids in a liquid and buoyancy in a bubbling fluidised bed is in the change in density of the fluid around the submerged sphere. Changes occur as a result of the defluidisation of bed material above a solid object and, beneath an object, as a result of gas bubbles forming as the gas flow changes direction. Specifically, the formation of a higher density region above a solid object in a fluidised medium, called a defluidised hood, will be the focus in this Chapter, as will be explained in Section 3.2.1.

In Section 3.2.2, the influence of defluidised hoods on particles near to the surface of a fluidised bed is explored by extending the theory of Rees (2005) for parallel-sided defluidised hoods. An alternative shape for defluidised hoods is investigated and compared to experimental results in Section 3.2.3. Next, Section 3.2.4 explores the maximum height of the defluidised hood based on a range of experimental observations.

In Section 3.3, the disruption of the defluidised hood by the emission of gas from the submerged object on which it forms is investigated using measurements of pressure and digital photographic analysis. In Section 3.3.1, a model is proposed to determine a threshold for the rate of emission of gas from the surface of a sphere beyond which a defluidised hood cannot form. Finally, the consequences of this for devolatilising biomass particles are discussed.

3.2 Buoyancy of large particles at the surface of fluidised beds

To start, the depth at which an inert solid object floats in an incipiently fluidised medium has been examined mathematically.

The following assumptions have been made:

1. At minimum fluidisation, the medium was assumed to have a constant voidage of ε_{mf} , and, consequently, a constant density.
2. The interaction between the floating objects and exogenous bubbles of fluidising gas in the fluidised bed was ignored.
3. The density of the fluidising gas is negligible compared to the density of the fluidised particles; consequently, the density of the displaced gas has been neglected in all buoyancy calculations.
4. The only forces considered were the weight of the object and the upthrust force from the displaced bed material. Form drag and momentum transfer from the fluidised particles has been neglected.
5. The object, floating in the fluidised medium, was assumed to be at an equilibrium position and stationary.
6. For simplicity of the analytical solutions presented later in the Chapter, the treatment was confined to the buoyancy of spheres, in three dimensions, and long cylinders, in two dimensions.

With reference to Fig. 3.1, a dimensionless draught, δ , is defined, such that the vertical distance between the bottom of the sphere and the surface of the fluidised bed is given by $a \times \delta$, where a is the radius of the sphere and δ is the dimensionless draught. Thus, $\delta \approx 0$ describes a sphere floating just above the fluid, $\delta = 1$ describes the case when the sphere is exactly half in and half out of the fluid, and $\delta = 2$ represents a sphere which is just fully submerged in the fluid.

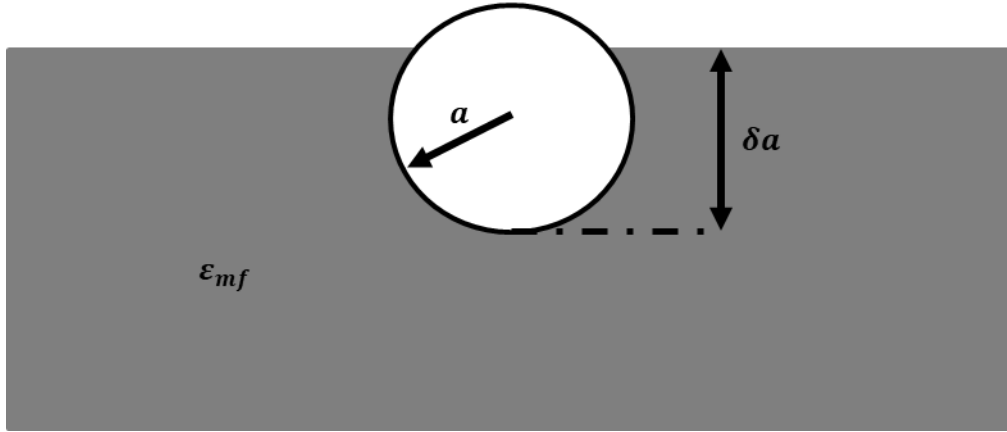


Fig. 3.1. A sphere of radius, a , floating at a depth of δa , in an incipiently fluidised medium of constant voidage ε_{mf} .

For a sphere floating in a fluidised medium, when δ is between 0 and 1, the volume of bed material displaced by the sphere, V_{disp} , is equal to that of a spherical cap of radius a and height $\delta \times a$. For δ between 1 and 2, the volume displaced is equal to a sphere of radius a , minus a spherical cap of radius a and height $a \times (2 - \delta)$. Hence, the volume displaced by the sphere is equal to

$$V_{disp} = \frac{4}{3}\pi a^3 - \frac{1}{3}\pi a^2(2 - \delta)^2(3a - a(2 - \delta))$$

$$V_{disp} = \frac{1}{3}\pi a^3 \delta^2(3 - \delta) \quad (3.1)$$

Equating the weight of the sphere to the weight of the displaced fluidised medium, and neglecting the density of the fluidising gas:

$$\frac{4}{3}\pi a^3 \rho_{sphere} g = \frac{1}{3}\pi a^3 \delta^2(3 - \delta) \rho_p (1 - \varepsilon_{mf}) g \quad (3.2)$$

where ρ_{sphere} is the density of the sphere, ρ_p is the density of the bed particles, ε_{mf} is the voidage of the bed at incipient fluidisation and g is the acceleration due to gravity.

Equation (3.2) can be simplified to

$$\frac{\rho_{sphere}}{\rho_p(1 - \varepsilon_{mf})} = \frac{\delta^2(3 - \delta)}{4} \quad (3.3)$$

The left-hand side of Eq. (3.3) is a dimensionless density ratio, R_ρ , which compares the density of the buoyant sphere and the density of the emulsion phase of the bed, thus

$$R_\rho = \frac{\rho_{sphere}}{\rho_p(1 - \varepsilon_{mf})} \quad (3.4)$$

The R_ρ predicted by Eq. 3.3 for inert spheres in a fluid of constant density is shown as a function of δ in Fig. 3.2. It forms a smooth sigmoidal curve passing through the origin, the point $\delta = 1, R_\rho = 0.5$ and the point $\delta = 2, R_\rho = 1$. The gradient of the curve is steepest where $R_\rho = 0$ or 1 as a consequence of the curvature of the sphere.

3.2.1 Buoyancy of plastic spheres at room temperature

Following the method described in Section 2.2, plastic spheres of diameter 0.02 m, with a range of densities, were produced. The spheres were added individually to incipiently fluidised beds of 180 – 200 μm silica sand, 600 – 750 μm silica sand, 200 – 355 porous alumina, and 450 – 600 μm α alumina. Thus, a wide range of density ratios, R_ρ , from ~ 0.2 to > 1 , were investigated. After becoming stationary, the distance between the surface of the incipiently fluidised bed and the bottom of the spheres was calculated from digital photographs as described in Section 2.2, with results shown in Fig. 3.2. The spheres were each pushed incrementally further into the bed and released to find at what depth, if any, the spheres became negatively buoyant.

It was found that all spheres for which $R_\rho > 0.98$ sank through the bed and remained at the distributor. For spheres with $R_\rho < 0.7$, the draught was related to the density ratio as predicted by Eq. (3.3), regardless of the bed material. For spheres with $R_\rho > 0.7$ in the 600 – 750 μm silica sand and $R_\rho > 0.8$ in the 355-425 μm porous alumina, a second, deeper stable position

was observed, which gives the substantial deviation from the behaviour predicted by Eq. (3.3). If pushed down deeper than this second stable depth, these spheres sank to the distributor.

The deviation from the predicted behaviour implies that one or more of the assumptions made about the structure of the bed around the spheres were incorrect. To gain more insight into the structure of the bed, observations were made in the 2D system involving a stationary cylinder, using the apparatus described in Section 2.4.

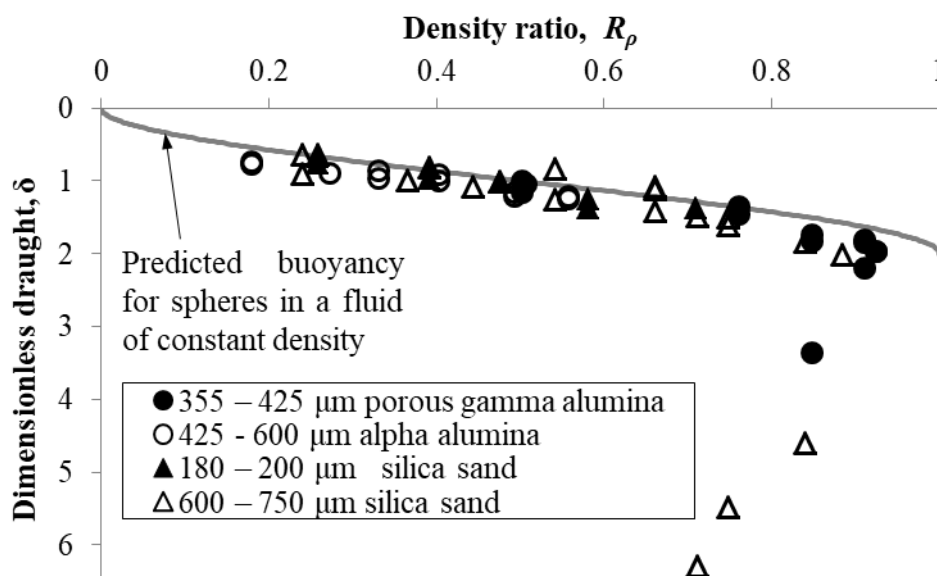


Fig. 3.2. Prediction of a dimensionless draught, δ , against a density ratio, R_ρ , for spheres near the surface of a fluid of constant density, Eq. (3.3) (—). Also plotted are the experimentally determined draughts of spheres of approximately 20 mm diameter in fluidised beds of: 180 – 200 μm silica sand (\blacktriangle), 600 – 750 μm silica sand (\triangle), 355–425 μm porous alumina (\bullet), and 425 – 600 μm α alumina (\circ).

A typical result from inspecting the homogeneity of the bed is presented in Fig. 3.3. This depicts a time-averaged image of a cylinder (shown in white), spanning a 2-D bed of incipiently-fluidised porous alumina particles, doped with iron oxide (dark grey), with a small fraction of undoped particles (white) to give a strong visual contrast between these particles and the rest of the bed. The transparent walls of the bed allowed the structure and direction of flow of the fluidised bed material around the cylinder to be observed under a range of fluidising conditions.



Fig 3.3. A 12 mm diameter cylinder, viewed from the end, in a 2-D bed of incipiently fluidised particles at room temperature. The image is a time-averaged image of 10 s recording. The bed is blurred around the cylinder; however, above the cylinder a region of stationary particles can be seen. The image indicates there could be localised variations in density in the bed material.

In Fig. 3.3, it can be seen that, above the cylinder, there is a region where the particles are individually discernable unlike the regions around the cylinder where the particles were in motion and, therefore, blurred. This zone of stationary particles is known as a defluidised hood and is a region in the wake of large, submerged objects where the voidage of the bed material is lower than the rest of the fluidised bed. Defluidised hoods of particles have been described by many authors in varying contexts: Glass and Harrison (1964), Hager and Schrag (1976), Kulkarni (1987), and Rao and Muller (2013) – atop a cylinder in a 2-D bed; Peeler and Whitehead (1982) in the context of horizontal tubes spanning a bed with a rectangular cross section; and Rees *et al.* (2005) who ascribed defluidised hoods as being responsible for increasing the apparent density of buoyant spheres. Assumption (1) presented at the beginning of the Chapter, that the voidage is constant everywhere, does not account for the defluidised hood. Accordingly, a model for buoyant spheres near the surface of fluidised beds incorporating defluidised hoods is considered next.

3.1.2 Parallel sided defluidised hood

Rees (2005) approximated the shape of the defluidised hood above a spherical particle as a short, vertical cylinder with a hemispherical top. The maximum height of the defluidised hood was found by Rees (2005) to be 1.5 times the sphere's diameter. The formation of the defluidised hood was invoked to explain why, in fluidised beds, particles with a density ratio, R_ρ , of less than unity sink in a fluidised medium despite being less dense than the emulsion phase of the bed. The sphere and the hood were taken as one body with an average density greater than the density of the emulsion phase of the bed. The fluidised hood described by Rees (2005) is only valid for objects where $\delta > 4$ such that the hood can form to its full height. For submerged spheres closer than this to the surface of a fluidised bed, however, it has been assumed here that the shape of the defluidised hood follows that described by Rees (2005) but is truncated at the bed's surface. Accordingly, in the present work, the profiles of the defluidised hoods expected for spheres, which are sequentially deeper in the bed, are presented in profile in Fig. 3.4.

Once a sphere in a fluidised bed has a draught of $\delta > 1$, as shown in Fig. 3.4 a), the bed particles directly above the sphere can become defluidised, and, consequently, the voidage in this region falls to the voidage of a randomly packed bed, ϵ_{pb} .

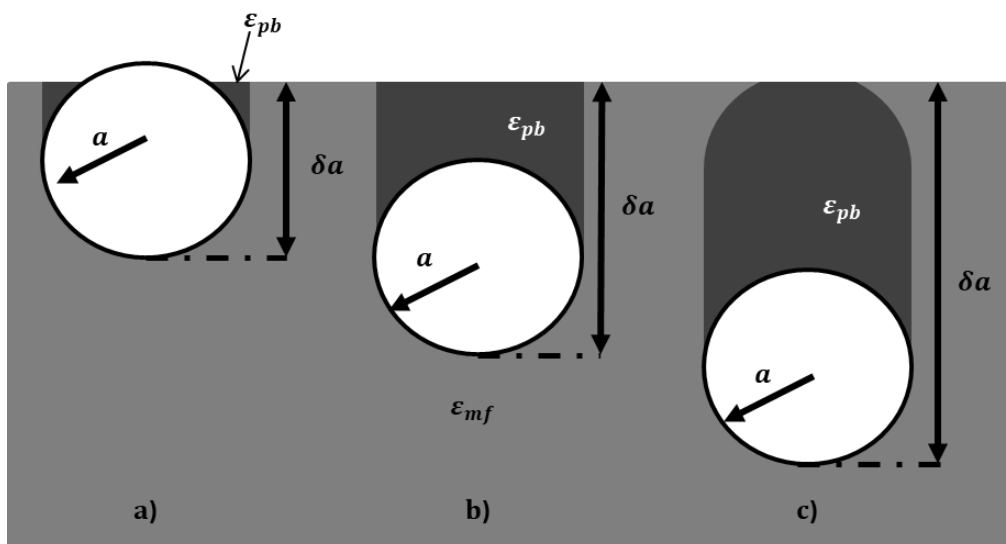


Fig. 3.4. The shape of the parallel sided defluidised hood as described by Rees (2005) with voidage of a packed bed, ϵ_{pb} but truncated for the cases: a) $1 < \delta < 2$, b) $2 < \delta < 3$, and c) $3 < \delta < 4$.

When $1 < \delta < 2$ the defluidised hood, shown in dark grey in Fig. 3.4 a), was assumed to take the shape of a short cylinder of height $a \times (\delta - 1)$ minus the truncated hemispherical space occupied by the upper half of the sphere. Therefore, the volume of the defluidised hood, V_{hood} , is

$$V_{hood} = \pi a^3 (\delta - 1) - \left\{ \frac{2}{3} \pi a^3 - \frac{\pi a^3}{3} (2 - \delta)^2 (1 + \delta) \right\}$$

and applying the principle of buoyancy to this new situation

$$\pi a^3 \frac{4}{3} \rho_s g + \left(\pi a^3 (\delta - 1) - \left\{ \frac{2}{3} \pi a^3 - \frac{\pi a^3}{3} (2 - \delta)^2 (1 + \delta) \right\} \right) \rho_p (1 - \varepsilon_{pb}) g = \pi a^3 \left(\frac{2}{3} + (\delta - 1) \right) \rho_p (1 - \varepsilon_{mf}) g,$$

resulting in

$$\frac{4}{3} \frac{\rho_{sphere}}{\rho_p (1 - \varepsilon_{mf})} + \frac{1}{3} - \frac{1}{3} \frac{1 - \varepsilon_{pb}}{1 - \varepsilon_{mf}} = \left(1 - \frac{1 - \varepsilon_{pb}}{1 - \varepsilon_{mf}} \right) \delta + \frac{1 - \varepsilon_{pb}}{1 - \varepsilon_{mf}} \delta^2 - \frac{1 - \varepsilon_{pb}}{3} \frac{1 - \varepsilon_{mf}}{\delta^3} \quad (3.5)$$

When $2 < \delta < 3$, the defluidised hood was assumed to have a flat top level with the surface of the fluidised bed as shown in Fig. 3.4 b) The defluidised hood then takes the form of a cylinder of height $(\delta - 1)$ minus the hemispherical space occupied by the upper half of the sphere. In this case the volume of the defluidised hood is

$$V_{hood} = (\delta - 1) \pi a^3 - \frac{2}{3} \pi a^3$$

and applying the principle of buoyancy

$$\pi a^3 \frac{4}{3} \rho_s g + \left((\delta - 1) \pi a^3 - \frac{2}{3} \pi a^3 \right) \rho_p (1 - \varepsilon_{pb}) g = \pi a^3 \left(\frac{2}{3} + (\delta - 1) \right) \rho_p (1 - \varepsilon_{mf}) g,$$

giving

$$\frac{4}{3} \frac{\rho_{sphere}}{\rho_p (1 - \varepsilon_{mf})} + \frac{1}{3} - \frac{5}{3} \frac{1 - \varepsilon_{pb}}{1 - \varepsilon_{mf}} = \left(1 - \frac{1 - \varepsilon_{pb}}{1 - \varepsilon_{mf}} \right) \delta \quad (3.6)$$

When $3 < \delta < 4$, the defluidised hood approaches the maximum height described by Rees (2005) and, hence, it was assumed that the top will become hemispherical, as shown in Fig. 3.4 c). The defluidised hood is now assumed to be a cylinder of height $2a$ and radius a , minus the hemispherical space occupied by the upper half of the sphere with a truncated hemisphere of radius a at the top

$$V_{hood} = 2\pi a^3 - \frac{\pi a^3}{3}(4 - \delta)^2(\delta - 1).$$

Applying the principle of buoyancy

$$\pi a^3 \frac{4}{3} \rho_s g + \left(2\pi a^3 - \frac{\pi a^3}{3}(4 - \delta)^2(\delta - 1) \right) \rho_p (1 - \varepsilon_{pb}) g = \pi a^3 \left(\frac{4}{3} + 2 - \frac{1}{3}(4 - \delta)^2(\delta - 1) \right) \rho_p (1 - \varepsilon_{mf}) g,$$

and thus

$$\frac{\left(\frac{4}{3} \frac{\rho_{sphere}}{\rho_p (1 - \varepsilon_{mf})} - \frac{10}{3} + 2 \frac{1 - \varepsilon_{pb}}{1 - \varepsilon_{mf}} \right)}{\frac{1 - \varepsilon_{pb}}{1 - \varepsilon_{mf}} - 1} + \frac{4}{3} = \frac{5}{3} \delta - \frac{1}{3} \delta^2 \quad (3.7)$$

Equations (3.5), (3.6) and (3.7) have been plotted in Fig. 3.2 and also in Fig. 3.5 for a bed of silica sand, $\rho_p = 2680 \text{ kg m}^{-3}$, $\varepsilon_{mf} = 0.42$ and $\varepsilon_{pb} = 0.37$, and for a bed of porous alumina particles, $\rho_p = 1430 \text{ kg m}^{-3}$, $\varepsilon_{mf} = 0.48$ and $\varepsilon_{pb} = 0.45$. Values for voidage and density of these materials were obtained experimentally, as described in Section 2.1.

Equation (3.6) predicts that if spheres with a density ratio of less than 0.89 in the 600 – 750 μm silica sand or 0.91 in the 355-425 μm porous alumina are buried, they will always resurface, even in the absence of bubbles. Spheres from this group, even when weighed down by the maximum possible size of defluidised hood, are still less dense than the bed they displace.

Equations (3.5), (3.6) and (3.7) predict that spheres with a density ratio, R_ρ , between 0.89 and 0.91 in the 600 – 750 μm sand or between 0.91 and 0.98 in the 355-425 μm porous alumina are able to float at the surface of a fluidised bed, but if they become submerged, for example by becoming smothered by a wave of bed particles produced by a bubble bursting at the surface of the bed nearby, they can reach a second stable position beneath the surface of the bed.

Equation (3.6) also predicts that spheres with a density ratio greater than 0.98 will always sink to the bottom of the bed and have no stable draught at the surface.

In the 600 – 750 μm silica sand experiments with plastic spheres, the largest stable depth was recorded at $\delta = 6.3$, as shown in Fig. 3.5, indicating that the maximum length of the defluidised hood for the coarse silica sand particles was around 2.7 times larger than the diameter of the sphere. This result significantly differs from the prediction by Rees (2005), whose model gives the length of the maximum hood as 1.5 times the diameter of the floating object.

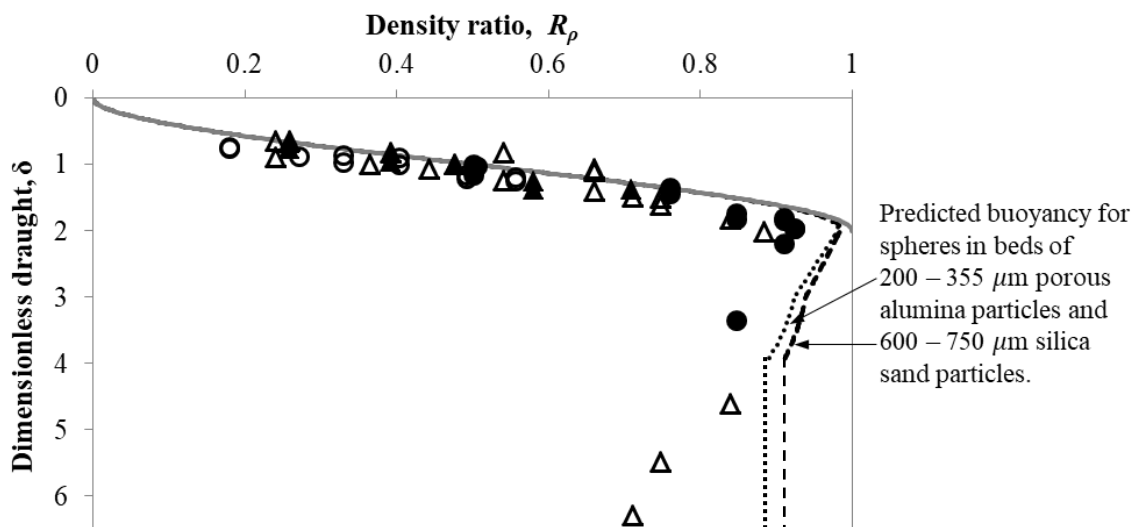


Fig. 3.5. Predictions of dimensionless draught, δ , against density ratio for spheres near the surface of a fluidised bed with a cylindrical defluidised hood as described by Rees (2005) for a bed of porous alumina (ϵ_{mf} and ϵ_{pb} are 0.48 and 0.45) (- - -) and a bed of coarse silica (ϵ_{mf} and ϵ_{pb} are 0.42 and 0.37) (· · ·) and without a defluidised hood (—). At values of δ below 1 a defluidised hood cannot form as the sphere is mostly proud of the surface of the bed, hence, floating objects in this region are expected to obey Eq. (3.3).

Also shown are the experimentally-determined draughts of spheres of approximately 20 mm diameter in fluidised beds of: 180 – 200 μm silica sand (▲), 600 – 750 μm silica sand (△), 200 – 355 μm porous alumina (●), and 450 – 600 μm α alumina (○).

The maximum density ratio for spheres, which remained at the surface of the bed in the experiments in beds of porous alumina and coarse silica sand particles, were 0.92 and 0.88, respectively, and both values are lower than the 0.98 predicted by Eq. (3.6). During the experiments, bed particles were observed loosely electrostatically adhered to the surface of the plastic spheres. This would increase the density of the spheres causing them to sink at a lower density than anticipated. Another possibility is the formation of a pile of bed particles, on top

of the spheres, proud of the surface of the fluidised bed, again, increasing the density of the combined object. Even so, Eqs. (3.5), (3.6) and (3.7) capture most of the behaviour of the experimental results.

The buoyancy behaviour shown in Fig. 3.5 compares very favourably with the force changing with penetration depth for a sphere pushed into a fluidised bed, measured by Rao and Muller (2013).

3.2.3 Tapered defluidised hood

Hager and Schrag (1976) described a form of defluidised hood with tapered sides as opposed to the parallel sides proposed by Rees (2005). Both are shown in Fig. 3.6.

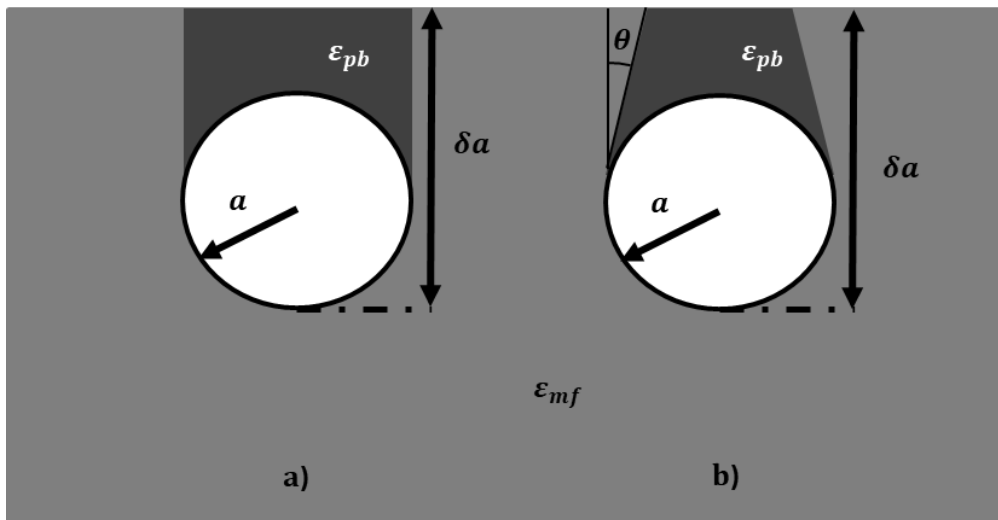


Fig. 3.6. Comparing a). a straight sided defluidised hood, of voidage, ϵ_{pb} as described by Rees (2005) with b). a conical hood with side angle θ .

Assuming (i) that when $1 < \delta < 2$ the buoyancy differs little from Eq. (3.3), because most experimental values of δ were within this range (as seen in Fig. 3.2), and (ii) that the effect of the rounding off of the top of the defluidised hood is smaller for conical hoods for $3 < \delta < 4$, then the volume of the conical defluidised hood for $2 < \delta < 4$ can be expressed by the volume of a conical frustum minus the volume of the spherical cap occupied by the top of the sphere. Accordingly, the volume of the frustum is given by

$$V_{frustum} = \frac{\pi a^3}{3} (\delta - 1 - \sin(\theta))(3\cos^2(\theta) - 3\cos(\theta)\tan(\theta)(\delta - 1 - \sin(\theta)) + (\delta - 1 - \sin(\theta))\tan^2(\theta))$$

and the volume of the spherical cap missing from the base of the frustum by

$$V_{spherical\ cap} = \frac{\pi a^3}{3} (1 - \sin(\theta))^2 (2 + \sin(\theta)),$$

hence, from buoyancy considerations:

$$\frac{4 \left(\frac{\rho_{sphere}}{\rho_p (1 - \varepsilon_{mf})} - 1 \right)}{1 - \frac{1 - \varepsilon_{pb}}{1 - \varepsilon_{mf}}} \quad (3.8)$$

$$= (\delta - 1 - \sin(\theta))(3\cos^2(\theta) - 3\cos(\theta)\tan(\theta)(\delta - 1 - \sin(\theta)) + (\delta - 1 - \sin(\theta))\tan^2(\theta) - (1 - \sin(\theta))^2(2 + \sin(\theta)))$$

For large values of θ the sides of the frustum will meet at the top which will limit the maximum height of the defluidised hood to less than the previous value of $\delta = 4$. In this case, the maximum value of δ becomes the distance from the bottom of the sphere to the top of the cone, given by

$$\delta = 1 + \sin(\theta) + \frac{\cos(\theta)}{\tan(\theta)} \quad (3.9)$$

The side angle, θ , for tapered defluidised hoods was found experimentally as follows. The defluidised hood above the same 12 mm cylinder, as shown in Fig. 3.3, was photographed through the clear 2-D bed described in Section 2.4. Time-averaged images were compiled and, for beds that were fluidised at $U/U_{mf} \sim 1$, the fluidised regions were clearly visible as flat grey areas, as shown by Fig. 3.7 a), while in defluidised regions the white grains of alumina were stationary, and, therefore, remained distinguishable. When the bed was at $U/U_{mf} \sim 2$ the time-averaged image showed translucent regions around the cylinder, as shown in Fig. 3.7 b), indicating the presence of bubbles which spanned the width of the bed. Above the cylinder, in Fig. 3.7 b), is a region, which appears darker than the rest of the bed but is not stationary – this can be inferred because the region is uniform grey with no visible bed particles and only a few particles directly atop the cylinder are stationary.

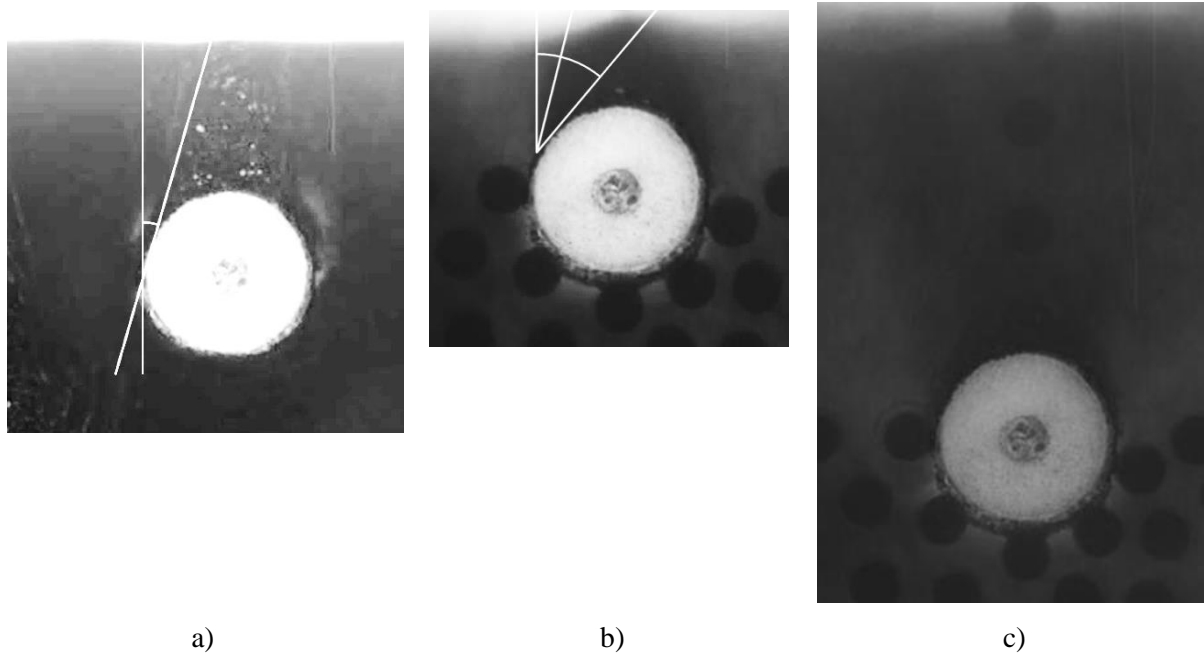


Fig. 3.7. Measuring the angle of repose of the defluidised hood above a cylinder (bright white circle in the centre of the image) in porous alumina spheres, doped with iron oxide, fluidised by N_2 at a) $U/U_{mf} \sim 1$ and $\delta \sim 4$, b) $U/U_{mf} \sim 2$ and $\delta \sim 3$, c) $U/U_{mf} \sim 2$ and $\delta \sim 6$. Shown in b) are the two possible angles of repose – the upper for the boundary between the denser region and the bulk fluidised bed, the lower the boundary between the denser region and the stationary particles above the cylinder. The images here have been positioned with the surface in each at the same height.

Although the boundaries between the stationary particles and the moving particles in Fig. 3.7.a) and between the opaque and translucent regions in Fig 3.7.b) are easy to discern, a considerable difficulty in determining the mean envelope of the defluidised hood from these images remains. This is because the action of bubbles passing close to the cylinder blurs the boundaries between the hood and the fluidising bed. When the cylinder was submerged lower in the bed, as shown in Fig. 3.7 c), the difference between the defluidised hood and the bed material was even more difficult to discern from the photographs.

As before, 10 s of images at 36 frames s^{-1} were used to compile a time averaged image for each value of U/U_{mf} and of δ . To find the value of θ , a straight line was drawn by eye over the boundary between the stationary and moving zones at $U/U_{mf} \sim 1$ and between the opaque and translucent zones at $U/U_{mf} \sim 2R$, as shown in Fig. 3.7 a) and b). The measured side angle of the defluidised hoods observed in beds of porous alumina particles at $U/U_{mf} \sim 1$ and 2 is shown in Fig. 3.8 for a range of depths.

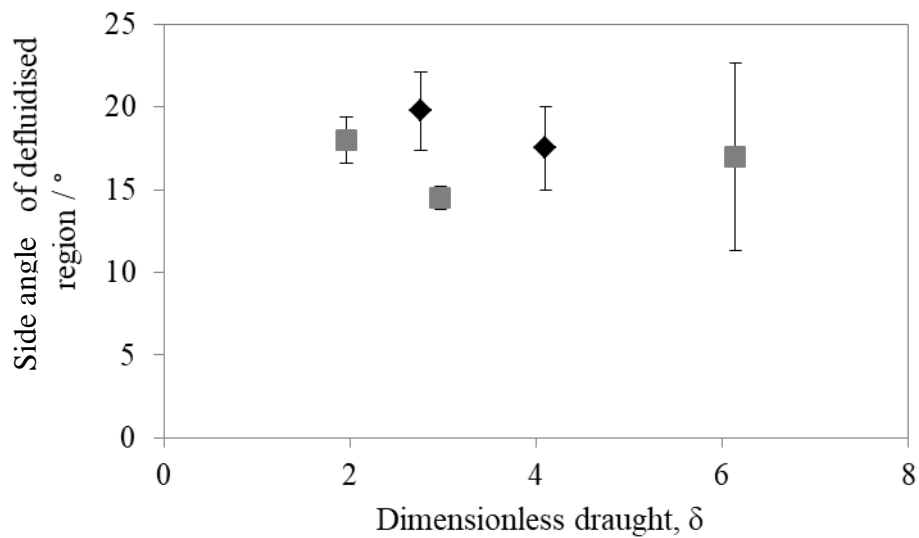


Fig. 3.8. The side angle of the defluidised hood above a cylinder in a fluidised medium at $U/U_{mf} = 1$ (◆) and 2 (■). The error bars represent the standard error in the experimental measurements.

The average value of the points in Fig. 3.8 gives an angle of 18° representing the angle between the randomly packed defluidised hood and the rest of the bed to the vertical plane.

Accordingly, Eq. (3.8) was plotted for the results in Fig. 3.2 and appears in Fig. 3.9. The curve given by Eq. (3.8) falls back a short distance from $R_\rho=1$ before approaching a vertical line. The results of the experiment, however, form a diagonal line extending much further back from $R_\rho=1$. The experimental evidence for the buoyancy of large spheres in a fluidised bed indicates that the envelope of defluidised material, which bears down upon a submerged sphere, is more likely to be parallel sided than tapered, as the data points for $\delta > 2$ appear to deviate strongly from what would be expected from spheres supporting a tapered defluidised hood.

From Eq. (3.9), a side angle of 18° gives a maximum height of the defluidised hood of 1.6 times the diameter of the sphere. The experimental results presented in Fig. 3.8, however, show

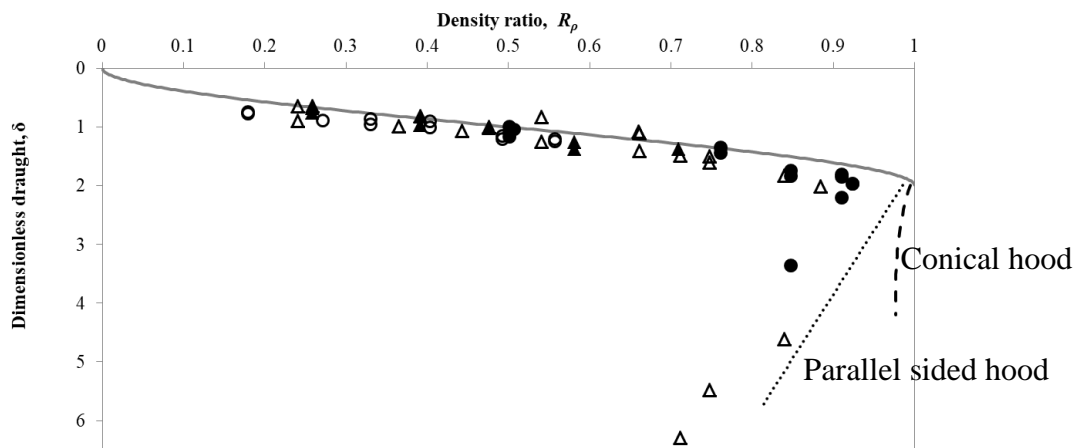


Fig. 3.9. Figure 3.2 updated: The dimensionless draught, δ , against density ratio, R_ρ , for spheres at equilibrium near the surface of a fluidised bed with a cylindrical defluidised hood as described by Rees (2005) but extended to $\delta = 5.8$ (•••) or a conical defluidised hood of side angle 18° as described by Eq. (3.8) (- -).

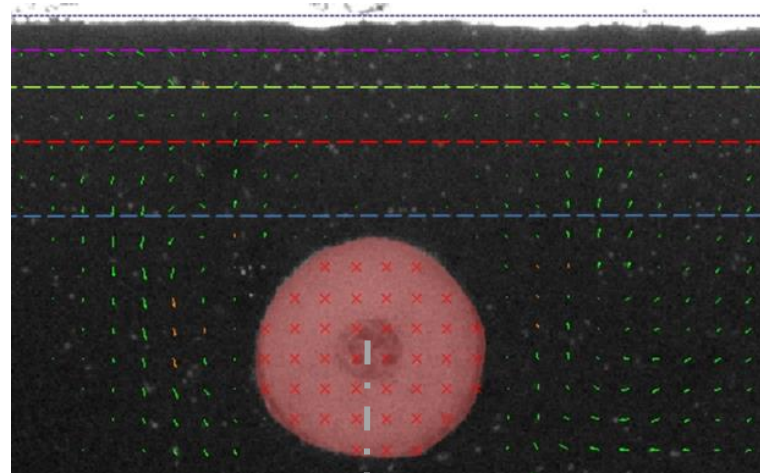
that the defluidised region extended above the submerged object substantially further than 1.6 times the diameter and, hence, the side angle measured from the photographs must give an underestimate of the total volume of material resting on the sphere. This agrees well with the conclusions drawn by Rao and Muller (2013), who stated that means other than photography were necessary to characterise the extent of the defluidised hood.

3.2.4 The size of the defluidised hood near the surface of the bed

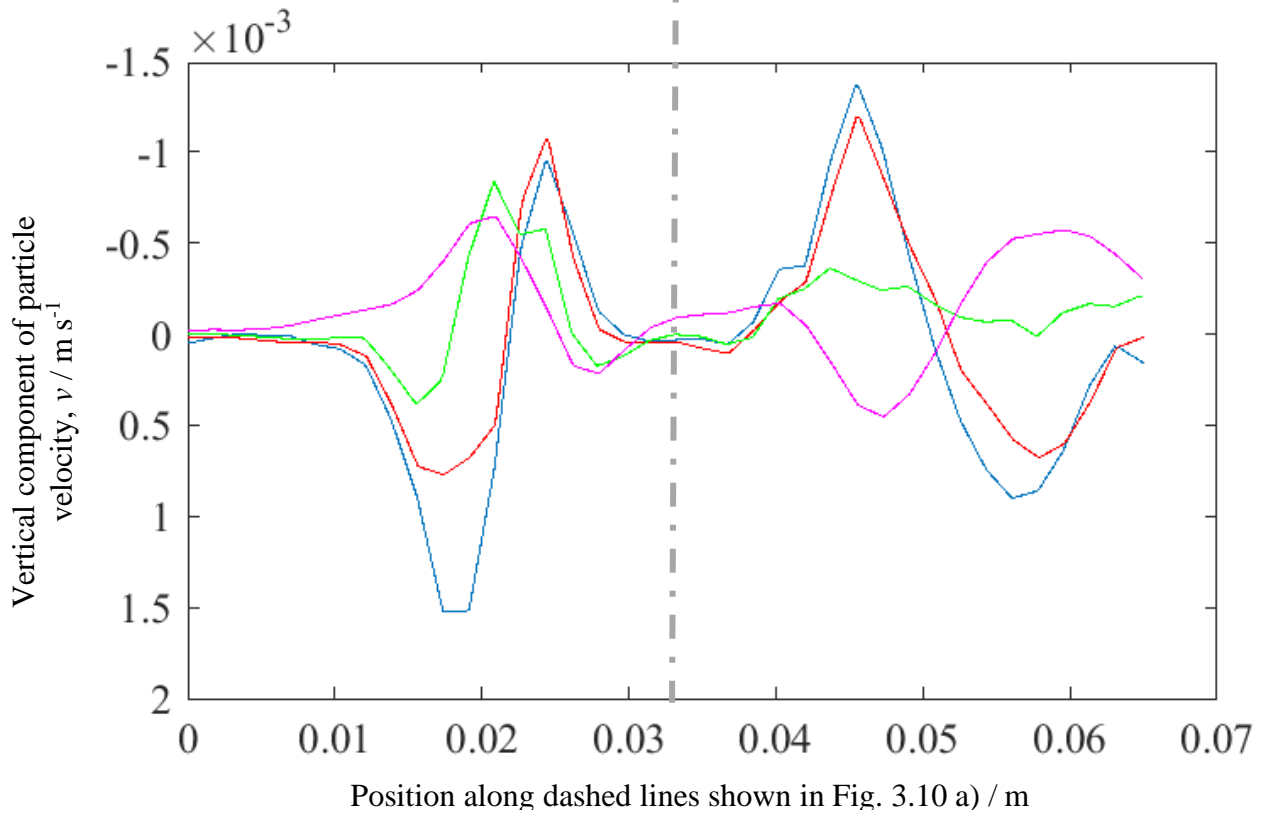
3.2.4.1 PIV analysis

Rao and Muller (2013) concluded that determining the size and shape of the defluidised hood from photographs was misleading owing to the presence of stationary, transitional and percolating regions within the stationary hood, and that alternative methods of detecting and distinguishing between regions which are stationary, moving but defluidised or fluidised should be used. Indeed, observing the movement of particles above the cylinder confirmed that there was a region where the particles were mostly stationary but were disturbed periodically by bubbles travelling up on each side of the cylinder. These disturbances had the tendency to move particles in the upper parts of the defluidised hood downwards and towards the edges of the hood until they were taken away into the fast-moving bed material on each side of the cylinder. Rao and Muller's (2013) observation agrees with that of Hager and Schrag (1976).

Particle image velocimetry (PIV) was used to find the time-averaged velocity for the bed particles in the vicinity of the 12 mm dia. cylinder in the 2-D bed for a variety of bed depths, as described in Section 2.4. The beds were fluidised at just above $U/U_{mf}=1$. An example output from the PIV analysis is shown in Fig. 3.10.a). Bubbles rising on each side of the cylinder cause an upward current in the bed particles, the majority of which then circulate round and down into the bed away from the cylinder. A small fraction of the particles return instead through the largely stagnant zone above the cylinder before once more entering the fast-moving channel on each side of the cylinder. This motion is more clearly shown by inspecting the vertical component of the velocity of the bed particles, v , shown in Fig. 3.10 b) measured along the dashed lines indicated in Fig. 3.10 a).



a)



b)

Fig. 3.10 a) A map of vectors (green arrows) representing the time averaged velocity of the bed particles in the vicinity of a horizontal cylinder (red) in a bed at $U/U_{mf} \sim 1$. b) The vertical component of velocity for bed material calculated for the dashed lines drawn horizontally in a) at the following heights above the centre of the 12 mm diameter cylinder: 8 mm (blue), 12 mm (red), 15 mm (green) 17 mm (magenta). The positive direction of the v component of the vectors is taken to be from top to bottom.

At 8 and 12 mm vertically above the centre line of the cylinder, Fig. 3.10 b) clearly shows rapidly rising particles on each side of the cylinder and the descending bed particles further away from the cylinder as well as a motionless region above the cylinder. At a horizontal height 15 mm above the centreline of the cylinder, this pattern is less pronounced and very close to the surface; at 17 mm above the cylinder the bed material vertically above the cylinder is in motion, although slower than the material to the left and right of it.

It was, however, still unclear from the PIV measurements where the material was fluidised or defluidised, because the incipiently-fluidised bed material might not necessarily be in motion. As the analysis of photographs was insufficient to find the extent of the defluidised hood, especially at higher values of U/U_{mf} , a new approach was investigated.

3.2.4.2 Measurements of pressure

To determine if the material in the hood above a cylinder, such as that shown in Fig. 3.7.c), was defluidised at $U/U_{mf} > 1$, and, therefore, supported by the cylinder rather than the flow of gas through it, a series of pressure measurements were taken using the pressure tappings built into the far wall of the 2-D bed. The probe measured the static gas pressure at the wall of the bed at a variety of locations around the cylinder without interrupting the flow of gas or the movement of the bed particles. The cylinder was buried in a bed of particles at $U/U_{mf} \sim 2$ to a depth of 0.026 m, or $\delta = 6.3$. The resulting time-averaged pressures measured in positions relative to the surface of the bed are shown in Fig. 3.11.

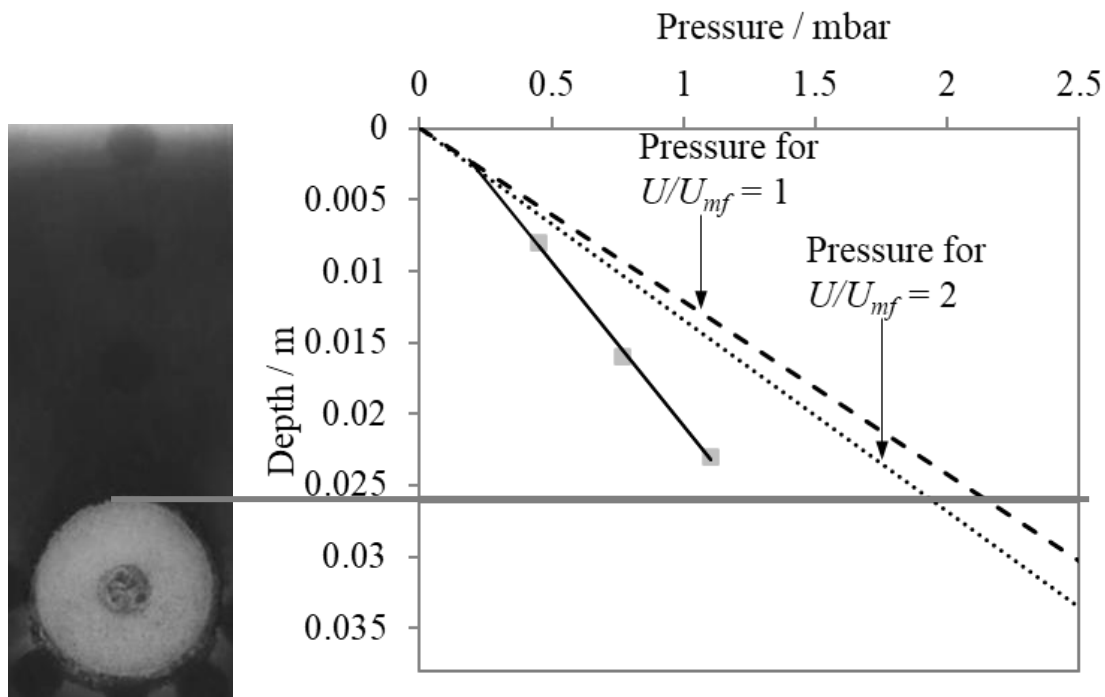


Fig. 3.11. The pressure distribution measured in a 2-D bed of fluidised porous alumina at room temperature at $U/U_{mf} = 2$. The top of the cylinder was located at a depth of 0.026 m, or $\delta = 6.3$ which is shown to the left of the chart to the correct scale for reference. The pressure in the bed material that is undisturbed by the cylinder's presence, for $U/U_{mf} = 1$ and 2 is shown by (- - -) and (\cdots), respectively. The values of pressure at three tappings vertically above the cylinder are shown by \blacksquare . The line of best fit (---) for the pressure in the defluidised hood above the cylinder has been extended to meet the lines of pressure far from the cylinder.

The pressure gradient in the gas percolating through the material directly above the submerged cylinder was significantly lower than the surrounding bed material and, indeed, was lower than the pressure gradient found when the bed was incipiently fluidised. From this one can conclude that the material above the cylinder, even when $U/U_{mf} > 1$ for the rest of the bed, is defluidised despite no static defluidised region being visible. By finding the point of intersection between the lines of best fit for the pressure distribution in the defluidised hood and that in the rest of the bed, an estimate for the maximum height of the defluidised hood was found. In the case shown in Fig. 3.11, the corresponding height is 0.029 m (measured from the axis of the cylinder to the top of the hood) or 2.4 times the diameter of the cylinder and this would occur were the cylinder immersed at $\delta = 5.8$. This agrees well with the deepest stable depth for buried buoyant spheres in 600 – 750 μm silica sand, discussed in Section 3.1.1, assuming that cylinders and

spheres can be treated equally. A hood of this size would not be possible if the defluidised hood were of the tapered form discussed in Section 3.1.3, the maximum height of which was found to be only 1.6 times the diameter of the cylinder. Rao and Muller (2013) found the maximum height of a defluidised hood above a sphere to be 2.1 times the sphere's diameter in a bed of glass beads.

The upper and lower boundaries for the sinking or floating behaviour depend on the difference between the density of the emulsion phase and the density of the defluidised hood and so will vary with bed material *cf.* Eq. (3.6). However, for silica sand and alumina the formation of a defluidised hood above an inert sphere with a density ratio of between 0.7 and around 0.95 can result in those particles, which would be expected to rise in a fluidised medium, instead sinking deep into the bed and only able to resurface if dragged by a passing exogenous bubble. Inert spheres for which $R_p < 0.7$, will rise to the surface through the emulsion phase of the bed regardless of the amount of defluidised material which is above them. However, the velocity at which they return to the surface will be slowed by the defluidised hood and therefore the formation of a defluidised hood should lead to an increase in the inventory of spheres which are beneath the surface.

The consequence of the above findings should be explored in the context of processing biomass particles in fluidised beds. Woody biomass has a wide density range of around 100 – 1200 kg m⁻³ (Mujumdar, 2015), while fluidised bed materials for combustion, gasification and chemical looping combustion have a particle density within a range of 900 (hollow cenosphere-based bed materials (Żukowski and Berkowicz, 2019) to 4400 kg m⁻³ for ilmenite (Grey *et al.*, 2013), or even higher, *e.g.* the carrier based on CuO, TiO₂ and Al₂O₃ described by Xin *et al.* (2020) at 4480 kg m⁻³. This gives a wide possible range of density ratios from 0.04 to 2.7. Most biomass species fall into the $R_p < 0.7$ range when fluidised in silica sand and so, during fluidised bed combustion, the formation of a defluidised hood will serve only to slow the rise of the biomass particles to the surface of the bed. Hence, the buoyancy of dense wood particles devolatilising in beds of lightweight bed particles can certainly be affected by the existence of a defluidised hood.

Some oxygen-carrying bed material has a lower density than silica sand, mostly where the looping agent is supported on a low-density support. For example, Hu (2015) prepared a CuO-based oxygen carrier supported on Ca₁₂Al₁₄O₃₃ which had an estimated particle density of 1700

kg m⁻³. For this material, biomass with a density greater than ~650 kg m⁻³ will have a density ratio $R_\rho > 0.7$ and could sink if a defluidised hood formed.

These conclusions neglect the bubbling action of fluidised beds operated at $U/U_{mf} > 1$ which drags the biomass particles towards the surface of the bed in the wake of rising bubbles, as discussed by Rowe *et al.* (1965). The conclusions also neglect the production of gas by the biomass particles. The next section explores how the gases, given off by a particle of biomass as it devolatilises shortly after being added to the fluidised bed, interact with the bed material above the particle.

3.3 The disruption of the defluidised hood by the emission of gas from the surface of a submerged object

When a sphere, upon which is deposited a defluidised hood, emits gas from its surface, such as in the case of devolatilising biomass particles, the gas emitted from the upper surface of the sphere must begin to permeate the defluidised hood. If the rate of emission is sufficiently high, it is envisaged that the material in the hood could be fluidised and hence the structure disrupted.

To investigate this, photographic images of a stationary cylinder immersed in a 2D fluidised bed were examined, bearing in mind the potential drawbacks of the technique discussed in Section 3.2.4. Photographs showing the disruption of a defluidised hood can clearly be seen in time-averaged images in Fig. 3.12. Figure 3.12 a) shows a zone of stationary particles above a cylinder which is not emitting gas, within a bed of incipiently fluidised particles. In Fig. 3.12 b), the cylinder is emitting gas from its surface with a radial velocity, U_d , of $2U_{mf}$, and there is little visual evidence of any defluidised hood. Similarly, for a vigorously bubbling fluidised bed at $U/U_{mf} \sim 2$, a defluidised zone, darker than the rest of the bed, can be seen above the cylinder in Fig. 3.12 c) when the cylinder is not emitting gas. However, in Fig. 3.12 d), where the cylinder is giving out gas at $U_d/U_{mf} = 2$ there is a paler zone above the cylinder and no evidence of defluidised material.

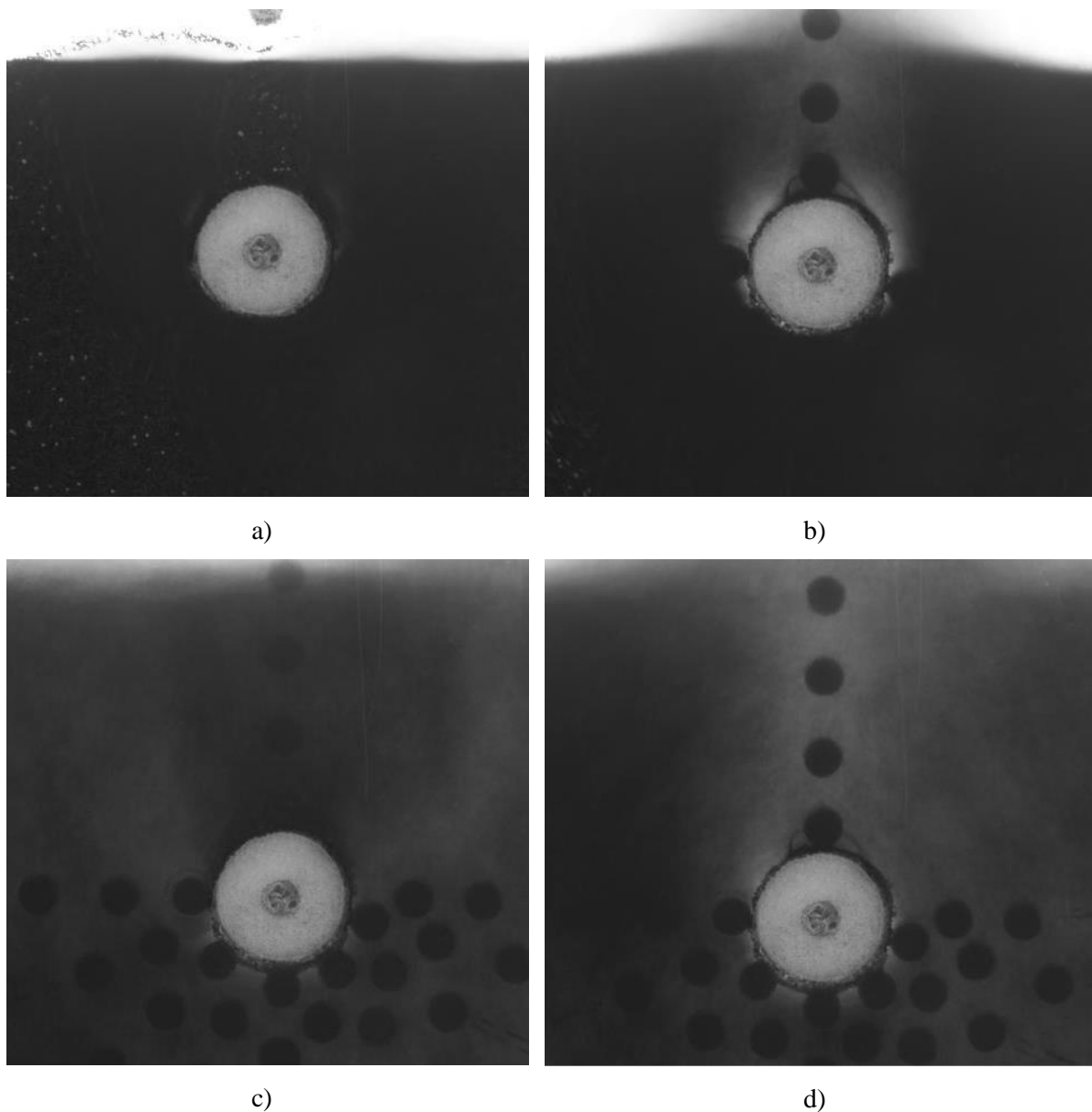


Fig. 3.12. Time-averaged images of a fluidised bed of porous alumina particles doped with iron oxide fluidised at a) and b) $U/U_{mf} \sim 1$, and c) and d) $U/U_{mf} \sim 2$. A submerged cylinder of a 12 mm diameter (white circle, centre) emitted gas at a) and c): $U_d/U_{mf} = 0$ and b) and d): $U_d/U_{mf} = 2$.

The two streams of bubbles, the source of which is discussed in detail in Chapter 4, which rose on each side of the submerged cylinder were seen to be drawn together above the cylinder as shown by the regions of low opacity in Fig. 3.12.b) and d). As U_d was increased, the rate of production of bubbles increased and the disruption to the defluidised hood by these bubbles also increased, as seen by comparing Fig. 3.12 a) with b) and c) with d).

As in Section 3.2.4.2, the pressure distribution in the bed material vertically above a cylinder at $\delta = 6.3$ was measured using the pressure tapplings in the 2D bed. The tapplings are clearly visible as the line of dark circles above the cylinder in Fig. 3.10 d). The readings of pressure for these tapplings, measured when the bed was fluidised at $U/U_{mf} = 2$, for $U_d/U_{mf} = 0, 0.5, 1, 2$ and 4 are plotted in Fig. 3.13.

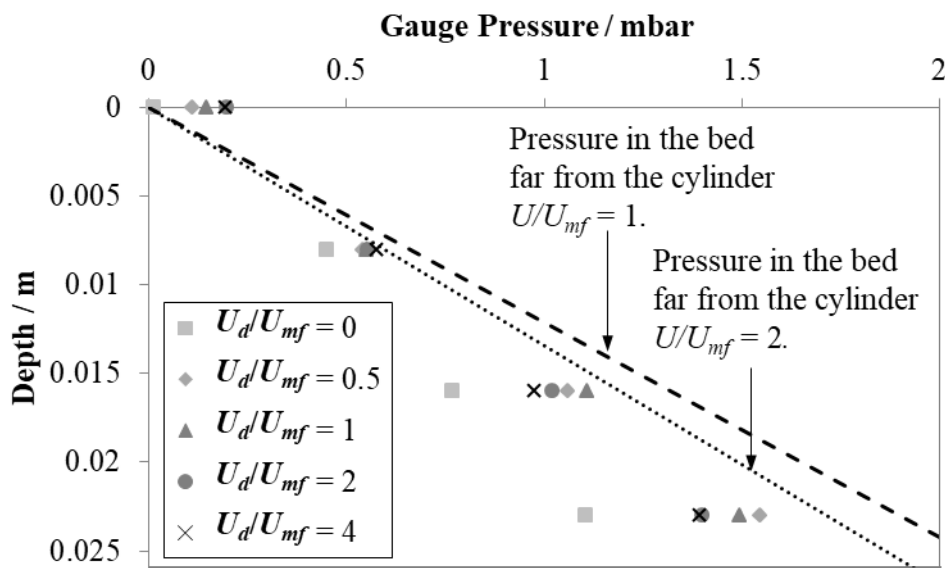


Fig. 3.13. The gauge pressure measured in a 2D bed of fluidised porous alumina at room temperature at $U/U_{mf} = 2$. The top of the cylinder is located at a depth of 0.026 m, or $\delta = 6.3$. The pressure in the bed material far away from the submerged cylinder for $U = U_{mf}$ and $2U_{mf}$ are shown by (- - -) and (\cdots) respectively. The values of pressure at four tapplings vertically above the cylinder are shown for: $U_d/U_{mf} = 0$ (\blacksquare), 0.5 (\blacklozenge), 1 (\blacktriangle), 2 (\bullet) and 4 (\times).

As the radial velocity of the gas leaving the submerged cylinder was increased from 0 to 0.5 times U_{mf} , the pressure gradient in the material above the cylinder approached that in the bed far away from the cylinder. When the radial velocity of gas was increased further the pressure gradient began to fall again as more of the bed above the cylinder was occupied by bubbles. The pressure readings at 0.026 m above the surface of the cylinder, nominally at 0 m depth in Fig 3.13, increase as U_d/U_{mf} increases. A spout of fast-moving bed particles formed above the cylinder and that pushed the local height of the surface up, as seen in Fig. 3.12 b). The pressure tapping, originally at the level with the surface, was now below the local surface, and so measured the pressure in the spout of particles. The pressure drop across this plume region of

high voidage above the cylinder was lower than the pressure drop in the bulk bed as the local U/U_{mf} was increased by the gas produced by the cylinder. Unfortunately, the distance between the pressure tappings limits the resolution of the pressure gradient measurements. For example, it would be difficult to discern at what value of U_d the entirety of the hood becomes fluidised, or how the size of the hood changes as U_d is increased from 0.

The value of U_d/U_{mf} at which the defluidised hood completely disappears must be lower than or equal to unity, because, at that rate of gas emission, the particles directly above a submerged sphere must be fluidised. For $0 < U_d < U_{mf}$, however the length of the defluidised hood is unclear. As can be seen from the time-averaged photographs of a cylinder in a 2-D incipiently fluidised bed in Fig. 3.14, the region containing stationary particles above the cylinder shrinks as the rate at which the cylinder produces gas increases. In fact, that region completely disappeared once $U_d/U_{mf} > 0.548$. As noted above, the stationary zone forms only part of the larger defluidised hood and the resolution of the pressure measurement technique in Section 3.1.4.2 was not high enough to find hood lengths of less than around 22 mm. Consequently, a modelling approach was attempted to find the length of the defluidised hood as a function of U_d/U_{mf} .

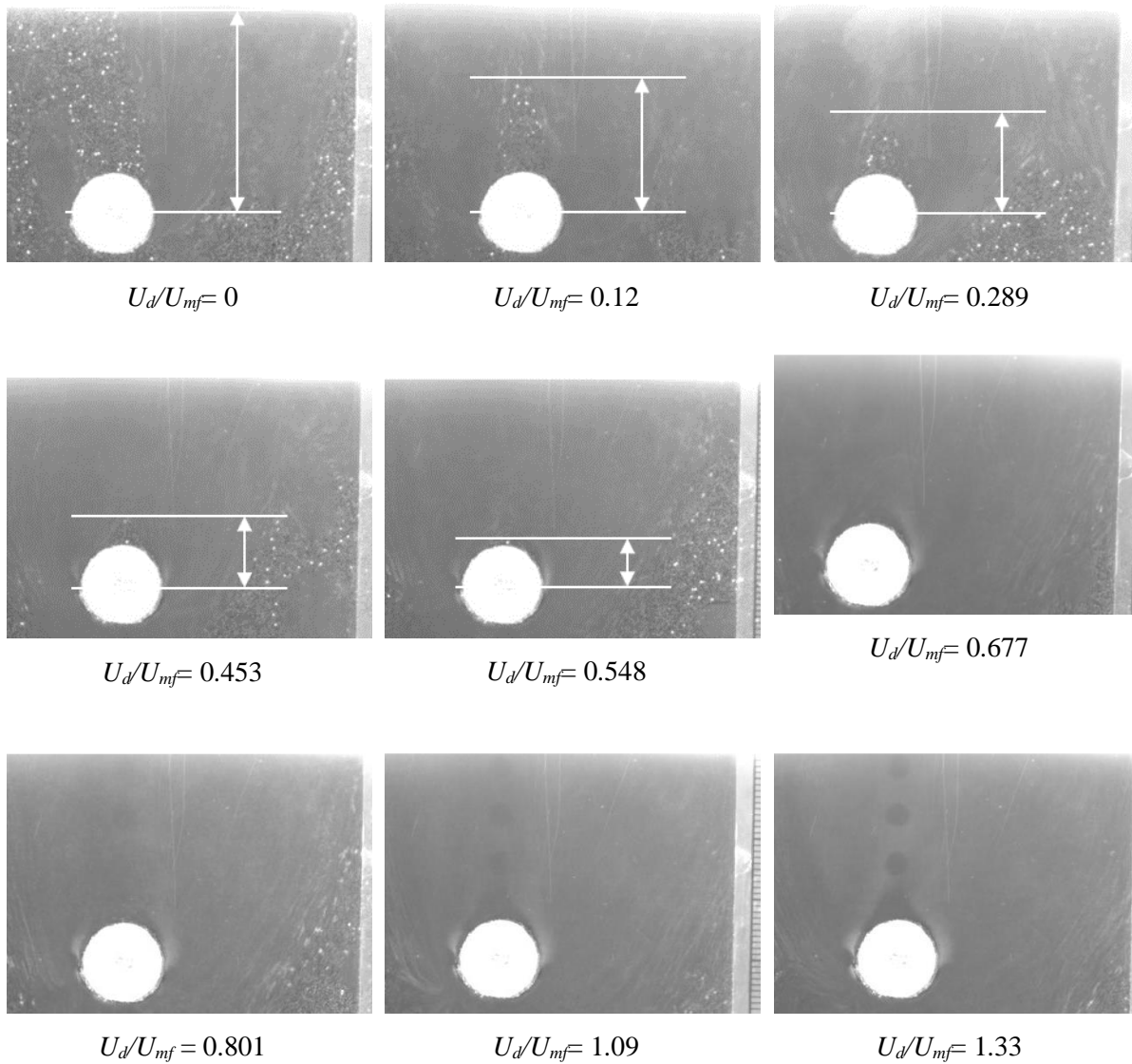


Fig. 3.14. Time averaged photographs of the bed around a 12 mm diameter cylinder emitting gas at U_d/U_{mf} between 0 and 1.33. From these, the length of the static region above the cylinder (if present) was measured, indicated by the white arrows and shown as the data points in Fig. 3.16.

3.3.1 Fluidisation of the defluidised hood by ingress of gas from an associated spherical object

Here, the defluidised hood above a sphere was approximated as a cylindrical region of defluidised particles, surrounded by an annulus of fast-moving gas bubbles and bed particles passing around the sphere. The radius of the hood was taken to be equal to that of the sphere with which it is associated. The length of the defluidised hood depends on the rate at which the gas from the fast-moving zone can percolate sideways into the defluidised region. A similar situation can be found at the distributor of fluidised beds where each jet of gas protrudes into an annulus of defluidised bed material.

Mamuro and Hattori (1968) developed a model, which describes the length of defluidised material surrounding a single gas jet into a fluidised bed. Within the model, gas percolates from the jet into the defluidised annulus until the point at which the material becomes fluidised. The geometry of their model (a cylindrical jet surrounded by an annulus of defluidised material) has been reversed here, as shown in Fig. 3.15.

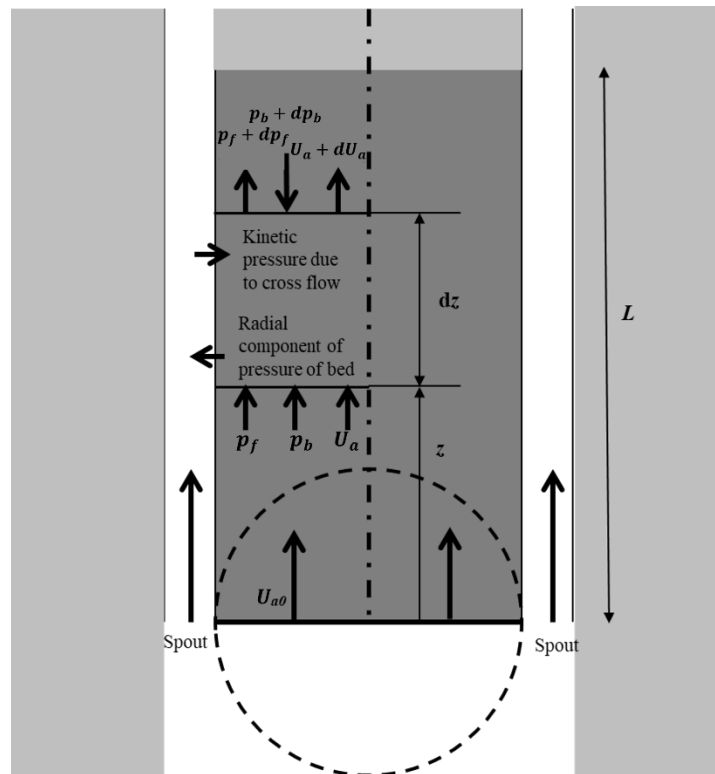


Fig. 3.15. Model for forces acting in the cylinder of material surrounded by an annular spout. The light grey Sections represent fluidised material with voidage of ϵ_{mf} , the dark grey represents defluidised material with voidage of ϵ_{pb}

The assumptions made here were:

- 1) The central cylinder of material was assumed to be a packed bed with a constant void fraction of ϵ_{pb} . Above the cylinder of defluidised material is material fluidised with void fraction ϵ_{mf} .
- 2) The solids in the cylinder were assumed to be stationary.
- 3) The friction between the cylinder and the spout was neglected.
- 4) The spout was assumed to have a void fraction of unity.
- 5) The central cylinder of defluidised material formed above a horizontal disk of radius a .

Performing a differential force balance axially on the element in Fig. 3.15

$$dp_b = -\rho_s(1 - \varepsilon_{pb})g dz - dp_f \quad (3.10)$$

where p_b is the bed solids pressure, ρ_s is the density of the solids, g is acceleration due to gravity and p_f is the fluid pressure. At the interface between the spout and the cylinder there is a balance between the kinetic pressure of the radial cross flow of gas and the pressure of the solids.

$$p_b = k \frac{\rho_f U_r^2}{2} \quad (3.11)$$

where U_r is the superficial velocity of the fluid in the radial direction and k is a constant, which relates radial pressure to axial pressure. Assuming that the axial flow of gas through the annulus obeys D'Arcy's law (a departure from Mamuro and Hattori (1968) who used Kozeny-Carman's equation):

$$-\frac{dp_f}{dz} = K U_A \quad (3.12)$$

where U_A is the superficial velocity of the fluid in the axial direction and K is the D'Arcy's law constant for the packed bed material in the cylinder.

Substituting eqs. (3.11) and (3.12) into Eq. (3.10):

$$-\rho_s(1 - \varepsilon_{pb})g + K U_A = k \rho_f U_r \frac{dU_r}{dz} \quad (3.13)$$

A mass balance on the fluid in the element gives

$$\frac{dU_A}{dz} = \frac{\pi D_S}{S_A} U_r \quad (3.14)$$

where D_S is the diameter of the spout and S_A is the cross-sectional area of the cylinder.

Substituting Eq. (3.14) into Eq. (3.13) gives

$$\frac{d}{dz} \left(U_r \frac{dU_r}{dz} \right) = \frac{\pi D_S K}{k \rho_f S_A} U_r \quad (3.15)$$

which has the general solution

$$U_r = C_1(z + C_2)^2 \quad (3.16)$$

where C_1 and C_2 are constants. Substituting Eq. (3.16) into Eq. (3.14) results in

$$\frac{dU_A}{dz} = \frac{\pi D_S}{S_A} C_1(z + C_2)^2 \quad (3.17)$$

which can be integrated with respect to z

$$U_A + B = \frac{\pi D_S}{3S_A} C_1(z + C_2)^3 \quad (3.18)$$

Applying the boundary condition: $z = 0, u_A = u_{A0}$ gives

$$U_A - U_{A0} = \frac{\pi D_S}{3S_A} C_1\{(z + C_2)^3 - C_2^3\} \quad (3.19)$$

The limit of the defluidised cylinder can be described by the position, z , at which the superficial vertical gas velocity, U_A is equal to U_{mf} , thus the bed material above this height is fluidised. Hence, when $z = L$

$$\left(U_r \frac{dU_r}{dz} \right)_{z=L} = 2C_1^2(L + C_2) = 0 \quad (3.20)$$

and therefore

$$C_1 = -L$$

so

$$U_A - U_{A0} = \frac{\pi D_S}{3S_A} C_1\{(z - L)^3 + L^3\} \quad (3.19)$$

Additionally, when $z = L, U_A = U_{mf}$

$$U_{mf} - U_{A0} = \frac{\pi D_S}{3S_A} C_1\{L^3\} \quad (3.19)$$

Hence,

$$\frac{U_A - U_{A0}}{U_{mf} - U_{A0}} = 1 - \left(1 - \frac{z}{L}\right)^3 \quad (3.20)$$

Rearranging Eq. (3.19) for L gives

$$L = \left(\frac{(U_{mf} - U_{A0})3a}{2C_1} \right)^{\frac{1}{3}} \quad (3.21)$$

where C_1 can be determined from

$$C_1 = \frac{3aU_{mf}}{2L_{max}} \quad (3.22)$$

Alternatively,

$$\frac{L}{L_{max}} = \left(\frac{(U_{mf} - U_{A0})}{U_{mf}} \right)^{\frac{1}{3}} \quad (3.23)$$

which is plotted in Fig. 3.16. For the defluidised hood above a sphere, rather than a horizontal disk as in the above derivation, emitting gas at U_d , the velocity U_{A0} was approximated by U_d , and it was assumed that the defluidised hood has been entirely fluidised when $L = a$.

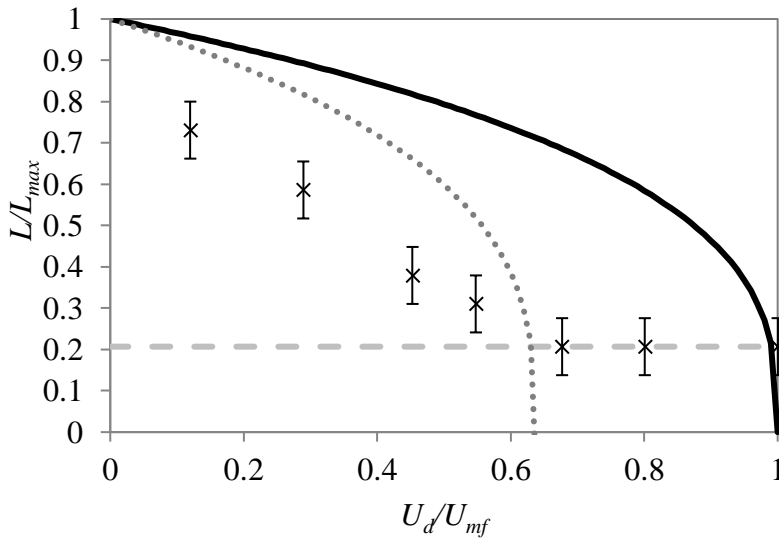


Fig 3.16. Theoretical length of the defluidised hood as a ratio of the length of a defluidised hood above an inert object. Equation (3.23) is given by the black line. The length of the stationary region, measured using the series of images in Fig. 3.14 is also shown (x). The position of the top of the 12 mm cylinder, shown in Fig. 3.14, is given by (- - -) The error bars represent the 2 mm error associated with the measurement of the height of the stationary region. Equation (3.23) corrected to account for the higher surface area of a cylinder compared to a flat plate is also shown (···)

Additionally, the measurements of length of the stationary zone, found from the images shown in Fig. 3.14, are plotted in Fig. 3.16 and show an approximately linear relationship between U_d/U_{mf} and L/L_{max} , where L_{max} was taken to be 0.029, as found for the 2-D bed and pressure tappings in Section 3.1.4.2.

The model, Eq. (3.23), appears to overpredict the length of the defluidised hood, which may reflect that it is derived from the theory for a single spout rather than for two spouts in close proximity, one on each side of the cylinder. Equation (3.23) neglects interaction between the spouts. However, an array of spouts of gas emitted by a drilled plate distributor at the bottom of a fluidised bed have been observed to merge, for example by Pore *et. al.* (2010). The attraction between the spouts could serve to shorten the defluidised region between the spouts. Indeed, in the time averaged images, such as Fig. 3.14, it is possible to see the regions of high voidage merging close above the cylinder.

A further consideration is the curvature of the cylinder or sphere from which the gas is emitted into the base of the defluidised hood. Rather than the quantity of gas released vertically beneath the hood being $2aU_d$ as for a rectangular plate of unit length and side length $2a$, a cylinder of radius a would emit πaU_d m³ of gas per unit length. This results in, for the case of a cylinder, $U_{a0_{avg}} = U_d \times \frac{\pi}{2}$, the result of which is plotted in Fig. 3.16, or equivalently for a sphere $U_{a0_{avg}} = 2U_d$. The experimental results shows that the static region was eliminated by $U_d/U_{mf} = 0.67$ and the corrected theory predicts the hood to be entirely fluidised by $U_d/U_{mf} = 0.62$ for a cylinder or when $U_d/U_{mf} = 0.5$ for a sphere.

The emission of gas from the surface of a submerged object can clearly fluidise the defluidised hood. In doing so, objects, for which $R_\rho > 0.7$ would no longer obey Eqs. (3.5), (3.6) and (3.7), which describe the buoyancy of inert spheres in a fluidised bed where parallel-sided defluidised hoods can form, and may, instead, behave more closely to the results of Eq. (3.3), the buoyancy of inert spheres in the absence of defluidised hoods. The disruption of the defluidised hood by the emission of gas from the objects will, in this event, lead to an increase in the buoyancy of the object, and could lead to an accumulation of the objects at the surface of the fluidised bed. Typical rates of devolatilisation of beech particles in hot fluidised beds are shown in Section 6.2.2 to exceed $U_d/U_{mf} = 0.5$ and so devolatilising beech particles can be expected not to possess a defluidised hood during devolatilisation.

3.4 The maintenance of an elevated fluidised cap of particles owing to the emission of gas from the surface of a buoyant object

So far, only defluidised hoods which are contained entirely below the surface of a fluidised bed have been discussed. This section aims to address another kind of hood of bed particles, sitting on top of spheres which emit gas and extending above the surface of the fluidised bed.

In a vigorously-bubbling fluidised bed, bubbles passing up through the bed will burst at the surface of the fluidised bed and project bed particles into the freeboard. Should these particles land on the top of a fuel particle floating on the surface of the bed surface in the vicinity, they could come to rest there and force the fuel particle deeper into the bed. The volume of bed material which could come to rest in a conical pile on the top of a sphere is, however, small. For example, taking a typical angle of repose, β , for dry sand of 34° for 0.5-1 mm sand as measured by Carrigy (1970), the ratio of volume of a conical pile on top of a sphere to the volume of the sphere itself is given by Eq (3.24), the derivation of which is given in Appendix 3.2.

$$\frac{V_{pile}}{V_{sphere}} = \frac{\{\sin^3(\beta) \tan(\beta) - (1 - \cos(\beta))^2(2 + \cos(\beta))\}}{4} \quad (3.24)$$

For $\beta = 34^\circ$, the ratio is just 0.011 which indicates that, unless the density ratio is extremely low, such a small volume of bed particles stacked above a floating sphere is unlikely to cause the sphere to sink into the bed. Using a 2-D fluidised bed, such a pile of bed particles was recreated above a cylinder and was observed to remain in place even when U/U_{mf} was greater than 1 as shown in Fig. 3.17 a) for the situation when no flow was forced through the cylinder, namely $U_d=0$. From Section 3.3.1 it is known that if $U_d/U_{mf} > 0.5$ any bed material above the cylinder will become fluidised and the nature of fluidised material is such that the angle of restitution is 0. In this event, Eq. (3.24) predicts that no pile can form on top of the cylinder. When gas was blown through the cylinder at $U_d/U_{mf} > 0.5$, the pile of bed material above the cylinder fell away as shown in Fig. 3.17 b). Of course, in Fig. 3.17, a fixed cylinder was used but bed particles are unlikely to form a neat conical pile on top of an object which is floating freely and subjected to the rigorous jostling of a bubbling fluidised bed.

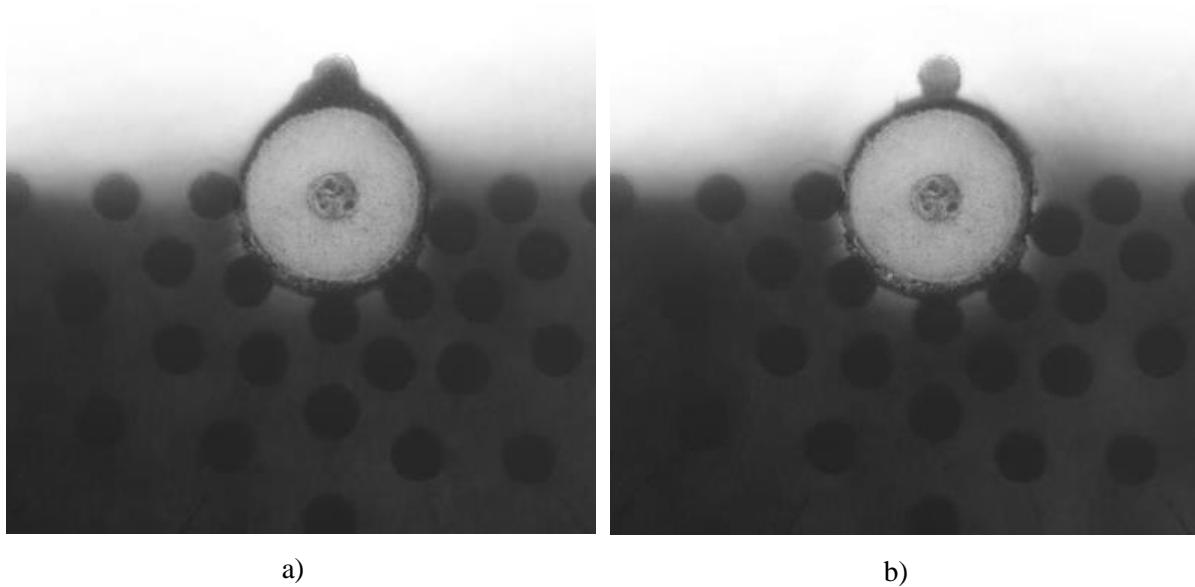


Fig. 3.17. Time averaged photographs showing the bed material above a 12 mm diameter cylinder at $\delta = 1$. Here $U/U_{mf} \approx 2$ and a) $U_d/U_{mf} = 0$ and b) $U_d/U_{mf} = 1.33$.

When the amount of bed material in the 2-D bed was increased, such that now the cylinder had a draught of $\delta = 2$, *viz.* the cylinder is just submerged completely beneath the surface of the bed, the behaviour of particles coming to rest on top of the cylinder was quite different. For an “inert” cylinder ($U_d = 0$), bed particles collected on top of the cylinder and the pile stuck out, proud of the surface of the fluidised bed as shown by the set of observations in Fig. 3.18.

It can be seen in Fig. 3.18 a) that the pile protruded higher above the upper surface of the cylinder, in contrast to what was seen in Fig. 3.17 for $\delta = 1$. When gas was supplied to the cylinder such that $U_d/U_{mf} > 0.5$. Fig. 3.18 b) shows that the region of particles did not fall away. The fast-moving channels of gas bubbles and bed particles rising on either side of the cylinder served to deliver more bed particles to the top of the cylinder, and also seemed to stabilise the cap of particles on top of the cylinder. During the experiments, the cap of particles was disrupted several times by manually sweeping away the particles. The cap rapidly reformed each time, indicating that the elevated cap of particles was a stable system, maintained by the delivery of particles from the bubbles erupting at the surface on either side. Even when U_d/U_{mf} was increased to 4, the cap of, now, fully-fluidised particles remained, despite being positioned well above the global surface of the bed. The cap had sides of angle 18° from the vertical, and a rounded top which had a radius similar to that of the cylinder

beneath it. As with the angle of repose for granular materials, the side angle of this fluidised cap is likely to depend on the shape of the particles, but this conjecture has not been examined in this work. In the absence of experiments with other bed materials, the value of 18° , measured in a bed of porous alumina, was used as an estimate for the side angle of fluidised caps in other bed materials.

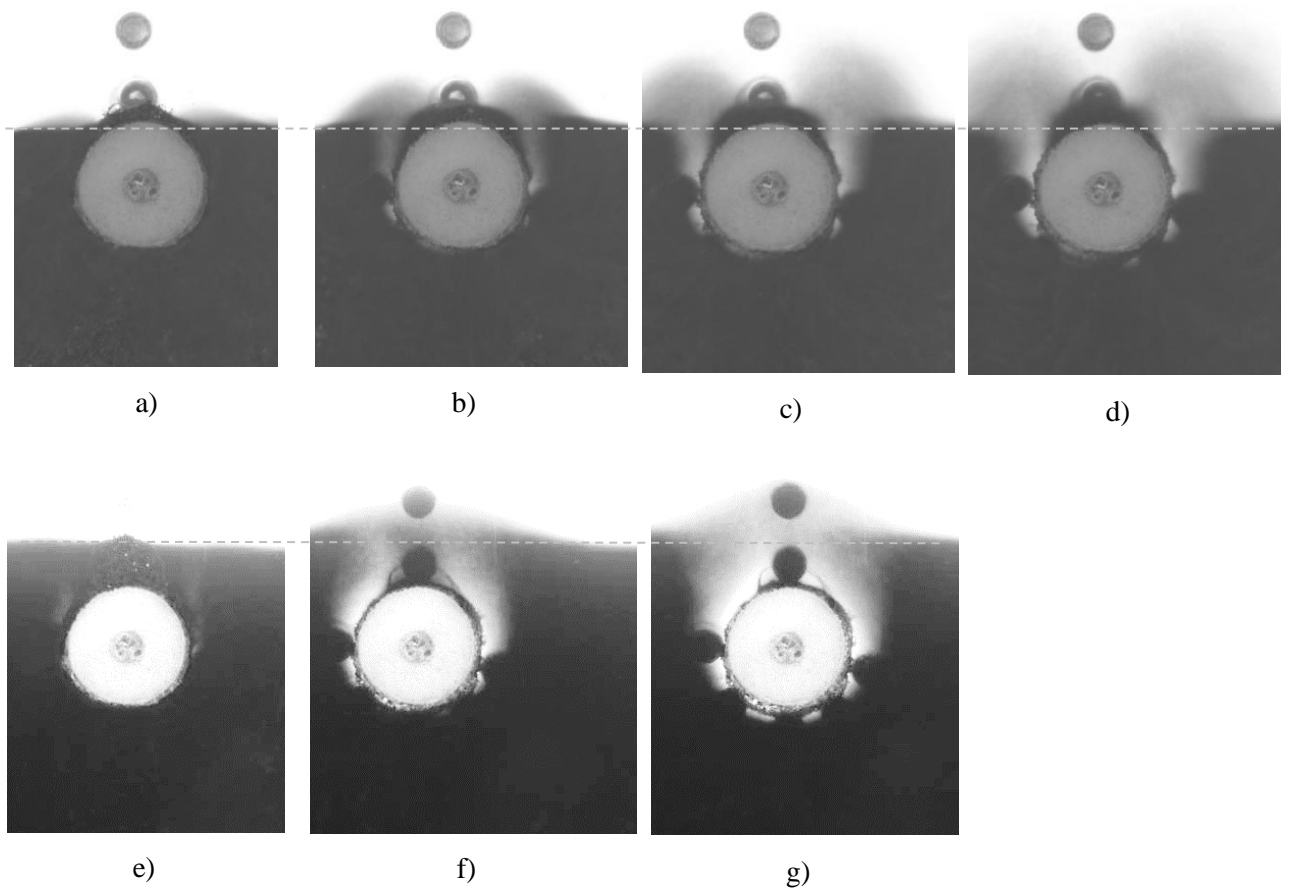


Fig. 3.18. Time averaged photographs of a 12 mm diameter cylinder when a) - d) $\delta \approx 2$ and e) - g) $\delta \approx 3$ for a and e) $U_d/U_{mf} = 0$, b and f) $U_d/U_{mf} = 1$, c and g) $U_d/U_{mf} = 2.3$, d) $U_d/U_{mf} = 4$.

From the photographs, the cap extended ~ 2 mm above the top of the cylinder or $\sim 1/3$ the radius, a . As the top of the cylinder was not quite level with the surface of the bed, the top of the cap protruded 2.8 mm above the surface of the bed, or 0.46 times the radius of the cylinder. The vertical extent of such a region is far smaller than a defluidised hood, which can have a maximum height up to 5.8 times the radius of the cylinder, as discussed in Section 3.1.4. The fluidised cap above the cylinder in Fig 3.18 c) had a volume, per unit length of $0.541a^2$ or

0.172 times the volume of the cylinder beneath it. Employing the same dimensions for a cap above a sphere, the cap would have a volume of $0.692a^2$ or 0.165 times the volume of the sphere. The derivation for these volumes is shown in Appendix 3.3. The volume of this fluidised cap is 18 times larger than the volume of particles which could rest in a loose pile on top of a sphere and also 1.8 times larger than the volume of defluidised hood shown in Fig. 3.4 a) and calculated assuming the top of the defluidised hood was level with the surface of the bed. As the part of the fluidised cap which protrudes from the bed surface does not displace any of the bed material it serves to contribute significantly to a surcharge on the sphere.

When the cylinder was even lower in the bed, for example at $\delta \approx 3$ as shown in Fig 3.18 e) – g), and the cylinder was not emitting gas, the defluidised hood formed, as expected – note the region of static particles above the cylinder in Fig. 3.18 e). When U_d/U_{mf} was > 0.5 , no permanent hood of particles was observed, as expected from the conclusions of Section 3.2.1. The streams of bubbles rising on each side of the cylinder joined together above the cylinder and created a region of bubbles and bed material rising above the cylinder as shown in Fig. 3.18 g)

In summary, the elevated cap of particles was only observed when $\delta \approx 2$. However, due to the limited number of draughts which were examined, the upper and lower bound of δ , for which a cap of particles can form stably, is unknown.

By taking into account the weight of the cap of fluidised particles above a cylinder the force balance Eq. (3.25) is arrived at

$$\begin{aligned} \pi a^2 \rho_s g l + 0.5409 a^2 l g \rho_p (1 - \varepsilon_{mf}) & \quad (3.25) \\ = 2a^2 l \rho_p (1 - \varepsilon_{mf}) g \int_{\frac{\pi}{2}}^{\pi} (\cos \theta + 1 - \delta) \cos \theta d\theta & \end{aligned}$$

The first term is the weight of the cylinder, the second term accounts for the weight of a cap of fluidised bed particles as depicted in Fig. 3.18 b), of height $4/3a$ from the centre of the cylinder. These should be equal to the integral of the pressure distribution across the underside of the cylinder.

Equation. (3.24) was rearranged to find a modified expression for the density ratio and yielded Eq. (3.25), below, valid when the upper surface of the cylinder is close to the surface of the fluidised bed: $1.5 < \delta < 2.5$ and when $U_d/U_{mf} > 0.5$ such that the cap is fully fluidised.

$$\frac{\rho_s}{\rho_p(1 - \varepsilon_{mf})} = \frac{1}{\pi}(2\delta - 2 - 0.5407) + \frac{1}{2} \quad (3.25)$$

The equivalent expression for a sphere would be:

$$\frac{\rho_s}{\rho_p(1 - \varepsilon_{mf})} = \left(\delta - \frac{1}{3} - \frac{0.6923}{\pi} \right) \frac{3}{4} \quad (3.26)$$

Eq. (3.26), for spheres which emit gas above $U_d/U_{mf} = 0.5$, is plotted, together with the prediction of Eqs. (3.5) and (3.6) for inert spheres, in Fig. 3.19 for $1.5 < \delta < 2.5$

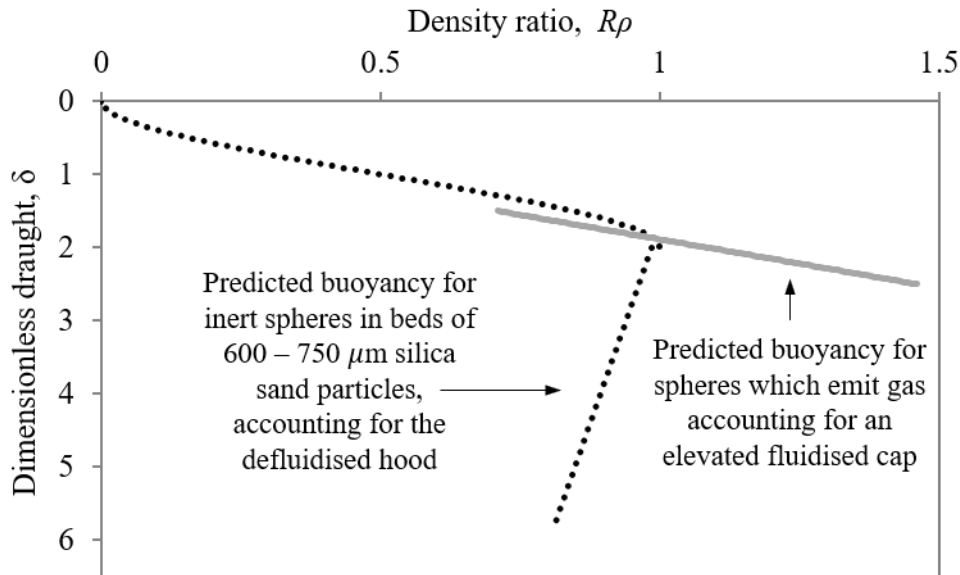


Fig. 3.19. A comparison between the expected buoyancy for inert spheres in a fluidised bed accounting for the defluidised hood, given by Eqs. (3.5) and (3.6), ($\cdot \cdot \cdot$), and for spheres emitting gas at above $U_d/U_{mf} = 0.5$, accounting for an elevated cap of bed material held trapped above the sphere ($—$), given by Eq. (3.26).

Figure 3.19 and Eq. (3.26) predict that fuel particles for which the density ratio is between 0.7 and 1, will come to a dynamic equilibrium at a slightly deeper draught (at most $0.18a$) than an inert counterpart, given by Eq. (3.5) owing to the weight of the elevated fluidised cap. For inert particles, a second stable depth is possible deeper within the bed owing to the formation of a defluidised hood as discussed previously and shown by the dog-leg in Fig. 3.19, given by Eq.

(3.6). However, when $U_d/U_{mf} > 0.5$ this can no longer form and the characteristic dog-leg in the buoyancy curve is not present. For fuel particles with a density ratio of between 1 and 1.46, Eq (3.26) predicts that a particle giving out gas may float near the surface of the bed where an equivalent inert particle would sink through the bed. This is because in this range, the elevated cap of particles, having sloping sides, weighs less than the bed material which would, otherwise, occupy the space between the fuel particle and the surface of the bed and consequently, a denser fuel particle may float than would be expected if the sphere were inert. Such an eventuality indicates that, if emitting gas at a sufficient rate, even particles denser than the bed, might remain close to the surface of the bed during devolatilisation.

Therefore, an interesting consequence of the elevated fluidised cap and fast-moving regions on either side of a particle emitting gas could be that a fuel particle with a density ratio higher than unity, could, if it reaches the surface of the bed, float stably just beneath the surface of the bed. If perturbed from this position, for example by a bubble passing nearby, however the particle may fall momentarily deeper into the bed such that the elevated fluidised cap can no longer form above it and the particle would then sink further from the surface until pulled back again under the influence of passing bubbles in the fluidised bed.

The elevated cap of particles might also result in fuel particles, over a range of density ratios between 0.7 and 1.46 becoming hidden from view just beneath the surface of a fluidised bed during devolatilisation. Consequently, observing the bed from above the surface, for example through an inspection window set into the freeboard of a fluidised bed combustor, might underestimate the degree of segregation of the fuel particles because they are just hidden from view by a thin layer of fluidised particles.

As the equilibrium draught of fuel particles between $0.5 < R_p < 1.5$, which encompasses a wide range of solid fuel and bed material combinations, changes depending on whether or not gas is emitted by the particle, any research directed at segregation phenomena should be undertaken at the appropriate temperature of the fuel-processing operation. The findings of studies into biomass segregation at room temperature, for example by Zhang *et al.* (2009), may be of limited utility for understanding the behaviour of the same particles in a combustor or gasifier.

Conclusions

The formation of a hood of defluidised bed material on top of a sphere floating in a fluidised bed serves to increase the effective density of the sphere and hood taken as a single object. In the context of particles of fuel, a bubble of gas bursting at the surface of the bed can throw bed material over the top of a fuel particle floating there and force it down into the bed. For spheres where $R_\rho < 0.7$, the sphere will resurface regardless of the depth to which it was initially forced, and irrespective of the bubbling state of the bed. Where $0.7 < R_\rho < 0.98$ the sphere, if forced far enough into the bed initially, may sink down into the bed and will only rise if caught in the wake of a passing exogenous bubble.

Defluidised hoods were found to contain a zone at their base where the bed particles were stationary. The material around the stationary zone was also found to bear upon the submerged object but was difficult to differentiate visually from the rest of the bed. This is because the particles in the hood above the stationary zone were in motion because of the drag from the fast-moving bubbles, the origin of which is examined in Chapter 4, passing on either side of the hood. The particles in the hood also move down and away from the hood as a result of gravity.

The concept that the envelope of the defluidised hood had tapering sides, where the side angle was found from the time-averaged images of defluidised hoods, was found to be inadequate to explain the maximum stable depths of inert spheres, and underpredicted the maximum length of a defluidised hood significantly. A parallel-sided defluidised hood was found to be a preferable model.

If the sphere is emitting gas from its surface at a velocity close to, or larger than, $0.5 U_{mf}$, and becomes buried, any material above the sphere cannot become defluidised. In this way, a sphere which is emitting gas can remain at the surface of a fluidised bed and resist becoming buried where a sphere of equivalent size and density, which is not emitting gas from its surface would otherwise sink.

A condition exists where a cap of fluidised bed particles can become trapped on the uppermost surface of a gas-emitting particle when it is near the surface of a fluidised bed. Consequently, fuel particles are able to, float slightly deeper than expected and may not be visible from the

top of the bed. Additionally it is theoretically possible for devolatilising fuel particles with a density ratio exceeding unity to float just beneath the surface of the bed.

The buoyancy of inert and gas-emitting spheres in a fluidised bed can be divided into five bands of density ratio in which the floating or sinking behaviour is distinct. Table 3.1 summarises the characteristics, assuming that segregation induced by exogenous bubbles neglected.

Table 3.1. Range of possible behaviours predicted by Eqs. (3.5 – 3.7) for inert particles and (3.26) for gas-emitting particles across five bands of density ratio.

Density ratio	Inert Sphere	Sphere emitting gas above $U_d/U_{mf} = 0.5$
0 – 0.7	Rise slowly to the surface from any depth. A defluidised hood is present until the particle broaches the surface of the bed.	Rise rapidly to the surface from any depth. No defluidised hood forms
0.7 – 0.9	Rise very slowly to the surface if buried at a shallow depth. A defluidised hood is present until the particle broaches the surface of the bed. Once there the particle is expected to float higher at the surface than a gas-emitting sphere. A small defluidised region may remain. If released beneath a critical depth the particle will slowly sink to the bottom of the bed under its defluidised hood.	Rise to the surface of the bed from any depth. Subsequently may remain just beneath the surface beneath an elevated cap of particles
0.9 - 1	Sink to the bottom of the bed from any depth under its defluidised hood, even if released from the surface of the bed.	Rise to the surface of the bed from any depth. Subsequently remains just beneath the surface beneath an elevated cap of particles
1 – 1.46	Sink to the bottom of the bed from any depth under its defluidised hood, even if released from the surface of the bed.	If close to the surface will remain there beneath an elevated cap of particles. Perturbation could result in the particle sinking. The particle can only return to the surface of the bed under the influence of bubble driven segregation as described by Multiple or Single bubble segregation mechanisms (Fiorentino <i>et al.</i> 1997 b).
>1.46	Sink to the bottom of the bed from any depth under its defluidised hood, even if released from the surface of the bed.	Sink to the bottom of the bed from any depth. The particle can only return to the surface of the bed under the influence of bubble driven segregation as described by Multiple or Single bubble segregation mechanisms (Fiorentino <i>et al.</i> 1997 b).

Biomass particles emitting gas in a fluidised bed are likely to have a sufficiently small density number that, during devolatilisation, they rarely become sufficiently buried for bubbles to form above them, because of the disruption of the defluidised hood caused by the gas they are emitting. Consequently, correlations for the penetration depth of solid fuel particles in fluidised beds, for example that given by Nienow *et al.* (1978a) cannot be applied to biomass particles, even if their accelerated rise to the surface caused by bubble-driven segregation is taken into account.

Chapter 4 Levitation of devolatilising particles in fluidised beds

4.1 Introduction

In previous Chapters, two principal mechanisms have been discussed which contribute to the segregation of devolatilising biomass particles in fluidised beds. In Chapter 1, it was noted that many authors have cited bubble-driven segregation, where devolatilising fuel particles are lifted to the surface in the wake of the endogenous bubbles they form, as described by Fiorentino *et al.* (1997 a and b). In this case, a devolatilising particle must be firstly buried deep enough within the bed for a bubble to form above it, if it is to be carried up in the bubble's wake. In Chapter 3 it has been demonstrated that particles which emit gas can a) rise faster and b) become buried less deeply than inert particles of the same size and density owing to the emitted gas disrupting the formation of a defluidised hood above the particle.

Rees (2005) discussed a model for determining whether a particle emitting gas, and positioned at the base of the bubble it is producing, will sink into, or rise with, the wake of the bubble. Rees (2005) suggested that the emission of gas from the underside of a particle could generate a region of higher pressure, which would support the particle. This Chapter firstly explores Rees's (2005) conjecture by exploring the hypothesis that lift is produced by the emission of gas from the underside of a sphere, or cylinder, in a fluidised bed. Such behaviour could result in fuel particles floating on the surface of the bed and making them less likely to become submerged and so increasing their residence time at the surface. To explore this hypothesis, a theory is developed in this Chapter for fuel particles behaving in a manner similar to that of a droplet of liquid boiling on top of a solid heated plate, which is above the "Leidenfrost" temperature for the droplet. The droplet floats because, upon contact with the hot surface, a pocket of vapour is maintained between the droplet and the surface. If analogous, the volatile matter (VM) produced by a solid piece of biomass heating up in a fluidised bed would serve to push the hot bed material away and lift the particle. The theory has then been investigated experimentally.

Additionally, this chapter analyses the behaviour of the voids produced beneath a gas-emitting particle, in order to obtain an experimental estimate of the upthrust on the gas-emitting particle from the surrounding fluidised particles.

4.2 Fluidised bed “Leidenfrost” hypothesis

The analysis of the floating behaviour starts with the hypothesis that the behaviour of a devolatilising particle on the surface of a bed is similar to the floating behaviour observed when droplets of liquid are deposited on a solid surface heated to a temperature substantially in excess of their boiling point. As noted in Section 4.1, above a critical temperature, the droplets float on a thin layer of vapour given off because of boiling of the droplet: a phenomenon known as the Leidenfrost effect. In fact, Teixeira *et al.* (2015) have shown that solid particles of cellulose heating up on a hot surface also manifest this behaviour whereby, above 700°C, the particles were lifted from the hot, polished surface. As with a liquid droplet, the presence of gas or vapour between the cellulose particles and the plate resulted in a reduced rate of heat transfer and, hence, the rate of production of volatiles decreased markedly.

The following analysis starts with the assumption that a particle dwelling at the surface of a fluidised bed does so as a consequence of the emission of gas from the periphery of a fuel particle. Following the discussion of Section 3.2, spheres emitting gas at $U_d/U_{mf} > 0.5$ are expected to bear a negligible defluidised hood and, thus, obey the buoyancy behaviour expected of inert objects floating in liquid, described by Eq. (3.3), unless the fuel particle’s upper surface is very close to the surface of fluidised bed, in other words, its dimensionless draught, $\delta = 2$. Close to $\delta = 2$, a cap of fluidised particles above the fuel particle can prevent the fuel particle from rising further out of the bed. Consequently, it must be assumed that for Leidenfrost behaviour to lead to segregation of biomass particles at the surface of a fluidised bed, the devolatilising object, at $\delta = 1$ would otherwise have sunk to $\delta > 2$ were it not emitting gas. Such a condition would suggest that once the emission of gas abates, the fuel particle would mix within the bed, even though its density has decreased as a result of losing its content of VM.

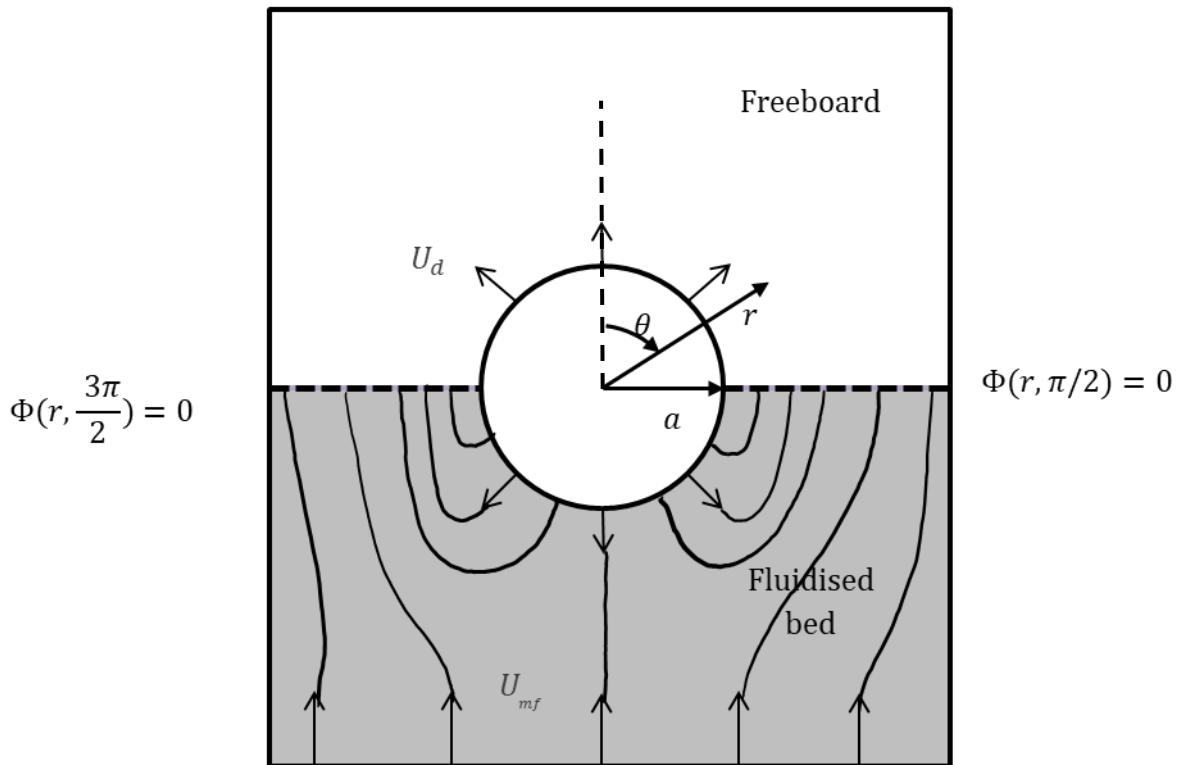


Figure 4.1. Schematic diagram showing the spherical particle, radius a , half submerged within a medium at incipient fluidisation with superficial fluidising gas velocity U_{mf} . The spherical surface emits gas at superficial velocity U_d . Φ is the velocity potential function, the horizontal line of $\Phi = 0$ represents the surface of the bed. The form of the streamlines that the Leidenfrost model assumes has been sketched onto this diagram.

To arrive at a working model, the analysis starts with the idealised situation shown in Figure 4.1. Here, a sphere of constant radius, a , is semi-submerged at the surface of an incipiently fluidised bed. The density of the sphere exceeds that of the density of the incipiently fluidised bed, so that it maintains its position as a consequence of the pressure field on its submerged surface and its weight. The pressure field is the net result of gas flowing through the fluidised bed at superficial velocity, U_{mf} , and gas being emitted from the sphere, with superficial velocity U_d at its periphery. To begin the analysis, the following additional assumptions were made:

- a) The two-phase assumption applies to the particulate phase, with the voidage, ϵ_{mf} , and superficial fluidising velocity, U_{mf} , being constant. The fluidising gas flow, above that required to fluidise the bed, is assumed to bypass the emulsion phase as bubbles or

voids. The interaction between these bubbles and the emitting particle is not considered in the present treatment.

- b) The system is isothermal at the temperature, T_∞ , of the bed.
- c) The gas produced by the particle is assumed to flow radially and uniformly away from the surface and it is assumed to have the same properties as the fluidising gas.
- d) Pseudo-steady conditions are used such that the particle size can be assumed to be constant.
- e) The flow of gas and particles is irrotational.
- f) Compressibility of the gas is ignored and the gas is assumed to permeate the emulsion phase under a pressure gradient proportional to the relative velocity between the fluidising gas, local velocity, \mathbf{v} , and the particles, local velocity, \mathbf{u} , viz. D'Arcy's Law applies:

$$\mathbf{u} - \mathbf{v} = -K\nabla p_f \quad (4.1)$$

where K is the permeability constant and p_f is the pressure in the gas.

In the sixth assumption, the value of K was found by comparing the pressure drop through the bed with the interstitial velocity at incipient fluidisation conditions, as described later. Also, the use of a single permeability constant to model the pressure drop through a fluidised medium, as utilised by Davidson & Harrison (1963), is addressed in detail, later in this section.

Following Davidson & Harrison (1963), if the voidage is everywhere constant, equal to ε_{mf} , then the continuity equations for the gas and particles, respectively, become

$$\nabla \cdot \mathbf{v} = 0 \quad (4.2)$$

and

$$\nabla \cdot \mathbf{u} = 0 \quad (4.3)$$

The velocities can be eliminated from Eqs. (4.1) to (4.3), yielding Laplace's equation

$$\nabla^2 p_f = 0. \quad (4.4)$$

As pointed out by Davidson & Harrison (1963), Eq. (4.4) is interesting in that the pressure distribution is unaffected by the motion of the particles, and is, in fact, the same as it would be in a fixed bed of particles.

To solve the system in Figure 4.1 for the pressure field, one needs to superpose solutions to Eq. (4.4) for (i) the sphere and (ii) the fluidised medium. For (i), consider the idealised system in

Fig. 4.2: a single sphere with its upper and lower surfaces emitting fluid at equal and opposite uniform velocity with the two hemispheres isolated from each other over their horizontal, diametral plane.

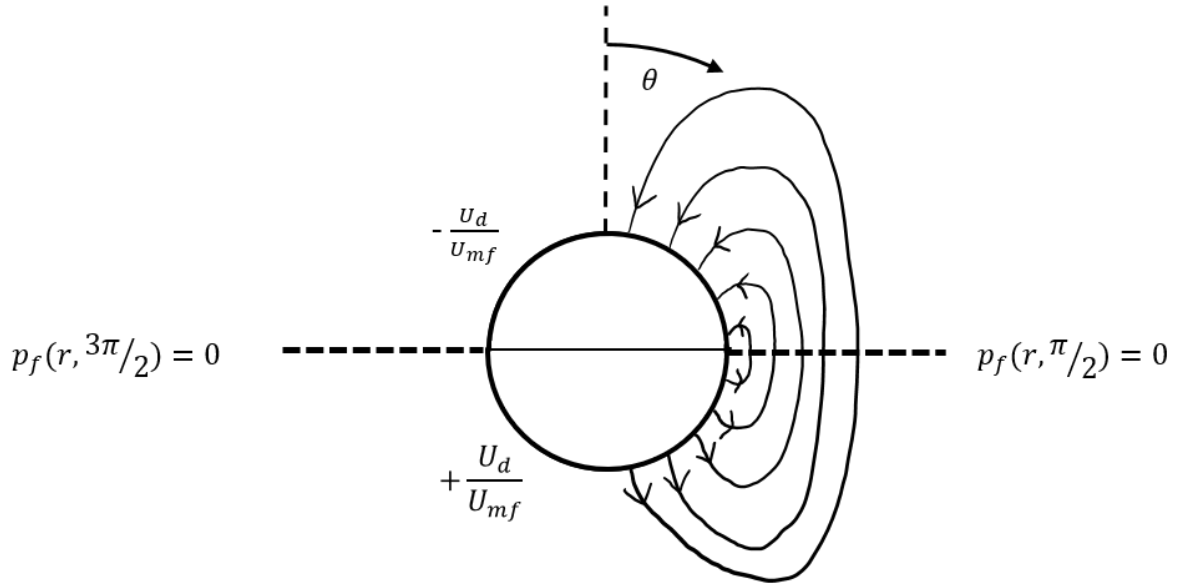


Figure 4.2. A sphere divided by a thin insulator, with its upper surface taking in gas at a radial velocity of $\frac{U_d}{\epsilon_{mf}}$ and lower surface emitting gas at a radial velocity of $\frac{U_d}{\epsilon_{mf}}$. The whole is immersed in a medium obeying D'Arcy's Law and a plane of zero pressure is imposed level with the diameter of the sphere. Also included is a sketch of the streamlines around the right hand side of the sphere.

Image theory is used here to allow the pressure at $\theta = 3\pi/2$ and $\theta = \pi/2$ to be equal to zero.

The zero pressure condition here represents the surface of the bed.

Since the fluid has been assumed to be inviscid, there can be no shear forces within the system and the flow is irrotational, viz. $\nabla \times \mathbf{u} = 0$:

$$\frac{\partial}{\partial r}(ru_\theta) - \frac{\partial u_r}{\partial \theta} = 0 \quad (4.5)$$

where u_θ and u_r are the circumferential and radial interstitial velocities respectively. This is satisfied by

$$u_r = \frac{\partial \Phi}{\partial r} \quad \text{and} \quad u_\theta = \frac{1}{r} \frac{\partial \Phi}{\partial \theta} \quad (4.6)$$

which defines the velocity potential Φ .

From D'Arcy's law, when the fluid flow is independent of particle motion, as deduced above

$$u_r = -K \frac{\partial p_f}{\partial r} \quad \text{and} \quad u_\theta = -\frac{K}{r} \frac{\partial p_f}{\partial \theta} \quad (4.7)$$

So a direct comparison between Eqs. (4.6) and (4.7) reveals that

$$\Phi = -K p_f \quad (4.8)$$

The sphere is immersed in a uniform medium, in which flow obeys D'Arcy's Law. The pressure, $p_f(r, \theta)$, at any point can be found from the general solution to Laplace's Equation (4.4) external to the sphere:

$$p_f(r, \theta) = -\frac{1}{K} \sum_{n=0}^{\infty} B_n r^{-(n+1)} L_n(\cos \theta) \quad (4.9)$$

where r is the radial distance from the centre of the sphere and θ is the azimuthal angle around the sphere. The B_n are constants and the L_n are the Legendre polynomial coefficients.

The boundary conditions at the surface of the sphere, within the fluidised medium are:

$$-\frac{K}{r} \frac{\delta p_f}{\delta \theta} \Big|_a = u_\theta = 0 \quad (4.10)$$

and

$$-K \frac{\partial p_f}{\partial r} \Big|_a = u_r = \frac{-U_d}{\varepsilon_{mf}} \quad 0 \leq \theta < \pi/2 \quad \text{and} \quad 3\pi/2 \leq \theta < \pi \quad (4.11)$$

$$-K \left. \frac{\partial p_f}{\partial r} \right|_a = u_r = \frac{+U_d}{\varepsilon_{mf}} \quad \pi/2 < \theta \leq 3\pi/2 \quad (4.12)$$

where u_θ and u_r are the circumferential and radial velocities respectively and U_d is the velocity of gas emitted from the surface of the sphere. Using the radial boundary conditions and Eq. (4.9) gives

$$u_r|_a \equiv f(\theta) = - \sum_{n=0}^{\infty} (n+1) B_n a^{-(n+2)} L_n(\cos \theta) \quad (4.13)$$

where $f(\theta) = -\frac{U_d}{\varepsilon_{mf}}$ for $0 \leq \theta < \pi/2$ and $+\frac{U_d}{\varepsilon_{mf}}$ for $\pi/2 < \theta \leq \pi$. Accordingly, the B_n are given by the orthogonality condition for Legendre polynomials:

$$B_n = \frac{(2n+1)a^{n+2}}{2(n+1)} \int_0^\pi f(\theta) L_n(\cos \theta) \sin \theta d\theta \quad (4.14)$$

Letting $x = \cos \theta$, Eq. (4.14) becomes:

$$\begin{aligned} B_n &= \frac{(2n+1)a^{n+2}}{2(n+1)} \int_{-1}^1 f(\theta) L_n(x) dx \\ &= \frac{(2n+1)a^{n+2}}{2(n+1)} (U_d/\varepsilon_{mf}) \left\{ \int_{-1}^0 L_n(x) dx - \int_0^1 L_n(x) dx \right\} \\ &= -\frac{(2n+1)a^{n+2}}{(n+1)} \frac{(-1)^k (2k)!}{2^{2k+1} k! (k+1)!} (U_d/\varepsilon_{mf}) \quad \text{for odd } n = 2k+1 \\ &= 0 \quad \text{for even } n \end{aligned} \quad (4.15)$$

The pressure distribution for the sphere in Figure 4.1 when placed in a uniform stream must now be evaluated. The potential flow function for a sphere placed in uniform gas flow, with $\frac{U_{mf}}{\varepsilon_{mf}}$ being the interstitial stream velocity a long distance upstream and downstream of the sphere, is

$$\Phi(r, \theta) = \frac{U_{mf}}{\varepsilon_{mf}} \cos \theta \left(r + \frac{a^3}{2r^2} \right) \quad (4.16)$$

Thus, using Eqs. (4.16) and (4.8), the pressure distribution in the gas around a quiescent sphere in a uniform stream is readily obtained by the addition of the potential functions. The result obeys all the boundary conditions for $\pi/2 \leq \theta \leq 3\pi/2$ and, accordingly, gives the pressure distribution below the surface of the bed for the system shown in Fig. 4.1. To proceed, it was assumed that the pressure variation around the upper surface of the sphere is negligible compared to that below and is approximately equal to that of the surface of the bed, *viz* $p_f(r, \theta) \approx 0$ for $-\pi/2 \leq \theta \leq +\pi/2$.

Hence, for the floating sphere for $3\pi/2 > \theta > \pi/2$:

$$p_f(r, \theta) = -\frac{U_{mf}}{\varepsilon_{mf}K} \cos \theta \left(r + \frac{a^3}{2r^2} \right) + \frac{1}{K} \sum_{n=0}^{\infty} B_n r^{-(n+1)} L_n(\cos \theta) \quad (4.17)$$

It is important to note that this method of analysis neglects form drag and, so far, holds for any sphere set into a porous D'Arcy medium and is independent of orientation, since gravitational force does not enter the derivation of Eq.(4.17). Once applied to fluidised beds the buoyancy of the sphere within the emulsion phase has to be taken into account, as discussed later in this section and in more detail in Section 4.2.1.

The resultant force, F , in the direction $\theta = 0$ is readily found from Eq. (4.17), thus:

$$F = \int_{\pi/2}^{\pi} p_f \cos(\theta) 2\pi a^2 \sin(\theta) d\theta \text{ at } r = a$$

$$F = \frac{U_{mf} \pi a^3}{\varepsilon_{mf}K} + \frac{U_d \pi a^3}{\varepsilon_{mf}2K} \quad (4.18)$$

with the second term simplifying since the only non-zero term in the resulting integration of the summation was for $n = 1$ in Eq. (4.15).

The intention of the analysis is to model the vertical forces acting on a sphere floating in a fluidised medium and, therefore, from this point in the analysis, the force given by Eq. (4.18),

acts in the opposite direction to the gravitational force. If the Leidenfrost condition *just* holds, a thin gas gap will appear around the lower surface of the sphere (*i.e.* for $\pi/2 < \theta < 3\pi/2$). In that case, the force in eq. (4.18) is equal to the weight of the particle, so

$$F = \frac{4}{3}\pi a^3 \rho_d g \quad (4.19)$$

where ρ_d is the density of the sphere. Since this solution is for a solid sphere emitting gas into a gas fluidised bed such that $\rho_f \ll \rho_p$, the density of the displaced gas has been neglected.

In the foregoing it has been assumed that the fluidised bed behaves as a D'Arcy medium and, therefore, has a linear pressure gradient, proportional to the velocity of the gas passing through it. At incipient fluidisation, the pressure gradient in the fluid must be sufficient to balance the buoyant weight of the fluidised particles, per unit area of bed and per unit height of bed, thus:

$$\nabla p_f = -(\rho_p - \rho_f)g(1 - \varepsilon_{mf}) \quad (4.20)$$

However, from Eq. (4.1) for incipient fluidisation, the pressure gradient is related to the interstitial gas velocity *via* the D'Arcy coefficient, K :

$$\frac{U_{mf}}{\varepsilon_{mf}} = -K\nabla p_f$$

hence, for a bed at incipient fluidisation:

$$K = \frac{U_{mf}}{\varepsilon_{mf}(\rho_p - \rho_f)g(1 - \varepsilon_{mf})} \quad (4.21)$$

In using a single value of K throughout the fluidised medium the assumption is made that the voidage and incipient fluidisation velocity of the medium are unchanged by the presence of a solid object in the bed and remain the same at all locations throughout the bed. This is an application of the two-phase assumption made at the start of this analysis.

From Eqs. (4.18), (4.19) and (4.21), a simple dimensionless condition for limiting flotation emerges:

$$\frac{4 \rho_d}{3 \rho_p} \frac{1}{(1 - \varepsilon_{mf})} = \left(\frac{U_{d \min}}{2U_{mf}} + 1 \right) \quad (4.22)$$

Accordingly, if $\frac{4 \rho_d}{3 \rho_p} \frac{1}{(1 - \varepsilon_{mf})} < \left(\frac{U_{d \min}}{2U_{mf}} + 1 \right)$ the sphere should just hover at $\delta = 1$ on a pocket of gas separating it from the fluidised medium. Conversely, if the inequality does not hold, the sphere will sink into the bed. Interestingly, Eq. (4.22) shows no dependence on diameter of the devolatilising particle.

An equivalent expression can be found for cylindrical geometries. The derivation is included in Section A4.1 and the derived pressure distribution predicted in the fluidised material surrounding a long cylinder at $\delta = 1$ is given by Eq. (4.23).

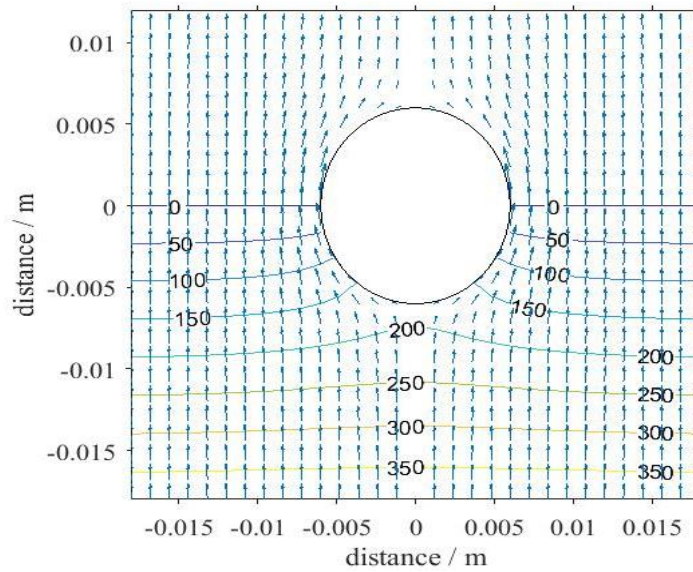
$$p_f(r, \theta) = -\frac{U_{mf} r}{\varepsilon_{mf} K} \left(1 + \frac{a^2}{r^2} \right) \cos(\theta) \quad (4.23)$$

$$+ \frac{4U_d}{\varepsilon_{mf} K \pi} \left(\frac{a^2}{r} \cos(\theta) - \frac{a^4}{9r^3} \cos(3\theta) \right)$$

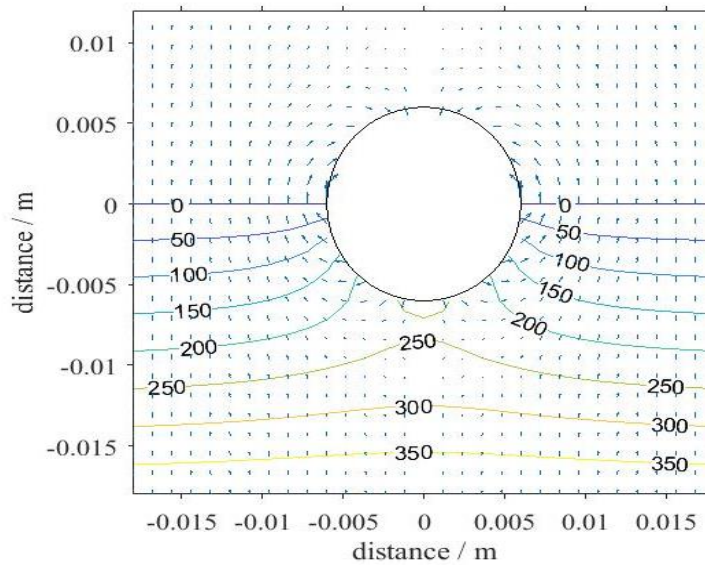
where the solution has been curtailed at $O(r^5)$.

Figure 4.3 shows the pressure distribution and gas velocity streamlines around a sphere of radius a , produced from the above analysis for the cases, $U_d/U_{mf} = 0$ and $U_d/U_{mf} = 2$.

From Fig. 4.3, the elevation in pressure directly beneath the sphere, predicted by Eq. (4.17) as a result of increasing U_d can be clearly seen. Fig. 4.3 a) shows that Eq. (4.17) predicts an elevation in pressure beneath a sphere even when it is not emitting gas.



a)



b)

Fig. 4.3. Lines of constant gauge pressure predicted by Eq. (4.17), shown in Pa, and gas velocity vector field around a sphere of 0.012 m diameter for a) $U_d/U_{mf} = 0$, and b) $U_d/U_{mf} = 2$. Although the vectors vertically above the centre line of the sphere are displayed they have no physical meaning, because when $\delta = 1$ the bed material is confined to the lower half of the sphere.

So far, an analytical solution has been used to solve the force balance on a sphere or cylinder for the case where $\delta = 1$. However, at other values of draught ($0 < \delta < 2$), there is no plane of symmetry available to obtain an analytical solution as above. Comsol multi-physics “porous

flow” was used to estimate the pressure distribution numerically, over the entire surface of a spherical particle at the surface of a porous medium for $0 < \delta < 2$. As in the analytical solution, the bed was modelled as a static porous solid and neglected the motion of the bed particles. The parameters used in the Comsol model are given in Appendix 4.2

Using the Comsol model, the force on a sphere was estimated as a function of the rates at which gas passed up through the bed and at which the sphere emitted gas. By balancing this upthrust force against the weight of the particle, the relationships between the density ratio and velocity ratio for values of δ between 0 and 2 were found and are shown in Fig 4.4. A good agreement was found between the Comsol curve at $\delta = 1$ and the analytical solution, indicating that, in the analytical solution, the assumption that the pressure over the top of the particle was negligible compared with that underneath, was reasonable.

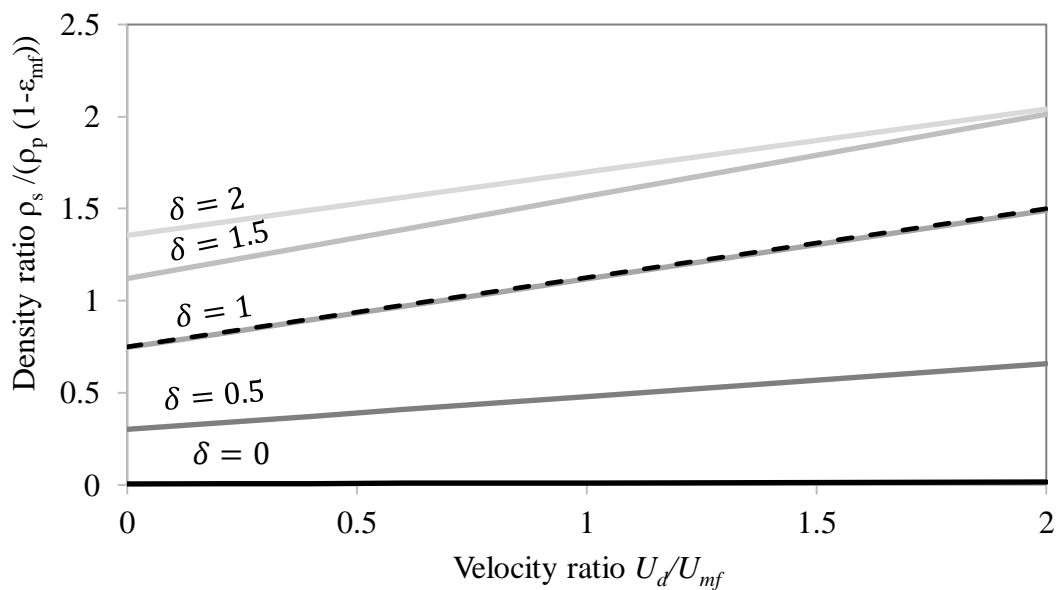


Fig. 4.4. The calculated critical density ratio for a particle emitting gas at a range of velocity ratios at values of δ between 0 and 2. Solid lines present result from Comsol simulations. The analytical solution for $\delta = 1$ is also shown (- - -).

Hence it was possible to find a relationship between the rate at which a particle emitted gas from its surface and its draught, assuming the density ratio remained constant. An example material used extensively in the investigations in Chapter 5 was dry ice. Figure 4.5 shows the draught predicted by the Comsol model for values of U_d/U_{mf} from 0 to 10 for a dry ice sphere

sublimating in a fluidised bed of silica sand. Figure 4.5 shows that a sphere of dry ice, if not emitting gas, would have a draught of just over 1.2. As U_d/U_{mf} increases, the draught of the dry ice sphere is predicted to decrease and approach zero asymptotically. Once U_d/U_{mf} exceeds 0.6 the sphere should, according to the model developed in this Chapter, float with the majority of its surface higher than the surface of the bed, *i.e.* $\delta < 1$.

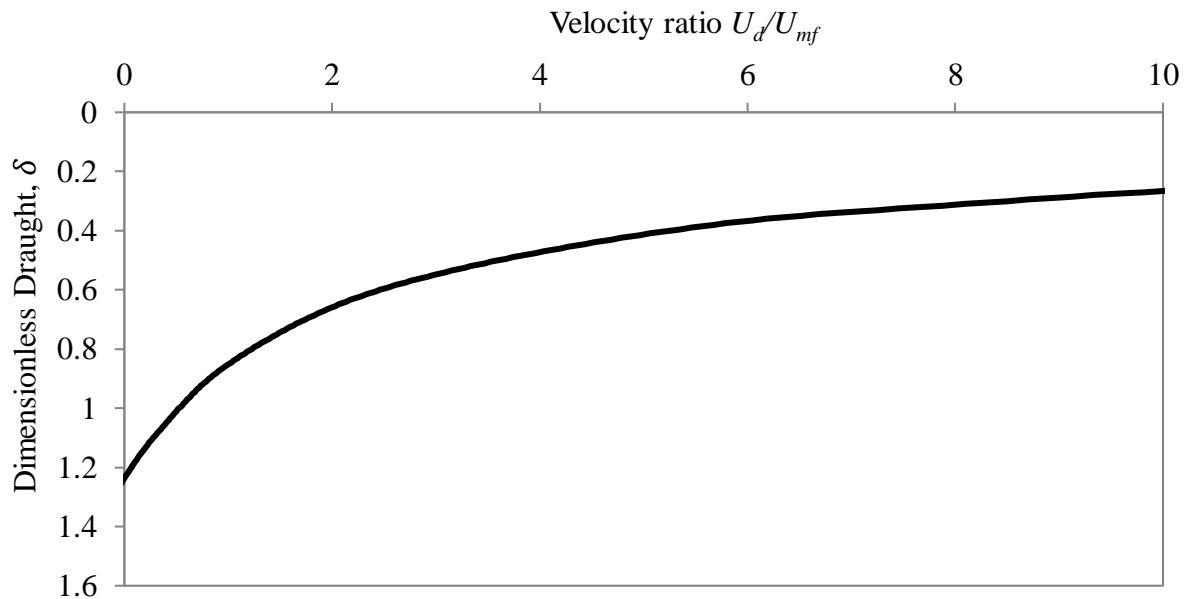


Fig. 4.5. Predictions from Comsol model for the dimensionless draught, δ , of a dry ice sphere floating in a bed of fluidised silica sand for practical values of velocity number.

More generally, Figs. 4.4 and 4.5 show that, if a particle emitting gas behaves in the way assumed in arriving at Eq. (4.22), the emission of gas from the surface of a solid particle serves to elevate that particle higher up, relative to the surface of the bed, than would be expected if that particle were not emitting gas.

The consequence of this behaviour for fuel particles, is that, during devolatilisation, the fuel should rise higher up at the bed's surface and, therefore be less likely to be buried by bed particles flung into the freeboard by bubbles erupting at the surface of the bed nearby. It should be noted that Eq. (4.22) gives an unrealistic result when $U_{d \min} = 0$. It indicates that the density ratio for an inert sphere, one not emitting a fluid, to sit at its diametral plane with $\delta = 1$ in a fluidised bed is

$$\frac{\rho_d}{\rho_p(1 - \varepsilon_{mf})} = \frac{3}{4} \quad (4.24)$$

However, a displacement calculation, such as Eq. (3.3) predicts that the density ratio in this case should be 0.5. The experimental results for the buoyancy of inert spheres, shown in Fig. 3.2, clearly show that such a sphere has a density ratio of just under 0.5. The large error in predicting the behaviour of an inert sphere brings into doubt the predictive power of the theory above for $U_{d \min} > 0$. The next section investigates the cause of this error in the model.

4.2.1 Buoyancy of a sphere assuming the pressure distribution in the fluidised bed is unchanged by the presence of the sphere.

In Section 4.2, the intuitive assumption was made that the presence of a solid object, floating in the fluidised medium would cause the gas to flow around it as shown in Fig. 4.6 a), causing a stagnation pressure underneath the sphere and that the rise in pressure beneath the sphere would be further elevated by the emission of gas from the sphere. This section investigates the consequences of assuming, instead, the somewhat unintuitive flow pattern shown in Fig. 4.6 b). Here the flow of gas through the bed material is unaltered by the presence of a sphere, even when the sphere emits gas.

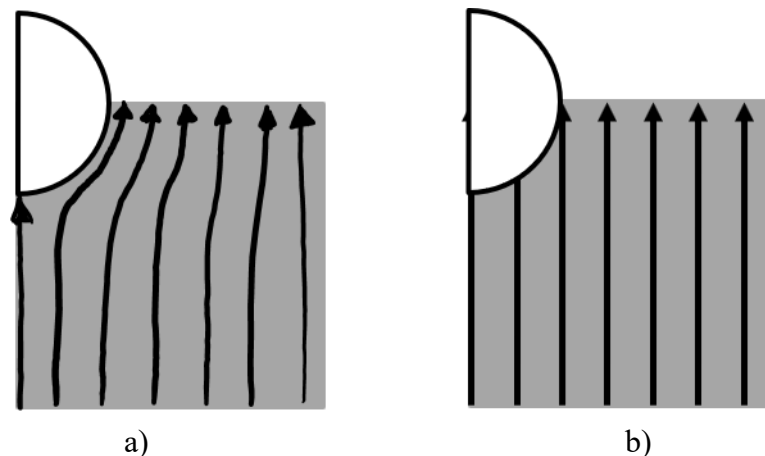


Fig. 4.6. Half profile sketch of the streamlines of the fluidising gas around a spherical object in a fluidised bed. a) shows the intuitive pattern of gas flowing around the sphere as used in the analysis of Section 4.2; b) Shows the flow pattern of gas passing through an undisturbed fluidised medium.

If the pressure distribution in the gas percolating through the fluidised bed material is unchanged by the presence of a sphere, *viz.* it remains linear according to:

$$\nabla p_f = -(\rho_p - \rho_f)g(1 - \varepsilon_{mf}) \quad (4.25)$$

and at the surface of a sphere at draught, δ , with reference to Fig. 4.1:

$$p_f = \rho_p g(1 - \varepsilon_{mf})\{a(\delta - 1 - \cos(\theta))\} \quad (4.26)$$

Letting $\delta = 1$ and, as before using:

$$\frac{4}{3}\pi a^3 \rho_d g = \int_{\pi/2}^{\pi} p_f \cos(\theta) 2\pi a^2 \sin(\theta) d\theta \text{ at } r = a \quad (4.27)$$

the following result is obtained:

$$\frac{4}{3}\pi a^3 \rho_d g = \frac{2}{3}\pi a^3 \rho_d (1 - \varepsilon_{mf})g \quad (4.28)$$

Hence, the expected result for a sphere floating at the surface of a fluidised bed with $\delta = 1$:

$$\frac{\rho_d}{\rho_s(1 - \varepsilon_{mf})} = \frac{1}{2} \quad (4.29)$$

In fact, this analysis gives the same result as the displacement calculation of Eq. 3.3 for any depth $0 < \delta < 2$.

The observation that the behaviour of inert spheres floating in a fluidised medium can be more accurately predicted by assuming that the pressure everywhere in the fluidised medium is given by Eq. (4.25) rather than Eq. (4.17) indicates that the pressure distribution and therefore the flow of gas through the fluidised medium is not changed significantly by the presence of the sphere. By integrating the vertical component of the fluid pressure around the underside of the sphere the same result was obtained as for a displacement calculation, hence, the linearly increasing gas pressure, found in an undisturbed fluidised medium is analogous to the hydrostatic pressure in a liquid.

The next section describes how the pressure distribution in the bed material around a submerged cylinder was measured experimentally and compared with the pressure gradient predicted by Eq. (4.23) to explore which set of streamlines, shown in Fig. 4.6, best describes the flow of gas near a solid object immersed in a fluidised bed.

4.3 Experimental validation of the fluidised bed Leidenfrost effect

In order to investigate experimentally the pressure distribution predicted by solutions of the Laplace equation derived in Section 4.2, pressure measurements were taken at room temperature using the 2-D bed described in Section 2.4. Here, gas was forced through a porous cylinder, trapped between the walls of a 2-D fluidised bed. A series of pressure tappings in the walls of the bed allowed measurements of the time-averaged gauge pressure of the gas in the fluidised medium at a variety of distances, vertically beneath the cylinder. For each pressure tapping, measurements were made for 30 seconds and the mean value of these was calculated. The measured pressure distribution beneath the cylinder for the cases where the 12 mm cylinder was either emitting gas or not are shown in Fig. 4.7. Also plotted in Fig. 4.7 is the pressure distribution predicted by Eq. (4.23) for $U_d/U_{mf} = 0$ and 3.5, and, additionally, the predicted pressure distribution in a fluidised medium in the absence of any obstacle, given by Eq. (4.25).

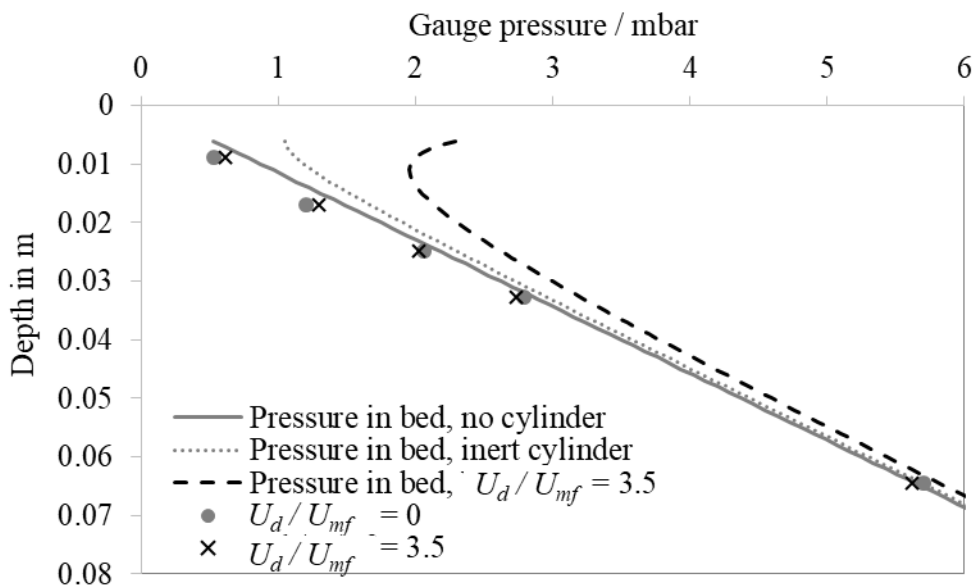


Fig. 4.7. The predicted pressure measured vertically beneath a cylinder of radius 0.005 m at the surface of a bed of fluidised porous alumina particles in a 2-D bed. Also shown are time-averaged experimental measurements of pressure for \bullet) $U_d/U_{mf} = 0$ and \times) $U_d/U_{mf} = 3.5$.

The pressure in the fluidised medium measured below the submerged cylinder closely follows the pressure distribution expected for a fluidised medium in the absence of a cylinder, given by

Eq. (4.25). The increase in pressure close to the underside of the cylinder, as predicted by the theory of Section 4.2, was not observed and no notable further increase in pressure was measured when U_d/U_{mf} was increased.

The theory of Section 4.2, both in the analytical solution and the Comsol simulations, was based on the assumption that the gas produced by the cylinder is forced into the emulsion phase of the fluidised bed until $U_d > U_{d,min}$. It is this extra flow forced through the porous medium which leads to the predicted local rise in pressure beneath the cylinder. However, the experimental evidence in Fig. 4.7 indicates that this cannot be the case. The gas emitted by the cylinder must, instead, pass around the cylinder as bubbles and consequently the assumption that the fluidised bed behaves as a medium with a single permeability constant, K , breaks down close to the cylinder or sphere. The implication of the experimental evidence is that, in the fluidised Group B particles used in this study, the two-phase assumption is quite robust. The pressure distribution measured beneath the cylinder more closely resembles that beneath a cylindrical void of the same size as described by Davidson and Harrison (1963) and shown in Fig. 4.8.

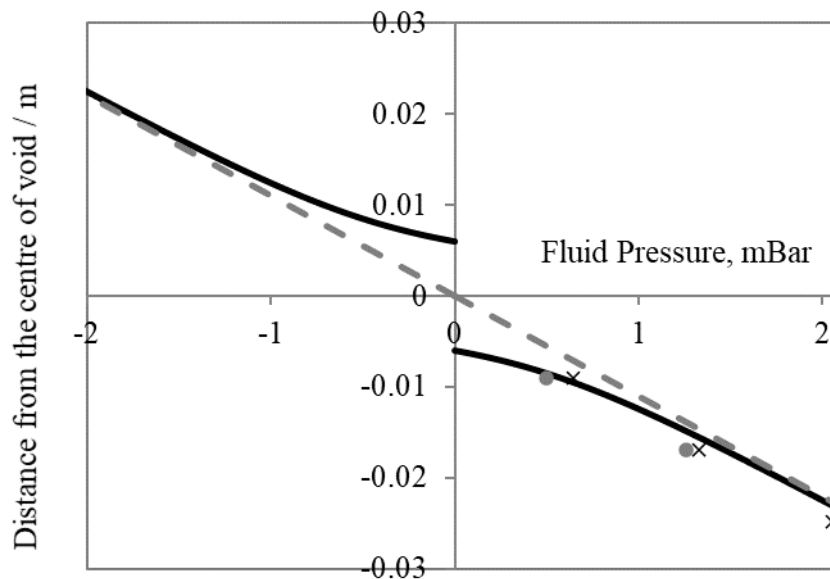


Fig. 4.8. The theoretical pressure distribution in the fluid vertically above and below a spherical void in a fluidised bed according to theory by Davidson and Harrison (1963). Also shown are time-averaged measurements of pressure for ●) $U_d/U_{mf} = 0$ and ✕) $U_d/U_{mf} = 3.5$.

This would indicate that gas from the fluidised material around the cylinder is drawn towards the cylinder, even when $U_d > 0$, rather than being pushed away and around it and that the velocity of gas relative to the particles may look more like that shown in Fig. 4.8 from Davidson and Harrison (1963, Fig 29, page 76). The cylinder offers a short-circuit for gas from the bed material. Smaller pressure tapings, closer to the surface of the cylinder would be a beneficial addition to the experimental apparatus to discover if the reduction in pressure trend continues close to the cylinder's surface.

The suggestion that the presence of the cylinder allows gas from the fluidised bed a short-cut route is supported by the work of Di Natale *et al.* (2010) and Rong *et al.* (1999) who described a region of increased voidage of between 0.9 and 0.8 next to the lower surface of objects in fluidised beds. The narrow region of high voidage allows gas to pass with a lower pressure drop per unit depth than gas passing through the fluidised medium. As such, the void represents a “short cut”, which leads to the streamlines of gas passing through the bed heading towards the submerged object, rather than around it. Such a flow pattern could induce a circulation of particles in the bed around the submerged object, which was neglected in the theory developed in Section 4.2. The consequences of such a circulation of particles is discussed in Section 5.5.3. Due to the incorrect, but intuitive, assumptions: a) that the presence of a solid object in a fluidised medium causes the gas streamlines in the bed to divert around the object and, b) that the gas emitted by an object in a gas fluidised bed passes into the emulsion phase of the fluidised material, the treatment in Section 4.2 of the phenomena associated with gas-emitting objects in fluidised beds, is misleading in the context of beds aggregatively fluidised by gas. However, in the context of particulate fluidised beds, gas flow rates in excess of the minimum fluidisation condition could pass into the emulsion phase rather than forming bubbles, causing the voidage of the bed material to increase. A modified form of the Leidenfrost theory above may yet yield results pertinent to particulate fluidised beds but this is beyond the scope of the current work.

The next section investigates the fate of both the fluidising gas which passes straight up underneath the sphere or cylinder (rather than diverting around it) and the gas which is emitted by the sphere or cylinder.

4.4 Analysis of the structure of the fluidised bed beneath a gas-emitting cylinder

Tempting though it might be to postulate that a devolatilising sphere forms a cushion of gas around itself, thereby isolating itself from the bed material, the results of Sections 4.2 and 4.3 have conclusively shown that the situation is more complicated and involves a region close to the sphere's, or cylinder's, surface which has a higher voidage than the rest of the emulsion phase of the fluidised bed. To determine more accurately what occurs near the surface of a submerged cylinder as the cylinder emits gas at different rates, the 2-D bed described in Section 2.4 was again used, this time filmed by a camera recording at 133 frames s^{-1} .

4.4.1 Experiment

As outlined in Section 2.4 a porous cylinder sandwiched between the clear acrylic walls of a 2-D bed, fluidised at room temperature, was imaged at 133 frames s^{-1} . The bed was fluidised at $U/U_{mf} \sim 1$ and bed material was added or removed to vary the position of the surface of the fluidised material relative to the cylinder such that $\delta = 1, 1.8$ or 6.2 . The porous cylinder was connected to a supply of air, the flowrate of which was set to achieve values of U_d/U_{mf} from 0 to 4.

Figure 4.9 shows a typical frame-wise progression of a bubble forming near the underside of a submerged cylinder, emitting gas at its surface at a velocity of $U_d/U_{mf} = 1$. The images are 7.5 ms apart in time. It is immediately apparent that rather than a uniform region with a higher voidage around the submerged cylinder, a string of bubbles form near the surface of the cylinder. Each bubble pushes bed particles ahead of it as it rises up and around the underside of the cylinder in a regular cycle. Referring to the angle, θ , in degrees in Fig. 4.9 a), the bed material was initially pressed up against the cylinder at 180° , but at $90, 135, 225,$ and 270° the cylinder was blanketed by a bubble on each side. In Fig. 4.9 b), 7.5 ms later, the bed material at the base of the cylinder was pushed away a small amount, suggesting the presence of a bubble there, even if the bubble cannot be seen. Movements such as this were nevertheless detected by comparing frames and observing changes in position of the bright white bed particles. By Fig. 4.9 c), the bubbles had grown and progressed up to the surface of the bed, pushing bed material further away from the upper part of the cylinder's surface, and the bed

had pushed back on to the cylinder flanks at 135 and 225°. Figure. 4.9 d) shows the two bubbles from each side of the cylinder breaking through the upper surface of the bed. Additionally, a new bubble at 180°, previously obscured by the adhesive which secures the cylinder to the walls of the bed, is now visible.

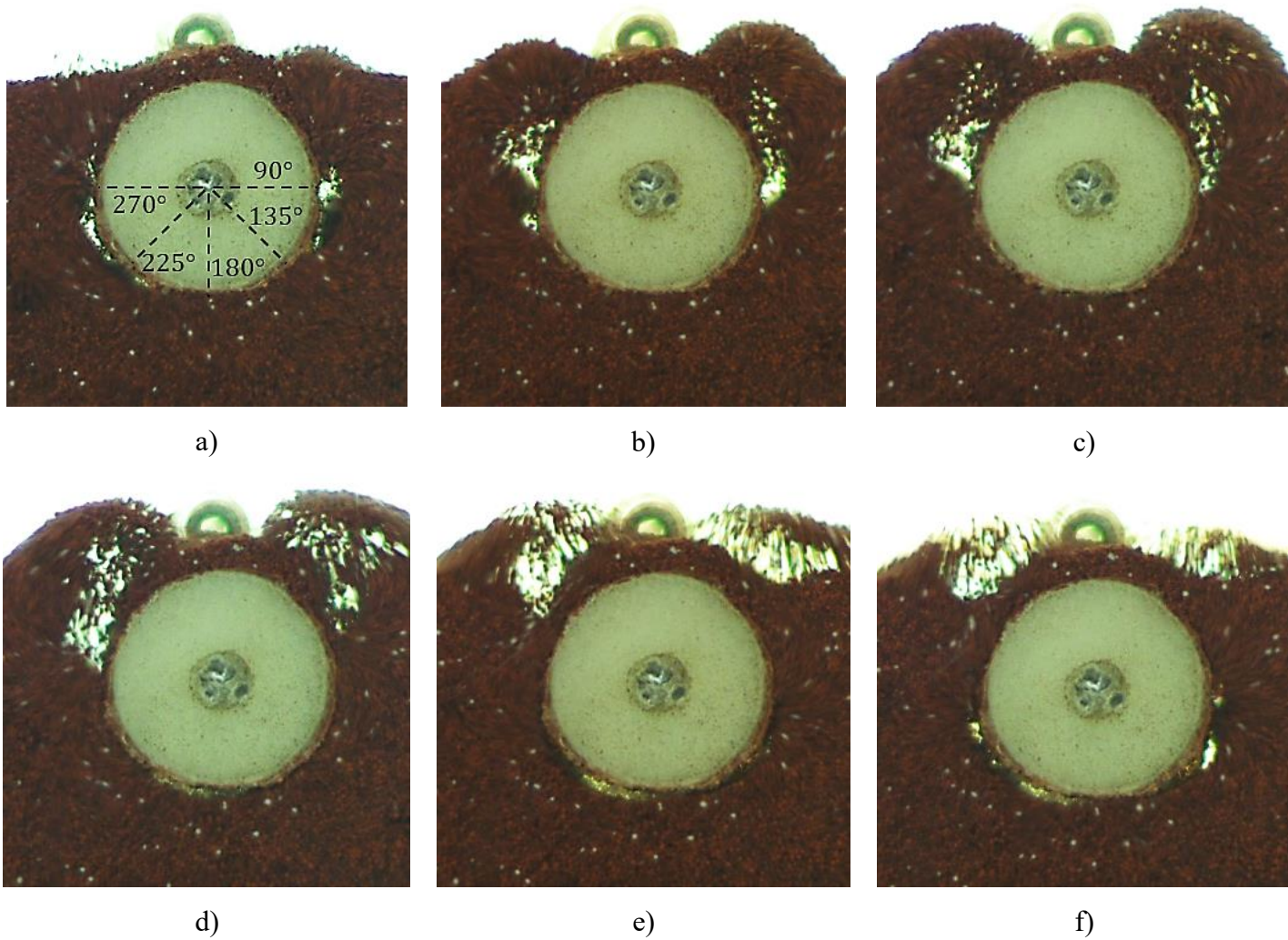


Fig. 4.9. A sequence of images showing the progression of a bubble forming and moving around the surface of a cylinder at $\Delta = 2$. Between each photograph, 7.5 ms elapses. The angles referred to in the text are included in a) for reference.

In Fig. 4.9 e), the bubble underneath the cylinder has crept around each side of the cylinder and has blanketed the entire lower half of the cylinder. The previous bubbles are now passing into the freeboard. Figure 4.9 f) shows the entirety of the underside of the cylinder still blanketed

by gas. However, the bed at 180° has started to push back up towards the cylinder and later was brought into contact with the cylinder's surface again, dividing the bubble to return the system to the state shown in Fig. 4.9 a). The bubbles did not always rise around each side of the cylinder in synchrony. Throughout the experiments the bubble rising on the right-hand side of the cylinder was often slightly ahead of the bubble on the left-hand side, suggesting that the state of fluidisation of the bed was not entirely uniform. Bubbles rising from the distributor and joining the bubbles at the surface of the cylinder also disrupted the regular pattern.

For analysis, the surface of the cylinder was divided into 24 sectors, each 15° , as shown in Fig. 4.10.

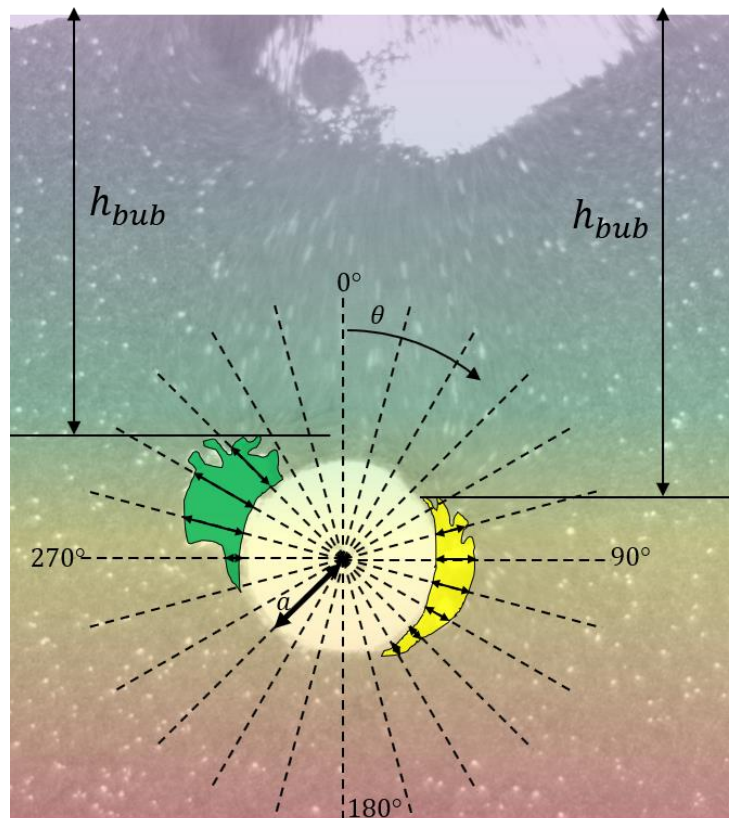


Fig. 4.10. An example photograph of a cylinder in a 2-D bed of doped porous alumina. The cylinder was submerged in the bed at $\delta = 6.2$, emitting gas $U_d/U_{mf} = 2.33$, while the bed was fluidised with $U/U_{mf} = 1$. The image has been falsely coloured to convey the pressure gradient in the bed material where red represents high pressure, through to purple, lower pressure. The bubbles (solid green and yellow regions) have been falsely coloured to show their corresponding pressure.

For each experiment at least three complete cycles of bubble formation, and resulting movement around the cylinder were analysed, amounting to about 18 frames or 135 ms. For

each frame, the presence, or otherwise, of a bubble and, if present, the width of the bubble measured radially from the surface of the cylinder to the bed material was recorded. Additionally, the distance between the uppermost extent of each bubble in each frame, and the surface of the bed, h_{bub} , as shown in Fig. 4.10, was recorded.

4.4.2 Analysis

The bubble fraction, local to the surface of the cylinder, τ

In every experiment, the cylinder in the photographs was divided into 15° sectors, as shown in Fig. 4.10. For each sector, the proportion of time that the surface of the cylinder in that sector was covered by a bubble, τ , was calculated by dividing the number of frames in which a bubble was present at that sector by the total number of frames over an integer number of cycles. This is not a volumetric fraction as it represents the proportion of time for which a bubble is present at the surface of the cylinder, rather than the proportion of volume occupied by a bubble but, for expedience, has been named the local bubble fraction and assigned the symbol, τ . The local bubble fraction was found to be independent of angular position around the cylinder as shown for a typical experiment in Fig. 4.11. This observation, and the magnitude of the local bubble fraction are similar to the observations and values found by Zhou and Zhao (2021) in a similar 2-D bed experiment, albeit with glass spheres rather than alumina particles.

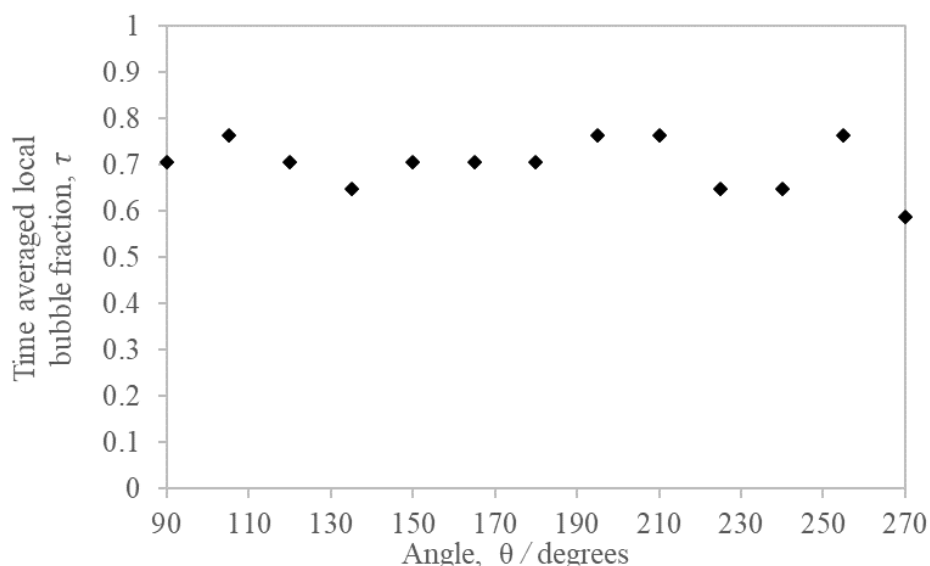


Fig. 4.11. The proportion of time, τ , for which each 15° segment around the underside of a cylinder at $\delta = 1.8$, $U_d/U_{mf} = 4$, was in direct contact with a bubble.

As τ did not vary significantly around the underside of the cylinder, it was taken to be approximately constant and, as such, the value of τ , for each experiment, taken as an average over the entire lower surface of the cylinder is shown in Fig. 4.12.

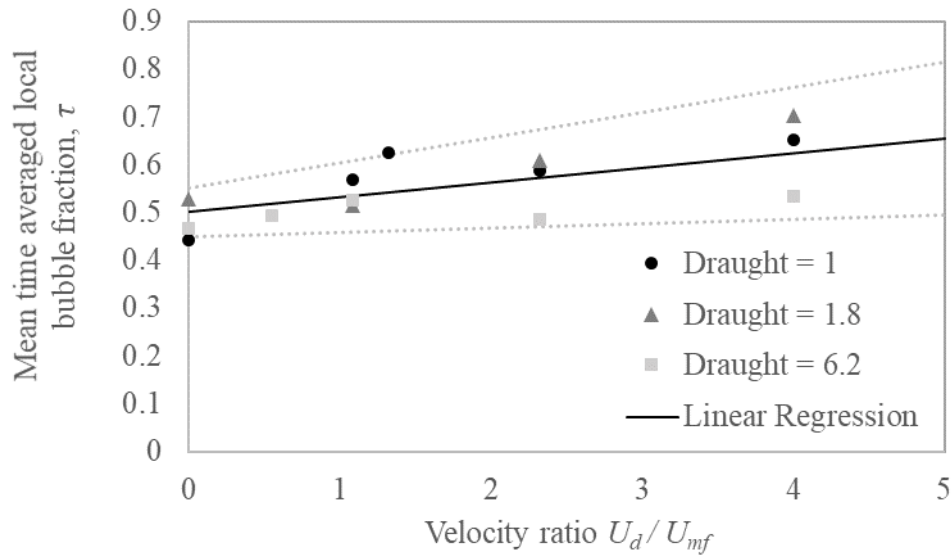


Fig. 4.12. The mean, time-averaged local bubble fraction at the lower surface of the cylinder at draught, $\delta = 1$ (\bullet), 1.8 (\blacktriangle) and 6.2 (\blacksquare). The straight line of best fit is shown ($—$) including the upper and lower 95% confidence bounds (\cdots).

The draught of the cylinder did not affect the local bubble fraction significantly and the void fraction was found to only increase slightly with U_d/U_{mf} . Although the individual values have been used in the analysis in this Section, a line of best fit was found by linear regression, as shown in Fig. 4.12 which gives Eq. (4.30).

$$\tau = m \frac{U_d}{U_{mf}} + c \quad (4.30)$$

where $m = 0.031 \pm 0.022$ and $c = 0.50 \pm 0.05$. The uncertainty represents the 95% certainty bounds for the linear regression. Equation (4.30) shows that, in general, τ increases with $\frac{U_d}{U_{mf}}$. Eq. (4.30) will be used in Section 5.5.3.

The pressure in a bubble

For each frame the pressure in the bubbles in contact with the cylinder was estimated by using the following assumptions:

- a) The pressure drop through a bubble was assumed to be far smaller than that through the bed material, such that the pressure everywhere in the bubble was the same as the pressure at the uppermost boundary of the bubble.
- b) The pressure at the uppermost boundary of the bubble was assumed to be the same as the pressure in the fluidised material at the top of the bubble, at h_{bub} . This assumption is in line with the analysis of Davidson and Harrison (1963), and is indicated in Fig. 4.10 by the application of uniform colours marking the bubbles.
- c) The pressure in the bed material was assumed to vary linearly, increasing away from the surface of the bed according to Eq. (4.25).

For each 15° sector the pressure in the bubble, p_{bub} , was calculated according to Eq. (4.31)

$$p_{bub} = h_{bub,avg} \rho_p g (1 - \varepsilon_{mf}) \quad (4.31)$$

where $h_{bub,avg}$ is the mean depth of the top the bubbles and is a function of angle around the cylinder, θ . The voidage at incipient fluidisation, ε_{mf} , was measured as described in Section 2.1.

The time averaged pressure around the underside of the cylinder

When each 15° sector of the cylinder was in intimate contact with the bed material, the pressure at the surface of the cylinder was assumed to be the same as that given by the pressure distribution in the bulk fluidised bed – that is, linearly increasing away from the surface of the bed according to Eq. (4.25). When each 15° sector of the cylinder was covered by a bubble the pressure across that section was assumed to be the same as the pressure in the bubble, p_{bub} , given by Eq. (4.31).

Hence, for each sector, a time-averaged effective pressure, calculated according to Eq. (4.32), was found.

$$p_{time\ average} = (1 - \tau) \rho_p g (1 - \varepsilon_{mf}) a (\delta - 1 - \cos(\theta)) + \tau p_{bub} \quad (4.32)$$

where a is the radius of the cylinder, τ is the time averaged local bubble fraction at the surface of the cylinder. Thus, the time-averaged pressure exerted on any sector of the cylinder is

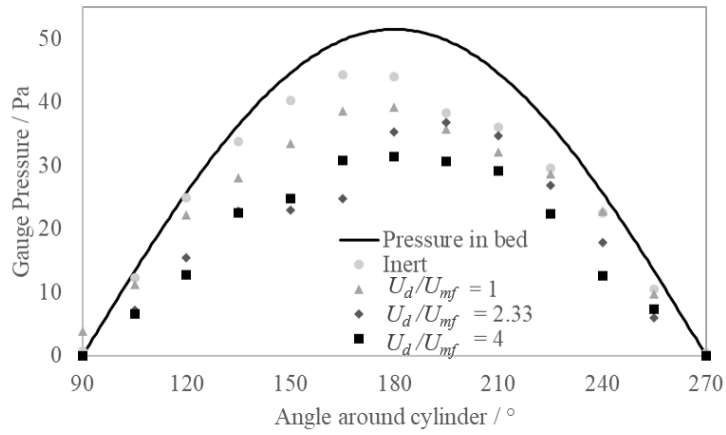
influenced by the bed particle density and voidage at incipient fluidisation, the local bubble fraction, τ , and the average height of the top of the bubbles, $h_{bub,avg}$.

4.4.3 Results

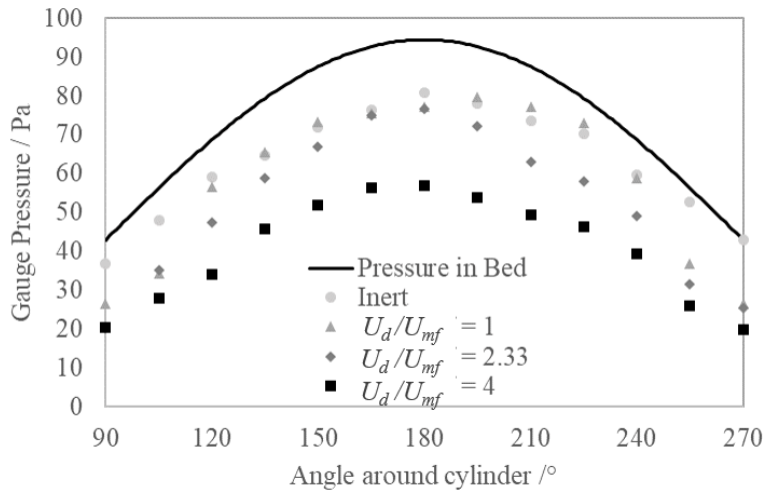
Estimation of the pressure distribution beneath a cylinder

The time-averaged effective pressure, estimated according to Eq. (4.32) at 15° intervals around the cylinder for $\delta = 1, 1.8$ and 6.2 , is shown in Fig. 4.13 in addition to the pressure in the bed material adjacent to the cylinder. Figure 4.13 shows that the time averaged pressure across the entire lower surface of a submerged, inert cylinder was typically lower than the pressure at the same height in the bed material. At higher values of U_d/U_{mf} , the time-averaged pressure was yet lower than for inert particles ($U_d/U_{mf} = 0$). The reduction in pressure is influenced to a greater degree by the bubbles becoming longer as U_d/U_{mf} increased and to a lesser degree by the small increase in τ as U_d/U_{mf} increased.

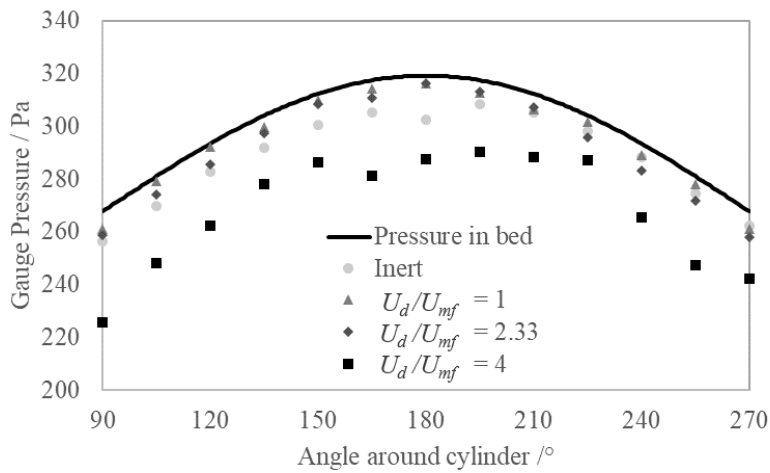
However, because inert cylinders have only small voids passing around their undersides, compared with those which emit gas, the voids circumnavigating the submerged cylinder were very narrow and could only be detected by the motion of the nearby bed particles. Gas flowing through such a narrow channel can hardly be expected to have a negligible pressure drop so, assumption b) is likely to be less valid for analysing the pressure in the bubbles on the underside of inert particles than for particles which emit gas and form larger bubbles ($U_d/U_{mf} \gg 0$). Consequently, the analysis is probably underestimating the time-averaged pressure at low values of U_d/U_{mf} . Nevertheless, the trend is clear: the pressure distribution beneath an inert cylinder is lower than would be expected if the presence of bubbles around the underside were not taken into account and this pressure will decrease further as U_d/U_{mf} increases.



a)



b)



c)

Fig. 4.13. The time averaged effective pressures in Pa estimated at 15° intervals around the underside of a cylinder submerged at a) $\delta = 1$, b) $\delta = 1.8$ and c) $\delta = 6.2$ in a fluidised bed at $U/U_{mf} \approx 1$. Also plotted is the pressure for the equivalent depth of undisturbed bed material (—)

The buoyancy of a cylinder emitting gas into a gas fluidised bed

For each experiment, the density ratio was calculated, such that a free cylinder under identical conditions, would neither sink nor float. Not only was the pressure distribution under the cylinder (Figs. 4.13 a-c) used but the consequences of any defluidised hoods or fluidised caps as discussed in Chapter 3 were also taken into consideration in this Section.

For each experiment it was assumed that the surface integral of the vertical component of the pressure underneath the cylinder supported both the weight of the cylinder and the weight of the material above the cylinder, giving the force balance, Eq. (4.33)

$$\pi a^2 \rho_s g + M_h g = -a \int_{\pi}^{\Theta} p_{time\ average} \cos(\theta) d\theta \quad (4.33)$$

where M_h is the mass of the column of bed material above the cylinder.

To determine M_h it is necessary to recall results from Chapter 3 on the structure of the bed above the cylinder. To recap: for $\delta = 1$ there are no bed particles above the cylinder, for $\delta = 1.8$ a cap of particles surmounts the cylinder (de-fluidised or fluidised, depending on the velocity of the fluidising gas), and for $\delta = 6.2$ there is either a defluidised hood or a column of fluidised bed material and bubbles rising above the cylinder (depending on the velocity of the fluidising gas).

Accordingly, the upper limit of the integration in Eq. (4.32), Θ , was $\frac{\pi}{2}$ for experiments at $\delta = 1$ and the gauge pressure around the upper side of the cylinder was assumed to be 0 (it was found in Section 4.2 that this was an acceptable approximation). For experiments at $\delta = 1.8$, the upper limit of the integration was also $\frac{\pi}{2}$ and the weight of the elevated cap of particles was included in the force balance, as in Section 3.3.

The bed above a cylinder at $\delta = 6.2$ presented a more complicated problem to estimate because it was shown in Chapter 3 that the bed material above the cylinder becomes completely fluidised above $U_d/U_{mf} = 0.5$. In the images taken at $\delta = 6.2$ for $U_d/U_{mf} > 1$, the bubbles did not leave the surface of the cylinder at $\theta = 90^\circ$ and 270° , instead, the bubbles carried on around the top of the cylinder as shown in Fig. 4.14.

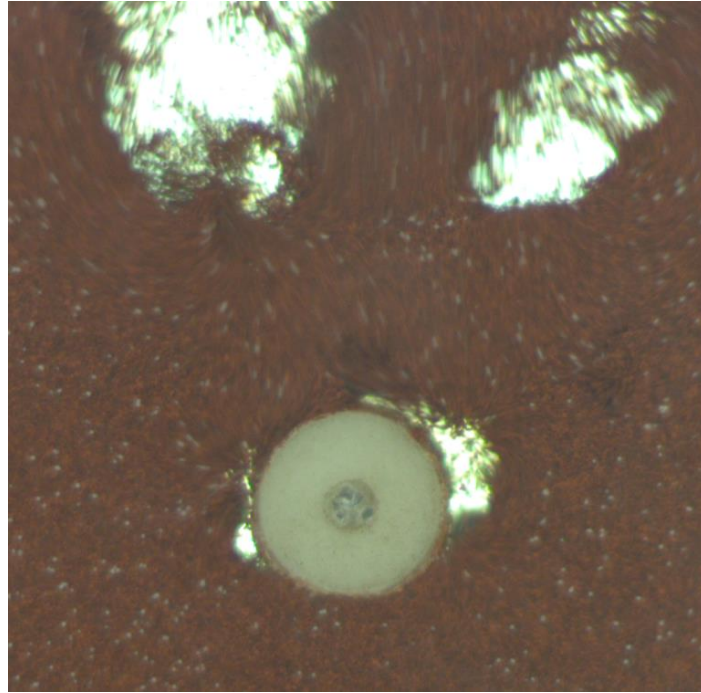


Fig. 4.14. Photograph of a cylinder in a fluidised bed at $\delta = 6.2$, at $U_d/U_{mf} = 2.33$. A bubble can be seen covering most of the upper surface of the right-hand side of the cylinder.

As a result, for experiments at $\delta = 6.2$ and $U_d/U_{mf} > 1$ it was necessary to carry out the analysis of Section 4.4.2, not only around the underside but all the way around the cylinder.

Hence the limit of integration for these cases was π rather than $\frac{\pi}{2}$.

From Eq. (4.33), the density ratio, $R_\rho = \frac{\rho_s}{\rho_p(1-\varepsilon_{mf})}$, for a cylinder at dynamic equilibrium was estimated for $\delta = 1, 1.2$ and 6.2 , and U_d/U_{mf} between 0 and 4, and shown in Fig. 4.15. The data points for each value of δ form lines which divide the space in Fig. 4.15 up into regions. To guide the eye, the different regions and lines which divide them are shown in Fig. 4.15. Each line of constant δ can be interpreted thus. To the left of the line is the region which indicates that a cylinder, here, would rise while to the right is the region which indicates that a cylinder would sink. The line of data points indicates the specific conditions for density and velocity ratios, which must be met for a cylinder to be at a dynamic equilibrium at that depth.

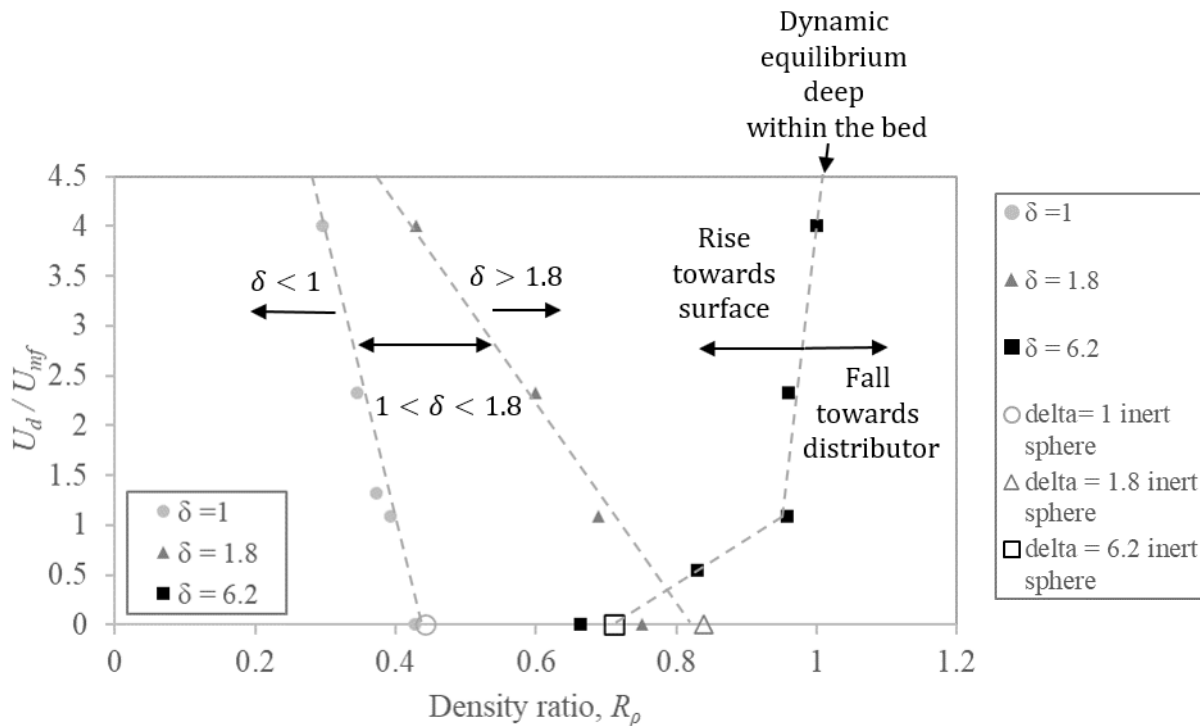


Fig. 4.15. The density ratio, predicted using observations of the structure of the fluidised bed and the inferred pressure distribution around a cylinder in a 2-D bed, of a cylinder in dynamic equilibrium emitting gas into an incipiently fluidised bed at rates of U_d/U_{mf} from 0 to 4 at depths $\delta = 1$ (\bullet), $\delta = 1.8$ (\blacktriangle) and $\delta = 6.2$ (\blacksquare). For comparison the density ratio of three inert spheres floating at $\delta = 1$ (\circ), $\delta = 1.8$ (\triangle) and $\delta = 6.2$ (\square) from the experiment described in Section 3.1.1 have been included. The chart has been divided into regions of different behaviour for cylinders which emit gas, freely floating in an incipiently fluidised bed, by dashed guidelines.

Each line of constant dimensionless draught is now investigated individually.

$\delta = 1$

Inert cylinders at dynamic equilibrium at $\delta = 1$ have a density ratio of around 0.44, as shown experimentally in Chapter 3. This is lower than the value of 0.5 predicted by the displacement of bed material owing to the reduced pressure underneath the cylinder caused by the bubbles as discussed above. As U_d/U_{mf} increases, the density ratio of a cylinder, at dynamic equilibrium, decreases slightly from around 0.44 to 0.3; a significant decrease from the density ratio of 0.5 predicted by the displacement of the bed material. As U_d/U_{mf} increases the cylinder would have to become lighter in order to retain its position within the bed and not sink down.

$\delta = 1.8$

Inert cylinders at dynamic equilibrium at $\delta = 1.8$ have a density ratio of between 0.75 and 0.84, significantly lower than 0.97, as predicted by only considering the displacement of the bed material. The cylinder supports a defluidised cap protruding above the bed surface as described in Section 3.3, and the pressure around the underside is lowered by the bubbles which form there. Both factors serve to decrease the density ratio for an inert cylinder at dynamic equilibrium at this depth. As U_d/U_{mf} increases, the density ratio for cylinders at dynamic equilibrium decreases as the pressure beneath the particle decreases further and the cylinder retains a cap of particles. As U_d/U_{mf} increases the cylinder would have to become lighter in order to retain its position within the bed and not sink down, by $U_d/U_{mf} = 4$ the density ratio of a cylinder at dynamic equilibrium falls to 0.43 nearing 50% of the density of an inert cylinder at rest at the same depth.

$\delta = 6.2$

Inert cylinders at $\delta = 6.2$ carry a tall defluidised hood; as a result, inert cylinders with a density ratio of greater than around 0.66 will sink, which agrees well with the observation made in Section 3.1, namely that an inert sphere of density ratio 0.71 was able to remain stationary at a maximum depth of $\delta = 6.3$ (Fig. 3.2).

As U_d/U_{mf} increases from 0, the defluidised hood shrinks according to the theory of Section 3.3. The shrinking of the hood more than counteracts the reduction in pressure caused to the increasing size of the bubbles underneath the cylinder and consequently a cylinder denser than for the inert case can remain at dynamic equilibrium. When U_d/U_{mf} exceeds unity 1, the bed material above the cylinder is entirely fluidised. In this case the density ratio of the cylinder which can still rise through the bed can near unity.

Once $U_d/U_{mf} > 1$, the density ratio for a cylinder in dynamic equilibrium does not change significantly away from ~ 1 . This is largely owing to the competing effects of the reduced pressure at the underside of the cylinder due to the longer bubbles and the reduced pressure on the upper surface of the cylinder owing to the bubbles encroaching on the upper surface. This trend can only be expected if the cylinder is low enough within the bed such that the bubbles can coalesce above it. The results for $\delta = 6.2$ should be independent of depth so long as the

cylinder is deep enough within the bed for the bubbles to not reach the surface of the bed before leaving the cylinder.

In the absence of experimental evidence pertaining to the structure of the bed beneath spheres emitting gas in fluidised beds, it will be assumed that the pressure distribution beneath, and bubble fraction at the surface, of spheres emitting gas in a fluidised bed are identical to those determined for cylinders in a 2-D fluidised bed. Lungu *et al.* (2018) state that the conclusions drawn from pseudo 2-D fluidised bed experiments generally agree with predictions from 2-D CFD simulations where interactions between the bed material and the wall are neglected. The exceptions to this generalisation are the velocity of the solids, as shown by Cloete *et al.* (2015), and bubble rise velocity, as investigated by Asegehegn *et al.* (2012). Both the velocity of the solids and the bubble rise velocity are slowed by the friction at the front and rear walls of a 2-D bed. Kunii and Levenspiel (1991) reported that the walls had a more significant effect on the rise velocity of the bubbles when the bubble diameter was larger than 0.125 times the bed diameter. Given that the bubbles underneath the gas-emitting cylinder in Section 4.4 spanned the width of the 2-D bed, one must conclude that the rise velocity of the bubbles around a sphere in a 3-D bed would be higher than that measured in the 2-D bed. Nevertheless, pseudo 2-D beds have been used extensively in the literature as a proven means of yielding useful insight into fluidisation phenomena in 3-D fluidised beds.

Two examples

A sphere of dry ice, in a fluidised bed of silica sand, density ratio 1.09, lies to the right-hand side of the $\delta = 6.2$ line in Fig. 4.15, and so, will stay submerged deep within the bed until U_d/U_{mf} is high enough, assuming that the trend in the line for $\delta = 6.2$ continues towards higher density ratios as U_d/U_{mf} increases beyond 4. By extrapolating this line, a value of U_d/U_{mf} of around 7 is needed for dry ice particles to rise to the surface. This prediction is investigated experimentally in Chapter 5.

A particle of beech wood in a fluidised bed of sand particles has a density ratio of approximately 0.5. Fig. 4.15 indicates that such a particle would have a draft of $1 < \delta < 1.8$ if it were inert (around 1.2 by linear interpolation); however, the emission of gas serves to increase the draught of the particle and at $U_d/U_{mf} \approx 3$ the beech would reach $\delta = 1.8$, if its density remained unchanged. The depths of spheres of beech, devolatilising in a fluidised bed of silica sand at 600°C is investigated in Chapter 6.

4.7 Conclusions

Leidenfrost type behaviour, where gas emitted from the surface of a particle can lift the particle away from the fluidised bed material was found to be unlikely to occur in aggregative fluidised beds. This is because the gas which is emitted by the particle does not permeate through the bed material which would increase the pressure underneath the particle, instead it forms bubbles, which pass around the particle. The pressure in the fluidising bed below a cylinder was found to decrease slightly when gas was emitted by the cylinder owing to these bubbles. It was reasoned that the bubbles produced near the surface of the cylinder offered a shortcut path for gas from the fluidised bed, lowering the pressure therein.

As excess fluid can pass into the fluidised phase of a particulate fluidised bed (where the difference in density between the particles and fluid is smaller than in aggregative fluidised beds), it is possible that, to a limited extent, the Leidenfrost type behaviour might be possible. Observations of the size and position of bubbles generated at, and passing around, the surface of a cylinder in a 2-D bed, which was incipiently fluidised, allowed the pressure distribution at the surface of the cylinder to be inferred, and to assess the possible effects of the bubbles on the buoyancy of the cylinder. As the velocity ratio U_d/U_{mf} increases, it was found that, generally, the density ratio of a cylinder at dynamic equilibrium, decreases. For cylinders which are deep in the bed, however, the buoyancy increases as the velocity ratio increases owing to the sweeping away of bed particles from the upper surface of the cylinder by the rising bubbles from each side of the cylinder.

Particles of solid biomass, devolatilising in a fluidised bed are likely to behave very differently to an inert particle when close to the surface of the fluidised bed. The VM which leaves the particle during devolatilisation will pass around the particle as bubbles and cause the biomass to have a deeper draught. Referring to Section 3.3, if deep enough ($\delta > 1.5$) the particle could form a fluidised cap of bed particles which would force it deeper still into the bed such that a stable depth may be reached at ($1.5 < \delta < 2.5$).

Speaking generally, then, the effect of the emission of gas from an object immersed in a fluidised bed depends on the position of the object, relative to the surface. This work has found that for cylinders, deep within the bed, the emission of gas serves to increase the buoyancy of the cylinder. If near to the surface of the bed, however, the emission of gas from the cylinder causes the buoyancy of a cylinder to decrease. Spheres are expected to show similar behaviour.

Chapter 5 The sublimation of spheres of dry ice in fluidised beds

Chapters 3 and 4 have shown that the structure of the fluidised bed close to a solid object changes depending on the rate at which that object is emitting gas. The rate of emission of gas was expressed as a dimensionless velocity ratio, defined as the ratio of the superficial velocity of the gas leaving the object, U_d , to the incipient fluidisation velocity, U_{mf} . The dimensionless draught, namely, the distance between the lowest part of the object and the surface of the bed divided by the radius of the object, was used to define the depth of an object. The draught of an object, which is emitting gas, was found to be sensitive to the velocity ratio, U_d/U_{mf} . In Chapters 3 and 4, a 2-D fluidised bed was used to determine the structure of the bed and pressure distribution around a fixed cylinder which was emitting gas. The density of a freely floating cylinder, at the same draught as the fixed cylinder used in the experiments was estimated and a relationship between draught, the density ratio and the velocity ratio was developed. Chapter 5 aims to determine if the effects explored in Chapters 3 and 4 have any bearing on the behaviour of spheres, which are free to move around in a 3-D fluidised bed.

In Chapter 4, it was found that as the velocity ratio (U_d/U_{mf}) increases, the contact area between the gas-emitting object and the bed decreases owing to an increase in the number of bubbles forming around the object. Chapter 5 now addresses the question of how the structure of the bed, and position of the particle, affect the heat transfer coefficient from the bed to the particle and, consequently, the rate at which the gas is subsequently emitted.

The motivation for the work in Chapters 3 and 4 was to understand how particles of biomass segregate in a fluidised bed during devolatilisation. Particles of biomass emit a wide range of gaseous species as they devolatilise. The exact composition of the volatile matter (VM) depends on the species of the wood, the rate of heating and the temperature of the fluidised bed. To simplify the analysis, dry ice was chosen as a model because it produces gas by sublimation, in turn controlled by the heat transfer from the bed to the particle (Scott, 2004). A further advantage of using dry ice rather than biomass for this study was that dry ice emits a single gaseous species, CO_2 , which is readily detected in low concentrations. The rate of sublimation throughout the lifetime of a single dry ice particle can, therefore, be determined by

measuring the CO₂ concentration in the exhaust gas from a fluidised bed and, subsequently, the heat transfer coefficient can be calculated.

5.1 Method

In Chapters 3 and 4, the experiments were carried out at room temperature and, largely, in a 2-D bed. In contrast, here, a fluidised bed contained within a quartz glass tube of 30 mm ID was used, mounted inside an electric tube furnace and heated to a range of constant temperatures between 150 and 900°C as outlined in Section 2.5. In a typical experiment, a single 6 mm diameter sphere of dry ice was manufactured and dropped into the fluidised bed. The concentration of CO₂ in the exhaust gas from the bed was measured and recorded once per second. Each experiment was run until the CO₂ concentration, measured by the off-gas analyser, had dropped to zero.

Three different sizes of silica sand were used to determine what effect, if any, the size of the bed material had on the circulation of, and heat transfer coefficient to, the spheres of dry ice. The experimental conditions investigated are given in Table 5.1. For each combination of bed particle size, bed temperature and superficial gas velocity, five experiments were performed. The sublimating spheres of dry ice caused the temperature of the bed to drop but not by more than 1% of the set-point temperature.

Table 5.1. Temperature ranges and bed particle sizes used in this work.

Bed particle size range / μm	Bed Temperature / $^{\circ}\text{C}$
200 - 355	250 - 800
355 - 425	300 - 700
425 - 600	550- 800

Although the work of Chapters 3 and 4 was focussed largely on beds where the gas velocity was just above the incipient fluidisation velocity, the intention of the work outlined in Chapter 5 was to recreate the fluidisation conditions of a bubbling fluidised bed combustor more faithfully by using values of U/U_{mf} of around 3.

The signal from the gas analyser was affected by the mixing of the gases within the freeboard and the sampling line; the method of deconvolution used to correct for this is described in Section 2.5. An example of the raw and deconvoluted gas traces is shown in Fig. 5.1, which

demonstrates how deconvolution sharpens the initial rise in the measured value of CO₂ mole fraction. As the apparent total time is found by calculating the time between the signal rising above and subsequently falling below a threshold value, the deconvolution shortens the apparent total time for the dry ice spheres to sublimate. The deconvolution method, and its limitations, are discussed in more detail in Appendix 2.2. In the absence of any mixing in the freeboard and sampling line, the rate of release of CO₂ rises almost immediately from zero to a maximum value at the start of an experiment, before decreasing, approximately linearly, to zero as will be further explained in Chapter 6, Section 6.1.2. Therefore, the time for the spheres of dry ice to sublimate completely, t_{sub} , measured from the experiments in this chapter, is likely to be an overestimate as the deconvolution cannot reproduce the near instantaneous rise in CO₂ production at the start of the experiments without severely affecting the shape of the tail of the curve. As the deconvolution process changes the shape of the start and end of the curve far more than the middle portion, any results obtained from the deconvoluted signal recorded during the first and last quarter of each experiment were treated with caution.

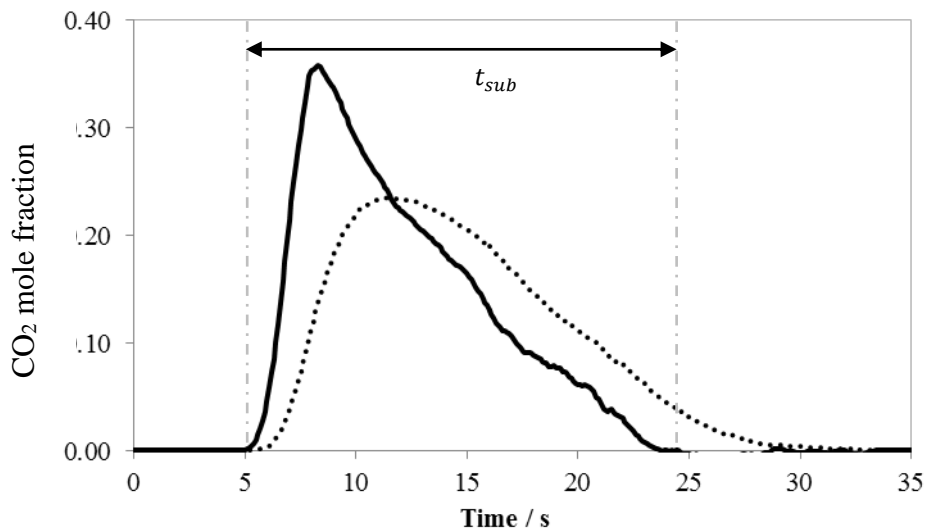


Fig. 5.1: Raw ($\cdot\cdot\cdot$) and deconvoluted and smoothed (—) CO₂ mole fraction trace for an example experiment. In this case a bed of 200-355 μm silica sand at $U/U_{mf} = 3.5$ at 650°C. The mixing time used in the deconvolution here was 3.0 seconds.

In addition to measuring the concentration of CO₂ in the exhaust gas from the fluidised bed, the surface of the bed was filmed from above and the photographs were recorded at

24 frames s⁻¹. As the diameter of the dry ice particles shrank and approached that of the bed particles, they became more difficult to discern from the bed particles. Consequently, there were generally fewer observations of the dry ice particles at the surface of the bed at the very end of each experiment. Further, the work of Di Felice *et al.* (1989) suggests that once the dry ice particles are smaller than ~3 times the bed particle diameter, d_p , the drag forces become more significant than buoyancy forces and so the analysis used in Chapters 3 and 4, which assume that the drag forces are negligible compared to the buoyancy forces, cannot be applied to the dry ice once it becomes so small. Consequently, the experimental results when the dry ice particle had become smaller than $3 \times d_p$ were ignored.

The rate of production of moles of CO₂, \dot{m}_{CO_2} , throughout each experiment was determined using the deconvoluted mole fraction of CO₂ measured in the exhaust of the fluidised bed, y_{CO_2} , and the known flow rate of nitrogen fluidising the reactor, \dot{m}_{N_2} . The radius of the sublimating particle, a , was then calculated assuming that the dry ice remained spherical and was homogenous with a density, $\rho_{CO_2\text{solid}}$, of 1562 kg m⁻³ (Wittemann 2003), using Eq. (5.1).

$$\dot{m}_{CO_2} = \dot{m}_{N_2} \frac{y_{CO_2}}{1 - y_{CO_2}} = -\rho_{CO_2\text{solid}} 4\pi a^2 \frac{dr}{dt} \quad (5.1)$$

It was assumed that the particles of dry ice remained spherical throughout, hence, the surface area of the particles was calculated using the radius. An estimate of the velocity of CO₂ produced at the periphery of the particle, U_d , over time, was found by assuming the gas was produced uniformly from the surface of the particle at the geometric mean temperature, T_{mean} of the dry ice particle temperature, $T_{particle}$, and the bed temperature T_{bed} , using Eq. (5.2)

$$U_d = \frac{RT_{mean}}{p \times 4\pi a^2} \dot{m}_{N_2} \frac{y_{CO_2}}{1 - y_{CO_2}} \quad (5.2)$$

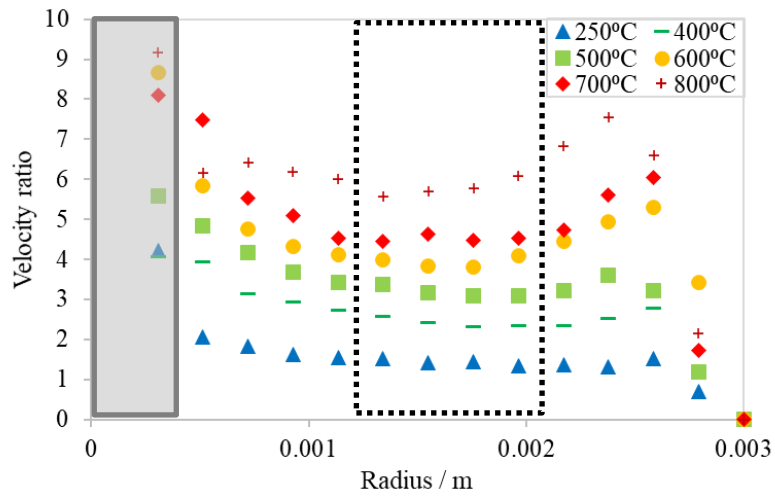
where R is the universal gas constant, $T_{particle}$ is the sublimation temperature of the dry ice particle at atmospheric pressure, assumed to be constant at 194.7 K, and p is the atmospheric pressure. The dry ice had a far lower temperature than the bed material with, at most, a temperature difference of 878 K. It is, therefore, highly likely that the bed material very close to the dry ice spheres was cooled significantly below T_{bed} . As the incipient fluidisation velocity

for any given material increases as the bed temperature decreases, it is, therefore likely that the value of U_d/U_{mf} calculated is an overestimate. If the bed material close to the dry ice is cooled to the geometric mean of the bed temperature and the particle temperature, the resultant error in the velocity ratio is up to 50% at the highest bed temperatures investigated in this Chapter. However, as shown in Section 5.5.4, fresh bed material is continually drawn in towards the gas-emitting particle. The bed particles are then swept rapidly over the surface of the gas-emitting particle by bubbles passing around it, as discussed in Section 4.4.1. Although individual bed particles are cooled as they sweep past the spheres of dry ice, it is unlikely that the fresh bed material beneath the sphere is cooled significantly because the value of heat transfer coefficients in bubbling fluidised beds are very high (Di Natale and Nigro, 2013) which limits the development of thermal gradients in the fluidised material.

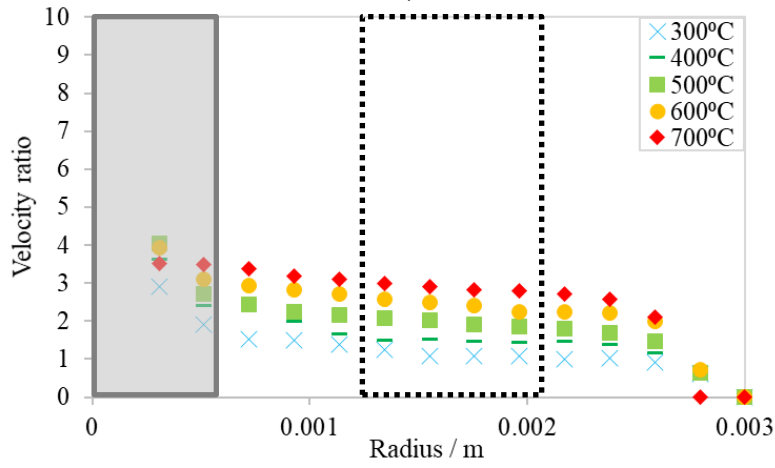
In addition to the experiments with dry ice, a few experiments were performed with inert spheres of 3 mm diameter and known density, as described in Section 2.5. In these experiments, the surface of the bed was filmed for 180 s after adding the inert particle and the fraction of time which the inert sphere spent at the surface of the bed was found. Additionally, the length of time the particle was visible at the surface of the bed was recorded.

5.2 The velocity ratio

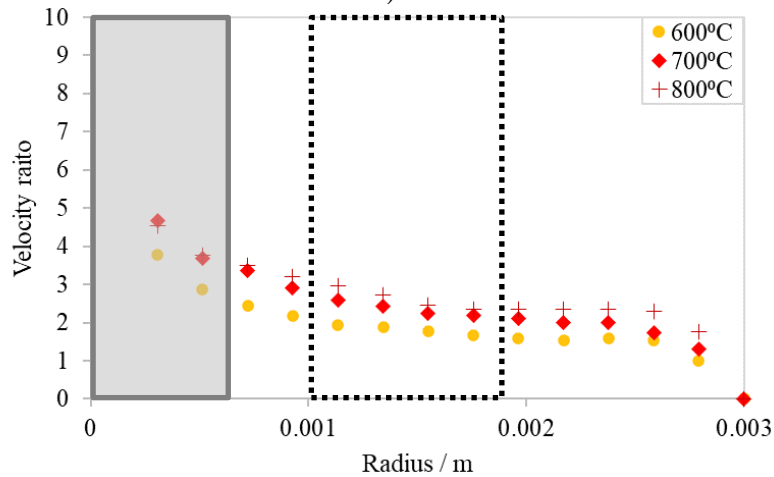
The velocity ratio, U_d/U_{mf} was identified as an important parameter in determining the structure of the fluidised bed around a sphere, and therefore in predicting its position within the bed. The velocity ratio was calculated at regular intervals throughout the sublimation of spheres of dry ice and is shown in Fig. 5.2 for the three different sizes of bed material. Each point on the plots shown in Fig. 5.2 represents the velocity ratio averaged across 5 experiments.



a)



b)



c)

Fig. 5.2. The velocity ratio, U_d/U_{mf} , for dry ice particles sublimating in beds of a) 200-355 μm , b) 355-425 μm and c) 425-600 μm silica sand, at a variety of bed temperatures as indicated in the legends. U/U_{mf} was 3. The grey shaded regions indicate when the particle was smaller than 3 times the size of the bed particles and no longer behaved as a “large” particle. The area inside the black dashed line is the middle third of the experiments over which an average value was taken and used in Fig. 5.3.

Typically, the velocity ratio initially rose rapidly before a period of steady increase. After the radius had decreased to around 0.0015 m the velocity ratio began to rise rapidly again. At bed temperatures higher than 250°C in the 200-355 μm bed, however, the velocity ratio was found to increase sharply before falling to a steady value before, once again, rising towards the end of the particle's lifetime. As described earlier, the shape of the curves at the start and end of the experiments (at high and low radius) were most affected by the deconvolution and hence may not give an accurate reflection of the real values of velocity ratio. Hence to visualise better the way U_d/U_{mf} with bed temperature and size of bed material, and to eliminate the effects of deconvolution, an average value was taken for the mid portion of the time where sublimation was occurring. The value of the velocity ratio increased as the radius decreased during the mid-portion of the deconvolution, so the average values taken are for the discussion of trends in velocity ratio only. These average values of U_d/U_{mf} are shown in Fig. 5.3.

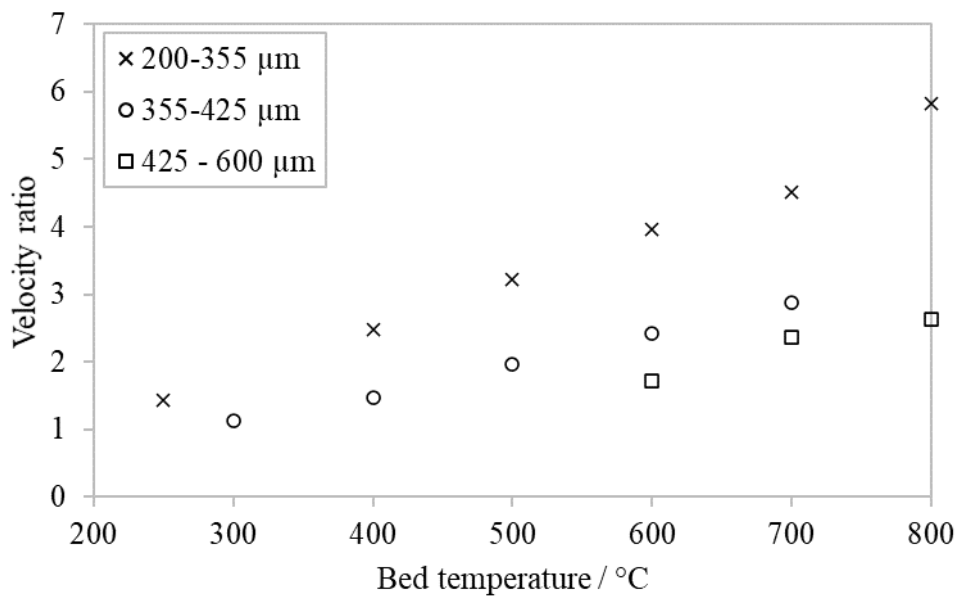


Fig. 5.3. Values of U_d/U_{mf} averaged over the mid portion of each set of experiments shown in Fig. 5.2.

The average velocity ratio, U_d/U_{mf} , increased as the bed temperature increased. The velocity ratio was highest in the 200-355 μm bed and lowest in the 425-600 μm bed owing largely to the increase in U_{mf} with larger bed particle size.

In all experiments the average velocity ratio was large enough for no defluidised hood to be formed above the particles, following the findings of Chapter 3. The density ratio for the dry ice particles was just slightly greater than 1.0, so, even in the absence of a defluidised hood, the dry ice particles were expected to be negatively buoyant until the velocity ratio was high enough to allow the particles to rise towards the surface of the bed.

The theory of Chapter 4 suggests that the velocity ratio should exceed around 5 for the dry ice particles in 425-600 μm bed and around 7 (extrapolating from Fig. 4.15) for dry ice particles in the 200-355 μm bed to rise towards the surface of the bed rather than sink to the distributor. Such high values of U_d/U_{mf} were achieved only at the very end of the experiments at the highest temperatures in the 200-355 μm bed. Despite the uncertainty in the values of U_d/U_{mf} at the end of the experiments, owing to the deconvolution, the experiments do indicate that, at high bed temperatures, the dry ice particles are more likely to be visible at the surface of the bed than at lower temperatures. However, as indicated in Fig. 4.15, a particle with density ratio of around 1 is unlikely to be able to remain at the surface of the bed, at dimensionless depth, $\delta < 2$. Therefore, it is unlikely that an increase in U_d/U_{mf} will significantly increase the length of time that the dry ice particles remain at the surface.

To verify these predictions, the proportion of time that the particles spent at the surface was determined using photographs of the surface of the bed.

5.3 Total time for sublimation

To determine the proportion of the lifetime of a particle spent at the surface of the bed, it was necessary to find the total time for sublimation for the dry ice spheres.

The total time for the particles to sublimate was measured by finding the point at which the concentration of CO_2 measured by the analyser, after the signal had been deconvoluted, first rose above 0.22% until the time at which it first fell to below 0.22%, which was chosen as the minimum threshold value above the noise in the signal from the analyser. The sublimation times are shown in Fig. 5.4.

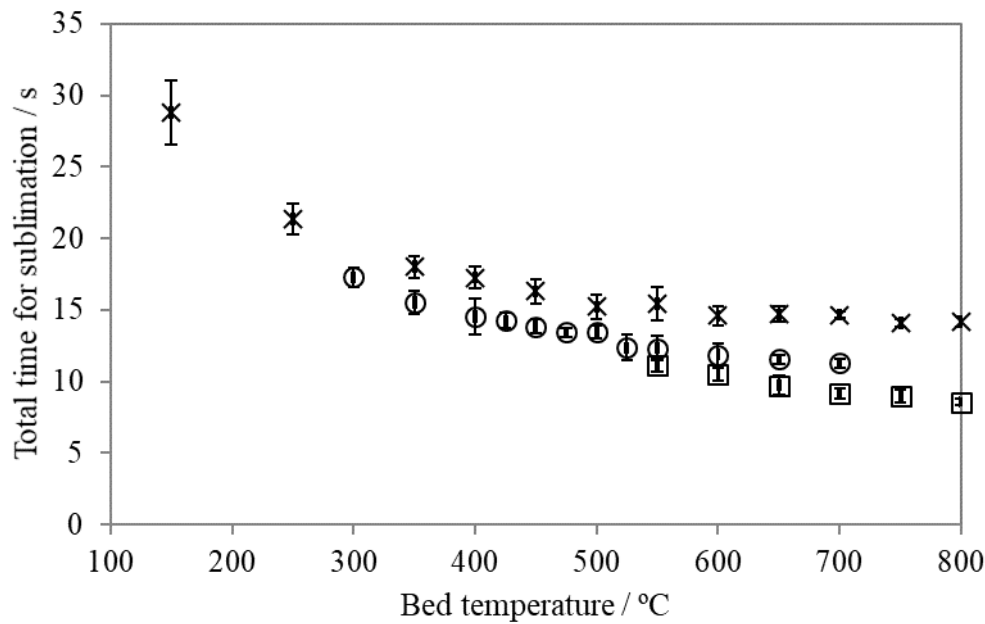


Fig. 5.4. The sublimation time for dry ice particles in beds of (X) 200 – 355 μm , (O) 355-425 μm and (□) 425-600 μm silica sand. Each point is an average from 5 experiments and the error bars represent one standard deviation across.

The time for sublimation, t_{sub} , was found typically to decrease as the bed temperature increased. In a bed of 200-355 μm silica sand, t_{sub} , decreased as the temperature of the bed increased from 150°C; however, above 650°C, t_{sub} became insensitive to the bed temperature, staying at around 16 s. In the 355-425 μm silica sand bed, t_{sub} also decreased as the temperature of the bed increased but the levelling off was less pronounced than in the 200-355 μm bed. In the 425 – 600 μm silica sand bed, t_{sub} appeared to decrease progressively with temperature over the smaller range of bed temperature investigated for this bed particle size with the rate of decrease falling at higher temperatures.

The dry ice spheres in the beds of finer particles took a significantly longer time to sublimate, t_{sub} , than those in the beds of coarse particles, indicating that the heat transfer coefficient from the bed material to the dry ice spheres was lower in the beds of smaller particles than in the beds of larger particles and that the effective heat transfer coefficient (which includes the radiative heat transfer) decreases as the bed temperature increases. This is a somewhat surprising result as Parmar and Hayhurst (2002) reported that the heat transfer coefficient between the bed material and a mobile sphere decreases as the size of the bed particles

increases, a result also found by Baskakov *et al.* (1973). The heat transfer coefficient is investigated further in Section 5.5.

5.4 Circulation of inert and dry ice spheres

The buoyancy of inert spheres in an incipiently fluidised bed is expected to follow a curve similar to that shown in Fig. 3.19 and the buoyancy of those with a density ratio greater than around 0.8 is expected to be sensitive to the presence of a defluidised hood. If a sphere falls to the right of the curve in Fig. 3.19 it is expected to sink through a bubbling fluidised bed and, if to the left, it will rise.

The proportion of time, for which 3 mm diameter spheres of porous alumina were visible at the surface of a bed of 200-355 μm silica sand, at $U/U_{mf} = 3$ was recorded over 180 s at a variety of bed temperatures and is shown in Fig. 5.5.

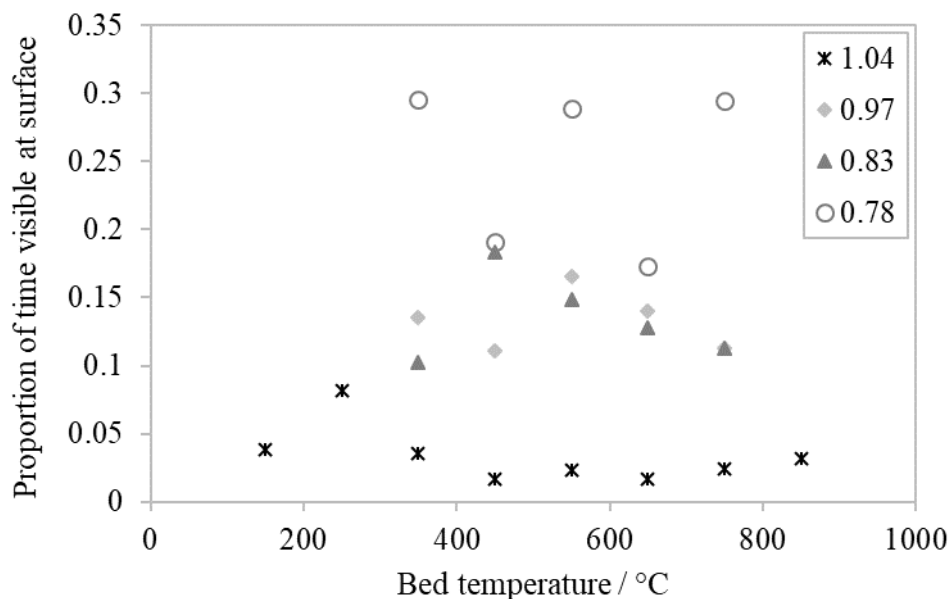


Fig. 5.5. The proportion of time for which alumina spheres of different densities were visible at the surface of a fluidised bed of 200-355 μm at $U/U_{mf} = 3$. The density ratio in each case is given in the legend.

Unlike in an incipiently fluidised bed where a particle is expected to either appear at the surface of the bed or to sink beneath the surface of the bed, when the bed is bubbling the inert particles move up and down within the bed and appear and disappear from the surface of the bed.

As anticipated, the denser spheres spent less time at the surface of the bed than those which were less dense. The sphere with a density ratio of 1.04 spent significantly less time at the surface of the bed than one with lower density ratio, because, irrespective of its position within the bed, it was always negatively buoyant and soon sank away from the surface of the bed. The particles which had density ratios of 0.97, 0.83 and 0.78 spent between 10 and 30% of their time visible at the surface of the bed. These particles, if buried deep enough, will bear a defluidised hood and become negatively buoyant; however, once at, or near, the surface of the bed the hood cannot form to its full height and the particles become positively buoyant.

The proportion of time which the spheres of dry ice in the experiment described in Section 5.1 spent at the surface of the fluidised bed of 200-355 μm silica sand at $U/U_{mf} = 3$ was found and is compared with an inert sphere of similar density in Fig. 5.6.

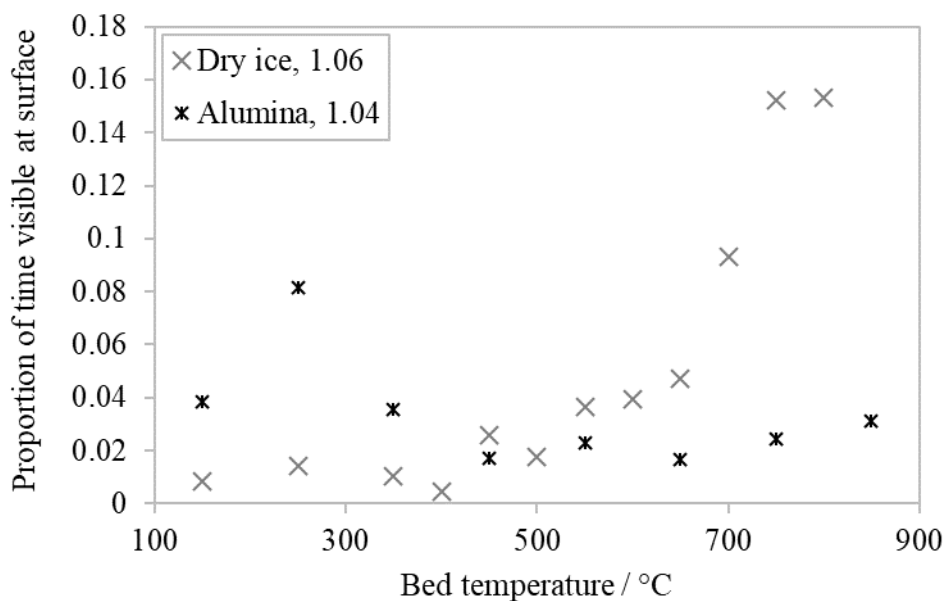


Fig. 5.6. The proportion of time spent at the surface of a fluidised bed of 200-355 μm silica sand at $U/U_{mf} = 3$, by an inert sphere (alumina) where the ratio between the density of the sphere and the density of the fluidised material is 1.04 and dry ice spheres where the density ratio is 1.06. Each dry ice point represents the average across 5 experiments.

The inert, alumina sphere and the dry ice particle had similar density numbers and, for temperatures $< 650^\circ\text{C}$, the length of time each visited the surface at any one visit were similar, indicating that both became buried at a similar rate and sank into the bed. However, at bed

temperatures of above 650°C, the dry ice particles visited the surface of the bed significantly more frequently, resulting in a far greater proportion of time spent at the surface than at lower temperatures. This coincides with the velocity ratio reaching higher values. The theory of Section 4.4 predicted that the gas-emitting particles which were buried deep within the bed would become more buoyant as the velocity ratio increase and, therefore, more likely to visit the surface more frequently than at low velocity ratios.

The total proportion of time spent at the surface of the bed, by dry ice particles, in the three bed particle sizes and the range of temperatures investigated is shown in Fig. 5.7.

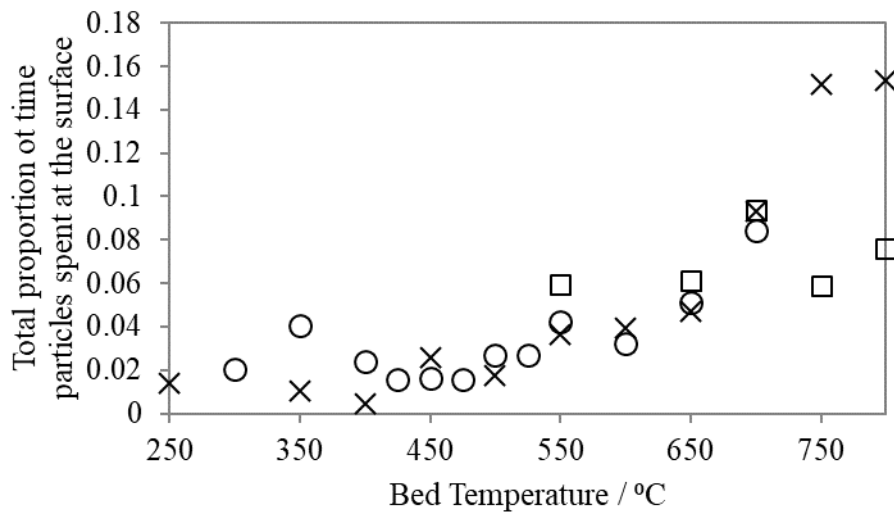


Fig. 5.7. The mean proportion of the particles' lifetime for which the dry ice particle was visible at the surface of the bed across the range of temperatures. Experiments in the 200-355 μm bed are shown as (x), 355 – 425 μm as (O) and 425 – 600 μm as (□).

A similar increase in time spent at the surface was observed in the 355 – 425 μm bed; however, experiments were not conducted above 700°C in this bed material. Given the paucity of results, no conclusions could be drawn for the influence of bed temperature on the total proportion of time spent at the surface of the bed by dry ice particles in the 425-600 μm bed material.

The increase in the proportion of time the dry ice spheres spent at the surface correlates with an increase in the proportion of time for which U_d/U_{mf} was large enough to lift the dry ice particles towards the surface of the bed as discussed in Section 4.4.3.

5.5 Experimental measurement of the heat transfer coefficient

Heat transfer from a bubbling fluidised bed to inert objects which are free to move and are larger than the bed particles, has been studied extensively in the literature. Agarwal (1991) and Parmar and Hayhurst (2002) investigated the heat transfer coefficient to mobile spheres immersed in a bubbling fluidised bed and summarised their results in an overall correlating equation. There has been considerably less published, however, on the heat transfer coefficient from the bed to an object which emits gas.

Scott *et al.* (2004) determined the heat transfer coefficient between fluidised beds of particles of various sizes, at ambient temperatures, and particles of dry ice and compared them with experiments using bronze spheres attached to a thin flexible thermocouple. They allowed for the transpiration effect of the CO₂ gas emitted by the particle, which resulted in a lowering of the measured heat transfer coefficient, as expected. Good agreement between the experiments with dry ice and bronze spheres showed that the structure of the fluidised bed around the dry ice was similar to that around the bronze spheres as the heat transfer was not significantly affected by the emission of gas by the dry ice. Owing to the ambient temperatures used in the fluidised beds employed by Scott *et al.* (2004), the velocity ratio in their experiments was relatively low, being ~ 0.025. As shown by Fig. 5.2, however, the velocity ratio for dry ice spheres in beds at higher temperatures is several orders of magnitude larger.

5.5.1 Calculation of the heat transfer coefficient

As described in Section 5.1, the volumetric flow rate of CO₂, Q_{sub} , for each experiment and consequently, the radius of each dry ice particle was calculated by assuming that the particle remained spherical, thus

$$\rho_g \int_0^t Q_{sub} dt = - \int_{a_0}^a 4\pi a^2 \rho_d da \quad (5.4)$$

where ρ_g is the density of gaseous CO₂ at T_{mean} and p_{atm} and ρ_d is the density of the solid CO₂. The radius of the dry ice spheres is a and their radius at the start of each experiment is a_0 .

The surface area of the particle of dry ice and the velocity at which gaseous CO₂ was emitted from its surface were also calculated. The effective heat transfer coefficient, h_{eff} , (including the radiative heat transfer) throughout each experiment was then calculated according to:

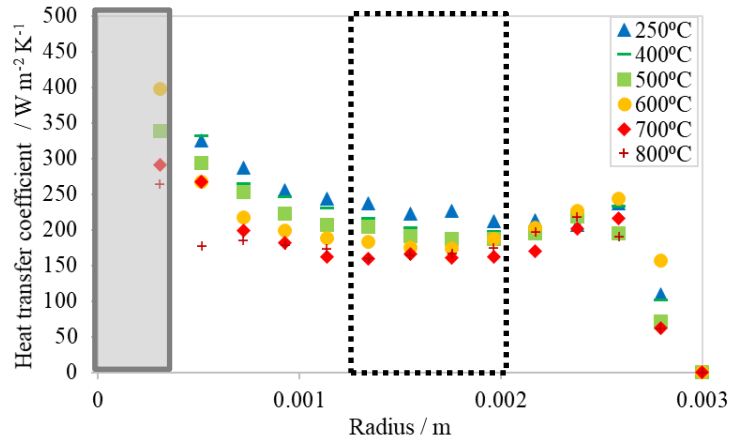
$$Q_{sub} = \frac{h_{eff} 4\pi a^2 (T_{bed} - T_d)}{\lambda_{sub} \rho_g} \quad (5.5)$$

where T_{bed} is the temperature of the fluidised bed, T_d is the temperature of the sublimating particle, assumed to be the equilibrium temperature at atmospheric conditions, 194.7 K, and λ_{sub} is the latent heat of sublimation of CO₂ at atmospheric pressure.

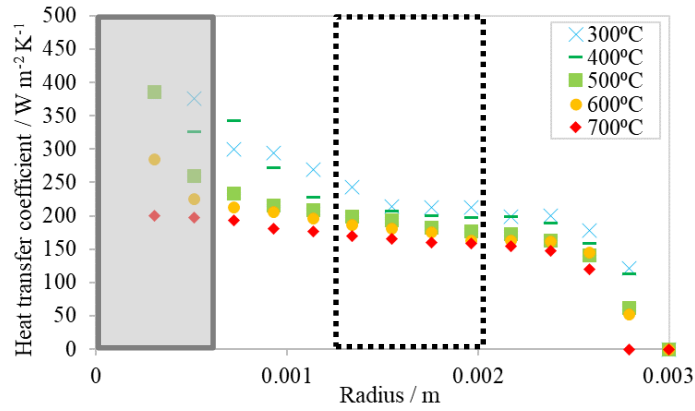
5.5.2 Results

The heat transfer coefficients between the fluidised bed and the dry ice particles were calculated for the experiments described in Section 5.1 using Eq. (5.5) and are shown in Fig. 5.8. As in Fig. 5.2, the shaded regions in Fig. 5.8 indicate where the dry ice particles were less than 3 times the diameter of the bed particles. Although the curves in Fig. 5.8 follow a similar shape to the curves in Fig. 5.2 for U_d/U_{mf} , the magnitude of the heat transfer coefficient typically fell as the bed temperature increased in all three bed particle sizes.

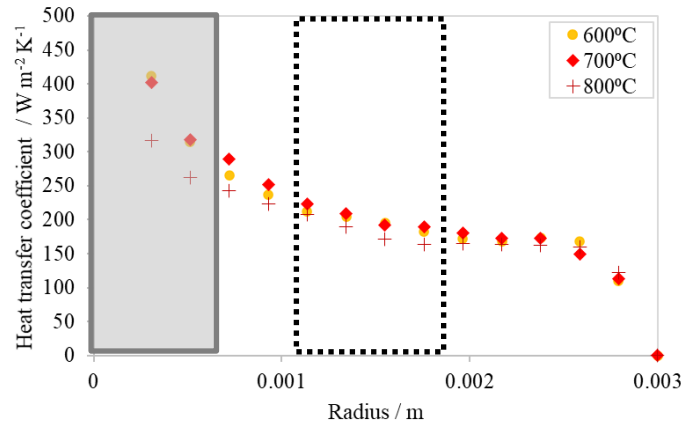
At the highest bed temperatures used, the rate at which the heat transfer coefficient increased, when the dry ice particle was less than 1 mm in radius, was smaller than that observed at lower bed temperatures. Indeed, in some cases, the heat transfer coefficient briefly reduced before increasing further at small particle radii, as shown by the inflection in Fig. 5.8 a) in the 800°C case. This coincides with the observation that the dry ice particles were present at the surface of the bed more frequently when the dry ice particles were small and in beds at very high temperatures, as discussed previously. Such a correlation may indicate that the heat transfer coefficient for a gas-emitting particle close to, or at the surface of the bed may be smaller than that for a gas-emitting particle circulating deep within the bed. This is explored in more detail in Section 5.5.4.



a)



b)



c)

Fig. 5.8. Experimentally calculated values of heat transfer coefficient for dry ice particles beds of a) 200-355 b) 355-425 and c) 425-600 μm silica sand $U/U_{mf} = 3$ and at the bed temperatures indicated in the legends. The grey shaded regions indicate when the particle was smaller than 3 times the average size of the bed particles and no longer behaved as a “large” particle. The regions enclosed by a dotted line were used to calculate average values of heat transfer coefficient.

As in Section 5.2, to facilitate comparison between the different beds and to eliminate the uncertainty at the start and ends of the experiments, average values of the heat transfer coefficient were calculated for the mid portion of each experiment. These values are shown in Fig. 5.9.

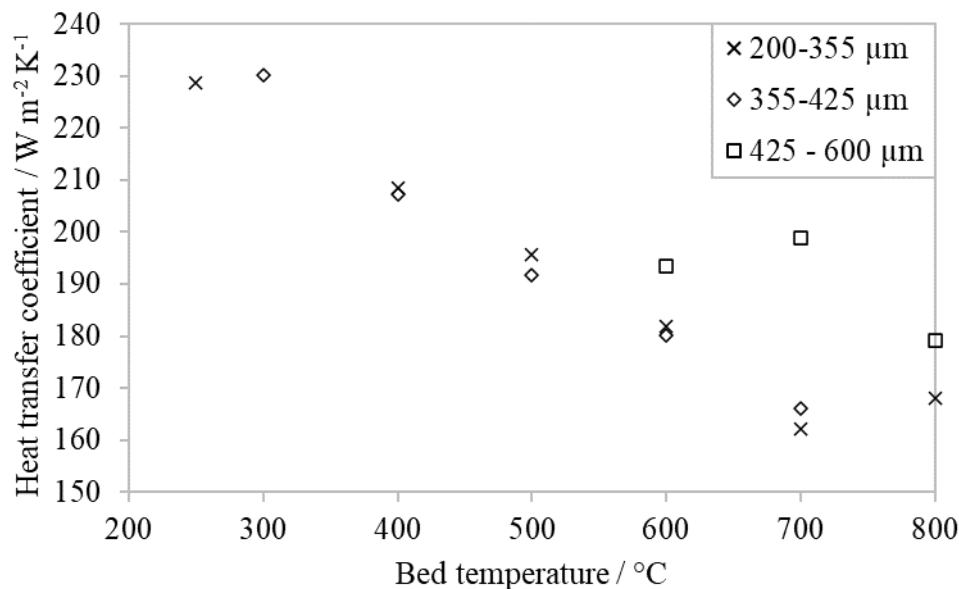


Fig. 5.9. Values of heat transfer coefficient averaged over the mid portion of each set of experiments shown in Fig. 5.8.

In the 200-355 μm and 355-425 μm beds the heat transfer coefficient fell as the bed temperature rose. The heat transfer coefficients were higher in the 425-600 μm bed than in the 200-355 μm or 355-425 μm beds.

5.5.3 Discussion

The heat transfer coefficient between the bed particles and the dry ice particles decreased as the bed temperature increased, in contradiction to the prediction for the heat transfer between the bed and an inert sphere by Hayhurst and Parmar (2002). Their model uses two components, a particle convective heat transfer coefficient, h_{pc} , added to the gas convective heat transfer coefficient, h_{gc} to give the effective overall heat transfer coefficient, h_{eff} . Their model was a modification of the model of Agarwal (1991), who originally split h_{pc} into two components, one for the portion of time that a circulating particle spent rising through the bed, $h_{pc,a}$, and one for when the circulating particle fell through the bed, $h_{pc,d}$. Additionally, a heat transfer coefficient for the proportion of time that the particle was in the bubble phase, h_{bub} was

described. The 5 different heat transfer coefficients were combined into a single effective heat transfer coefficient according to Eq. (5.6).

$$h_{eff} = P'h_{pc,a} + (P - P')h_{pc,d} + ph_{gc} + (1 - P)h_{bub} \quad (5.6)$$

Here P is the probability that the mobile sphere is in the emulsion phase rather than in a bubble and, P' is the probability that the mobile sphere is in the emulsion phase while ascending to the surface of the bed.

The model of Agarwal (1991), the predictions of which are shown in Fig. 5.10 for the 200 – 355 μm bed, did not include radiative heat transfer or any means of including the way in which the emission of gas from the particle in question changed the heat transfer coefficient. The model of Agarwal (1991) overestimates the heat transfer coefficient significantly, despite not including the radiative heat transfer, and predicts that the heat transfer coefficient should rise as the bed temperature increases. However, the experimental results in Fig 5.10 show the opposite trend.

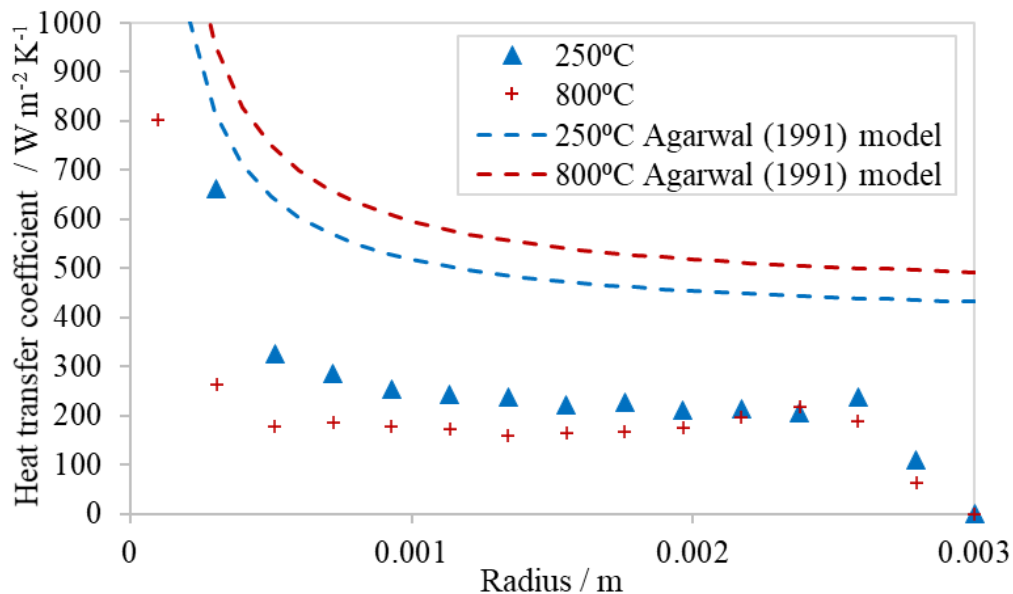


Fig. 5.10. Experimentally calculated values of heat transfer coefficient for dry ice particles in a bed of 200-355 μm silica sand at $U/U_{mf} = 3$. Also shown are the predictions from the model of Agarwal (1991) for the heat transfer coefficient at 250°C (---) and 800°C (---). The predictions of the model, modified to account for radiative heat transfer, transpiration cooling and the fraction of the surface of the dry ice in contact with the bed particles as indicated in Appendix 5.2 at 250°C (—) and 800°C (—).

Figure 5.11 shows the heat transfer coefficient for dry ice spheres in fluidised beds of different sized particles at 700°C and the predictions of the model of Agarwal (1991), which predicts that the heat transfer coefficient changes little with bed particle size. Parmar and Hayhurst (2002) concluded that the heat transfer coefficient decreases as the bed particle size increases. However, the experiments suggest that for the dry ice and silica sand system, the heat transfer coefficient follows the opposite trend.

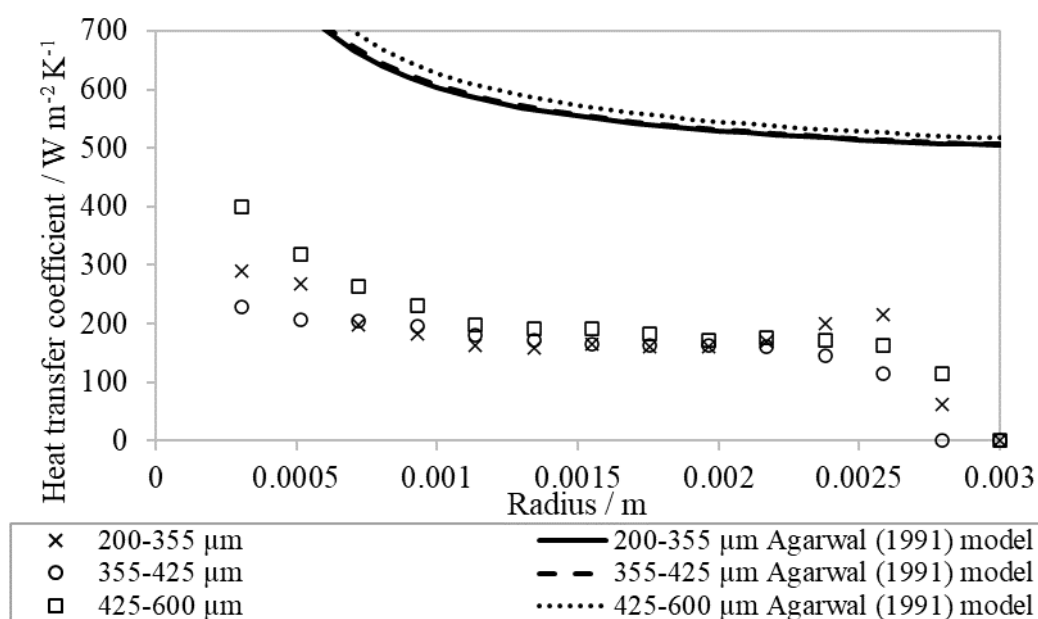


Fig. 5.11. Experimentally calculated values of heat transfer coefficient against time at 700°C in a bed of 200-355 μm (×), 355 – 425 μm (○) and 425 – 600 μm (□) diameter silica sand at $U/U_{mf} = 3$. Also shown are the predictions from the model of Agarwal (1991) for the heat transfer coefficient at 700°C in a bed of 200-355 μm (—), 355-425 μm (- -) and 425-600 μm (· · ·) silica sand.

The observations and theory of Chapters 3 and 4 found that the structure of the bed close to a gas-emitting object depended on the value of the velocity ratio U_d/U_{mf} . The values of U_d/U_{mf} were typically lower for the dry ice devolatilising in beds of larger particles compared to beds of smaller particles. It is likely, therefore, that the trends in heat transfer coefficient with bed particle size are linked to the way in which spheres which emit gas are able to disrupt the structure of the bed around them more in beds of small particles rather than in large ones and, therefore, decrease the heat transfer coefficient further. In Section 4.4.2 it was found that proportion of time that the surface of a particle, which was emitting gas, was blanketed by bubbles and, therefore not in direct contact with the bed material, increased as the rate of gas

emission was increased. The heat transfer coefficient model should, therefore, be modified to account for the changes to the structure of the bed around particles which emit gas.

5.5.4 Modifications to a steady state heat transfer model using experimental observations.

The model of Agarwal (1991) has been used as a basis, with an expression from Parmar and Hayhurst (2002) used to replace a fitted parameter in the original model. Agarwal's (1991) model has been modified in three ways to simulate better the heat transfer to the spheres of dry ice as they sublime.

Firstly, radiative heat transfer was added to the model to account for the wide range of temperatures investigated as the radiative component becomes significant at bed temperatures higher than 600°C. Two radiative heat transfer coefficients were required to account for the proportions of time which the particle spent in a bubble and in close proximity to the bed material.

Secondly, the effect of the emission of gas from the dry ice on the gas convective heat transfer coefficient was added to the model. Scott (2004) corrected for this by altering the gas convective heat transfer using the technique described by Bird *et al.* (2002) and found the corrected heat transfer coefficient satisfactory for predicting the heat transfer to spheres of dry ice sublimating in fluidised beds at room temperature. The same method was applied to the model of Agarwal (1991) such that a corrected gas convective heat transfer coefficient, \dot{h}_{gc} was used in place of h_{gc} .

Finally, using the results of Section 4.4.2, the effect of the bubbles passing around the spheres of dry ice was included in the model. The proportion of the surface of the spheres of dry ice which was blanketed by bubbles, τ , was found to increase as the velocity ratio, U_d/U_{mf} , increased according to Eq. (4.30):

$$\tau = m \frac{U_d}{U_{mf}} + c \quad (4.30)$$

This was found to be sensitive to the depth of the particle; however, for simplicity, average coefficients $m = 0.031 \pm 0.022$ and $c = 0.50 \pm 0.05$ were found. The fraction of the sphere

of dry ice which is in contact with the bed particles, the “coverage fraction”, f_c , is given by Eq. (5.7):

$$f_c = 1 - \tau = 1 - m \frac{U_d}{U_{mf}} - c \quad (5.7)$$

The weighting of the heat transfer coefficients was modified using the empirical relationship Eq. (4.30) to give the following modified heat transfer model and described in detail in Appendix 5.1.

$$\begin{aligned} h_{eff} = & f_c P' h_{pc,a} + f_c (P - P') h_{pc,d} + P h_{gc} \\ & + (1 - P) h_{bub} + P h_{rad} \\ & + (1 - P) h_{rad,bub} \end{aligned} \quad (5.8)$$

The model, thus modified, is shown in Figs. 5.15 and 5.16. The modified model gives a much closer fit to the experimental values of the effective heat transfer coefficient than the original and correctly predicts the fall in heat transfer coefficient as the bed temperature increases. As in the model of Agarwal (1991), the particle convective heat transfer coefficients dominate when the gas-emitting particle is large and the gas convective heat transfer coefficients dominate when the gas-emitting particle approaches the same diameter as the bed particles. The radiative components can be ignored until bed temperatures of 800K.

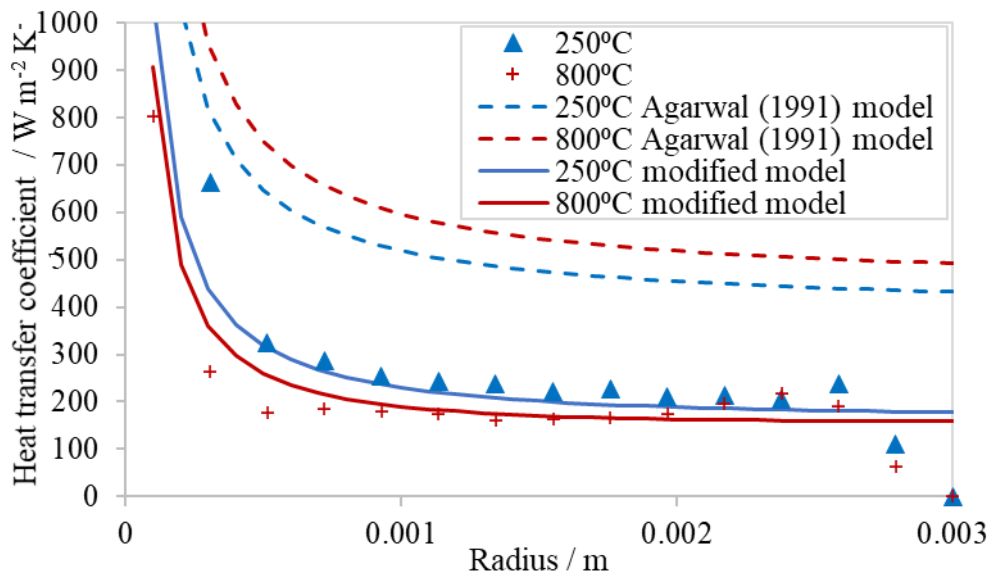


Fig. 5.15. Experimentally calculated values of heat transfer coefficient for dry ice particles in a bed of 200-355 μm silica sand at $U/U_{mf}=3$. Also shown are the predictions from the model of Agarwal (1991) for the heat transfer coefficient at 250°C (---) and 800°C (---). The predictions of the model, modified to account for radiative heat transfer, transpirative cooling and the fraction of the surface of the dry ice in contact with the bed particles as indicated in Appendix 5.2 at 250°C (—) and 800°C (—).

The modifications to the model, although simple, give a good approximation for the instantaneous heat transfer coefficient for the dry ice particles as they sublimated. The model assumed that the dry ice particles travelled up and down within the bed in much the same way as an inert particle. This is reasonable until the rate at which the dry ice sphere emitted gas was high enough to lift the spheres more rapidly to the surface such that they spent a larger proportion of time there, which occurred in the 200-355 μm bed above 700°C as shown by Fig. 5.6. A dry ice particle close to the surface of the bed must experience a significant reduction in contact between itself and the bed particles. Thus, to model fully the heat transfer to a sphere which emits gas in a fluidised bed, its position, and its tendency to either circulate within the bed or segregate must be modelled and a separate heat transfer coefficients used for the time at which the particle is at the surface or circulating.

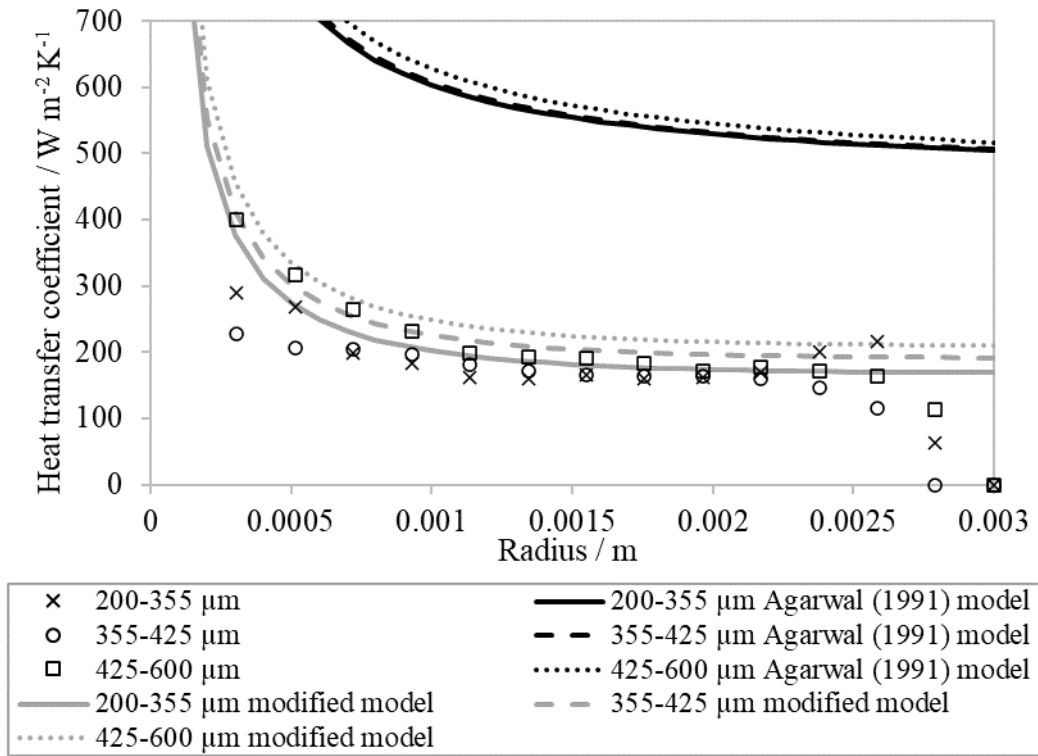


Fig. 5.16 Experimentally calculated values of heat transfer coefficient against time at 700°C in a bed of 200-355 μm (×), 355 – 425 μm (○) and 425 – 600 μm (□) diameter silica sand at $U/U_{mf} = 3$. Also shown are the predictions from the model of Agarwal (1991) for the heat transfer coefficient at 700°C in a bed of 200-355 μm (—), 355-425 μm (- - -) and 425-600 μm (⋯⋯⋯) silica sand. The predictions of the model, modified to account for radiative heat transfer, transpirative cooling and the fraction of the surface of the dry ice in contact with the bed particles as indicated in Appendix 5.2 at 700°C in a bed of 200-355 μm (—), 355-425 μm (- - -) and 425-600 μm (⋯⋯⋯) silica sand.

The model used for the coverage fraction, from the observations of the 2-D experiment in Section 4.4.2, crudely assumes that the linear relationship between U_d/U_{mf} and f_c is independent of depth, bed particle size, temperature and can be extrapolated beyond $U_d/U_{mf} = 4$. Further experiments are necessary to either validate the assumptions or to provide empirical relationships between the coverage fraction and bed size, and temperature and higher values of U_d/U_{mf} .

In addition to including how U_d/U_{mf} influences the proportion of the heat transfer surface which is in direct contact with the bed material, several other phenomena might need to be taken into account in an improved heat transfer coefficient model. The rate at which new packets of bed

particles are brought into contact with a sphere and swept away is an important part of h_{pc} . For the gas-emitting cylinder in the experiment in Section 4.4, it was found that the emission of gas encouraged the circulation of the bed material in the vicinity of the gas-emitting cylinder. A circulation cell of bed particles on each side of the cylinder is shown by the streamlines generated using Particle Image Velocimetry, PIV, in Fig. 5.12. The circulation cells suggest that the surface of the cylinder is supplied with more fresh bed material as U_d/U_{mf} increases. However, with particular reference to the dry ice spheres in Section 5.5.1, the bed material in the circulation cells may become cooler than the bed temperature if the heat transfer from the rest of the bed particles and the fluidising gas to the bed particles in the circulation cells is not rapid enough.

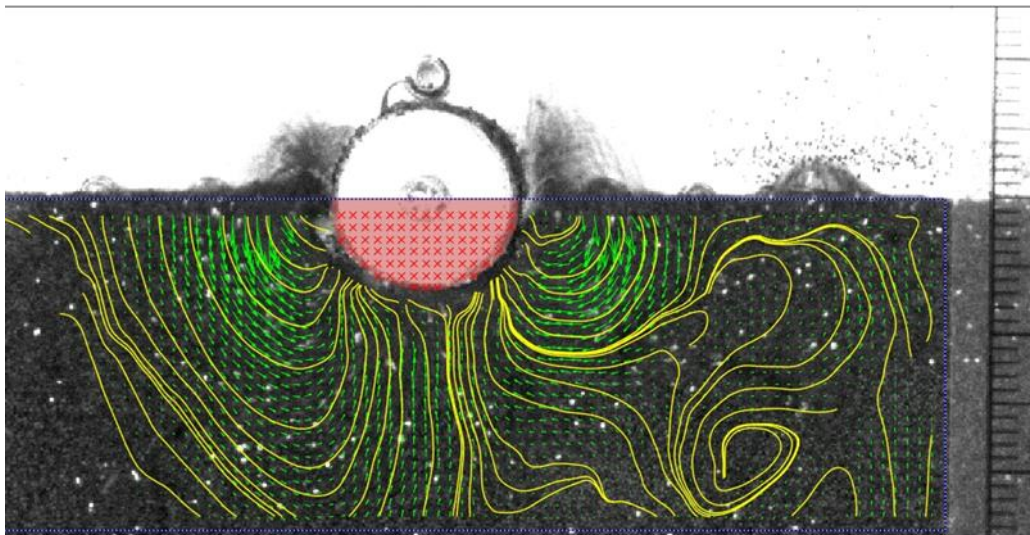


Fig. 5.12. The mean particle velocity vectors and streamlines, generated using PIV, close to a 12 mm diameter cylinder in a fluidised bed at $U/U_{mf} = 1$. The cylinder pictured is emitting gas at $U_d/U_{mf} = 1.8$.

In Section 4.4.1, the action of the bubbles passing around a gas-emitting cylinder was described. Packets of bed particles were pushed up, around the cylinder ahead of the rising bubbles. The width of these packets of bed particles was approximately the same as the width of the bubbles, measured radially away from the surface of the cylinder. The width of the bubbles passing around the gas-emitting cylinder in the 2-D bed experiment described in Section 4.4.1 was measured and is shown in Fig. 5.13. As U_d/U_{mf} increased, the width of the bubbles passing around the cylinder, and therefore, the packets of bed particles, increased linearly. The width of the bubbles also appeared to be sensitive to the dimensionless depth of

the gas-emitting cylinder as when the cylinder was close to or at the surface, $\delta < 2$, the bubbles were narrower than when the cylinder was deep within the bed.

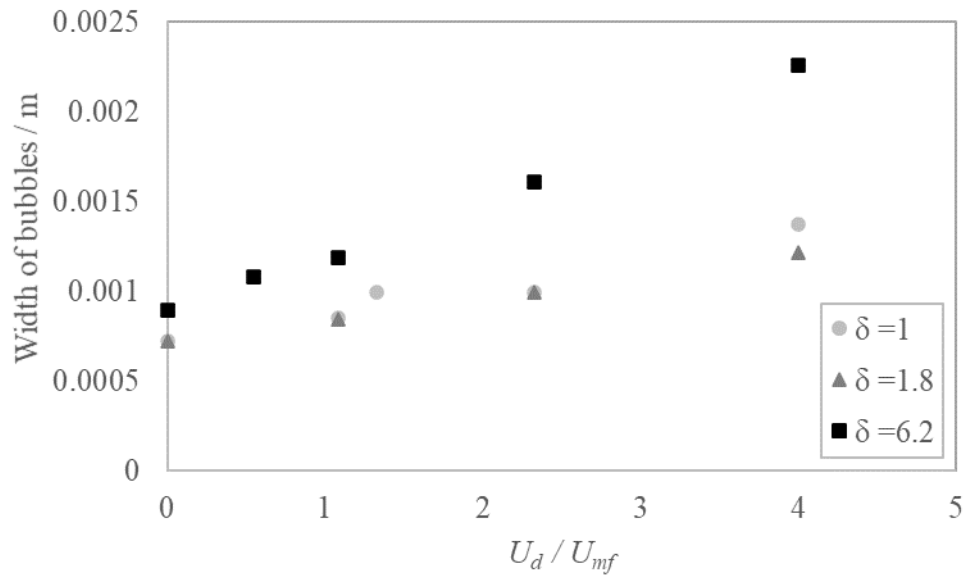


Fig. 5.13. The width, measured radially from the centre of a 12 mm diameter cylinder, of the bubbles passing around a gas-emitting cylinder in a fluidised bed at $U/U_{mf} = 1$.

The surface renewal time, an important parameter in h_{pc} is also a function of the frequency at which bubbles pass around an object. In the modified model described above it was assumed that the renewal of packets of particles was driven mainly by the movement of the dry ice sphere up and down through the bed material. For lighter particles which float at the surface of the fluidised bed, however, the surface renewal time will be determined by the frequency and speed of the bubbles passing around the sphere. From the experiment in Section 4.4 it was found that the frequency at which bubbles pass around a gas-emitting cylinder in an incipiently fluidised bed increased as U_d/U_{mf} increased for $0 < U_d/U_{mf} < 1$. However, the trend thereafter is less clear.

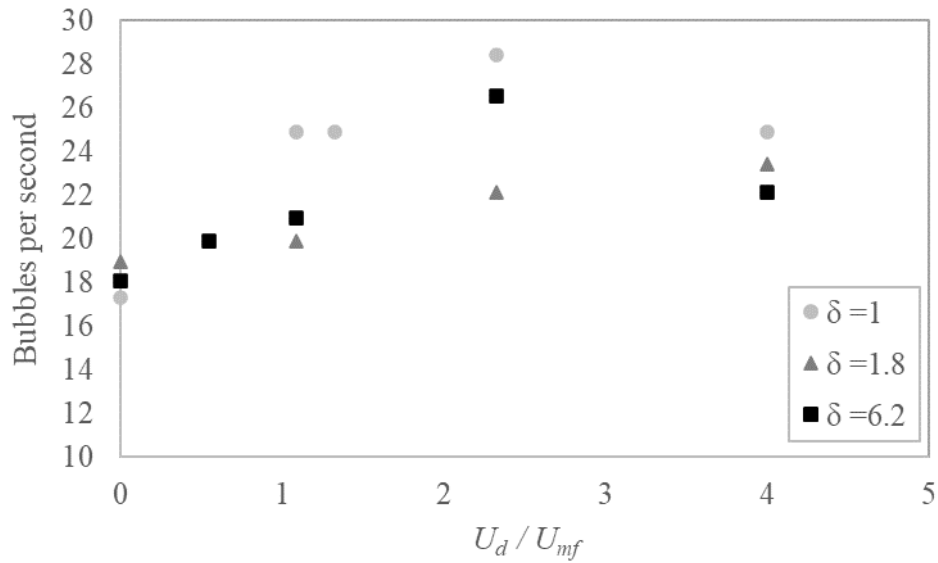


Fig. 5.14. The frequency of bubbles passing around a gas-emitting cylinder of 12 mm diameter in an incipiently fluidised bed.

Of course, results for the velocity of bubbles and bed particles, measured using a 2-D bed, are affected by the walls of the bed, as discussed by Cloete *et al.* (2015) and Asegehegn *et al.* (2012). A clearer understanding of the width and renewal frequency of the packets of bed particles should be obtained if possible using non-intrusive 3-D experiments, such as nuclear magnetic resonance or electrical capacitance tomography, or modelled with DEM. These techniques would allow in future for a more complete heat transfer model between the bed material and spheres which emit gas to be built up.

5.5.5 Assessing the steady state assumption

The diameter of the dry ice particles rapidly decreases as they sublime so the experiments described in Section 5.1 are inherently transient in nature. Scott *et al.* (2004) discussed the applicability of a heat transfer coefficient to non-steady state conditions and concluded that the temperature profile of the fluidised bed must quickly approach that of the steady state temperature profile to allow the system to be taken to be at pseudo steady state and, therefore, for a coefficient of heat transfer to be defined. In the case of gas-emitting particles, the surface of the particle is partially in contact with the bed material and partially blanketed by gas, as discussed above and in Chapter 4. The heat transfer is not dominated by any one part of the heat transfer coefficient, so characteristic time constants for both conduction through a thin

boundary layer in the gas next to the surface of the particle, and conduction through the packets of fluidised bed material which are delivered to the surface of the particle have been considered.

Scott *et al.* (2004) described, for objects with limited contact with the bed particles, the time constant for a steady state temperature profile to be established within a thin thermal boundary layer of gas adjacent to an object in a fluidised bed is

$$\tau_{fluid} = \frac{\delta_{th}^2 \rho_f C_{p,f}}{k_f} \quad (5.3)$$

where ρ_f , is the density of the gas in the boundary layer, assumed to be largely CO₂ at the mean of the particle temperature and the bed temperature, 1.17 kg m⁻³, $C_{p,f}$ is the specific heat capacity of the boundary layer gas, 1190 J kg⁻¹ K⁻¹, and k_f is the thermal conductivity of the boundary layer gas, 0.030 W m⁻¹ K⁻¹, δ_{th} is the thickness of the thermal boundary layer of gas given by $\frac{d_p}{\phi}$ where ϕ was found using Eq. (A5.5) to be 0.000049 m. The values of ρ , C_p , k and δ_{th} , were evaluated for bed temperatures of 800°C for the largest bed particles used in the experiments, 425 to 600 μm, giving the maximum value of $\tau_{fluid} = 1 \times 10^{-4}$ s. In this time, the greatest change in volume for any of the particles of dry ice was approximately 0.001% of the total particle volume.

Packets of bed particles, are swept past the surface of the gas-emitting particle, and the temperature gradient will only extend as far as the boundary of the packets. If it is assumed that the bubbling behaviour of the spheres of dry ice in Section 5.5.1 was similar to the bubbling behaviour of the gas-emitting cylinder in Section 4.4, the packets of bed particles were found to be swept past the surface of a cylinder at a rate of at least 17 per second as shown in Fig. 5.14, which gives a maximum contact time between the packets of bed particles and the dry ice of the order of 0.1 s (noting that at most two successive bubbles were simultaneously in contact with the cylinder at any one time). As the shortest sublimation time measured for a sphere of dry ice in Section 5.3 was 9 s, at least 90 packets of bed particles would pass the surface of the sphere in the time it took to sublimate entirely.

Thus, assuming that heat transfer occurred under pseudo-steady conditions is reasonable for all the experiments conducted here and hence, an estimate of the instantaneous heat transfer coefficient can be found using the experiment described in Section 2.5.

5.6 Conclusions

Although, even at the lowest temperature the value of U_d/U_{mf} was high enough to eliminate any defluidised hoods, the density of the dry ice was sufficiently high that this was not sufficient to change the circulation of the dry ice spheres away from that of equivalent density inert spheres. A sudden increase in the length of time that particles spent at the surface of the bed was observed when the velocity ratio was high at high bed temperatures. This agrees with the work of Section 4.4 which predicted that a high value of U_d/U_{mf} is necessary for particles with a density ratio of great than 1 to become positively buoyant. The total time for sublimation showed that the heat transfer coefficient to the dry ice particles was not obeying the trends observed for inert particles.

The heat transfer coefficient was found to decrease as the bed particle size decreased and the temperature of the bed increased. Such an observation indicates the importance of the structure of the bed material around objects which emit gas into fluidised beds, affecting the heat transfer coefficient. During the devolatilisation of biomass in fluidised beds, such changes in bed structure are also likely to occur and so should be adequately addressed in models.

Models for radiative heat transfer and the effect of the change in structure on the particle convective and gas convective heat transfer coefficients were included into a modified heat transfer model and shown to give a much better prediction for the heat transfer coefficient measured experimentally. The importance of the changes in the structure of the bed, and the position of the particle within the bed, for the heat transfer coefficient and, ultimately, the rate at which sublimation of dry ice occurs, has been demonstrated. The results are important also for predicting the rate devolatilisation during fluidised bed combustion of biomass.

Chapter 6 Devolatilisation of spheres of beech wood

In Chapter 5, the behaviour of dry ice in a hot fluidised bed was investigated with reference to the theory developed in Chapters 3 and 4. The theory, although applicable to all situations where a solid sphere or cylinder emits gas into a bubbling fluidised bed, was intended, ultimately, for predicting the behaviour of particles of biomass as they heat up and devolatilise in a hot fluidised bed. Therefore, the present chapter is focused on devolatilising biomass particles and investigates a) the velocity of gas at the surface of a sphere of biomass, and b) the position of the biomass relative to the surface of the fluidised bed during the period of devolatilisation.

6.1 Analysis of the volatile matter

As discussed in Chapters 3 and 4, the length of a defluidised hood above a solid object within a fluidised medium, and the structure of the bed around that object, change as the velocity of the gas emitted by that object changes. Both the disruption of the defluidised hood and the formation of bubbles at the underside of the object affect the depth at which that object is at dynamic equilibrium.

Estimating the velocity of the gas emitted by the spheres of dry ice when injected into a hot fluidised bed in Chapter 5 was achieved by measuring the concentration of CO₂ downstream of the reactor. In the case of a sphere of wood, undergoing devolatilisation, the situation is far more involved. During devolatilisation, the gas emitted by beech wood results from the thermal decomposition of the organic matter and is a mixture of many compounds, referred to, collectively, as volatile matter (VM). Volatile matter contains largely carbon, hydrogen, oxygen and nitrogen (Lu *et al.*, 2019).

The composition of the VM, emitted by a particle of wood in a fluidised bed, depends on many factors including the size, heating rate, thermal and chemical treatment of the wood particle. The heating rate depends, in turn, on the heat transfer coefficient between the bed and the external surface of the particle, itself a function of the size of bed particles, U/U_{mf} , and bed temperature among other factors. Common methods used to characterise the composition of the VM emitted during the pyrolysis of biomass in fluidised beds often involve a continuous or batch feed of many biomass particles (Pattiya, 2011, Shen and Zhang, 2003 and Neves *et*

al., 2017). During such studies, the heavier components of the VM in the exhaust gas are typically condensed in impinger bottles of solvent, collected batch-wise, and analysed using a variety of methods depending on the mean molecular mass of a particular product fraction. A portion of the exhaust gases is typically sampled continuously to detect the concentration of the lighter products of pyrolysis, such as CO₂, CO and CH₄. Because of the batch-wise analysis and the feed of many fuel particles at once, these methods do not allow the evolution of gas to be resolved over the lifetime of a single devolatilising particle. Volford *et al.* (2021) used a fast flame ionisation detector (FID) to find the rate of devolatilisation, resolved over the devolatilisation time for single particles of spruce. They found that the mass lost by each particle of spruce was proportional to the area under the FID trace, and so the FID trace could be used as an estimate for the rate of mass loss throughout the devolatilisation process. However, without knowing the composition of the VM emitted by the spruce, finding the molar flowrate of VM was not possible. Detecting and accounting for the vast array of compounds making up the VM is a formidable task; therefore, the experiment described in this section, utilising the apparatus described in Section 2.7, was developed to greatly simplify the analysis. Rather than detect all the species, the technique defines a single, hypothetical compound, which has the average molecular mass and composition of all the species. Although models assuming the VM is a single species, or two species, representing the tar and the gas, have been used in kinetic modelling of devolatilisation (*e.g.* Di Blasi, 1993), few studies have attempted to characterise the molecular weight of their single representative species. Several researchers have assumed a mean composition of the single representative species. For example, Saastamoinen *et al.* (2000) assumed the VM from wood was CH_{2.26}O_{0.99}, Zhou *et al.* (2005) assumed CH_{1.84}O_{0.96} for the VM produced from the devolatilisation of straw, and Galletti *et al.* (2016) assumed C_{1.06}H_{2.24}O_{0.92}N_{0.0028}S_{0.0002} for VM from wood chips. All three studies used the properties of the solid fuel to derive the composition of the species and did not attempt to characterise the actual average molecular mass of the VM. The experiment described in this section finds both the mean molecular mass and the mean composition of the VM.

6.1.1 Method

The mass of 5 beech particles was determined using a balance, before and after devolatilisation in a fluidised bed at 600°C. The process is described in Section 2.3 and the masses are shown in Table 2.3. A mean change in mass of 85.4% ± 1.2% was found, this being the proportion of mass lost due to the VM and moisture emitted.

The content of C, H, and N in the beech, and the char formed from it, was found using ultimate analysis. The amount of ash in the wood and char was found by subjecting a sample of each to a 5°C s⁻¹ temperature ramp programme in a thermogravimetric analyser under oxidative conditions from room temperature to 900°C. The oxygen content was estimated by assuming that it made up the rest of the mass of the beech and the char and the resultant composition compared well with that found by Demirbaş (1997) and Wang *et al.* (2005). Other elements were ignored. By comparing the composition from the ultimate analysis with the ash content from the TGA experiment, the composition of the VM was inferred. The weight % compositions of the beech, char and VM are shown in Table 6.1.

Table 6.1. Composition of beech and its char from TGA and ultimate analysis. Also given is the composition of the VM produced during pyrolysis at 600°C in a fluidised bed, calculated using the difference in composition between the beech and the char.

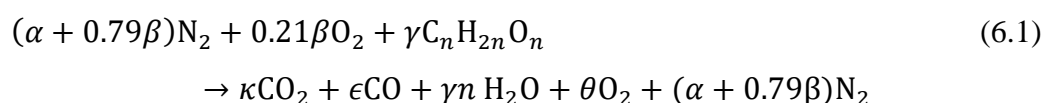
Component	Beech composition wt%	Beech char (pyrolysis in a fluidised bed at 600°C) composition wt%	Volatile Matter composition wt% (mol %)
Carbon	45.9	80.1	40.0 (25.1)
Hydrogen	6.0	2.5	6.6 (49.8)
Nitrogen	0.0	0.0	0.0 (0.0)
Ash	0.5	3.2	-
Oxygen (balance)	47.6	14.2	53.4 (25.1)

The VM was found to contain carbon, hydrogen and oxygen in molar ratios of approximately 1.0:2.0:1.0. The mean composition of the VM can, therefore, be expressed as C_nH_{2n}O_n and, as this composition has been arrived at by considering the difference in composition between the beech and its char, this single compound averages all gaseous species emitted by the beech as it transforms into char. Hence, it accounts for the lighter compounds for example H₂O, CO, CO₂, H₂, CH₄ as well as the heavier compounds. The formula C_nH_{2n}O_n is similar to the compositions of single species used to represent VM by Saastamoinen *et al.* (2000), Zhou *et al.* (2005) and Galletti *et al.* (2016).

From the stoichiometric formula, the molecular mass of the proposed average species for VM can be expressed as approximately 30×*n* g mol⁻¹. If *n* is found to be large, then the average velocity of the VM leaving the particle will be smaller than if *n* were small. To estimate the

velocity of the VM at the surface of the biomass spheres, n must be found, hence the experiment described in Section 2.7 was developed as a means of determining its value.

Thus, a single sphere of beech was introduced to a 30 mm I.D. bed of sand fluidised by N_2 at $600^\circ C$. A baffle was placed in the freeboard close to the surface of the bed and the pressure drop across the baffle was measured. The constant pressure drop across the baffle caused by the fluidising gas was subtracted from the recorded pressure drop, which was subsequently used to infer the molar flowrate of VM emitted by the biomass. In the freeboard directly above the baffle, air was introduced into the hot N_2 and VM mixture and a glowing wire was used to ignite the mixture, creating a gaseous flame. The CO , CO_2 and CH_4 concentration of the exhaust gases were measured. It was assumed that: a) all the VM combusts to form only CO_2 , CO and H_2O , b) the N_2 was inert and c) the O_2 fed to the freeboard was in excess. By comparing the molar flowrate of CO_2 and CO to the molar flowrate of VM, determined using the pressure drop across the baffle, the value of n was found. Hence, the overall combustion reaction is arrived at:



where the Greek letters describe the molar flowrate of: α , N_2 fed to the distributor of the reactor, β , air fed above the baffle, γ , evolved VM, κ , CO_2 in the freeboard, ϵ , CO in the freeboard, θ , O_2 in the freeboard. The assumption that the composition of the VM does not change through the devolatilisation process is examined in Section 6.1.2.

The flowrates of CO and CO_2 respectively are given by Eqs. (6.8) and (6.9), the derivation of which is given in Appendix 6.1.

$$\epsilon = \frac{[CO] \times (\beta + \alpha)}{1 - \frac{[CO]}{2}} \quad (6.8)$$

$$\kappa = [CO_2] \times \left(\beta + \alpha + \frac{\frac{[CO] \times (\beta + \alpha)}{1 - \frac{[CO]}{2}}}{2} \right) \quad (6.9)$$

From the carbon balance:

$$\gamma n = \kappa + \epsilon \quad (6.10)$$

and, assuming that n remains constant throughout devolatilisation:

$$n = \frac{\kappa + \epsilon}{\gamma} \quad (6.11)$$

Hence, by comparing the molar flowrate of the VM, γ , with the combined flowrates of CO₂ and CO, ϵ and κ , which arise owing to the combustion of the VM, n was evaluated, yielding an average value for the molar mass of the species comprising the VM.

6.1.2 Validation using the sublimation of dry ice

The experimental technique described in Sections 2.7 and 6.1.1 was validated using a system where the molar flow rate of gas emitted by a particle, γ , does not change between the surface of the particle and the freeboard. A system which satisfies this condition is the sublimation of a sphere of dry ice. In this case, the flowrate of CO₂, found by measuring the pressure drop over the baffle, and the flowrate of CO₂, found by measuring the concentration of CO₂ in the freeboard, should be identical and yield the result $n = 1$. The flowrate of CO₂, determined using both methods, is shown, for an exemplary experiment, in Fig. 6.1.

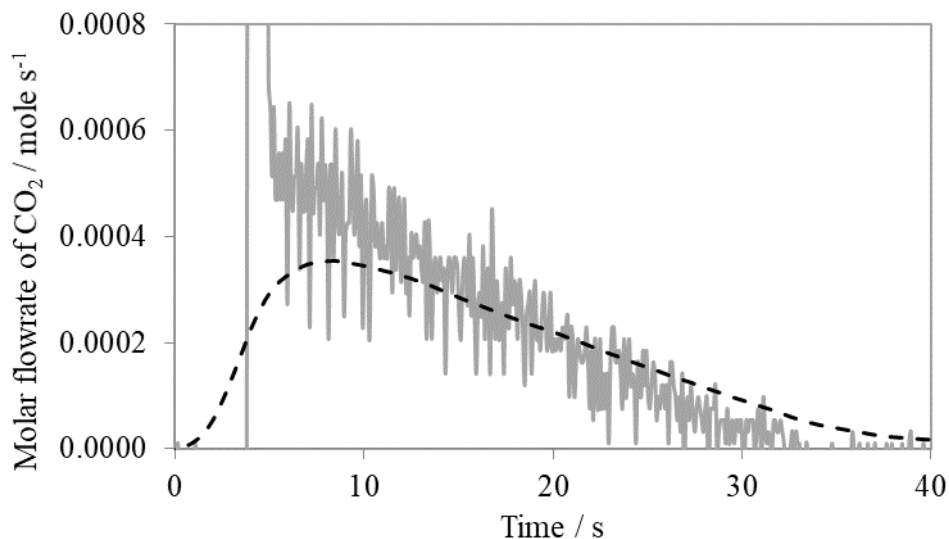


Figure 6.1. The molar flow rate of CO₂ given off by an 8 mm diameter sphere of dry ice in a fluidised bed at 600°C, $U/U_{mf} = 1.5$. The CO₂ flowrate was calculated using the pressure drop across a baffle (—) and using the concentration of CO₂ measured in the freeboard (- - -). The signal from the CO₂ measurement was deconvoluted.

The flowrate of CO₂ away from the dry ice particle immediately after the sphere was dropped into the bed could not be measured as it took between 1 and 3 s to correctly insert the baffle into the apparatus. This process is noticeable in the results from the pressure drop calculations as the large spike in flow of gas past the baffle at 4 to 7 seconds in Fig. 6.1. The flowrate of CO₂ given by the two methods show a similar curve, which decreases linearly, after the initial rise in flowrate at the start of the experiment. The gradient of the lines in Fig. 6.1 should be the same. However, there was a disparity between the gradient of the two lines. The response time for the pressure measurement was much faster than for the measurement made by the gas analyser. Although the signal from the gas analyser was deconvoluted according to the method set out in Appendix 2.2, the deconvolution process was insufficient to completely correct the shape of the curve. The two curves in Fig. 6.1 should have the same gradient, because in this experiment $n = 1$; however, the pressure gradient is 1.6 times the composition curve gradient. In steady state conditions the mixing in the sampling line has no effect on the value of concentration obtained; however, in the dry ice experiments the concentration steadily fell. The influence of the deconvolution method on the results was eliminated by analysing the area below the curves, which corresponded to the total number of moles of CO₂ emitted. This value was checked against the expected number of moles of CO₂ in an 8 mm diameter sphere of dry ice, 0.0080 ± 0.0003 moles as described in Section 2.31. Figure 6.2 shows the cumulative sum of moles of CO₂, calculated from both experimental methods and normalised by 0.0080 moles. Both methods of measuring the gas flowrate gave a carbon balance of 90%, agreeing on the total number of moles of CO₂ which were detected. If an average value is taken over the experiment, the method can satisfactorily determine the number of carbon atoms per molecule of gas emitted by a particle beneath the baffle. In this case, it is approximately 1, which is as expected for spheres of dry ice giving off CO₂.

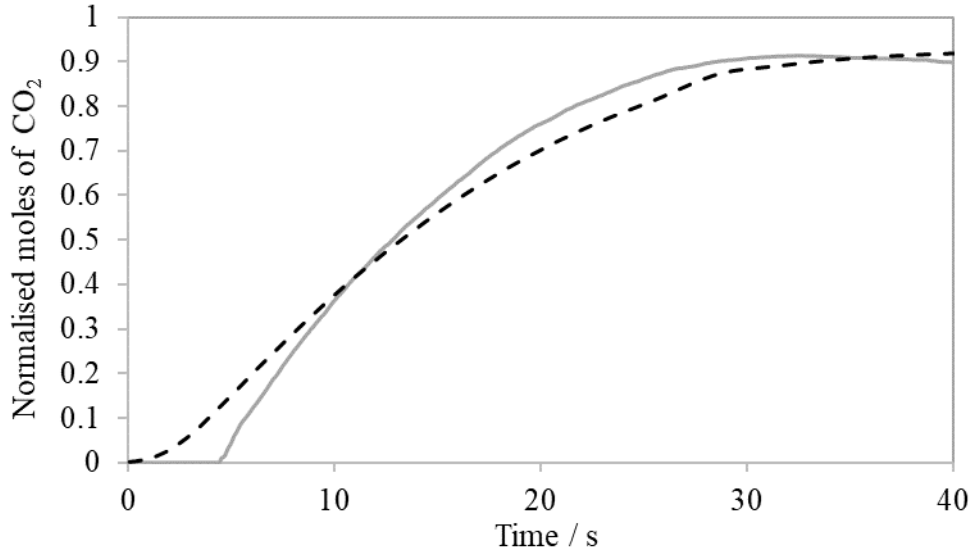


Fig. 6.2. The cumulative emission of CO₂ from the dry ice particles, normalised by the number of moles of CO₂ in a single dry ice sphere as calculated using the pressure difference across a baffle (—) and by measuring the CO₂ concentration in the freeboard (- -).

The analysis assumes that the properties of the gases passing the baffle, the composition of which change during the sublimation of the dry ice sphere, do not affect the discharge coefficient for the annular gap between the baffle and the reactor. Knowing the maximum flowrate of CO₂ the size of the error this assumption introduces to the calculation of the molar flowrate can be established. The density of the gas passing the baffle, at 600°C changed from 0.39 kg m⁻³, pure N₂, to 0.50 kg m⁻³ for the mixture of N₂ and CO₂. The Reynolds number, using the hydraulic diameter of the annular gap between the baffle and the reactor walls, passing the baffle at the peak flowrate was of the order of 15, if the gas had the density of N₂, or 21 if the gas had the density of N₂ mixed with CO₂. As the flow was laminar, the discharge coefficient was approximated as $C_f = 16/Re$. As a first approximation, ignoring entry effects, the velocity of gas through the gap between the baffle and the reactor is

$$U_{gap}^2 \propto \frac{\Delta p}{C_f \rho_f} \quad (6.12)$$

Hence the assumption about constant properties of gas gives a 2.7% error in the prediction of U_{gap}^2 from the measured pressure drop, which is acceptable.

6.1.3 Results for the devolatilisation of beech spheres

Following the validation of the experimental technique using dry ice, but noting its shortcomings, which are that the experiment fails to capture the first 1 to 3 seconds of each experiment, and that the experiment is sensitive to the mixing in the gas sample line, the technique was used to find the average number of carbon atoms per molecule of VM, n , produced by beech during devolatilisation.

To measure the total number of moles of carbon, the VM must be combusted between the baffle and the sampling line inlet so that the carbon can be detected using CO₂ and CO sensors. To validate the assumption that the combustion of the VM is stable and that all the VM combusts, the concentrations of CO, CO₂ and CH₄ in the freeboard were measured during pyrolysis experiments where the VM was combusted. The concentrations of CH₄, CO₂ and CO during the pyrolysis of a single 10 mm diameter sphere of beech at 600°C, following combustion of the VM, are shown in Fig. 6.3.

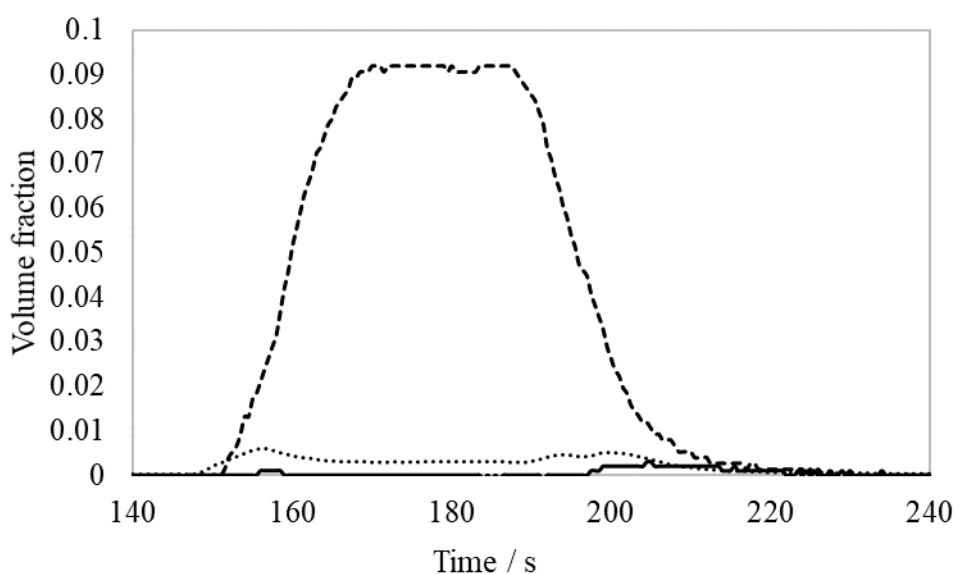


Fig. 6.3. The concentrations of CO₂ (---), CO (.....) and CH₄ (—) measured during the devolatilisation of a single 10 mm sphere of beech in a fluidised bed at 600°C. The measurement was taken downstream of combustion of the VM in the freeboard.

The CH₄ concentration was zero for most of the experiment indicating that all the VM combusted in the ignition zone above the baffle. Small concentrations of CH₄ were detected,

concurrent with visual observation of soot and smoke between 150 and 160 s, and between 200 and 220 s. For a short time at the start and end of the experiment the mixture of VM and air is below the lower flammability concentration of the VM and combustion cannot occur. Therefore, near the start and end of devolatilisation the presence of CH_4 and the observation of smoke indicates that incomplete or no combustion was occurring for short periods of time. Additionally, the concentration of CO was higher at the start and end of the experiment. For the mid portion of the experiment the CO_2 and CO concentrations were stable and constant through time in the example shown in Fig. 6.3. As shown in Fig. 6.4, however, the ratio of CO_2 to CO was not constant across repeated experiments. This indicates that during the experiments the completeness of combustion was sensitive to uncontrolled factors such as the position and temperature of the ignition coil. These coils were hand wound and regularly burnt out during the experiments, potentially leading to the variation in CO to CO_2 ratio between experiments. Consequently, it could not be assumed that the ratio of CO to CO_2 produced was constant and reproducible and hence the experiment could not be simplified by measuring only CO_2 using the rapid CO_2 analyser and inferring the concentration of CO from that.

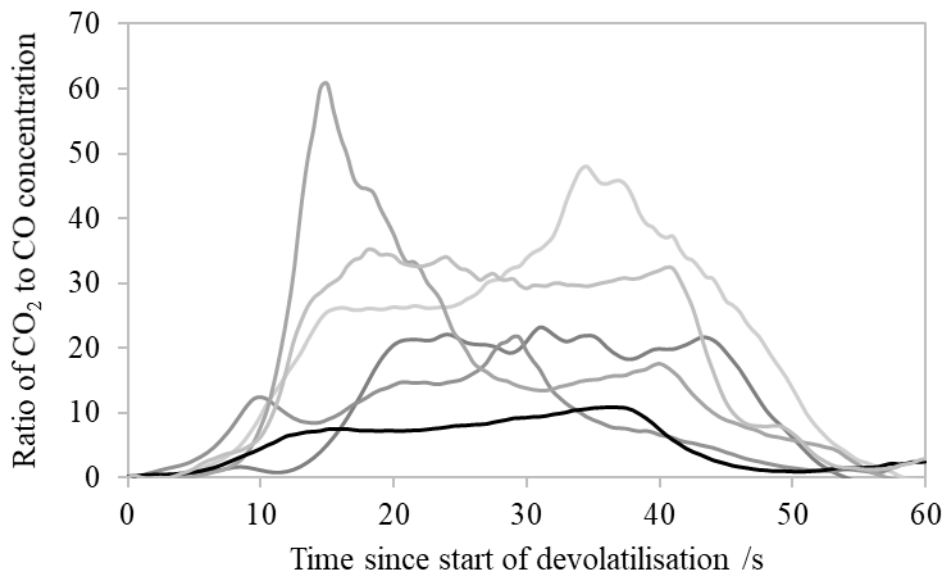


Fig.6.4. The ratio of CO_2 to CO concentration measured during the devolatilisation of single 10 mm beech spheres in a fluidised bed at 600°C for 6 experiments. The measurement was downstream of the VM combustion zone in the freeboard.

In addition to measuring the concentrations of the CO₂ and CO to find their respective molar flowrates, the molar flowrate of the VM and fluidising gas was calculated by measuring the pressure drop across a close-fitting baffle just above the fluidised bed surface and below the combustion zone. The values of molar flowrate of VM, calculated using the pressure measurements, were noisy (*c.f.* Fig. 6.1), therefore, to aid the comparison between the two methods of measuring molar flowrate, the integrals of the flowrates were compared. These were normalised by the number of moles of carbon atoms expected in the VM for each sphere, 0.0285 moles of carbon per gram of beech, as shown in Fig. 6.5. The carbon balance for the CO₂ and CO ranged from 0.80 to 1.12.

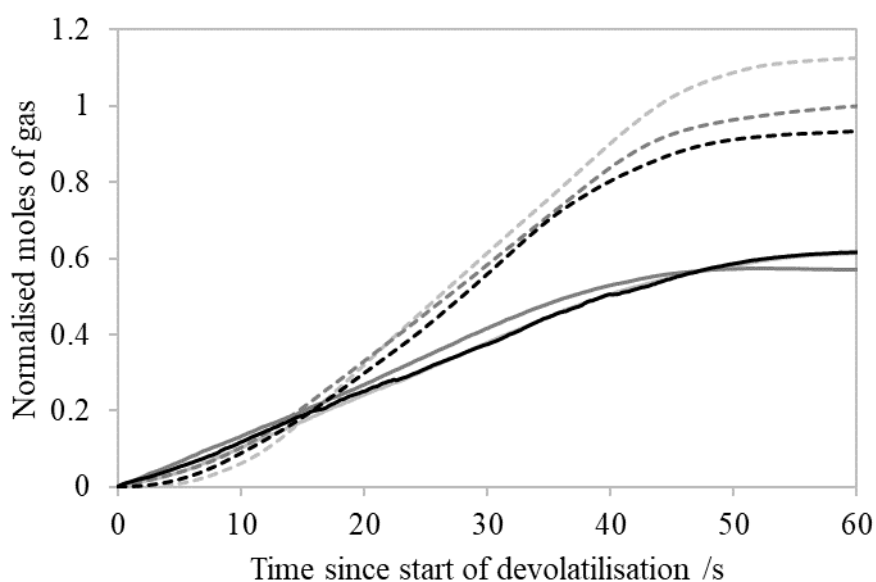


Fig. 6.5. The cumulative moles of VM emitted by beech spheres measured using the pressure drop over the baffle (solid lines). Also shown is the cumulative moles of CO₂ and CO produced during the combustion of the VM (dashed lines). Both curves were normalised by the expected number of carbon atoms found in the VM for each sphere.

The variation in the carbon balance from the composition measurement method is unlikely to be attributable solely to the variation in the amount of VM emitted by the beech spheres as this had a standard deviation of 1.2 wt% as shown in Table 2.3. It is probable that the variations in the time at which ignition and extinction of the combustible mixture of gases above the baffle occurred contributed to the difference in the carbon balance between experiments. The uncertainty at the start and end of the devolatilisation was compounded by the pressure spikes

caused by the rapid insertion of the baffle. The curves for the production of gas, calculated using the composition of CO₂ and CO in the exhaust gas, in Fig. 6.5 are approximately linear between seconds 15 and 35. Consequently, further analysis was performed by taking this 20 s section from the middle of each devolatilisation experiment, during which the combined flowrates of CO₂ and CO and the flowrate of VM were constant. The mean rate of devolatilisation and production of CO₂ and CO from the combustion of VM was obtained by determining the gradient of the approximately straight-line sections, an example of which is shown in Fig. 6.6. The ratio between the combined flowrates of CO₂ and CO, and the flowrate of VM was not determined at the start and end of the experiment, so the results are only applicable to the mid-portion of devolatilisation experiments.

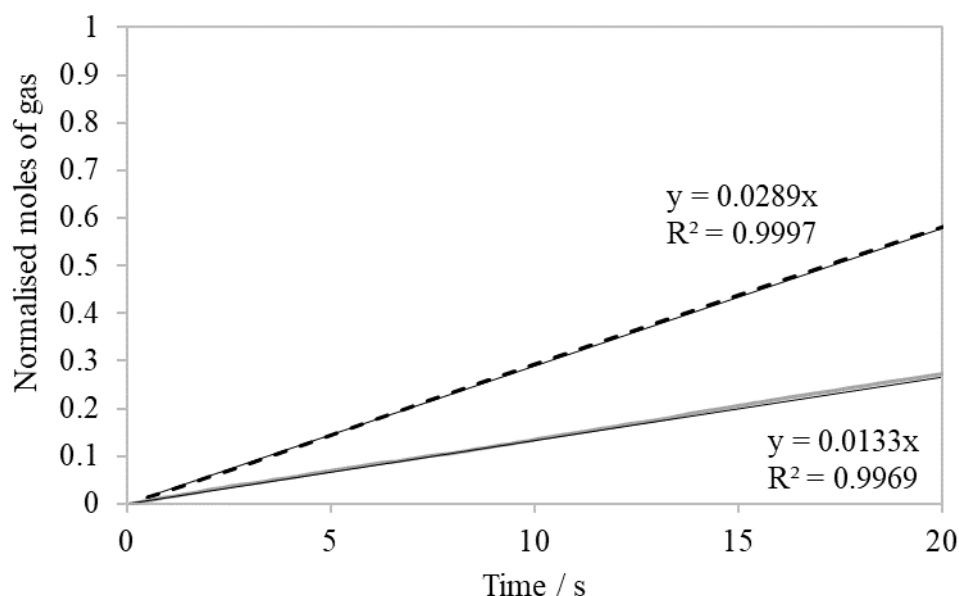


Fig. 6.6. The mid portion of one pair of curves from Fig. 6.5. Shown are: the cumulative emission of VM from the beech particles as measured using the pressure drop over the baffle (—) and the cumulative emission of CO₂ and CO from the combustion of the VM (- - -). Both lines are normalised by the number of moles of carbon in the sphere of beech. The lines of best fit (—) and their equations are also shown.

The molar flowrate of VM, and the combined molar flowrate of CO₂ and CO, were linearly proportional to each other for the mid portion of the devolatilisation process. This shows that the mean number of carbon atoms per molecule of VM did not change significantly during the mid-portion of devolatilisation and, for this portion at least, the assumptions in the analysis in

Section 6.1.1 are reasonable. By dividing the rate of emission of CO₂ and CO by the rate of emission of VM, the mean composition of the VM was found, as shown in Table 6.2.

Table 6.2. The difference between the molar flowrate of CO₂ and CO, arising from the combustion of VM, and the molar flowrate of VM during the devolatilisation of 10 mm diameter spheres of beech in a bed of silica sand at 600°C, fluidised by nitrogen at $U/U_{mf} = 1.5$.

	Composition measurement		Pressure measurement	
Mass of particle / g	Normalised rate of production of moles of CO and CO ₂ / s ⁻¹	Carbon balance	Normalised rate of production of moles of gas / s ⁻¹	Ratio of rates of production of gas “ <i>n</i> ”
0.436	0.0289	1.13	0.0133	2.17
0.418	0.0249	1.02	0.0143	1.74
0.351	0.0255	0.93	0.0126	2.03
Mean	0.0264	1.03	0.0134	1.98
Standard deviation	0.00216	0.10	0.00085	0.22

The ratio between the flowrate of VM and the flowrate of CO₂ and CO, *n*, was found to be 2.0 ± 0.2 based on three experiments. This suggests that the chemical formula of a single species, which represents the entire mixture of compounds which comprise the VM emitted by a 10 mm diameter sphere of devolatilising beech, is C_{2.0}H_{4.0}O_{2.0}. This species is a model species which represents the molar mass and mean composition of the VM and may not, necessarily, exist as a constituent part of the VM. This model of the VM indicates that for every mole of CO₂ and CO detected downstream of combustion of the volatiles, 0.51 moles of VM were emitted by the biomass particle. The representative species allows the molar flowrate of the volatile matter to be calculated in the experiments in Section 6.2 and is of use wherever it is impractical to measure directly the molar flowrate of gas leaving a particle.

It was assumed in the analysis, just as in Section 6.1.2, that the change in the properties of the gas passing the baffle did not affect the discharge coefficient. Having found the mean molar mass of the VM using this method, 60 g mole⁻¹, and knowing the maximum molar flowrate of VM, measured during the experiments to be 1.5×10^{-4} moles s⁻¹, the error that the assumption has introduced can be assessed. The density of the gas passing the baffle, at 600°C changed from 0.39 kg m⁻³, pure N₂, to 0.50 kg m⁻³ for the mixture of N₂ and VM. In the absence of available information about the viscosity of gaseous C₂H₄O₂ it has been assumed that the

viscosity is similar to that of N_2 at $600^\circ C$. The Reynolds number, using the hydraulic diameter of the annular gap between the baffle and the reactor walls, passing the baffle at the peak flowrate was of the order of 9, if the gas had the density of N_2 or 12 if the gas had the density of N_2 mixed with $C_2H_4O_2$. Because the flow was laminar, as in Section 6.1.2, the discharge coefficient was approximated as $C_f = 16/Re$ and the velocity past the annulus for a given pressure drop was, again, assumed to be given by Eq. (6.12) as a first approximation. Hence, the assumption that the density of the gas does not change the discharge coefficient gave a 1.7% error in the prediction of u^2 from the measured pressure drop, which is acceptable.

6.2 The velocity of the volatile matter emitted from beech spheres floating freely in a bed fluidised by air

The mean composition of the VM emitted by 10 mm dia. spheres of beech devolatilising in a bed of silica sand fluidised by nitrogen at $600^\circ C$ was found in the previous section to be $C_{2.0}H_{4.0}O_{2.0}$. The reactor had an internal diameter of 30 mm. The experiments described in this, and the following Section 6.3 were carried out using silica sand in a larger fluidised bed reactor, of 0.143 m diameter, as described in Section 2.8. In addition to the larger diameter, the bed used in this section and Section 6.3 was fluidised by air rather than nitrogen. Owing to the much greater ratio between the flow of fluidising gas and the flow of VM in this larger bed, compared to the smaller bed used in Section 6.1, and the over-bed feeding arrangements for the fuel particles in the larger bed, a close-fitting baffle to measure the flowrate of VM was not practicable. However, by assuming that the VM could still be represented by $C_{2.0}H_{4.0}O_{2.0}$, unaffected by the fluidising gas and by the value of U/U_{mf} , an estimate of the molar flowrate of the VM could still be obtained by measuring the CO_2 and CO concentration in the freeboard and the overall flowrate of fluidising gas. Because the rate of devolatilisation of wood in a hot fluidised bed is so rapid, the VM blankets the biomass particle and prevents oxygen from reaching the surface of the wood (Scala and Solimene, 2013). The VM subsequently combusts in a diffusion flame some distance away from the surface of the wood particle. Consequently, a sphere of beech, devolatilising in a bed fluidised by air, can be treated in a similar manner to those in the experiments in Section 6.1.2 so long as any additional heat transfer arising from the thermal radiation from the diffusion flame does not significantly alter the heat transfer to the particle and hence the rate of emission of VM. Hence, it was assumed that beech spheres devolatilising and combusting in the bed of sand fluidised by air at $600^\circ C$ produced VM of the

same mean composition as those devolatilised in the small fluidised bed used in Section 6.1 at 600°C.

6.2.1 Method

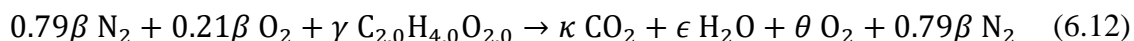
The experiments described in Sections 6.2 and 6.3 were undertaken in a fluidised bed of 0.143 m diameter at University College London. This fluidised bed was used as it is fitted with X-radiography equipment, allowing the contents of the bed to be observed in profile. This section deals with the measurement of the composition of the off gases, following combustion of the VM. The X-radiography is dealt with in Section 6.3.

In each experiment, a single sphere of beech was weighed and its diameter was measured before it was dropped into the fluidised bed. The bed of silica sand was fluidised by air at a range of values of U/U_{mf} between 1.2 and 2.9 at 500 and 600°C. In the absence of suitable experimental verification, it was assumed that the same mass of volatiles would be lost, 85.4% of the total mass of the sphere of beech, during devolatilisation at 500°C as at 600°C, on the basis that Volford *et al.* (2021) found that the mass lost, during devolatilisation, by particles of spruce of the same size was similar at 500, 600 and 700°C. However, it should be noted that Gomez-Barea *et al.* (2010) found that the yield of the larger components of VM which condense at room temperature, decreased as the bed temperature was increased and that the yield of lighter components increased. Hence it is likely that n will be greater at 500°C than at 600°C and, hence, that the U_d at 500°C is probably overestimated.

The density of each sphere of beech was modified by drilling a short blind hole, of 2 mm diameter, to a depth of 4.5 mm into the end grain of the spheres and hammering a particle of lead into the beech; in doing so, beech spheres with a range of density ratios were produced. Here, the density ratio is the ratio of the density of the sphere of beech, with its lead payload, to that of the emulsion phase of the fluidised bed: values from 0.5 to 0.8 were produced.

The composition of the gas in the freeboard was measured with a SprintIR-R CO₂ sensor and Cambridge Sensotec analyser. The latter confirmed that no CH₄ or CO was present in the exhaust from the reactor and so the VM was completely combusted by the oxygen in the fluidising air to produce CO₂ and the CO₂ concentration alone measured by the Sprint-IR sensor was sufficient to calculate the molar flowrate of the VM. Hence, the combustion of the

VM emitted by each sphere of beech was assumed to take place according to the following instantaneous steady state equation:



Here, β is the molar flowrate of air through the reactor, γ is the molar flowrate of volatiles produced by the wood, κ is the molar flowrate of CO_2 in the exhaust gas, ϵ is the molar flowrate of H_2O in the exhaust gas, and θ is the molar flowrate of O_2 in the exhaust gas. It should be noted that Reaction (6.12) differs from Reaction (6.1) because, here, the bed is fluidised by air rather than N_2 , with air introduced separately as described in Section 6.1. Additionally, the composition of the volatiles was known in Reaction (6.12) and the production of CO was known to be negligible.

The molar flowrate of CO_2 is given by Eq. (6.13), the derivation of which is given in Appendix 6.2.

$$\kappa = \frac{[\text{CO}_2]\beta}{(1 - [\text{CO}_2])} \quad (6.13)$$

The $(1 - [\text{CO}_2])$ term in Eq. 6.20 accounts for the water from combustion as there was no CaCl_2 trap used on this sample line. Hence, the molar flowrate of CO_2 in the exhaust gases from the reactor was found from the CO_2 concentration and the known molar flowrate of air into the reactor, β . The cumulative production of CO_2 was found for each single particle experiment, three examples of which are shown in Fig. 6.7. Carbon dioxide was produced in two distinct regimes: for around the first 40 s, the CO_2 was produced more rapidly than during the subsequent char combustion as shown by the two distinct gradients in Fig. 6.7. Carbon balances for each experiment are given in Table 6.3. The grey shaded region represents the portion of each curve which was fitted with a straight line for use in Section 6.2.2.

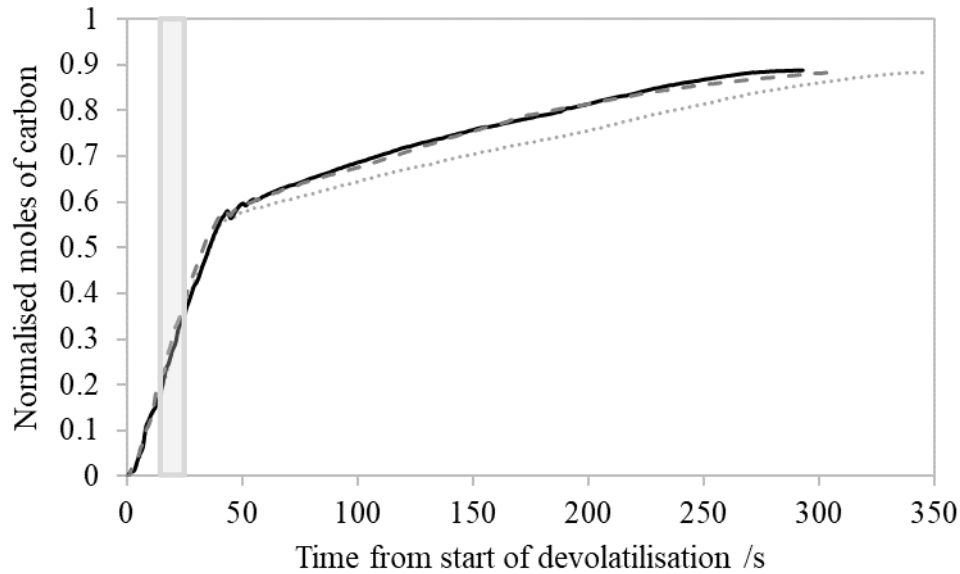


Fig. 6.7. Cumulative carbon balances for the combustion of beech spheres at $U/U_{mf} = 2.2$, at 600°C , normalised by the number of moles of carbon in each beech sphere. Shown here are spheres of density 1039 (.....), 881 (—), and 755 (- - -) kg / m^3 . The different densities were achieved by adding different amounts of lead to the spheres of beech. The grey shaded rectangle indicates the section of the devolatilisation curves which were fitted with straight lines – shown in Fig. 6.8.

Experiments with an overall carbon balance of less than 0.8 were rejected. The carbon balances were consistent across most experiments at 600°C , although varied a little more at 500°C . The carbon balances were typically better for the experiments at high flowrates at 500°C . This could indicate that, at lower flowrates, air from the laboratory was able to dilute the concentration of CO_2 in the upper portion of the freeboard from which the sampling line drew gas.

Table 6.3. Overall carbon balances for the combustion of beech spheres.

Bed Temperature / °C	U/U_{mf}	Density / kg m ⁻³	Overall Carbon balance	Volatile matter carbon balance
500	1.2	966	0.80	0.75
500	1.2	1056	0.88	0.83
500	1.8	931	1.03	0.92
500	1.8	808	1.10	1.10
500	2.4	979	0.95	0.83
500	2.4	971	1.04	0.95
500	2.4	762	1.06	0.97
600	1.4	842	0.96	0.85
600	1.4	1035	0.88	0.82
600	1.4	861	0.84	0.78
600	2.2	1039	0.88	0.82
600	2.2	755	0.88	0.86
600	2.2	881	0.89	0.88
600	2.9	687	0.88	0.87
600	2.9	1008	0.88	0.85
600	2.9	851	0.88	0.86

6.2.2 The rate of emission of volatile matter

The molar flowrates of CO₂ were divided by the average number of carbon atoms per VM molecule, n , found in Section 6.1.2 to be 2.0 at 600°C, to obtain an estimate of the molar flowrate of VM. As in Section 6.1.2, a steady state value of molar production of VM was found and is shown in Fig. 6.8. The analysis was carried out by using a best fit straight line through the cumulative production of VM curves over 15 seconds in the middle of the devolatilisation time as indicated by the grey highlighted region in Fig. 6.7. Fifteen, rather than twenty, seconds was used in this section reflecting the longer mixing time for the composition measurement in apparatus in this section compared with the apparatus in Section 6.1.2.

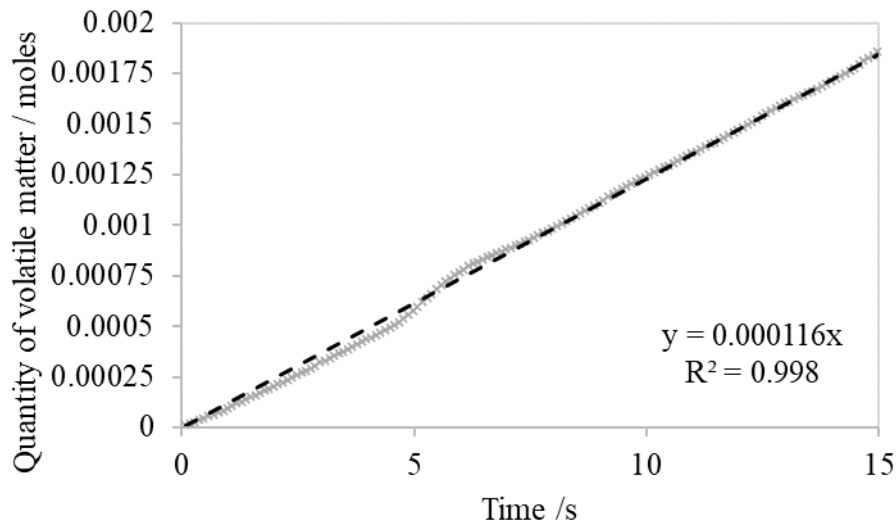


Fig. 6.8. The line of best fit (- -) for middle 15 second portion of devolatilisation for a sphere of beech at $U/U_{mf} = 2.2$, 600°C . Also shown is the equation of the line of best fit forced through the origin, the gradient of which gives the mean molar flowrate of VM for the middle portion of the devolatilisation.

The steady molar flowrate of volatiles away from the beech spheres during the mid-portion of devolatilisation for each experiment is plotted in Fig. 6.9 against the mass of beech in each 10 mm diameter sphere of beech. The rate of production of VM increased for spheres which initially contained a greater mass of wood. The experiments in the large diameter bed, at 600°C , fluidised with air showed similar values of rate of production of VM to the experiments in the small diameter bed, 600°C , fluidised by nitrogen in Section 6.1.1, shown in Fig. 6.7. This similarity indicates that the rate of emission of VM was sufficient to exclude the oxygen in the fluidising air from the particles such that the devolatilisation was independent of the fluidising gas used. The presence of a flame, at the surface of the bed, caused by the combustion of VM in the bed fluidised by air did not significantly alter the value of rate of production of VM compared with that found in the bed fluidised by nitrogen.

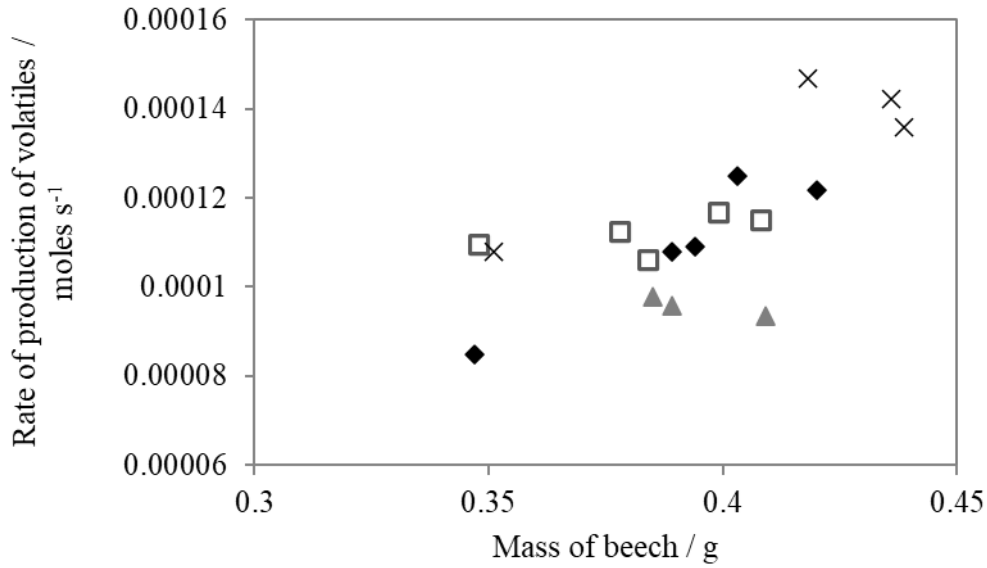


Fig. 6.9. The molar flow rate of VM produced by beech spheres against the mass of beech contained within the sphere at 600°C and $U/U_{mf} = 1.5$ (\blacktriangle), 2.3 (\square) and 3 (\blacklozenge). The experiments from Section 6.1.1 are represented by (x).

To calculate the velocity of the gaseous VM as it was emitted from the surface of the spheres of beech, estimates of the surface area of the beech and the temperature of the gases were required.

In Section 2.3.3 it was found that char particles had a radius of 0.81 times the radius of the original beech particle. As shown in Fig. 6.8, during the mid-portion of devolatilisation the rate of production of VM was found to be approximately constant, therefore it was assumed that the mass, m , and the volume, V , of the beech particles decreased linearly during devolatilisation according to Eqs. (6.13) and (6.14) respectively.

$$0 \leq t \leq t_{devol} \quad m = m_0 \left(1 - \frac{(1 - 0.146)}{t_{devol}} t \right) \quad (6.13)$$

$$0 \leq t \leq t_{devol} \quad V = \frac{4}{3} \pi a_0^3 \left(1 - \frac{(1 - 0.524)}{t_{devol}} t \right) \quad (6.14)$$

where a_0 is the initial radius of the beech sphere, m_0 is the initial mass of the spheres of beech and t_{devol} is the devolatilisation time. Here, the time, t , is measured from the start of devolatilisation. After the devolatilisation time, t_{devol} , the char will start to combust, and the radius and mass of the particle will decrease further such that Eqs. (6.13) to (6.16) are no longer

valid. Equation (6.13) ensures that the mass decreases to 0.146 times the original mass. This was the mean value of mass loss found for beech spheres of 10 mm diameter devolatilising in a fluidised bed at 600°C. The external, nominal surface area was assumed to decrease proportionally to the time of devolatilisation to the power of 2/3 giving Eq. (6.15).

$$0 \leq t \leq t_{devol} \quad A_{surface} = 4\pi a_0^2 \left(1 - \frac{(1 - 0.524)}{t_{devol}} t\right)^{\frac{2}{3}} \quad (6.15)$$

where $A_{surface}$ is the surface area of the devolatilising beech sphere.

The radius was, therefore, assumed to decrease proportionally to the time of devolatilisation to the power of 1/3, giving Eq. (6.16).

$$0 \leq t \leq t_{devol} \quad a = a_0 \left(1 - \frac{(1 - 0.524)}{t_{devol}} t\right)^{\frac{1}{3}} \quad (6.16)$$

The value of 0.524 ensures that the radius is 0.806 times the original radius when $t = t_{devol}$, 0.524 being the cube of 0.806. The devolatilisation time, t_{devol} , was defined as the time at which the two distinct sections of the curves shown in Fig. 6.7, which form straight lines, intersected. The intersection gives the time at which the higher rate of production of CO₂ associated with devolatilisation changed to the more gradual rate of CO₂ produced during the combustion of the char.

The temperature of the VM produced by the spheres of beech influences the molar density of the VM and hence must be known to find the velocity at which the VM is emitted. As the devolatilisation progresses, the particle heats up and so the temperature of the VM will increase through time and approach the temperature of the bed. In this work it has been assumed that the VM leaves the sphere of beech at T_{bed} , such that U_d will be overestimated during the early stages of devolatilisation. The VM was assumed to follow the ideal gas rule and hence, the velocity of the VM emitted by the beech particle was found according to Eq. (6.17).

$$U_d = \frac{\kappa R T_{bed}}{n p A_{surface}} \quad (6.17)$$

where κ is the molar flowrate of CO₂ in the exhaust from the reactor, n , is the mean number of carbon atoms per molecule of VM, p is the pressure of the gas at the surface of the sphere of devolatilising beech, assumed to be atmospheric, and R is the universal gas constant.

The ratio of the velocity of gas emitted from the surface of the particle, U_d , to U_{mf} , was found throughout the devolatilisation process, at 600 and 500°C, and results are shown in Fig. 6.10. Although the envelope of each curve was broadly similar across the conditions investigated, it can be observed that U_d/U_{mf} was slightly higher at 600°C than at 500°C. The velocity ratio fluctuated significantly throughout the course of devolatilisation; however, it is unclear if this is a product of the deconvolution process or if it was caused by an unsteady rate of released of VM as discussed by Volford *et al.* (2021). For the majority of devolatilisation all the spheres of wood emitted gas at a high enough rate to disrupt the formation of a defluidised hood but the velocity ratio for all experiments were far lower in magnitude than those achieved by the sublimating dry ice in Chapter 5.

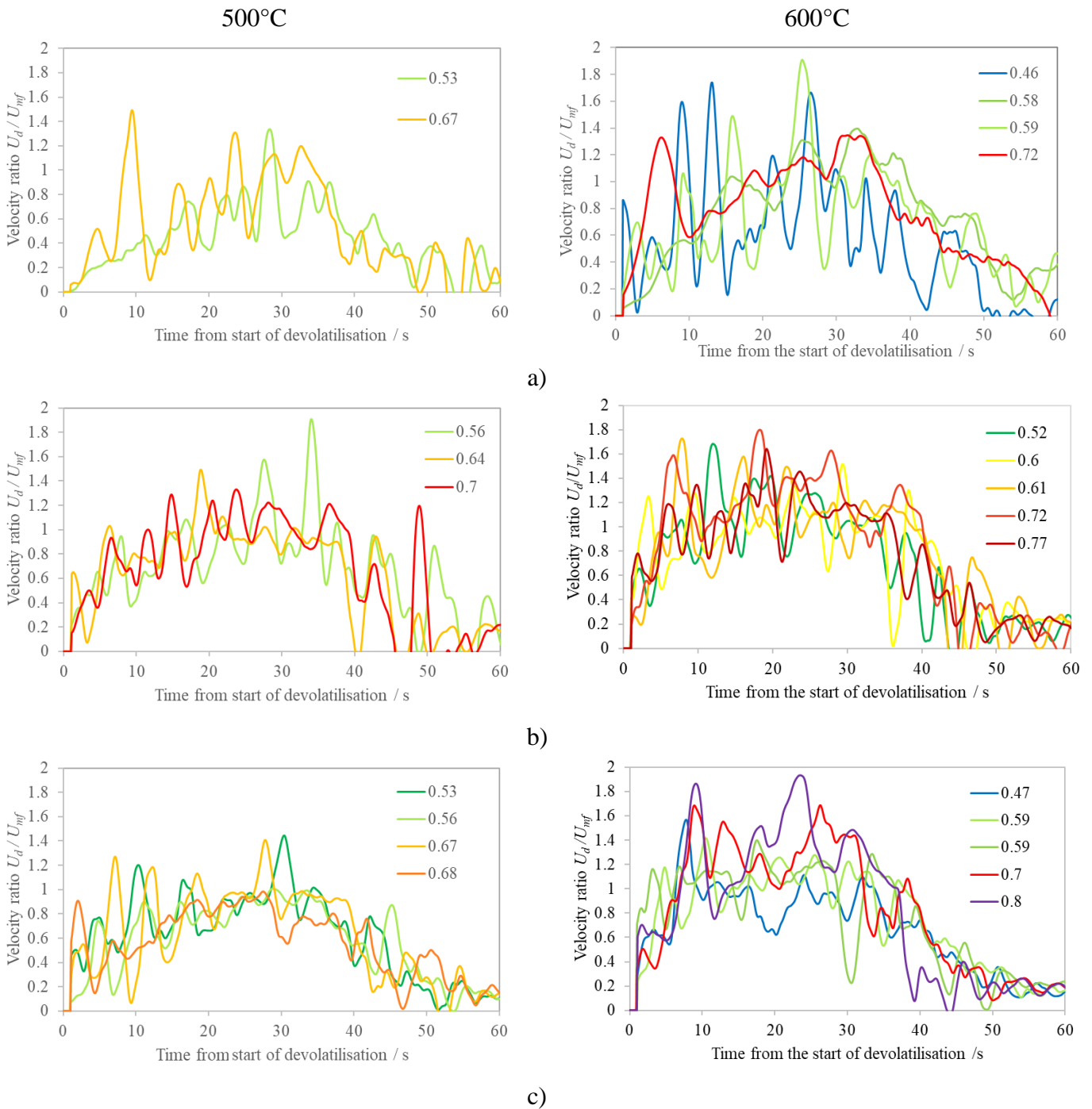


Fig. 6.10. The values of U_d/U_{mf} averaged over 2 seconds during devolatilisation of beech spheres of different density ratios (given in the legends) at 600°C and 500°C at a) $U/U_{mf} \approx 1.3$, b) $U/U_{mf} \approx 2$ and c) $U/U_{mf} \approx 2.7$

The method of measuring the flowrate of the combustion products of the VM and using the mean composition of the VM to determine U_d/U_{mf} was validated by comparing it with the values of U_d/U_{mf} obtained during the experiment developed in Section 6.1. Figure 6.11 shows

the velocity ratio, measured using the pressure drop method described in Section 6.1.1, for the VM emitted by beech spheres. The curves have been smoothed with a moving average over 2 seconds to reduce the noise originating from the pressure measurement.

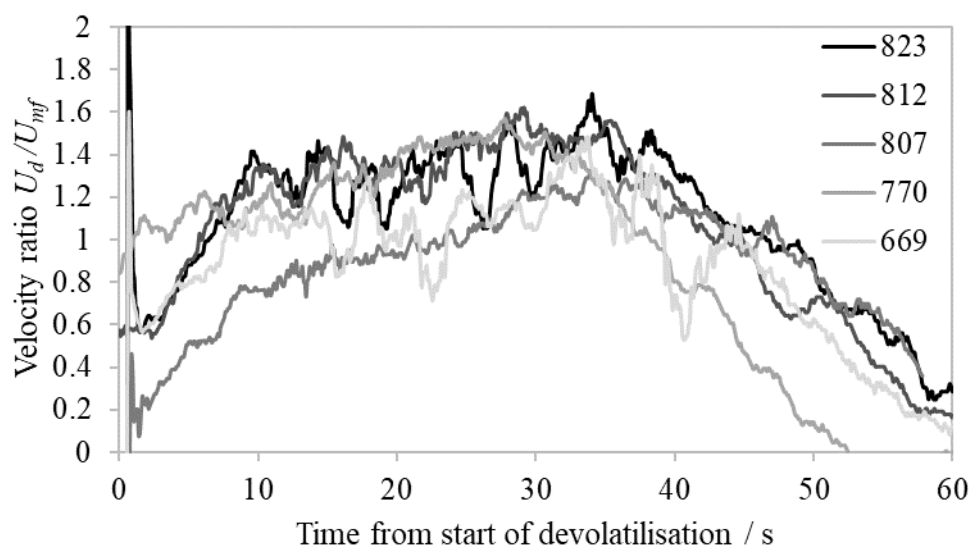


Fig. 6.11. The ratio of radial velocity of VM at the surface of the beech spheres, U_d , over the minimum fluidisation velocity, U_{mf} . The devolatilisation of five spheres of beech in fluidised beds of silica sand at 600°C at $U/U_{mf} = 1.5$ is shown with starting densities of 669, 770, 807, 812 and 823 kg m^{-3} . Dividing the density of the particles by the density of the fluidised medium yields the density ratios of 0.46, 0.53, 0.56, 0.56 and 0.57 respectively for comparison with the results in Fig. 6.10.

Although the values of U/U_{mf} are not identical between experiments in Sections 6.1.1 and 6.2.1 (Fig 6.10 a) and b) are at $U/U_{mf} = 1.3$ and 2 respectively and Fig. 6.11 is at $U/U_{mf} = 1.5$), the curves shown, calculated using the two different methods, have adequate similarity in shape and amplitude to justify the indirect approach to calculating the molar flowrate of VM described in Section 6.2.1.

The curves in both Fig. 6.10 and Fig 6.11 show that U_d stayed largely around the value of U_{mf} ; however, given the fluctuations in the value of U_d/U_{mf} it is difficult to ascertain if the velocity ratio was a function of the density ratio. Therefore, a mean value for the velocity ratio over the mid-portion of the devolatilisation time was taken such that Fig. 6.10 was collapsed into one simpler graph for each temperature as shown in Fig. 6.12.

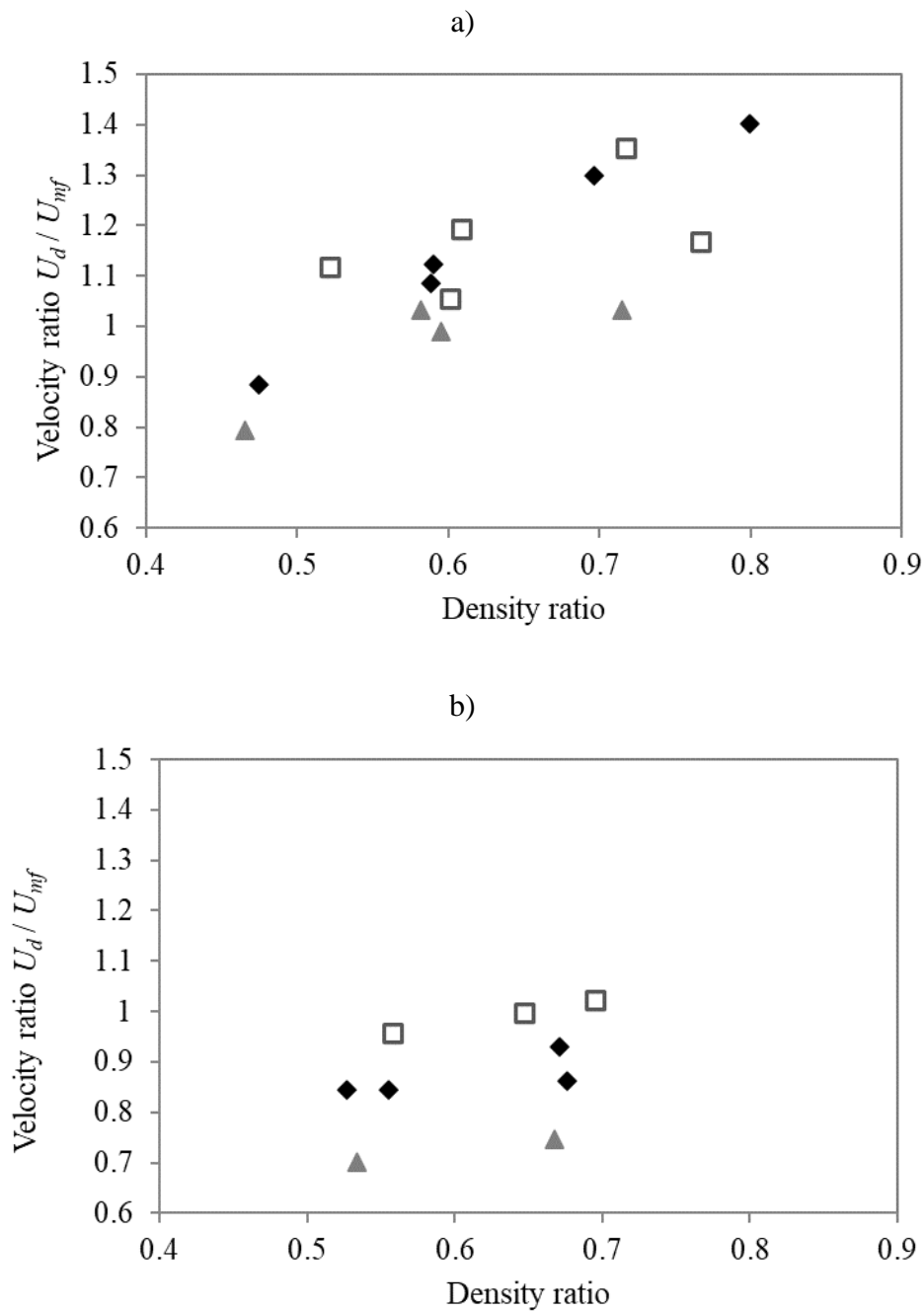


Fig. 6.12. The values of U_d/U_{mf} during devolatilisation of beech spheres at a) 600°C and b) 500°C at $U/U_{mf} \approx 1.3$ (\blacktriangle), 2 (\square) and 2.7 (\blacklozenge).

Figure 6.12 shows that at 600°C the value of U_d/U_{mf} attained by the spheres of beech during the mid-portion of the devolatilisation time was higher than that obtained by spheres of beech at 500°C. Figure 6.12 may also indicate that the experiments carried out at a lower velocity of the fluidising gas, $U/U_{mf} \approx 1.3$, had slightly lower values of U_d/U_{mf} than those carried out at

$U/U_{mf} \approx 2$ and 2.7. The external heat transfer coefficient between a bed of sand and a 6 mm diameter sphere of graphite was found to increase sharply when U/U_{mf} was increased above unity in an experiment carried out by Scott *et al.* (2004). The heat transfer coefficient was found to continue to increase in this case from around $250 \text{ W m}^{-2} \text{ K}^{-1}$ at $U/U_{mf} \approx 1$ to around $350 \text{ W m}^{-2} \text{ K}^{-1}$ at $U/U_{mf} \approx 2$. Such an increase in the external heat transfer coefficient might be responsible for the increased rate of emission of VM.

The value of U_d/U_{mf} possibly increases as the density ratio increases, an effect which appears more pronounced in the experiments at 600°C than those at 500°C . However, the results given in Fig. 6.12 are insufficient to draw a firm conclusion on this.

According to the theory developed in Section 3.2, all the values of the velocity ratio, U_d/U_{mf} , measured for the experiments with beech in the bed, fluidised by air, were sufficient to ensure a defluidised hood could not form. The lack of a defluidised hood would increase the buoyancy of the spheres of beech, deep within the bed compared to inert spheres. However, as discussed in Section 3.3, if the beech spheres are close to the surface a fluidised cap of particles can form which may serve to decrease the buoyancy of spheres of beech during their devolatilisation, compared to inert spheres.

The next section describes how the dimensionless draught of the spheres of beech was measured simultaneously with the experiment described in this section and how the potential correlation among U_d/U_{mf} , the draught and the density ratio was investigated.

6.3 Measurement of the draught of freely floating beech spheres

Yates *et al.* (2002) describe the use of X-ray analysis for studying fluidisation. From the X-ray attenuation the voidage of the bed can be measured and the size and velocity of rising bubbles can readily be determined. In this work the X-ray images are used to track the position of spheres of beech relative to the surface of a fluidised bed. Particles of biomass, however, are not distinguishable in the X-ray images from the bed particles so, the spheres of beech each had a chunk of lead added to them. The lead allowed the position of the beech sphere to be located inside the fluidised bed using X-ray imaging while the beech devolatilised. The mass

of lead added to each sphere was chosen to achieve a range of different densities of spheres of beech.

The images recorded during devolatilisation were analysed according to the process described in Section 2.11. As the bed temperature was far above the melting temperature of the lead, it was assumed that the lead melted soon after the particle was introduced to the bed. Figure 2.13, from Section 2.6.3, shows that the centre of an undrilled sphere of beech, introduced into a fluidised bed of sand at 600°C reached the melting temperature of lead (327.5°C) within 30 s. The pieces of lead inserted into the spheres of beech were exposed at one end to the hot gases of the fluidised bed. Lead has a smaller heat capacity than the beech so the pieces of lead must have melted before the middle of each beech sphere had reached 327.5°C. The capillary length of liquid lead in air at 600°C is approximately 2 mm, the same as the diameter of the hole drilled in the beech spheres. It was, therefore, assumed that the lead formed a liquid droplet inside the hole in the beech, held there by its surface tension. The position of the bottom of the ball of lead, relative to the bottom of the beech particle was found by assuming that the lead was drawn in as far as possible into the hole within the beech particle and did not move during the experiment, as diagrammatically presented in Fig. 6.13.

The results are divided into two sections, firstly, in Section 6.3.1, the floating behaviour of inert particles is compared with that of gas-emitting particles in a set of experiments at 600°C. In Section 6.3.2, a second set of experiments is investigated where, in addition to the depth of the beech particles, the gas composition measurements discussed in detail in Section 6.2, were made simultaneously.

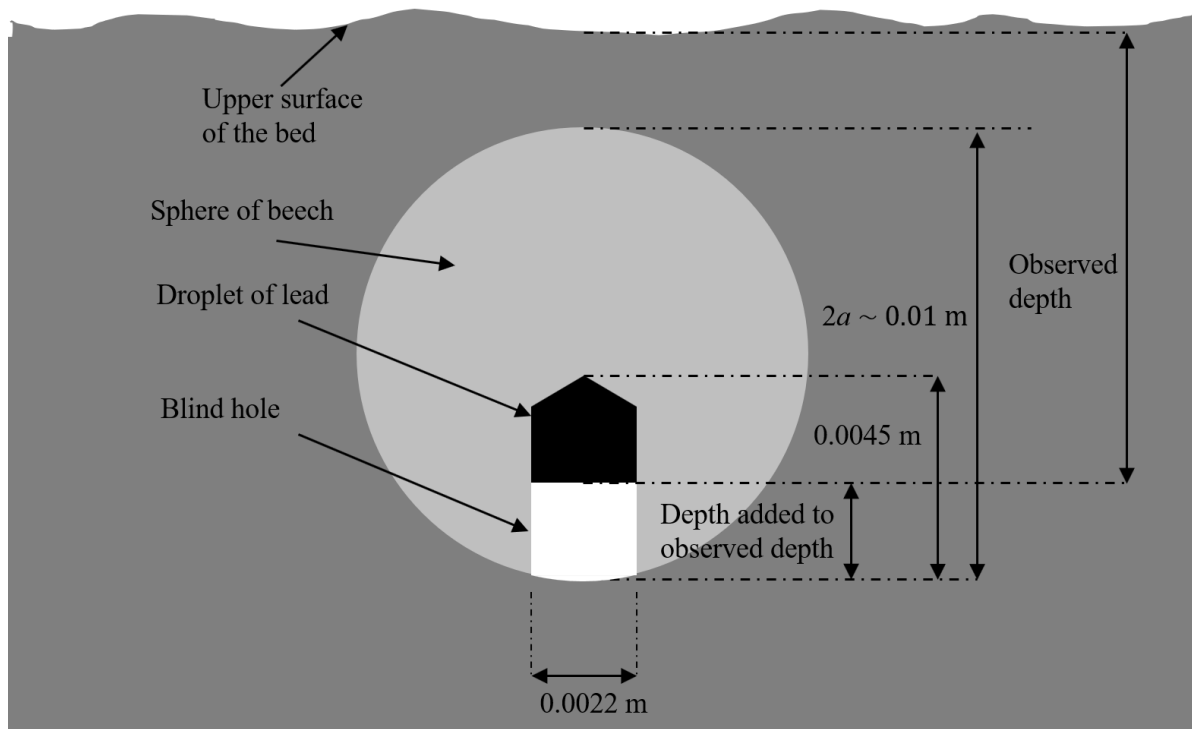


Fig. 6.13. Schematic diagram of a sphere of beech containing a droplet of lead, which is held within a blind hole in the beech by surface tension.

6.3.1 Comparing the floating behaviour of inert particles at ambient temperature with particles emitting gas at 600°C

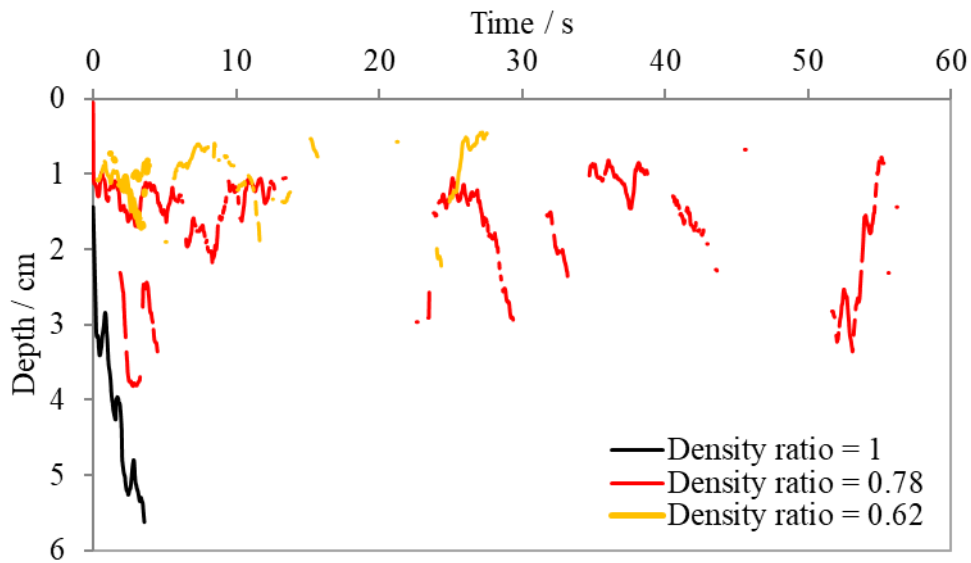
When added to a fluidised bed at room temperature, the beech spheres remained inert. According to the theory presented in Section 3.2, they should bear a defluidised hood and so float at a depth slightly lower than the dotted line in Fig. 3.19, owing to the bubbles of fluidising gas which form at the underside of the solid inert spheres, as discussed in Section 4.4.3.

Here, in each experiment, a sphere of beech, prepared with a piece of lead inside it, was dropped into the fluidised bed at room temperature and the X-ray machine was immediately activated. X-ray images were recorded for around 60 s at a time at 36 frames s^{-1} . The position of the bottom of the small lump of lead was located in each image and the vertical distance between it and the surface of the bed was calculated as shown by the observed depth, defined in Fig. 6.13.

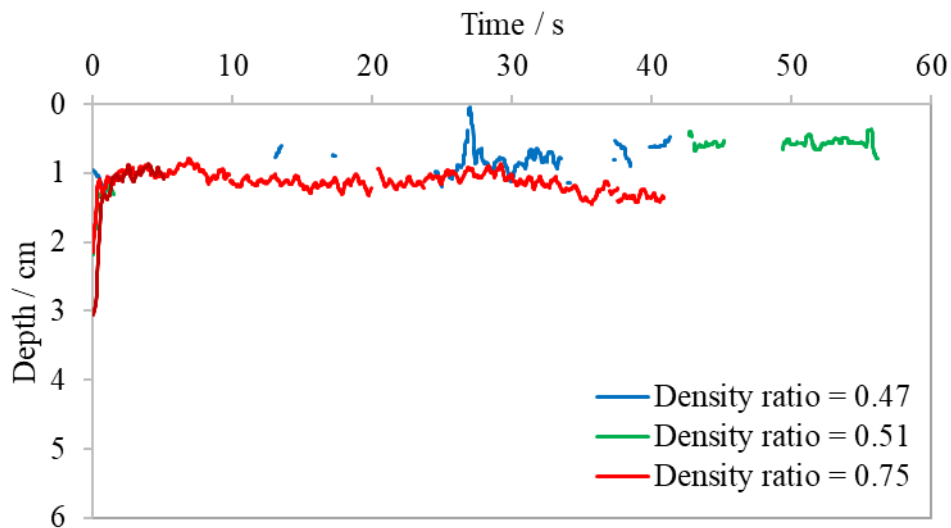
The depths of three beech spheres with density ratios of 1.00, 0.78, and 0.62, in a bed of silica sand fluidised by air at room temperature at $U/U_{mf}=1.5$, are shown in Fig. 6.14 a).

It can be seen that the sphere of beech with a density ratio of 1 sank down to the distributor and never re-surfaced; however, on its journey downwards short upward steps were made, which were induced by rising exogenous bubbles, when the particle was briefly entrained in their wake. The sphere with a density ratio of 0.78 rose and fell from 0.7 to 4 cm deep in the bed. Its stepwise journeys up and down through the bed material indicate a strong influence of the exogenous bubbles. The particle with a density ratio of 0.62 remained largely between 0.5 and 1.5 cm below the surface of the bed. The average depth through time of the particles with density ratio of 0.78 and 0.62 was 1.5 and 1.0 cm, respectively. Expressed as dimensionless draught, defined in Section 3.1, the values were $\delta = 3.0$ and 2.0, respectively, with a standard deviation in δ of 1.1 and 0.95.

The draughts of spheres of beech in a hot fluidised bed were monitored using X-ray imaging as before. The positions of the particles relative to the position of the surface of the bed are shown in Fig. 6.14 b), recorded in a bed, fluidised by air, at 600°C at $U/U_{mf} \approx 1.5$ beech spheres in the fluidised bed at 600°C did not move up and down in the bed as far as the spheres recorded at room temperature. Referring to Fig. 6.14 a), the sphere with a density ratio of 0.78 in the fluidised bed at room temperature fell and rose between 0.7 and 4 cm whereas the sphere with a similar density ratio of 0.75 in the bed at 600°C maintained a less varied position around 1 cm below the bed surface.



a) Room temperature



b) 600°C

Fig. 6.14. The depth of beech spheres in a fluidised bed of silica sand at a) room temperature and b) 600°C. The bed was fluidised by air at $U/U_{mf} = 1.5$. The data have been smoothed using a moving average extended over 0.4 s.

6.3.2 Experiments at 500 and 600°C

Two further sets of experiments were carried out where both the positions of beech spheres were monitored during their devolatilisation in a fluidised bed at 600 and 500°C, and the gas composition in the freeboard was measured simultaneously (the results of which were presented in Section 6.2). The draughts of the beech spheres throughout the experiments are shown in Fig. 6.15.

Figure 6.15 is plotted in terms of the dimensionless draught, δ , rather than depth in cm. To do so, the radius of the particle through time was estimated, according to Eq. (6.16), which gives a linear decrease in the volume of the particles through time.

As U/U_{mf} increased, the variation in the draught of the particles also increased as shown in Fig. 6.15 where the traces of particle position become increasingly noisy as U/U_{mf} increases. However, even at $U/U_{mf} \approx 2.9$, the particles which were devolatilising still travelled vertically within the bed far less than inert particles in a bed at $U/U_{mf} \approx 1.5$, shown in Fig. 6.14 a). The inert particles dealt with in Section 6.3.1, descended deeper into the bed than those emitting gas, which appear, from Fig. 6.15, to maintain a more stable vertical position within the bed.

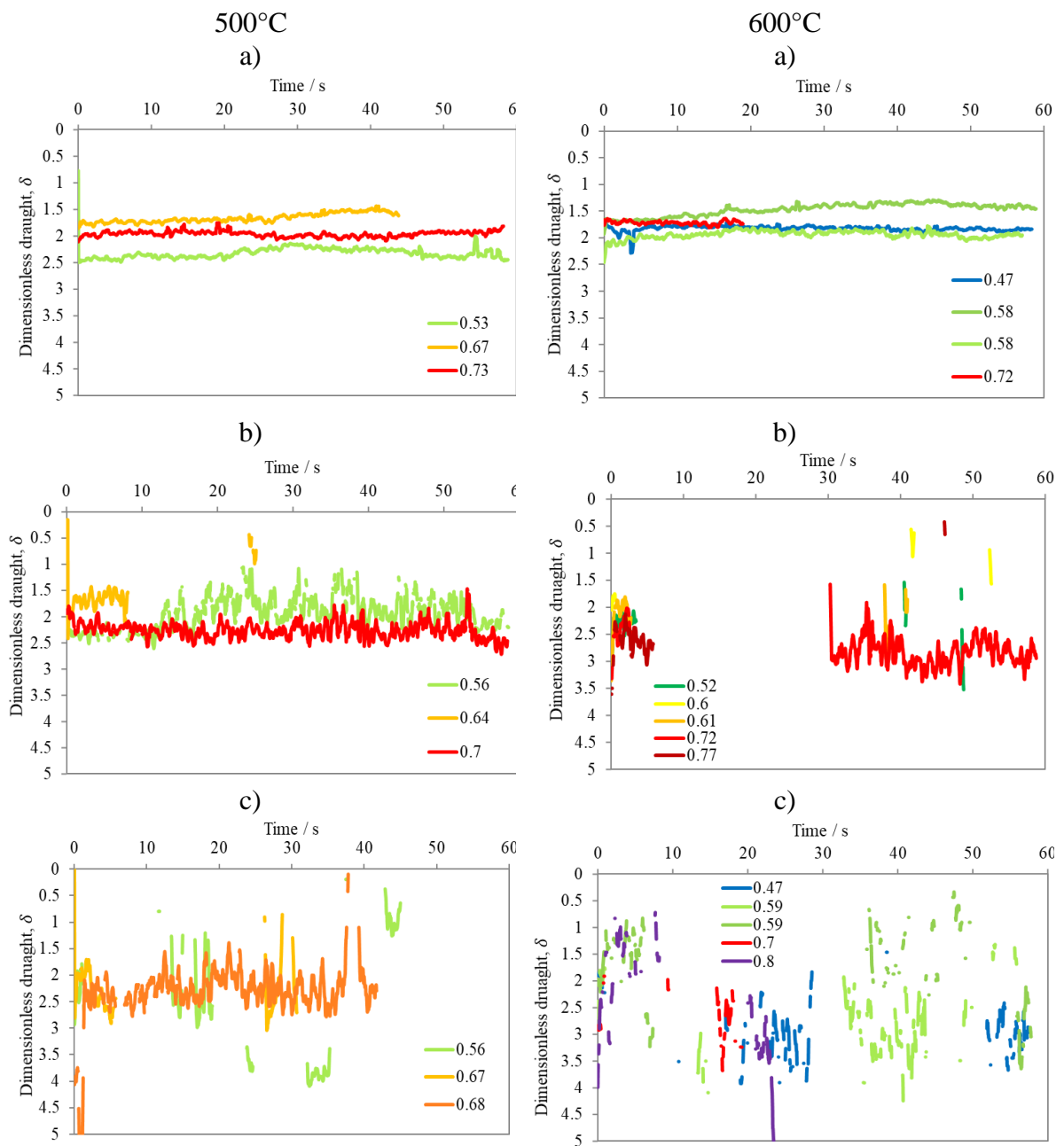


Fig. 6.15. The dimensionless draught, δ , of beech particles in a bed of sand particles fluidised by air at 500 and 600°C at $U/U_{mf} \approx$ a) 1.3, b) 2 and c) 2.9. The data have been smoothed over 0.4 s using a moving average. The density ratio of the beech spheres at the start of each experiment are given in the legends.

As particles of biomass lose both mass and volume during devolatilisation, the density ratio of biomass spheres changes with time. Consequently, the density of the beech spheres was estimated throughout devolatilisation by assuming, as before, that the loss of mass through time from the beech spheres was approximately linear and that the mass of lead within the spheres of beech remained constant. Therefore, the density of a sphere at time, t , was calculated as:

$$0 \leq t \leq t_{devol} \quad \rho_{sphere} = \frac{m_{lead} + m_0 \left(1 - \frac{(1 - 0.85)t}{t_{devol}}\right)}{\frac{4}{3}\pi a_0^3 \left(1 - \frac{(1 - 0.524)t}{t_{devol}}\right)} \quad (6.19)$$

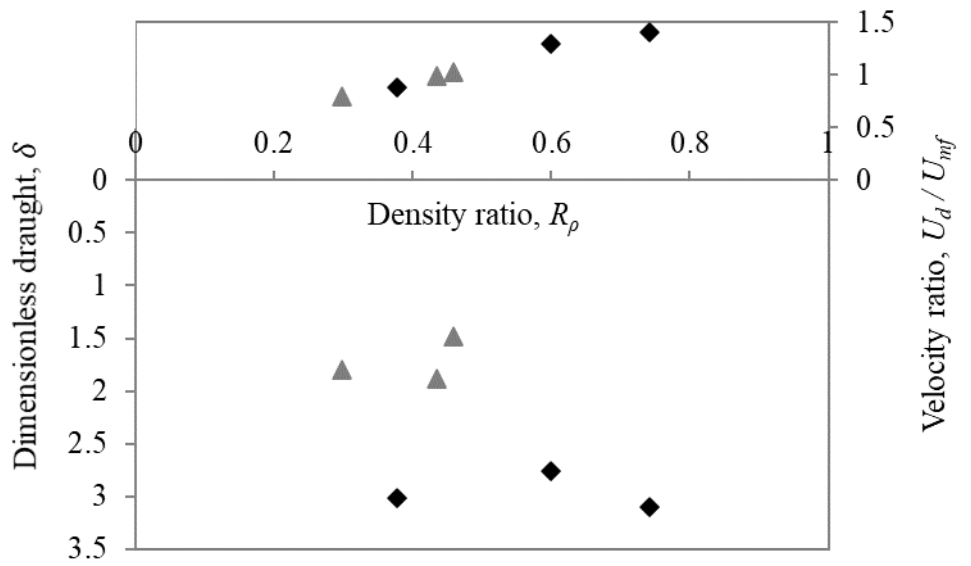
where m_{lead} is the mass of lead inserted into the beech sphere at the start of the experiment, m_0 is the mass of the sphere of beech at the start of the experiment and a_0 is the radius of the sphere of beech at the start of the experiment. The density ratio R_ρ was then found throughout the experiments according to Eq. (6.20).

$$R_\rho = \frac{\rho_{sphere}}{\rho_p(1 - \varepsilon_{mf})} \quad (6.20)$$

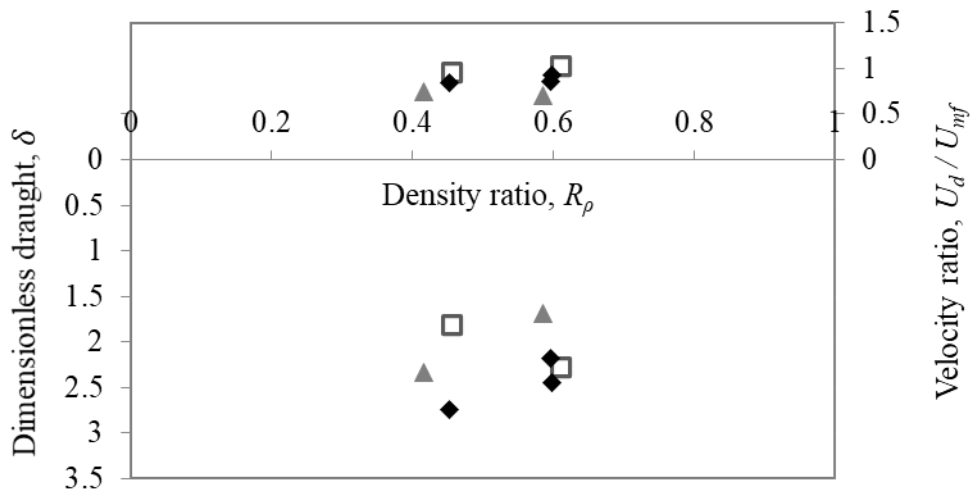
where the denominator represents the density of the emulsion phase in the bed.

The mean values of the density ratio, R_ρ , the velocity ratio, U_d/U_{mf} , and the dimensionless draught of the beech spheres, δ , were calculated over the available data points for the mid portion of devolatilisation (from $\frac{t_{devol}}{3}$ to $\frac{t_{devol}}{3} + 15$ s) and are shown in Fig. 6.16.

Unlike the experiments at room temperature, with inert particles, there is no clear trend between the density ratio and the draught of a sphere of beech that produces gas. There is also little evidence to suggest that the draught of the sphere was proportional to the rate of emission of gas from the sphere.



a) 600°C



b) 500°C

Fig. 6.16. Averaged over the mid third of the devolatilisation time, the mean values of the velocity ratio, U_d/U_{mf} , the density ratio, R_ρ , and the dimensionless draught, δ , for spheres of beech devolatilising in fluidised beds of silica sand at a) 600 and b) 500°C at $U/U_{mf} \approx 1.3$ (▲), 2 (□) and 2.7 (◆).

6.3.3 Discussion

Nienow *et al.* (1978) studied the depth to which light “flotsam” particles which had a tendency to remain in the upper region of a fluidised bed of denser and smaller “jetsam” particles could sink before returning to the surface of the bed. Their correlation is given in by Eq. (6.18),

$$H_d = 1.2H(U - U_{mf})^{0.5} \quad (6.18)$$

where H_d is the depth to which a flotsam particle will sink, H is the fluidised bed height. In the experiment shown in Fig. 6.14, H was 0.18 m, U_{mf} was 0.047 m s⁻¹ and U was 0.071 m s⁻¹. Under these conditions, Eq. (6.18) predicts that the flotsam particles should be able to sink only as far as $H_d = 3.2$ cm. With reference to Fig. 6.14, this prediction seems accurate for a sphere with a density ratio of 0.78, which is similar to the density ratio of coal in a bed of fluidised silica sand at room temperature, the situation studied by Nienow *et al.* (1978). The particle with a density ratio of 0.62 in Fig. 6.14, does not sink as low into the bed as the particle with a density ratio of 0.78. Clearly, the distance, H_d , to which a large particle in a bed of smaller ones sinks, is a function of the density as well as the bubbling behaviour in the bed.

The work of Chapters 3 and 4 indicates that H_d is also likely to be a function of U_d/U_{mf} , hence, the next section aims to investigate how U_d/U_{mf} influences the draught of spheres of beech. For the spheres of beech to emit gas, $U_d > 0$, the fluidised bed must be at a temperature at which devolatilisation occurs. For comparison, in Table 6.6, the average depths of the spheres of beech from Fig. 6.15 are shown alongside the predicted depths to which inert “flotsam” particles will sink, predicted by Eq. (6.18) from the correlation of Nienow *et al.* (1978). Table 6.6 shows that the devolatilising beech spheres remain at a far shallower depth than if they were inert and although spheres of beech in beds with higher gas velocity were deeper than those in fluidised beds closer to minimum fluidisation conditions, the increase in depth with U/U_{mf} was less significant than predicted by the model suggested by Nienow *et al.* (1978). This suggests that particles which are emitting gas are less sensitive to becoming buried by passage of exogenous bubbles than inert particles. The difference between the depth to which inert particles become buried and light, gas-emitting particles suggests that the model by Nienow *et al.* (1978) is not an accurate means of estimating the depth to which gas-emitting particles with a density ratio of less than 1, or for a velocity ratio of anything more than ~ 0.1 (beyond this the defluidised hood becomes significantly shorter), circulate and so should not be used in heat transfer models for biomass devolatilising in fluidised beds. The modified heat

transfer model of Agarwal (1991) which was developed in Section 5.5.4, therefore, is unlikely to give accurate predictions of heat transfer to biomass particles as it assumes that they will circulate in a similar fashion to inert particles (as was the case for dry ice particles below a critical bed temperature). Instead, the model should be modified to account for the particle remaining close to the surface of the bed.

Table 6.6. Values of the bed height and the depth to which a flotsam particle will sink, H_d , as given by Eq (6.16) from the correlation of Nienow *et al.* (1978). Also given are the values of H_d for beech particles. As the radius of the particles decreases, the value of δ_{max} increases.

	500°C		600°C	
U/U_{mf}	Nienow <i>et al.</i> (1978) for inert particles	Maximum depth of devolatilising spheres of beech	Nienow <i>et al.</i> (1978) for inert particles	Maximum depth of devolatilising spheres of beech
1.3	$H_d = 0.019$ m	0.009 m	$H_d = 0.018$ m	0.011 m
2	$H_d = 0.038$ m	0.013 m	$H_d = 0.035$ m	0.014 m
2.9	$H_d = 0.057$ m	0.019 m	$H_d = 0.052$ m	0.019 m

The stability of the devolatilising spheres of beech close to the surface of the fluidised bed was anticipated in the work of Chapter 4 where it was postulated that the emission of gas may cause a particle to become more deeply buried if it starts very high up in the bed. For particles very low down in the bed, however, it was found that the emission of gas, and the inherent buoyancy of the particles then causes the particle to be drawn up closer to the surface of the bed. These two counter-acting mechanisms, bringing deep particles up and shallow particles down might result in their coming to rest at a point of equilibrium causing the apparent stability of the beech particles observed here.

To put this work into the context of the work of Chapters 3 and 4, Figs. 3.19 (which shows the position for inert spheres in an incipiently fluidised medium) and 4.16 (which shows the relationship between the velocity ratio and density ratio for particles at three depths) were replotted to include the locations of the beech devolatilisation experiments from this chapter, shown in Figs. 6.17 and 6.18, respectively.

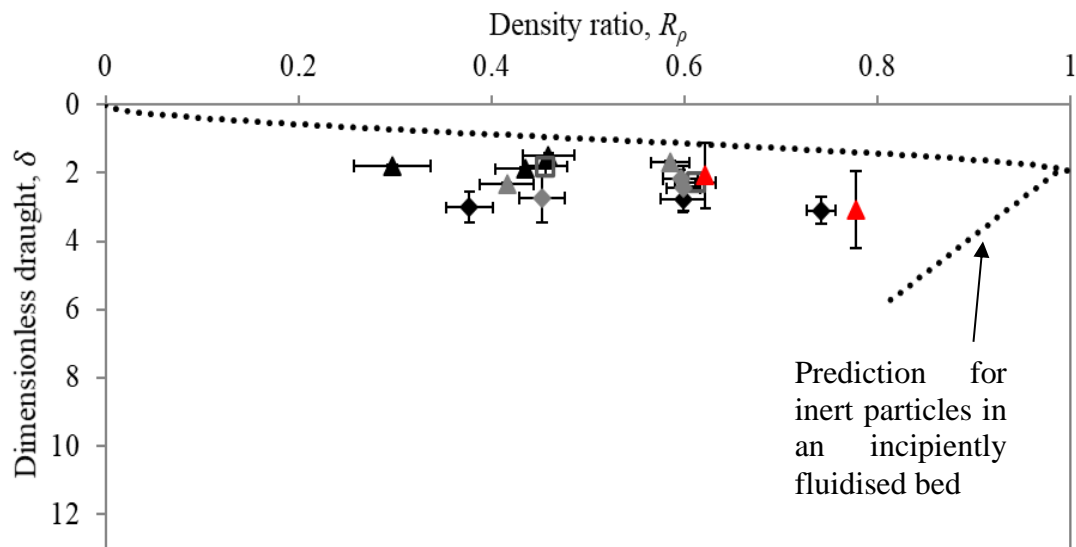


Fig. 6.17. The dimensionless draught, δ , for beech spheres devolatilising at 600°C (black markers), 500°C (grey markers) and room temperature (red markers) at $U/U_{mf} \approx 1.3$ (\blacktriangle/\triangle), 2 (\blacksquare/\square) and 2.7 (\blacklozenge/\lozenge). The error bars represent a single standard deviation. Also shown is the curve for the dynamic equilibrium depth of inert spheres (in the absence of the effect of the bubbles discussed in Section 4.4.2). The depth $\delta = 13$, represents the approximate location of the distributor.

The values of δ for the inert spheres of beech in a fluidised bed at $U/U_{mf} = 1.5$, shown in Fig. 6.17 are larger than predicted by the curve for inert spheres in an incipiently fluidised medium. This shows that δ increases as U/U_{mf} increases and that the exogenous bubbles serve to circulate the inert spheres of beech within a region close to the bed's surface. The spheres of beech which emit gas, shown in Fig. 6.17 also have a higher draught than predicted for an inert sphere in an incipiently fluidised medium and those at higher values of U/U_{mf} have a higher draught than those at lower values of U/U_{mf} . The standard deviation in the vertical position of the spheres of beech which emit gas is far smaller than the standard deviation for inert spheres, however, which suggests that the emission of gas from a sphere has a stabilising effect on the draught of the particle.

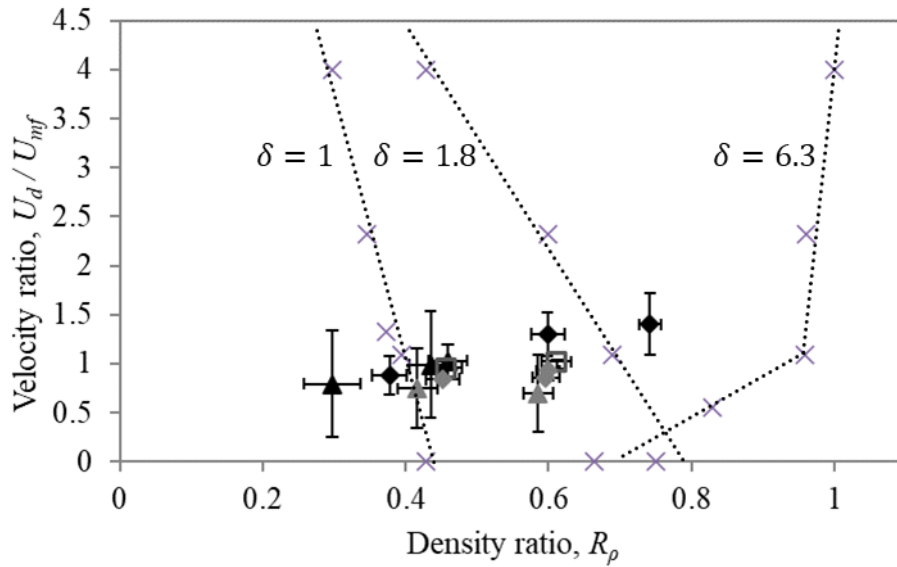


Fig. 6.18. The velocity ratio, U_d/U_{mf} , for beech spheres devolatilising at 600°C (black markers) and 500°C (grey markers) at $U/U_{mf} \approx 1.3$ ($\blacktriangle/\blacktriangle$), 2 (\square/\square) and 2.7 ($\blacklozenge/\blacklozenge$). The error bars represent a single standard deviation. Also shown are the lines of constant depth drawn through the experimental results from Section 4.4.3 (\times).

In Chapter 3, it was found that a defluidised hood is unlikely to form above a sphere which emits gas faster than $U_d/U_{mf} \sim 0.5$: Fig. 6.18 shows this is the case for all the experiments with spheres of beech at 500 and 600°C. As such, when a bubble, which bursts at the surface of the fluidised bed close to the sphere of beech, scatters bed material on top of the sphere of beech, the biomass particle is more likely to return rapidly to its original depth if it is emitting gas, than if it were inert.

The theory of Chapter 4 largely ignored the effect of exogenous bubbles. The shortcut for the fluidising gas, discussed in Section 4.4.3, offered by the presence of the sphere of beech could cause bubbles rising in the bed to be drawn laterally towards the underside of the beech spheres. If more bubbles are drawn to the beech spheres, the time-averaged pressure around the underside of the sphere is likely to decrease, which could explain the increased depth of the beech spheres which emitted gas at high values of U/U_{mf} .

The beech spheres devolatilising at 500°C typically emitted gases at a slightly lower value of U_d/U_{mf} than those at 600°C and all exhibited similar floating behaviour near the surface of the fluidised medium. None sank to the bottom of the bed or made trips deep within the bed, and

rather all stayed close to the surface but at a deeper draught than predicted by the theory of Chapter 4, shown as the lines of constant δ in Fig. 6.18. The lines of constant δ signify the values of the velocity ratio which would be required to maintain the position of a particle were the density ratio to change.

The likelihood of an active particle rising or falling within a fluidised bed is a function of at least three variables: the velocity at which it gives out gas, the density ratio, and the particle's position within the bed. It is likely that the excess fluidisation velocity, U/U_{mf} is also an important variable. However, as U/U_{mf} was not studied in Chapters 3 and 4 it is not considered further. Therefore, the rise or fall criterion for spheres in a fluidised bed is best viewed as a surface in a 3D space, with axes (x,y,z) where x is the velocity ratio, y is the density ratio and z is the draught. Consider, first, inert spheres. Here, the edge of the surface along $x = 0$ should follow the curve shown in Fig. 6.18 derived in Section 3.1.2 for inert spheres. Moving along the x axis, we can consider the surface stretched between the lines of constant dimensionless draught, given by the diagonal lines in Fig. 6.18; this surface, shown in Fig. 6.19, represents the point at which particles are at dynamic equilibrium. In a system free of exogenous bubbles, should a particle be to the right (as drawn in Fig. 6.19) of the "sink or float" criteria it will sink down from that position until it either reaches the "sink or float" criteria, or it reaches the bottom of the bed. Should a particle fall to the left of the surface it will rise until it meets the surface and reaches dynamic equilibrium.

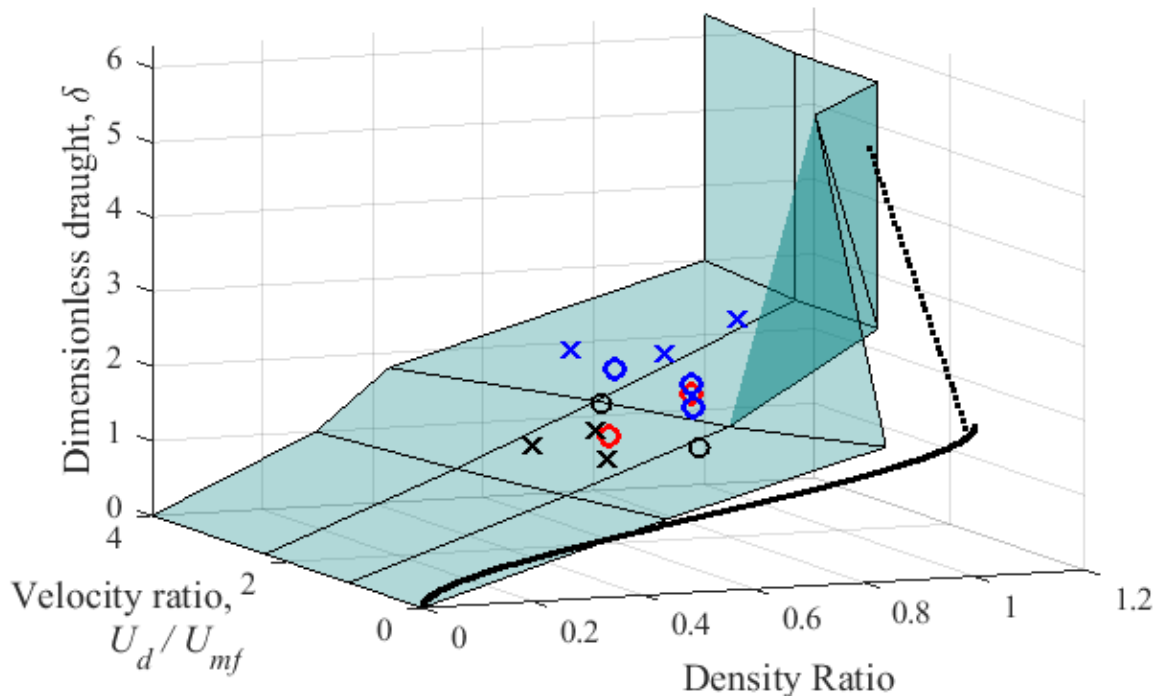


Fig. 6.19. An attempt to characterise a sink or float criterion for spheres which emit gas into fluidised beds. Here, the shaded surface represents the theoretical position for dynamic equilibrium derived using the theory of Chapters 3 and 4. The location of spheres of beech during the mid-portion of their devolatilisation time is given at 600°C (x) and 500 °C (o). Experiments at $U/U_{mf} \approx 1.3$ are shown by black markers, $U/U_{mf} \approx 2$ by red markers, and $U/U_{mf} \approx 2.7$ by blue markers.

Although not clear when compressed into a 2-D graph, the experimental points in Fig. 6.19 are all to the left and above the surface, indicating that, according to the theory of Chapters 3 and 4, if undisturbed, these particles should rise until they reach the position indicated by the shaded surface of Fig. 6.19.

The surface shows that the expected draught of a sphere of beech in an incipiently fluidised medium is largely independent of the velocity ratio if the velocity ratio is greater than 1, as once a defluidised hood can no longer form, the effect of further increasing the velocity of the gases emitted by the sphere on the buoyancy of the sphere diminishes significantly. The effect of the defluidised hood is shown by the spike in the near right hand side of Fig. 6.19. The near vertical part of the surface running along the right-hand side of the graph, which extends right up to the distributor, represents the point beyond which the particle is simply too dense to rise to the surface irrespective of the existence or otherwise of a defluidised hood.

To Fig. 6.19 the location of the dry ice spheres from Chapter 5 can be added. These had a density ratio of around 1.04. Values of the velocity ratio measured in the experiments varied from 0 to around 8 so the “sink or float” criteria surface was extrapolated to higher U_d/U_{mf} values, as shown shaded in red in Fig. 6.20.

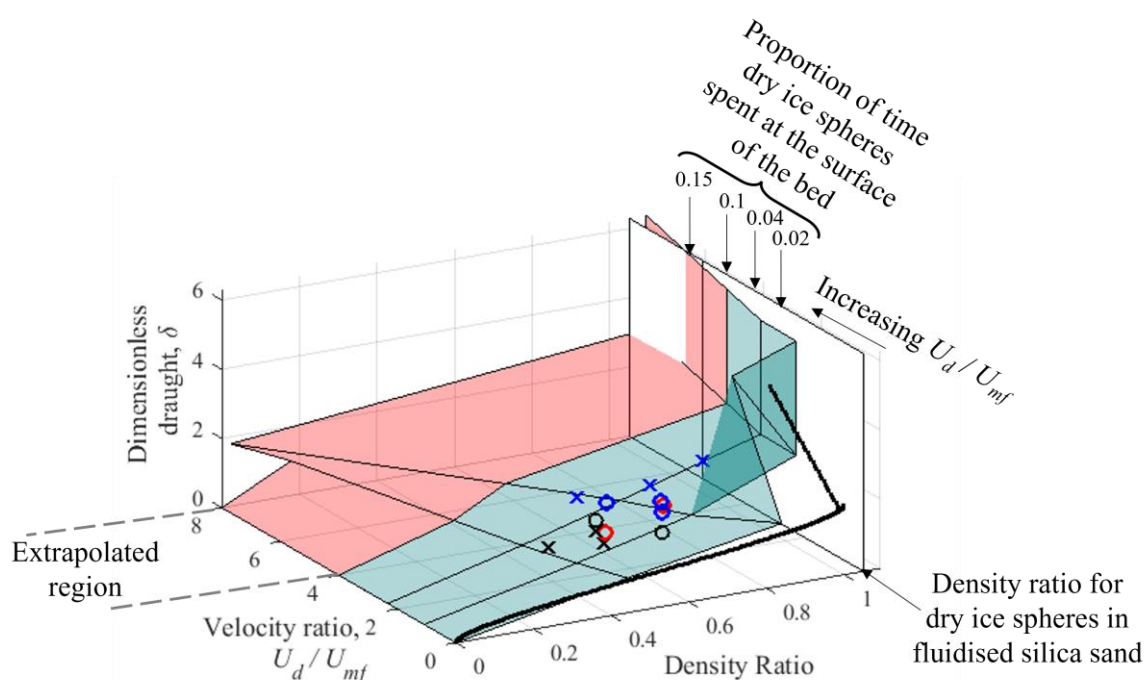


Fig. 6.20. The shaded surface represents the theoretical position for dynamic equilibrium derived using the theory of Chapters 3 and 4. The red portion shows the theory from Chapters 3 and 4 extrapolated to higher values of U_d/U_{mf} . The plane on which dry ice spheres in beds of silica sand exist is shown in white. The arrows indicate the tendency of the particles to sink or float as observed in the experiments in Chapter 5. Also shown are the locations of spheres of beech during the mid-portion of their devolatilisation time is given at 600°C (x) and 500 °C (o). Experiments at $U/U_{mf} \approx 1.3$ are shown by black markers, $U/U_{mf} \approx 2$ by red markers, and $U/U_{mf} \approx 2.7$ by blue markers.

The dry ice spheres spent a far longer proportion of their time near the surface of the bed close to where the white plane shown in Fig. 6.20, which represents dry ice in silica sand, intersects with the extrapolated “sink or float” criterion surface from Chapters 3 and 4.

The surface shown in Fig. 6.19 maps the “sink or float” criteria for any large sphere, which emits gas in an incipiently fluidised bed of smaller particles. Where U/U_{mf} is greater than 1, the spheres will, as in the case of the beech particles, have an average depth slightly deeper than

predicted, tending towards the predicted depth at high values of U_d/U_{mf} . The chart could prove useful for designing fluidised bed processes, providing information about combinations of fuel and bed particles that can minimise the accumulation of fuel particles at the surface of the fluidised bed.

By making the crude estimation that values of U_d/U_{mf} attained by different fuels are proportional to the VM content, a quick exploration of the chart can be made for other fuels. For example, a sphere of bituminous coal with 27 wt% VM and a density of 1300 kg m^{-3} may attain a maximum U_d/U_{mf} of around 0.3 at 600°C and have a density ratio of 0.91, if in a fluidised bed of silica sand. Such a particle, regardless of its draught will fall to the right of the surface in Fig. 6.18 and will sink into the bed.

In experiments at room temperature, Agu *et al.* (2019) loaded a mixture of woodchips and sand, density ratio = 0.3, into a bed and fluidised the mixture. They found that the woodchips tended to move towards the surface of the bed and segregate there. They also performed the experiment with wood pellets and sand, density ratio 0.8, and found that the pellets had a tendency to sink downwards. At 600°C , however, both the woodchips and the wood pellets will devolatilise, and Fig. 6.19 would suggest that both are likely to rise to the surface of the bed, regardless of the depth at which they start which emphasises the importance of carrying out experiments under realistic conditions. The surface shown in Fig. 6.19 can be used as a guide for the design and operation of a fluidised bed reactor handling solid fuels so that devolatilising biomass particles remain deep beneath the surface of the bed. These suggestions have been divided into two sections based on the density ratio.

Particles with a density ratio greater than 0.7 to 1.0.

The velocity ratio, U_d/U_{mf} , would have to remain much lower than 1 for particles with a density ratio greater than 0.7 not to segregate. Such a condition could be met by using torrefied biomass. Torrefaction would increase the density ratio and decrease the volatile content of the fuel. The velocity ratio could be kept low by using a low bed temperature such that the rate of emission of VM and the resulting U_d were low while U_{mf} were large, assured by using large bed particles. A high value of U/U_{mf} would also aid in ensuring the biomass particles were well distributed in the bed.

Particles with a density ratio less than 0.7

For biomass particles in fluidised beds with a density ratio less than ~ 0.7 , the avoidance of segregation where the particles are trapped at the surface of the bed is very unlikely. If U/U_{mf} were high, the particles would be positioned slightly lower within the bed, but still close to the surface, hence, the emitted VM would have little chance to contact the bed material.

Caution must be taken with these recommendations, however, as the experiments within this Chapter and Chapter 5 have explored only a small volume of the space shown in Fig. 6.20 and more experiments are required to refine and validate the “sink or float” criteria beyond those portions of the 3-D space shown in Fig. 6.20 occupied by dry ice and spheres of beech in beds of fluidised sand.

Most biomass particle and fluidised bed material combinations are likely to have a density ratio < 0.7 and so it is unlikely that segregation can be avoided under most practicable fluidising conditions.

6.4 Conclusions

The complicated mixture of VM emitted by devolatilising spheres of biomass can be represented by a single species for the purposes of estimating the velocity of the VM as it leaves the surface of the biomass particles. For spheres of beech, devolatilising in a fluidised bed at 600°C the representative species was found to be $\text{C}_{2.0}\text{H}_{4.0}\text{O}_{2.0}$. Using this it was found that the velocity of gas emitted by beech spheres at 600°C was sufficient to disrupt the formation of defluidised hoods above the spheres and to support the formation of a fluidised cap of bed particles above the spheres.

When gas was emitted by beech spheres, they were found to remain at a stable depth just beneath the surface of the fluidised bed rather than rising and falling a certain way into the bed, as was the case for inert particles. This indicated that defluidised hoods did not form above the beech particles as indicated by the theory of Chapter 3. The possibility of a floating position just beneath, rather than on the surface, of the bed was also suggested in Chapters 3 and 4.

The experiments indicated that the beech spheres came to dynamic equilibrium slightly lower down within the bed than predicted by the theory of Chapters 3 and 4. The attraction of rising

exogenous bubbles to the undersides of the beech particles was postulated as the cause of this as the spheres of beech in beds at higher superficial fluidising velocities were found to have larger draught.

Segregation of biomass particles in fluidised beds can be avoided but a high density ratio, low U_d/U_{mf} and high U/U_{mf} is required. Additionally, the work presented here demonstrates that even particles with a high density ratio are liable to become trapped at the bed surface if U_d/U_{mf} is sufficiently high.

For particles of raw biomass in fluidised beds it is unlikely that operating conditions or bed material could be contrived to avoid the segregation behaviour. However, by decreasing the volatile content and increasing the density of the fuel, for example through torrefaction, such that the criterion for sinking developed in Section 6.3.3 is met throughout devolatilisation, the segregation can be prevented.

In chemical looping combustion the density of the bed materials is typically quite high; for example 5170 kg m^{-3} for magnetite (Lu *et al.* 2018). To avoid segregation of biomass fuels in beds of these materials, the fuel needs to have a particle density greater than 1954 kg m^{-3} and a low value of U_d/U_{mf} . It is unlikely that such a density could be achieved even through torrefaction of the biomass fuel where the maximum density found in the literature was 1440 kg m^{-3} (Köser *et al.*, 1982) unless most of the volatile content of the fuel is removed during torrefaction.

Chapter 7 Conclusions

The work presented has focused on investigating the segregation of particles of a solid fuel in beds fluidised by a gas. It deals with systems in which fuel particles are substantially larger than the inert particles composing the fluidised bed itself and where the initial particle density of the fuel differs from that of the fluidised bed particles. Fuels with a high proportion of volatile matter (VM) were of particular interest. Previous work on segregation has tended to fall into one of two camps. In the first, it has been assumed that the segregation characteristics of fuel particles are independent of whether or not the fuel particle emits gas. The second has taken the position that particles which emit gas segregate solely under the action of bubbles thus produced. The work in this thesis was undertaken to rationalise the interaction between particles which emit gas and the fluidised bed.

In Chapter 3, the theory of defluidised hoods, as investigated by Rees (2005) and others, was extended to include situations where the fuel particles that are covered by a hood are close to the surface of the bed. Here, the “hood” refers to a burden of defluidised bed particles deposited on the upper surface of a fuel particle, thus altering the combined density of the hood and the particle. By assuming the defluidised hood cannot extend above the level of the top surface of the fluidised bed, a correlation was established experimentally for the buoyancy of inert spheres as a function of density ratio; this compared favourably with work by Rao and Muller (2013) who measured the force on submerged objects close to the surface of the fluidised bed. The density ratio, R_ρ , was defined as the ratio of the densities of the gas-emitting particle and the emulsion phase of the fluidised bed. The defluidised hood, although, in fact, consisting of several regions with distinct voidages and patterns of particle circulation, was found to be best described by a parallel-sided region of defluidised bed particles of height 2.4 times the diameter of the sphere on which it rests. If submerged deeply enough in the bed, fuel particles with a density ratio between 0.7 and 1, can sink down lower into the bed under the weight of the defluidised hood that forms.

The work on defluidised hoods was extended by investigating the effect of the rate of emission of gas from a sphere on the stability and overall envelope of the defluidised hood produced. The length of the hood was found to decrease as the superficial radial velocity of gas emitted

by the sphere at its periphery, U_d , increased. The theory developed by Mamuro and Hattori (1968) for modelling maximum spoutable bed height, was modified and found to predict the point at which the defluidised hood became entirely fluidised. Once U_d was greater than around $0.5 \times$ the minimum fluidisation velocity, U_{mf} , the defluidised hood had become entirely fluidised. To link the behaviour of the fluidised bed particles with the rate of emission of gas, the velocity ratio was defined as U_d/U_{mf} . Once U_d/U_{mf} was sufficiently high, the volume and density of the defluidised hood no longer needed to be taken into account when determining the net buoyancy of the gas-emitting particle. Consequently, when the velocity ratio is high enough, particles with a density ratio of between 0.7 and 1 no longer sink into the bed under the weight of a defluidised hood, because the hood cannot form, and will always rise to the surface.

In a complication of the foregoing picture, the structure of the fluidised bed around a gas-emitting particle was found to be sensitive to the position of the particle relative to the surface of the bed. To describe the position of the particle in the bed the concept of the dimensionless draft, δ , was used where the vertical distance from the base of a particle to the surface of the bed is given by $\delta \times$ the radius of the particle. When δ was between 1.5 and 2.5, it was found that when $U_d/U_{mf} > 0.5$ a stable region, or cap, of fluidised particles could form on top of the gas-emitting particle. It is possible for this cap to protrude above the mean upper surface of the fluidised material in contrast to a defluidised hood, which cannot protrude above the surface of the fluidised bed. Fluidised caps were found to be stable, because the bed particles are constantly delivered to the upper side of the gas-emitting particle by bubbles emerging from its underside, so that the fluidised cap can reform when disturbed. A particle bearing the weight of a fluidised cap is forced slightly deeper into the bed than an equivalent inert particle.

Chapter 4 investigated the hypothesis that the gas emitted by a fuel particle in a fluidised bed might form a pocket of higher pressure in the fluidised material beneath the particle in much the same manner as a droplet of liquid exhibiting Leidenfrost behaviour. Although persuasive, the model developed failed to adhere rigidly to the two-phase theory of fluidisation. It was found experimentally that, rather than emitted gas entering the emulsion phase, and thereby, in theory, increasing locally the voidage within the particulate phase beyond that expected at incipient fluidisation, all the gas emitted by the particle formed bubbles instead. Therefore, for these beds of Geldart Group B solids, the two-phase assumption holds rigidly. The bubbles

provide a shortcut for the gas that fluidises the bed material around the particle because the pressure gradient in the bubbles is very much lower than the pressure gradient in the fluidised bed material. Hence, rather than increasing the pressure, the emission of gas from the particle actually reduces the pressure beneath the particle. Indeed, it was found that the pressure distribution in the bed material beneath a gas-emitting particle in a fluidised medium resembled that found beneath a bubble or void in a fluidised medium, as determined by Davidson & Harrison (1963). The way that the gas emitted by a particle interacted with the surrounding bed material was studied using a 2-D bed and particle image velocimetry. It was found that, when a gas-emitting particle was close to the surface of the bed, the bubbles it produced pushed packets of bed particles up and around the gas-emitting particle and erupted at the surface of the bed. The bed particles sank from the surface of the bed and were drawn towards the gas-emitting particle before being again pushed around it and deposited on the surface of the bed once more.

The size and frequency of the bubbles was used to determine the time-averaged pressure distribution around a gas-emitting particle by assuming the pressure drop across a bubble was negligible. The result of the change in the distribution of pressure, as U_d and therefore the number and size of bubbles at the surface of the gas-emitting particle was increased, depended on the depth of the particle within the bed. If at the surface of the bed, the reduction in pressure underneath a gas-emitting particle, causes it to become buried slightly deeper into the bed. If deep within the bed, however, the buoyancy of the particle is increased by the emission of gas increasing the rate at which it rises in the bed material. This is because, at high values of the velocity ratio, U_d/U_{mf} , the bubbles formed were found to sweep away the bed material above the gas-emitting particle more than that beneath it which reduced the pressure around the top of the particle more than that beneath it. This effect is additional to the bubble driven segregation mechanism described by Fiorentio *et al.* (1997a) wherein the gas-emitting particle rises upwards on top of the wake of the bubbles it emits. The reduction in buoyancy when a gas-emitting particle is close to the surface of the bed and the increase in buoyancy when a gas-emitting particle is deep within the bed suggests that a stable depth may exist close to the surface of the bed at around $\delta = 2.5$, at which gas-emitting particles will remain until they have finished emitting gas.

Chapter 5 dealt with gas-emitting spheres which were free to move around in a 3-D bed. Spheres of dry ice were dropped into a hot fluidised bed to attempt to simulate the devolatilisation of fuel particles. Dry ice was chosen because it emits a single, readily-detectable gas. Silica sand was used as a bed material such that the density ratio was slightly greater than 1. The velocity ratio, U_d/U_{mf} , was calculated for each experiment; its value increased as the spheres of dry ice grew smaller by sublimation and mean values of between 1 and 6 were recorded. The velocity ratio increased with temperature of the fluidised bed and, for a given temperature, was higher in beds of small particles than in beds of large ones. For all conditions investigated, the velocity ratio was of sufficient magnitude to ensure that defluidised hoods could not form above the dry ice particles. As anticipated by the theory developed in Chapters 3 and 4, the dry ice particles stayed largely submerged until the velocity ratio increased sufficiently to bring the particles to the surface. Once there, however, the particles were no more buoyant than if they were inert.

The heat transfer coefficient between the dry ice particles and the bed material was also investigated as the devolatilisation of biomass is controlled by both external and internal heat transfer yet little research has explored heat transfer to gas-emitting particles. Not only was the heat transfer coefficient found to be significantly lower than for inert particles, but it decreased as the size of the bed material decreased and as the bed temperature increased. Both these observations are opposite to what is expected for the heat transfer to inert particles. The observation was attributed to a decrease in contact between the surface of the gas-emitting particle and the bed material, as U_d/U_{mf} increased. Consequently, a modified heat transfer model was derived. This accounted for the bubbles at the surface of a gas-emitting particle as well as the rapid emission of gas and the cooling of nearby bed particles. By doing so, the accuracy of the heat transfer coefficient model was greatly improved and a good agreement was found between the model and the experimental results.

In Chapter 6, the position and behaviour of spheres of biomass, as they devolatilised in a hot fluidised bed, was observed in real time using X-radiography. In order to measure the velocity ratio, a novel method for measuring the molar flowrate of VM leaving a biomass particle was developed. The method involved finding the mean molar mass and composition of the VM such that the concentration of combustion products alone could be used to calculate the molar flowrate of the VM. It was found that, for 10 mm diameter spheres of beech introduced to a

fluidised bed at 600°C, (the maximum temperature which could be reached by the fluidised bed equipped with X-radiography equipment) the VM could be represented by the mean species $C_{2.0}H_{4.0}O_{2.0}$. Thus, it was deduced that the velocity ratio produced by the particles of beech, in a bubbling fluidised bed of silica sand at 600°C, rose to a value of around 1 before falling again as devolatilisation ended. This velocity ratio was found to be significantly lower than the velocity ratio observed for dry ice spheres at the same bed temperature, but was sufficiently high to disrupt defluidised hoods forming above the particles and to reduce the pressure around the underside of the beech spheres. When the position of the spheres of beech inside the fluidised bed was observed using X-radiography, it was found that, rather than rising and falling under the bubbling action of the bed or by bubble-driven segregation, the particles of beech remained close to the surface of the bed. Their position vertically within the bed was far more stable than that of inert particles in a similarly bubbling bed. This observation validates the work in Chapter 4, which predicted that such a stable condition close to the surface of the bed could exist.

The overall conclusion from this work is that the simple pictures of segregation published in previous work are insufficient to account for the range of behaviour observed in the present work. This thesis has demonstrated that several important phenomena concerning the structure of the fluidised bed around a gas-emitting particle have an important bearing on the segregation of particles which emit gas or VM. These include:

- changes to the extent of the defluidised hood which can form on top of the floating particle,
- a cap of fluidised particles forming higher than the surface of the fluidised bed, above the gas-emitting particle,
- bubbles forming around the underside of gas-emitting particle causing the pressure there to be lower than it would otherwise have been,
- bubble-driven segregation, as reported by other work.

These changes to the structure of the fluidised material around a gas-emitting particle lift the particle to the surface of the bed, as described elsewhere, but then keep the particles close to the surface of the fluidised bed until devolatilisation has finished.

An analogy to hydrostatic pressure was found to give a better prediction of the buoyancy of inert and gas emitting spheres than the assumption that the stagnation pressure of the fluidising

gas diverting around a particle, elevated further by the gas emitted by said sphere, provides the upthrust to keep the sphere afloat. This implied, and was supported by experimental evidence, that in fact, the fluidising gas does behave as if the sphere is a solid object in its path but rather a void through which to preferentially flow. This is due to the creation of a short cut path for the gas around the sphere, an effect which is further enhanced when the sphere is giving out gas. By Carefully studying the flow of bed particles and of bubbles around a particle under the action of the emission of gas it was possible to accurately predict the heat transfer to gas emitting particles.

The emission of gas was also found to reduce the heat transfer between the gas-emitting particle and the bed material as a consequence of the changes in the structure of the bed material in the vicinity of the large particle. A model was developed which accounted for the following effects:

- The reduction in the gas convective heat transfer caused by the rapid emission of gas from the particle,
- The reduction in the particle convective heat transfer as a consequence of the reduction in contact between the bed material and the gas-emitting particle caused by the bubbles,
- The addition of radiative heat transfer to the model, adjusted to account for the reduction of the temperature of the bed particles close to the gas-emitting particle.

It was shown that the behaviour of fuel particles in fluidised beds is distinct from inert particles, resulting in both the velocity ratio and the density ratio being important in determining the segregation of and heat transfer coefficient to devolatilising particles of biomass in hot fluidised beds.

By closely scrutinising the interaction between gas emitting particles and the fluidised bed material around them, using simple visual observation, the knowledge of their buoyancy, tendency to self-segregate and heat transfer was advanced.

In the context of achieving the combustion of biomass in a chemical looping system, particles of biomass in beds of fluidised oxygen looping material typically fall within a regime where segregation is always likely to occur even if the density of the bed material is greatly reduced or U_{mf} greatly increased. Consequently, there are few means of addressing the unhelpful tendency for biomass particles to accumulate near the surface of a fluidised bed during devolatilisation. To avoid VM being released directly into the freeboard of a fluidised bed

combustor or gasifier, the biomass would need to be prevented from rising to the surface of the bed by structures submerged in the bed or by using a multi-staged bed in which the VM released by biomass particles at the surface of one fluidised bed is converted in a subsequent fluidised bed downstream. Such measures might be the only practicable means of improving the conversion of VM in a bubbling chemical looping combustor handling biomass and, therefore, reducing the cost of operation and improving the viability of the process on an industrial scale.

Chapter 8 Further Work

A number of areas of further work are suggested, either to investigate tentative findings in the present work which could not be explored further or to follow new leads arising from the research. Thus, suggested further work is as follows.

- 1) **Extending research on 2-D beds to 3-D systems.** Substantial investigations were undertaken in Chapters 3 and 4 on 2-D fluidised beds, for ease of visualisation and ease of measuring pressures. As a result, the experiments of 2-D systems have informed the thinking on 3-D systems, later in the dissertation. Ideally, the observations in the 2-D case with a gas-emitting cylinder need to be repeated with gas-emitting spheres in a 3-D bed. A porous sphere fed with air *via* a thin tube, submerged in a cylindrical fluidised bed could be used and a narrow pitot tube used to determine if the pressure distribution near the sphere is comparable with that measured in the 2-D bed. The surface of a sphere submerged in a fluidised bed cannot be visually observed so techniques such as Nuclear Magnetic Resonance (NMR), as used by Pore *et al.* (2015) and Rice (2018) for investigating bubbles in a fluidised medium, and discrete element modelling might be employed to observe and interpret the void fraction near the gas-emitting particle and the extent of defluidised hood.
- 2) **Leidenfrost behaviour.** In Section 4.3, it was found that the two-phase behaviour of aggregatively fluidised beds prevented Leidenfrost behaviour. It was postulated that the behaviour might be possible in (a) particulate fluidised beds *e.g.* Geldart Group B solids at high pressures or (b) solids in which some increase in particulate phase voidage prior to bubbling is possible, *e.g.* Geldart Group A solids. In such cases, the buoyancy of gas-emitting spheres in a smoothly might be much higher than in beds of Group B particles at normal conditions. Therefore, the 2-D bed experiments where the pressure in the bed material close to a cylinder which emits fluid should be repeated in a particulate fluidised bed. Owing to the difficulties of achieving stable gas fluidisation with fine particles at room temperature it may be beneficial to instead carryout the investigation in a liquid fluidised medium. For example, a cylinder emitting liquid into a 2-D bed of glass ballotini at minimum fluidisation might show a local increase in pressure beneath the cylinder as the flow rate of liquid from the cylinder is increased. If the pressure beneath such a cylinder is elevated by the emission of the fluid from the cylinder this would indicate that the theory

of Section 4.2 might hold some predictive capabilities for spheres which emit fluid in particularly fluidised beds.

- 3) **Extending the range of bed materials for experiments with dry ice.** The experiments in Chapter 5 addressed a fuel and bed material pair where the density ratio was around 1.04. By repeating the experiment with spheres of dry ice in beds of γ and α -alumina particles instead of silica sand, the behaviour of spheres of dry ice with density ratios of around 2.0 and 0.72 respectively could be observed. At a density ratio of 0.72, a similar behaviour to the spheres of beech in silica sand from Chapter 6 is expected, albeit with a significantly higher velocity ratio. Additionally, much higher and lower velocity ratios could be investigated on account of the very different values of U_{mf} which the different bed materials would have which would enable a wider exploration of the “sink or float” described in Section 6.3.3.
- 4) **Heat transfer.** Further work is required to extend the heat transfer coefficient model from Section 5.5.4 to fuel particles which do not circulate around the bed but, rather, stay close to the surface of the bed (e.g. devolatilising beech wood in beds of silica sand).

As developed in this dissertation, the heat transfer model assumes that the gas-emitting sphere experiences different rates of heat transfer depending on whether the sphere is ascending or descending through the particulate phase of a fluidised bed or is inside a bubble. Consequently, a number of different particle convective, gas convective and radiative components of heat transfer are required. If a gas-emitting particle maintains a stable position relative to the surface of the bed, such as was observed with combusting biomass, then it is possible that single particle convective, radiative and gas convective heat transfer components will be sufficient. The main modification required would be to the rate of replacement of the packets of bed particles used in the particle convective heat transfer coefficients. Currently, the model assumes that the action of the gas-emitting sphere moving up or down relative to the bed material drives the replacement of packets of bed particles at the surface of the sphere. For spheres which remain stationary within the bed, however, the replacement of packets of bed particles is driven by endogenous bubbles, generated by the sphere itself, as well as passing bed bubbles which pass up and around the sphere. Experimental measurements of the velocity of the packets of bed particles past the gas-emitting cylinder in a 2-D bed, as described in Chapter 4, could be

used to find a correlation with the rate of packet replacement as a function of U_d/U_{mf} and U/U_{mf} and δ .

- 5) **Extending the range of fuels and combustion conditions.** The method of finding the mean composition of volatile matter (VM), developed in Section 6.1 should be used to determine the mean composition of VM from different biomass fuels at a range of temperatures. The information gathered would be invaluable in modelling the devolatilisation of biomass and for further work in larger-scale fluidised beds, as discussed below.

Indeed, the large-scale fluidised bed with X-ray apparatus used in Section 6.3 could be used to determine the behaviour of biomass fuels at higher temperatures than explored in Section 6.3 (600°C), if possible, and different bed materials to inspect a wider range of values of density ratio and velocity ratio. In doing so a more comprehensive map of the sink or float criteria could be built up.

- 6) **General map describing sinking or floating.** Further work is required to improve the resolution of the “sink or float” criteria proposed in Chapter 6. The work from which the criteria was derived was limited to the conditions $U/U_{mf} = 1$, $U_d/U_{mf} \approx 0, 1, 2$ and 4 and $\delta = 1, 1.8$ and 6.2 and a single bed material. For $1 < \delta < 3$, significant changes to the structure of the bed around a gas-emitting particle occur so further experiments in the 2-D bed described in Section 4.4 with a range of bed heights would be beneficial. In doing so, further lines of constant δ could be added to Figs. 4.12 and 6.19. Similarly, the way in which U/U_{mf} , and different bed particle sizes influence the structure of the fluidised material near a gas-emitting particle should be examined.

- 7) **Practicable means of preventing segregation.** It is clear from the conclusions in this dissertation that innovative means must be employed to prevent the segregation of biomass fuel near the surface of fluidised beds during devolatilisation. Some promising work has been undertaken by Li *et al.* (2021) in structures to trap devolatilising particles beneath the surface of the bed and redistribute the VM. The work in this dissertation suggests that if a stable surface could be generated beneath the surface of the bed, for example beneath a gas pocket in a diving bell type structure, the apparent stability of particles and strength and reliability of their tendency to segregate near a fluidised bed surface could be used to trap fuel particles there until devolatilisation had ended. Such a device would enable the mixing

of the VM with the fluidising gas and the redistribution of the volatiles throughout the fluidised material without requiring additional staged fluidised beds and still allowing the char particles to become well distributed throughout the bed after devolatilisation has ceased.

References

- Adánez, J., Abad, A. (2019). Chemical-looping combustion: Status and research needs, *Proceedings of the Combustion Institute*, **37**(4), 4303-4317.
- Agarwal, P. K. and O'Neill, B. K. (1988). Transport phenomena in multi-particle systems-I. Pressure drop and friction factors: unifying the hydraulic-radius and submerged-object approaches. *Chem. Eng. Sci.*, **43**, 2487-2499.
- Agarwal, P.K. (1991). Transport phenomena in multi-particle systems—IV. Heat transfer to a large freely moving particle in gas fluidized bed of smaller particles, *Chem. Eng. Sci.*, **46**, 1115-1127
- Agu, C. E., Tokheim, L., Pfeifer, C., Moldestad, B. (2019). Behaviour of biomass particles in a bubbling fluidized bed: A comparison between wood pellets and wood chips, *Chemical Engineering journal*, **363**, 84-98.
- Amaya-Santos, G., Chari, S., Sebastiani, A., Grimaldi, F., Lettieri, P., Materazzi, M. (2021). Biohydrogen: A lifecycle assessment and comparison with alternative low-carbon production routes in UK, *Journal of Cleaner Production*, **319**, 128886.
- Asegehegn, T. W., Schreiber, M., Krautx, H. J. (2012). Influence of two- and three-dimensional simulation on bubble behavior in gas-solid fluidized beds with and without immersed horizontal tubes. *Powder Technology*, **219**, 9-19.
- Basakov, A. P., Berg, B. V., Vitt, O. K., Filippovsky, N. F., Kirakosyan, V. A., Goldobin, J. M., Maskaev, V. K. (1973). Heat transfer to objects immersed in fluidized beds, *Powder Technology*, **8**, 273-282.
- Bhave, A., Taylor, R. H. S., Fennell, P., Livingston, W. R., Shah, N., Dowell, N. Mac, Dennis, J., Kraft, M., Pourkashanian, M., Insa, M., Jones, J., Burdett, N., Bauen, A., Beal, C., Smallbone, A., Akroyd, J. (2017). Screening and techno-economic assessment of biomass-based power generation with CCS technologies to meet 2050 CO₂ targets, *Applied Energy*, **190**, 481-489.
- Bird, R. B., Stewart, W. R., Lightfoot, E. W. (2002). *Transport Phenomena* (2nd edition), Wiley, 703-706.
- Botterill, J. S. M. (1975). *Fluid-bed heat transfer*, London: Academic Press, 237.
- Bridgwater, A.V. (1994). Catalysis in thermal biomass conversion, *Applied Catalysis A: General*, **116**, 5-47.
- Bronson, B., Preto, F., & Mehrani, P. (2012). Effect of pretreatment on the physical properties of biomass and its relation to fluidized bed gasification. *Environmental Progress & Sustainable Energy*, **31**(3), 335–339.
- Bruni, G., Solimene, R., Marzocchella, A., Salatino, P., Yates, J. G., Lettieri, P., & Fiorentino, M. (2002). Self-segregation of high-volatile fuel particles during devolatilization in a fluidized bed reactor. *Powder Technology*, **128**(1), 11–21.
- Carrigy, M. A. (1970). Experiments on the angles of repose of granular materials. *Sedimentology*, **14**, 147-158
- Chirone, R., Miccio, F., & Scala, F. (2004). On the Relevance of Axial and Transversal Fuel Segregation during the FB Combustion of a Biomass, *Energy & Fuels*, **18**, 1108-1117.
- Cloete, S., Johansen, S. T., Zaabout, A., Annaland, M. S., Gallucci, F., Amini, S. (2015). The effect of frictional pressure, geometry and wall friction on modelling of a pseudo-2D bubbling fluidised bed reactor. *Powder Technology*, **283**, 85-102.

- Cluet, B., Mauviel, G., Rogaume, Y., Authier, O., Delebarre, A. (2015). Segregation of wood particles in a bubbling fluidized bed. *Fuel Processing Technology*, **133**, 80-88
- Cooke, R.B., Goodson, M.J., Hayhurst, A.N. (2003). The combustion of solid wastes as studied in a fluidized bed. *Transactions of the Institution of Chemical Engineers Part B*, **81**, 156-165.
- Cui, H., Grace, J. R. (2007). Fluidization of biomass particles: A review of experimental multiphase flow aspects. *Chemical Engineering Science*, **62**, 45-55.
- Davidson, J. F. & Harrison, D. (1963). *Fluidised Particles*, Cambridge: Cambridge University Press.
- Demirbaş, A. (1997). Calculation of higher heating values of biomass fuels. *Fuel*, **5**, 431-434.
- Dennis, J, S. (2013), “Properties of stationary (bubbling) fluidised beds” in Scala, F. (Ed), *Fluidized bed technologies for near-zero emission combustion and gasification*, Sawston: Woodhead publishing.
- Devi, L., Ptasinski, K. J., Janssen, F. J. J. (2003). A review of the primary measures for tar elimination in biomass gasification processes. *Biomass and Bioenergy*, **24**(2), 125–140.
- Di Blasi, C. (1993). Modelling and simulation of combustion processes of charring and non-charring solid fuels, *Progress in Energy and Combustion Science*, **19**, 71-104.
- Di Felice, R., Foscolo, P. U., Gibilaro, L. G. (1989). The Experimental Determination of the Interaction Force on Spheres Submerges in Liquid Fluidized Beds, *Chem. Eng. Process.*, **25**, 27-34.
- Di Natale, F., Bareshino, P., Nigro, R. (2010). Heat transfer and void fraction profiled around a horizontal cylinder immersed in a bubbling fluidised bed. *International Journal of Heat and Mass Transfer*, **53**, 3525-3532.
- Di Natale, F., Nigro, R. (2013). ‘Heat and mass transfer in fluidized bed combustion and gasification systems’ in Scala, F. (Ed), *Fluidized bed technologies for near-zero emission combustion and gasification*, Sawston: Woodhead Publishers.
- Dudák, M., Novák, V., Kočí, P., Marek, M., Blanco-García, P., Jones, G. (2014). Prediction of diffusivity and conversion of n-decane and CO in coated Pt/ γ -Al₂O₃ catalyst depending on porous layer morphology, *Applied Catalysis B: Environmental*, **150-151**, 446-458.
- Emiola-Sadiq, T., Wang, J., Zhang, L., Dalai, A. (2021). Mixing and segregation of binary mixtures of biomass and silica sand in a fluidized bed. *Particuology*, **58**, 58-73.
- Fajardy, M., Mac Dowell, N. (2017). Can BECCS deliver sustainable and resource efficient negative emissions? *Energy & Environmental Science*, **10**, 1389-1426.
- Fiorentino, M., Marzocchella, A., Salatino, P. (1997a). Segregation of fuel particles and volatile matter during devolatilisation in a fluidized bed reactor – I. Model development. *Chemical Engineering Science*, **52**, 1893 – 1908.
- Fiorentino, M., Marzocchella, A., Salatino, P. (1997b). Segregation of fuel particles and volatile matter during devolatilisation in a fluidized bed reactor – II. Experimental. *Chemical Engineering Science*, **52**, 1909 – 1922.
- Flemmer, R. L. C. and Banks, C. L. (1986). On the drag coefficient of a sphere. *Powder Technology*, **48**, 217-221.
- Fotovat, F., Chaouki, J., Bergthorson, J. (2013). Distribution of large biomass particles in a sand-biomass fluidized bed: Experiments and modeling [sic]. *AIChE Journal*, **60**(3), 869-880.

- Fuss, S., Canadell, J. G., Peters, G. P., Tavoni, M., Andrew, R. M., Ciais, P., Yamagata, Y. (2014). Betting on negative emissions, *Nature Climate Change*, **4**(10), 850–853.
- Galletti, C., Giomo, V., Giorgetti, S., Leoni, P., Tognotti, L. (2016). Biomass furnace for externally fired gas turbine: Development and validation of the numerical model, *Applied Thermal Engineering*, **96**, 372-384.
- Gayán, P., Aba, A., de Diego, L. F., García-Labiano, F., Adánez, J. (2013). Assessment of technological solutions for improving chemical looping combustion of solid fuels with CO₂ capture. *Chemical Engineering Journal*, **233**, 56-69.
- Geldart, D. (1973). Types of fluidization, *Powder Technology*, **7**, 285-292.
- Gelperin, N. I., & Einstein, V. G. (1971). Heat transfer in fluidized beds. In J. F. Davidson, & D. Harrison (Eds.), *Fluidization*. London: Academic Press.
- Glass, D.H., Harrison, D. (1964). Flow patterns near a solid obstacle in a fluidized bed, *Chemical Engineering Science*, **19**, 1001-1002.
- Gomez-Barea, A., Nilsson, S., Barrero, F. V., Campoy, M. (2010). Devolatilization of wood and wastes in fluidized bed, *Fuel Processing Technology*, **91**(11), 1624-1633.
- Grace, J. R. and Lim, C. J. (2013). Properties of circulating fluidized beds (CFB) relevant to combustion and gasification systems, In Scala, F. (Ed), *Fluidized bed technologies for near-zero emission combustion and gasification*, Sawston: Woodhead Publishing Limited.
- Hager, W.R., Schrag, S.D. (1976). Particle circulation downstream from a tube immersed in a fluidized bed, *Chemical Engineering Science*, **31**, 657-659.
- Hoffmann, A.C., Janssen, L.P.B.M., Prins, J. (1993). Particle segregation in fluidised binary mixtures. *Chemical Engineering Science*, **48**, 1583-1592.
- Hu, W. (2015). Development and characterisation of a copper-based oxygen carrier for chemical-looping with oxygen uncoupling (CLOU), PhD Thesis, University of Cambridge, Cambridge.
- Hurskainen, M. & Vainikka, P. (2016). 7 – Technology options for large scale solid-fuel combustion. In: Oakley, J. (Ed), *Fuel Flexible Energy Generation. Solid, Liquid and Gaseous Fuels*. Woodhead Publishing Limited
- IPCC, 2021, Climate Change 2021: The Physical Science Basis. Contribution of Working Group I to the Sixth Assessment Report of the Intergovernmental Panel on Climate Change [Masson-Delmotte, V., P. Zhai, A. Pirani, S.L. Connors, C. Péan, S. Berger, N. Caud, Y. Chen, L. Goldfarb, M.I. Gomis, M. Huang, K. Leitzell, E. Lonnoy, J.B.R. Matthews, T.K. Maycock, T. Waterfield, O. Yelekçi, R. Yu, and B. Zhou (eds.)]. Cambridge University Press. In Press.
- Ismail, A. F., Khulbe, K., Matsuura, T. (2015). *Gas Separation Membranes: Polymeric and Inorganic*, Springer International Publishing, Switzerland
- Keegan, H. J., Weidner, V. R. (1966) Infrared Spectral Reflectance of Frost [Letter to the editor], *Journal of the optical society of America*, **4**, 523-524.
- Kersten, S. R. A., Wang, X., Prins, W., Van Swaaij, W. P. M. (2005). Biomass pyrolysis in a fluidized bed reactor. Part 1: Literature review and model simulations. *Industrial & Engineering Chemistry Research*, **44**(23), 8773-8785.
- Knowlton, T. M. (2013). Fluidized bed reactor design and scale-up. In: Scala, F. (Ed), *Fluidized bed technologies for near-zero emission combustion and gasification*, Sawston: Woodhead Publishing Limited.
- Köser, H. J. K., Schmalstieg, G., Siemers, W. (1982). Densification of water hyacinth - basic data, *FUEL*, **61**, 791-798.
- Kulkarni, A. (1987). Defluidized zone over a horizontally immersed tube in a fluidized bed, *Chemical Engineering Science*, **42**, 1245-1247.

- Kunii, D. and Levenspiel, O. (1969). *Fluidisation Engineering.*, Boston: Butterworth-Heinemann
- Lettieri, P. (1999), A study of the influence of temperature on the flow behaviour of solid materials in a gas fluidised bed, PhD thesis, University of London, UK
- Lettieri, P. & Yates, J. G. (2013), "New Generation X-Ray Imaging for Multiphase Systems" in *The 14th International Conference on Fluidization – From Fundamentals to Products*, ECI Symposium Series.
- Li, C., & Suzuki, K. (2009). Tar property, analysis, reforming mechanism and model for biomass gasification—An overview. *Renewable and Sustainable Energy Reviews*, **13**(3), 594–604.
- Li, X. Lyngfelt, A. Mattisson, T. (2021). An Experimental Study of a Volatiles Distributor for Solid Fuels Chemical-Looping Combustion Process. *Fuel Processing Technology*, **220**, 106898.
- Lu, C., Li, K., Wang, H., Zhu, X., Wei, Y., Zheng, M., Zeng, H. (2018). Chemical looping reforming of methane using magnetite as oxygen carrier: Structure evolution and reduction kinetics, *Applied Energy*, **211**, 1-14.
- Lu, Z., Chen, X., Yao, S., Qin, H., Zhang, L., Yao, X., Yu, Z., Lu, J. (2019). Feasibility study of gross calorific value, carbon content, volatile matter content and ash content of solid biomass fuel using laser-induced breakdown spectroscopy. *Fuel*, **258**, 116150.
- Lyngfelt, A., Brink, A., Langørgen, Ø., Mattisson, T., Rydén, M., Linderholm, C., (2019). 11,000 h of chemical-looping combustion operation—Where are we and where do we want to go? *International Journal of Greenhouse Gas Control*, **88**, 38-56.
- Lyngfelt, A., Leckner, B. (2015). A 1000 MW_{th} boiler for chemical-looping combustion of solid fuels – Discussion of design and costs, *Applied Energy*, **157**, 475-487
- Madrali, E. S., Ercikan, D., Ekinçi, E. (1991). Changes in fuel particle structure and its effect on segregation in fluidized beds during the initial combustion stages, *FBC – technology and the environmental challenge*, 139-147.
- Mamuro, T., Hattori, H. (1968). Flow pattern of fluid in spouted beds, *Journal of chemical engineering of Japan*, **1**, 1-5.
- Materazzi, M., Taylor, R., Cairns-Terry, M. (2019). Production of biohydrogen from gasification of waste fuels: Pilot plant results and deployment prospects. *Waste Management*, **94**, 95-106.
- Mattisson, T., Lyngfelt, A., & Leion, H. (2009). Chemical-looping with oxygen uncoupling for combustion of solid fuels. *International Journal of Greenhouse Gas Control*, **3**(1), 11–19.
- Mendiara, T., Abad, A., de Diego, L. F., García-Labiano, F., Gayán, P., Adánez, J. (2013). Biomass combustion in a CLC system using an iron ore as an oxygen carrier, *International Journal of Greenhouse Gas Control*, **19**, 322-330.
- Mickley, H.S. and Fairbanks, D.F. (1955). Mechanism of heat transfer to fluidized beds. *AIChE J.*, **1**, 374-384.
- Milne T. A, Evans R. J. (1998). Biomass gasification “tars”: their nature, formation and conversion. *National Renewable Energy Laboratory, Golden, CO, USA NREL Report no.: NREL/TP-570-25357*.
- Moghtaderi, B. (2012). Review of the Recent Chemical Looping Process Developments for Novel Energy and Fuel Applications. *Energy Fuels*, **26**, 15–40.

- Neves, D., Matos, A., Tarelho, L., Thunman, H., Larsson, A., Seemann, M. (2017). Volatile gases from biomass pyrolysis under conditions relevant for fluidized bed gasifiers, *Journal of Analytical and Applied Pyrolysis*, **127**, 57-67.
- Nienow, A. W. and Chiba, T. (1985). Fluidization of dissimilar materials. In Davidson, J. F., Harrison, D. and Clift, R. (Eds), *Fluidization* (2nd edn), London: Academic Press.
- Nienow, A. W., Rowe, P. N., Chiba, T. (1978a). Mixing and segregation of a small proportion of large particles in gas fluidized beds of considerably smaller ones. *A.I.Ch.E. symp. Ser.* **74**(176), 45.
- Nilsson, S., Gómez-Barea, A., Cano, D. F. (2012). Gasification reactivity of char from dried sewage sludge in a fluidized bed, *Fuel*, **92**(1), 346–353.
- Parmar, M. S., Hayhurst, A.N., (2002), The heat transfer coefficient for a freely moving sphere in a bubbling fluidised bed. *Chem. Eng. Sci.*, **57**, 3485-3494.
- Patil, K. N. Huhnke, R. L. Bellmer, D. D. (2007). Influence of Internal Baffles on Mixing Characteristics of Biomass in a Fluidized Sand Bed. *International Commission of Agricultural Engineering*, 1-9.
- Pattiya, P. (2011). Bio-oil production via fast pyrolysis of biomass residues from cassava plants in a fluidised-bed reactor, *Bioresource Technology*, **102**, 2, 1959-1967.
- Peeler, J.P.K., Whitehead, A.B. (1982). Solids motion at horizontal tube surfaces in a large gas–solid fluidized bed, *Chemical Engineering Science*, **37**, 77-82.
- Pore, M., Ong, G.H., Boyce, C.M., Materazzi, M., Gargiuli, J., Leadbeater, T., Sederman, A.J., Dennis, J.S., Holland, D.J., Ingram, A., Lettieri, P., Parker, D.J. (2015). A comparison of magnetic resonance, X-ray and positron emission particle tracking measurements of a single jet of gas entering a bed of particles. *Chemical Engineering Science*, **122**, 210-218.
- Prins, W., Siemons, R., Van Swaaij, W. P. M., & Radovanovic, M. (1989). Devolatilization and ignition of coal particles in a two-dimensional fluidized bed. *Combustion and Flame*, **75**(1), 57–79.
- Rao, P., Muller, M. (2013). Characterization of de-fluidized regions in the wake of submerged objects in a small particle fluidized bed, *Powder Technology*, **243**, 53-58.
- Rapagnà, S., Jand, N., Kiennemann, A., & Foscolo, P. U. (2000). Steam-gasification of biomass in a fluidised-bed of olivine particles. *Biomass and Bioenergy*, **19**(3), 187–197.
- Record, S. J. (2004). *The mechanical Properties of wood*. [Online] Accessed 1 October 2020, Available from: <http://www.gutenberg.org/files/12299/12299-h/12299-h.htm>
- Redko, T., Volford, A., Marek, E. J., Scott, S. A., Hayhurst, A. N. (2020). Measurement of the times for pyrolysis and the thermal diffusivity of a pyrolyzing particle of wood and also the resulting char, *Combustion and Flame*, **212**, 510-518.
- Rees, A. C. (2005). The behaviour of buoyant particles in gas-fluidised beds. Ph.D. thesis, University of Cambridge
- Rees, A. C., Davidson, J. F., Dennis, J. S., & Hayhurst, A. N. (2006). The Rise of Buoyant Fuel-Particles in a Slugging Gas-Fluidized Combustor. *Chemical Engineering Research and Design*, **84**(4), 319–327.
- Rees, A. C., Davidson, J. F., Dennis, J. S., Hayhurst, A. N. (2005). The rise of a buoyant sphere in a gas-fluidized bed, *Chemical Engineering Science*, **4**, 1143-1153.
- Rice, N. P. (2018). Investigation of Multiphase Reactor Hydrodynamics Using Magnetic Resonance Imaging. Ph.D. thesis, University of Cambridge

- Rong D, Mikami, T., Horio, M. (1999). Particle and bubble movements around tubes immersed in fluidized beds – a numerical study, *Chemical Engineering Science*, **54**, 5737-5754.
- Rowe. P. N., Partridge, A. W., Cheney, A. G., Henwood, G. A., Lyall, E. (1965). The mechanisms of solids mixing in fluidized beds. *Tans. I. Chem. Engrs.*, **43**, 157-165.
- Ruoppolo, G., Miccio, F., Miccio, M., Brachi, P., Chirone, R. (2021). Sewage sludge ashes as a primary catalyst for the abatement of tar in biomass gasification: Bubbling versus spouted-fluidized bed configuration. *Can J Chem Eng*, **99**, 1706-1714.
- Saastamoinen, J. J, Taipale, R., Horttanainen, M., Sarkomaa, P. (2000). Propagation of the ignition front in beds of wood particles, *Combustion and Flame*, **123**, 1–2, 214-226.
- Saucedo, M. A. (2013). The gasification of solid fuels and its relation to chemical-looping and oxy-fuel combustion. Ph.D. thesis, University of Cambridge.
- Scala, F. & Chirone, R. (2004). Fluidized bed combustion of alternative solid fuels. *Experimental Thermal and Fluid Science*, **28**(7), 691–699.
- Scala, F. & Solimene, R. (2013). ‘Conversion of solid fuels and sorbents in fluidized bed combustion and gasification’, in Scala, F. (ed) *Fluidized bed technologies for near-zero emission combustion and gasification*. Sawston: Woodhead Publishing Limited.
- Schlünder, E. U. (1982). *Seventh international conference on fluidised combustion*, 195.
- Schnellmann, M. A. (2018). Chemical Looping Combustion: A Multi-Scale Analysis, PhD Thesis, University of Cambridge, UK.
- Scott, S. A. (2004). The Gasification and Combustion of Sewage Sludge in a Fluidised Bed, PhD thesis, University of Cambridge, Cambridge.
- Scott, S. A., Davidson, J. F., Dennis, J. S., Hayhurst, A. N. (2004). Heat Transfer to a Single Sphere Immersed in Beds of Particles Supplied by Gas at Rates above and below Minimum Fluidization. *Ind. Eng. Chem. Res.*, **43**(18), 5632–5644
- Shen, L., Zheng, D. (2003). An experimental study of oil recovery from sewage sludge by low-temperature pyrolysis in a fluidised-bed, *Fuel*, **82**(4), 465-472.
- Solimene, R., Marzocchella, A., & Salatino, P. (2003). Hydrodynamic interaction between a coarse gas-emitting particle and a gas fluidized bed of finer solids. *Powder Technology*, **133**(1), 79–90.
- Szücs, B., Szentannai, P. (2019). Experimental Investigation on Mixing and Segregation Behavior of Oxygen Carrier and Biomass Particle in Fluidized Bed. *Periodica Polytechnica Mechanical Engineering*, **63**(3), 188-194.
- Teixeira, A. R., Krumm, C., Vinter, K. P., Paulsen, W. D., Zhu, C., Maduskar, S., Joseph, K. E., Greco, K., Stelatta, M., Davis, E., Vincent, B., Hermann, R., Suszynski, W., Schmidt, L. D., Fan, W., Rothstein, J. P., Dauenhauer, P. J. (2015). Reactive Liftoff of Crystalline Cellulose particles, *Scientific Reports*, **5**, 11238.
- Thielicke, W., (2020). PIVlab - particle image velocimetry (PIV) tool (<https://www.mathworks.com/matlabcentral/fileexchange/27659-pivlab-particle-image-velocimetry-piv-tool>), MATLAB Central File Exchange. Retrieved April 3, 2020.
- UNFCCC, 2015. Adoption of the Paris agreement - Paris Agreement text English. Retrieved from http://unfccc.int/files/essential_background/convention/application/pdf/english_paris_agreement.pdf
- Urciuolo, M., Solimene, R., Chirone, R., & Salatino, P. (2012). Fluidized bed combustion and fragmentation of wet sewage sludge. *Experimental Thermal and Fluid Science*, **43**, 97–104.

- Valenzuela, I. A. and Glicksman, L. R. (1985). Gas Row distribution in a bubbling fluidized bed. *Powder Technol.* **44**, 103-113.
- Volford, A., Redko, T., Marek, E. J., Bond, Z. W. M., Hayhurst, A. N. (2021). Using a flame ionisation detector to measure the rate and duration of pyrolysis of a biomass particle, *Combustion and Flame*, **230**, 111438.
- Wang, X., Kersten, S.R.A., Prins, W., van Swaaij, W.P.M. (2005). Biomass pyrolysis in fluidized bed reactor. Part 2: experimental validation of model results, *Ind Eng Chem Res*, **44**, 8786-8795.
- Wittemann. (2003). Physical Properties of Carbon Dioxide. [Online]. Accessed 1 October 2020 Available from: http://www.r744.com/files/pdf_088.pdf
- Xavier, A. M., & Davidson, J. F. (1981). Heat transfer to surfaces immersed in fluidised beds and in the freeboard region. *A.I.Ch.E. Symposium Series*, **77**, 368–373.
- Xin, T., Mingze, S., Haibo, Z. (2020). Kinetics of redox reactions of CuO@TiO₂-Al₂O₃ for chemical looping combustion and chemical looping with oxygen uncoupling, *Combustion and Flame*, **213**, 255-267.
- Yang, Z., Duan, L., Li, L., Liu, D., Zhao, C. (2020). Movement and mixing behavior of a single biomass particle during combustion in a hot fluidized bed combustor, *Powder Technology*, **370**, 88-95.
- Yates, J. G., Cheesman, D. J., Lettieri, P., Newton, D. (2002). X-Ray Analysis of Fluidized Beds and Other Multiphase Systems, *KONA Powder and Particle Journal*, **20**, 133-143.
- Zhang, Y., Jin, B., Zhong, W. (2009). Experimental investigation on mixing and segregation behavior of biomass particle in fluidized bed, *Chemical Engineering and Processing: Process Intensification*, **48** (3), 745-754.
- Zhou, H., Jensen, A.D. Glarborg, P., Jensen P.A., Kavaliauskas, A. (2005). Numerical modeling of straw combustion in a fixed bed, *Fuel*, **84**, 4, 389-403.
- Zhou, L., Zhao, Y. (2021). CFD-DEM simulation of fluidized bed with an immersed tube using a coarse-grain model, *Chemical Engineering Science*, **231**, 116290.
- Żukowski, W., Berkowicz, G. (2019). The combustion of liquids and low density solids in a cenospheric fluidised bed. *Combustion and Flame*, **206**, 476-489.

Nomenclature

Symbol	Quantity	Units
\dot{h}_{gc}	The gas convective heat transfer coefficient modified to account for transpirative cooling.	$\text{W m}^{-2} \text{K}^{-1}$
\dot{m}_{N_2}	Molar flowrate of N_2	mol s^{-1}
\dot{m}_{CO_2}	Rate of production of moles of CO_2	mol s^{-1}
h_{bub}	The distance from the top of a bubble to the top of the fluidised bed	m
h_{eff}	The effective heat transfer coefficient	$\text{W m}^{-2} \text{K}^{-1}$
$h_{rad,bub}$	Radiative heat transfer coefficient when a particle is inside a bubble.	$\text{W m}^{-2} \text{K}^{-1}$
h_{rad}	Radiative heat transfer coefficient	$\text{W m}^{-2} \text{K}^{-1}$
A_0	Area of bed per orifice in the distributor	m^2
$A_{surface}$	Surface area of a particle of biomass	m^2
C_{Da}	Drag coefficient for a sphere inside a bubble	-
$C_{D\epsilon a}$	Porosity dependant drag coefficient	-
$C_{p,f}$	Specific heat capacity of the boundary layer gas	$\text{J kg}^{-1} \text{K}^{-1}$
C_p	Heat capacity of the bed particles	$\text{J kg}^{-1} \text{K}^{-1}$
H_d	The depth from the surface to which an inert particle will circulate	m
M_h	Mass of the column of bed material above a submerged object	kg
P'	Probability that the mobile sphere is in the emulsion phase, while ascending to the surface of the bed.	-
Q_{sub}	Volumetric flowrate of CO_2 away from a sublimating particle of dry ice	$\text{m}^3 \text{s}^{-1}$
R_ρ	The density ratio	-
T_{bed}	Temperature of the fluidised bed	K
T_{mean}	Mean temperature of the fluidised bed and a particle	K
$T_{particle}$	Temperature of a particle	K
U_A	Axial component of the superficial velocity of the fluid	m s^{-1}
U_D	The velocity of a mobile sphere falling through the emulsion phase	m s^{-1}
U_{bub}	Rise velocity of bubbles	m s^{-1}
U_r	Radial component of the superficial fluid velocity	m s^{-1}
V_{disp}	Volume of bed material displaced by a particle	m^3
d_{bub}	Mean diameter of bubbles	m
f_1	Frequency of coalescence of bubbles per cross sectional area of the bed	$\text{s}^{-1} \text{m}^{-2}$
f_c	The fraction of a particle's surface which is in contact with the bed material.	-
k_e	Thermal conductivity of the emulsion phase	$\text{W m}^{-1} \text{K}^{-1}$
k_e^0	Effective thermal conductivity of a packed bed and static fluid	$\text{W m}^{-1} \text{K}^{-1}$
k_f	thermal conductivity of the boundary layer gas	$\text{W m}^{-1} \text{K}^{-1}$
m_0	Initial mass of a particle of biomass	kg
m_{lead}	Mass of lead added to a particle of biomass	kg
p_b	Pressure of the bed solids	Pa
p_{bub}	The pressure inside a bubble	Pa

p_f	Pressure of the fluidising gas	Pa
t_2	Contact time between packets of bed particles and a gas-emitting particle	s
t_{devol}	Total time for devolatilisation to occur	s
u_e	Interstitial velocity of the fluidising gas	$m s^{-1}$
u_r	Radial interstitial velocity	$m s^{-1}$
u_θ	Circumferential interstitial velocity	$m s^{-1}$
y_{CO_2}	Mole fraction of CO_2	-
δ_{th}	Thickness of the thermal boundary layer	m
ϵ_{bub}	Void fraction for the bed attributable to bubbles	-
ϵ_{mf}	Voidage of the fluidised bed at incipient fluidisation	-
ϵ_{pb}	Voidage of a randomly packed bed of particles	-
λ_m	Modified free path of gas molecules	m
λ_{sub}	The latent heat of sublimation of CO_2 at atmospheric pressure	J
μ_f	Viscosity of fluid	Pa s
ρ_{CO_2solid}	Density of dry ice	$kg m^{-3}$
ρ_d	Density of devolatilising particle	$kg m^{-3}$
ρ_p	Density of the bed particles	$kg m^{-3}$
ρ_{sphere}	Density of the inert or gas-emitting sphere	$kg m^{-3}$
σ_d	Molecular collision diameter	m
τ_{fluid}	Time constant for a thermal boundary layer to reach steady state	s
ϵ_{bed}	Emissivity of the bed material	-
ϵ_d	Emissivity of a devolatilising particle	-
a	Radius of the gas-emitting cylinder or sphere.	m
a_0	The radius of a particle before devolatilisation or sublimation have occurred.	m
C_f	Discharge coefficient	-
d_p	Diameter of a bed particle	m
D_S	Diameter of a spout	m
F	View factor	-
g	Gravitational acceleration	$m s^{-2}$
h	The vertical distance between the surface of the bed and the bottom of the porous cylinder.	m
h_{bub}	Gas convective heat transfer coefficient inside a bubble	$W m^{-2} K^{-1}$
h_{gc}	Gas convective heat transfer coefficient	$W m^{-2} K^{-1}$
h_{pc}	Particle convective heat transfer coefficient	$W m^{-2} K^{-1}$
$h_{pc,a}$	Particle convective heat transfer coefficient for an ascending particle.	$W m^{-2} K^{-1}$
$h_{pc,d}$	Particle convective heat transfer coefficient for a descending particle.	$W m^{-2} K^{-1}$
K	D'Arcy's law permeability constant	$kg m^{-3} s^{-1}$
L	Length of the defluidised hood	m
l	Thickness of a pseudo 2-D bed	m
L_{max}	The maximum length of a defluidised hood	m
p	Pressure	Pa
p_{atm}	Atmospheric pressure	K
Pr	Prandtl number	-
r	Radial coordinate	m

R	Universal gas constant	$\text{m}^3 \text{Pa K}^{-1} \text{mol}^{-1}$
Re_{pub}	Reynolds number for gas flowing past a sphere inside a bubble	-
S_A	Cross sectional area of the defluidised hood	M
T_{bed}, T_{∞}	Fluidised bed temperature	K
t_{sub}	Time for total sublimation of a sphere of dry ice	s
U	Superficial gas velocity	m s^{-1}
\mathbf{u}	Local velocity of the bed particles	m s^{-1}
u_{AO}	The axial fluid velocity at the base of a defluidised hood	m s^{-1}
U_d	Peripheral velocity of at the surface of a gas-emitting particle	m s^{-1}
U_{gap}	Velocity of gas through a thin gap	m s^{-1}
U_{mf}	Superficial gas velocity at minimum fluidisation conditions	m s^{-1}
U_R	Rise velocity of a mobile sphere in the wake of a bubble	m s^{-1}
\mathbf{v}	Local velocity of the fluidising gas	m s^{-1}
z	Cross section factor	-
λ	Mean free path of gas molecules	m
Φ	Velocity potential	$\text{m}^2 \text{s}^{-1}$
Φ	Fraction of the heat transfer surface in contact with the bed particles inside each packet of the emulsion phased.	-
F	Force	N
H	Total height of the fluidised bed	m
P	Probability that a mobile sphere is in the emulsion phase	-
Re_p	Particulate phase Reynolds number	-
V	Volume of a particle of biomass	m^3
m	Mass of a particle of biomass	kg
n	The average number of carbon atoms per molecule of volatile matter	-
n	Number of molecules per unit volume	m^{-3}
q	Tortuosity of the emulsion phase	-
t	Time	s
α	Molar flowrate of N_2	mol s^{-1}
β	Angle of repose of particles	radians
β	Molar flowrate of air	mol s^{-1}
γ	Molar flowrate of volatile matter	mol s^{-1}
γ	Accommodation coefficient	-
δ	Dimensionless draught of particles in fluidised beds	-
θ	Side angle of a hood of particles, circumferential co-ordinate	radians
θ	Molar flowrate of O_2	mol s^{-1}
κ	Molar flowrate of CO_2	mol s^{-1}
σ	Stefan–Boltzmann constant	$\text{W m}^{-2} \text{K}^{-4}$
τ	The proportion of time for which a surface is in contact with a bubble.	-
ϵ	Molar flowrate of CO	mol s^{-1}
ϕ	Ratio between the diameter of the bed particles and the thickness of the gas film around a heat transfer surface	-

Appendices

Appendix 2: Experimental

A 2.1 Analysis of the size distribution of bed particles

All the bed material used in this dissertation was first graded by sieving. Size fractions were obtained and labelled according to their upper and lower sieve sizes. A sample from each was analysed using a Morphologi G3 Microscope (Automated Particle Size Characterisation System) according to the following protocol. First, 57 mm³ of the sample was obtained by means of a calibrated scoop. This was added to the microscope's dispersion chamber. The sample was dispersed over a glass slide using the automatic dispersion system. It was found that 57 mm³ was sufficient to include enough particles for the larger size fractions but not to overcrowd the slide for the smaller size fractions of particles. It was important to avoid overcrowding as this increased the chance of particles touching and being counted as one single large particle by the microscope.

The microscope was then focused and calibrated. An intensity threshold was set to allow the program to identify the dark particles against the light background. The microscope performed a scan over the particles on the slide and counted the number of particles. The perimeter length and area of each particle was also calculated. An image of every particle was stored.

Following the scan, the outliers in size and slenderness were removed from the collection of images – these included particles of dust and fibres as well as clusters of particles in contact with each other.

After filtering the results, the program calculated the distribution of circle equivalent diameters of the particles as well as the distribution of circularity. Results are shown in Table A2.1 and the mean and 10th and 90th percentiles are given to show the spread of the size distributions.

Table A2.1. Size distribution of the bed materials used in this thesis.

Particle material	Upper and lower sieve size	Number of particles analysed	Mean Circle equivalent diameter / μm	Mean Circularity
Silica sand	425-600	401	637	0.868
Silica sand	355-425	952	512	0.866
Silica sand ¹	355-425	664	526	0.861
Silica sand	200-355	1246	432	0.849
Silica sand	180-200	6568	232	0.849
Porous alumina	355-425	897	440	0.887
Porous alumina	200-355	3656	292	0.871
Porous alumina	150-200	6974	207	0.897
Silica sand for Chapter 6.	-	4816	262	0.824

¹. Measured before any experiments – all other measurements were taken from sand which had been used for some time in experiments.

A 2.2 Deconvolution

The measured value of concentration of species in the gas phase can differ from the actual value owing to the delay and mixing in the gas sampling line. To correct for this, deconvolution was used to bring the measured signal closer to the signal in the absence of the sampling line. Scott (2004) outlined the method of deconvolution which has been used throughout this dissertation. The sampling line is modelled as a Continuously Stirred Tank Reactor (CSTR) in series with a Plug Flow Reactor (PFR). The time constant that described the characteristic mixing time in the CSTR was measured by fitting an exponential decay model to an analyser's response to a step change in concentration. A typical step response for the CO₂ sensor used in Chapter 6 is shown in Fig. A2.1.

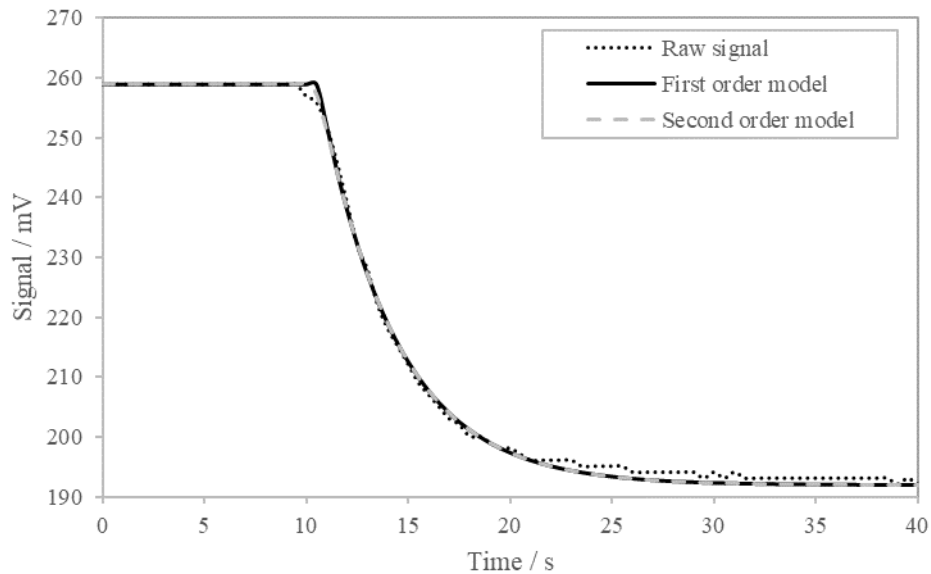


Fig. A2.1. The response of the Sprint-IR CO₂ sensor to a step change in CO₂ concentration (· · ·) and the best fit first order model for its response (—). Also shown is the best fit second order model for its response (- - -).

As shown in Fig. A2.1 the step response of a model of a single CSTR in series with a PFR provides a reasonable fit for the step response of the sample line used in Chapter 6. The first order model cannot, however, replicate the rounded corner prior to the steep drop in concentration at around 11 seconds in Fig. A2.1. A second order model (two CSTRs in series with a PFR) is able to capture that feature to some extent.

The use of a second order model provides a better fit than the first order model but is more computationally expensive during deconvolution and the deconvoluted signal is far noisier than the first order model. As shown in Fig. A2.2 the deconvolution of the raw signal produces a very spiky trace which needs to be smoothed using a moving average. Sudden changes in he concentration can not be replicated owing to the smoothing that is required. When a very long mixing time was used the smoothed deconvoluted signal was found to become negative near the inflection point between devolatilisation and char combustion leading to errors in the data processing.

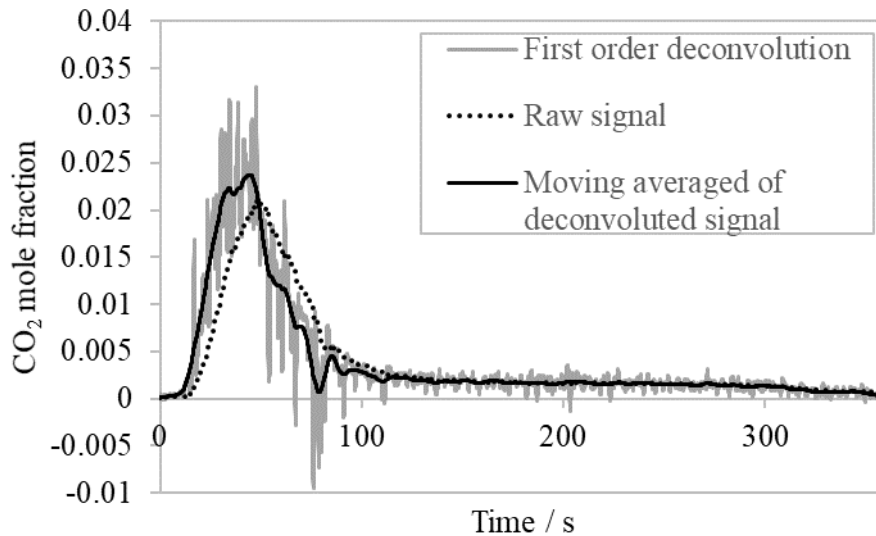


Fig. A2.2. The raw, deconvoluted and smoothed signals from a CO₂ sensor detecting the CO₂ concentration from the combustion of a single sphere of wood. The method of deconvolution makes little difference to the char combustion portion from 100 s onwards but is important during the devolatilisation part.

To minimise the amount of smoothing required, and therefore preserve better the original shape of the curves it was decided to improve the sample line such that the step response could be better modelled by a first order model rather than using higher order deconvolution methods in this dissertation. This was achieved by building sampling systems which had a high flowrate, small filters with a low cross-sectional area and sensors with very low mixing times.

A 2.3 Image processing

The X-ray images were analysed using MATLAB, first by correcting for the slight pin-cushion distortion in the images using the “lensdistort” function with a distortion factor of 0.15. Next, a scale factor was taken from a known length of lead visible in the X-ray images, as shown in Fig 2.17 a). The contrast was improved using the “imadjust” function and the noise was reduced using the “Wiener2” function. The position of the surface of the bed was found in each image by defining the boundary between the light portion of the image, the freeboard, and the darker portion as shown in Fig 2.17 g) using the function “imbinarize” with a contrast threshold of 0.48. The lowest most position of the lead (dark black) was then located and the distance in pixels between the bottom of the lead and the surface of the bed was measured. A square of

lead of length 1 cm (just visible at the top of Fig. A2.3 a)) was used as a reference length scale for converting pixels to millimetres. A degree of parallax error in the measured location of the spheres, relative to the surface of the bed introduces error into the measured depth of the spheres. The images were produced using divergent X-ray beams originating from a source mounted vertically beneath the position of the surface of the bed (*c.f.* Fig. 2.16) Despite best efforts to correct for parallax, the sphere of beech moving from the side of the bed closest to the X-ray source to that furthest away would lead to an error in the value of delta of ± 0.4 .

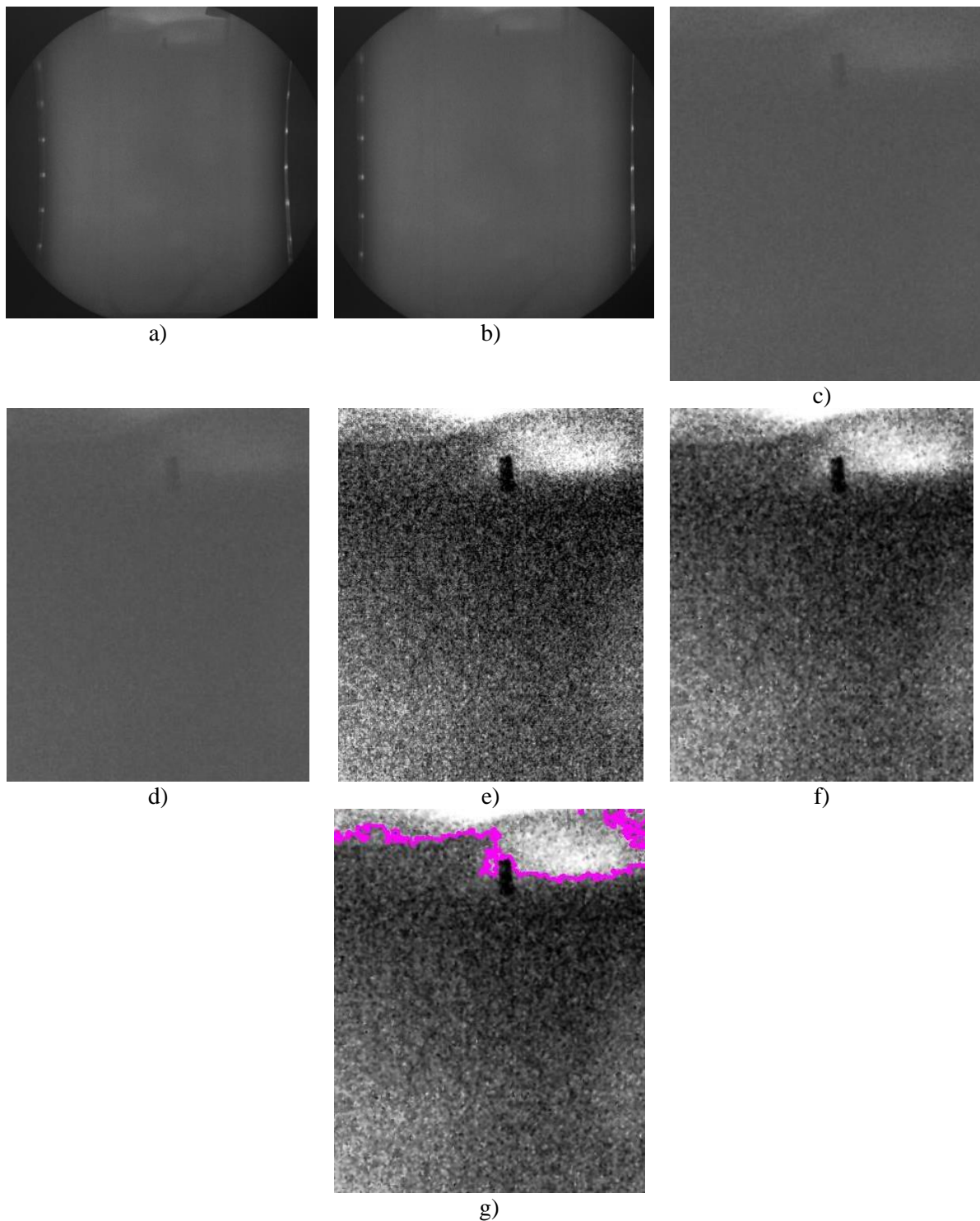


Fig. A2.3. a). Raw image, b) de-pinched, c) cropped to region of interest, d) top to bottom intensity gradient removed, e) contrast improved, f) “Wiener2” function applied, g) surface located (in pink).

Appendix 3: Defluidised Hoods

A 3.1. Maximum height of a conical defluidised hood on top of a sphere.

For a conical defluidised hood on top of a sphere of radius a submerged at depth δa , the maximum depth the sphere can attain before the volume of the hood stops increasing occurs when the top of the hood forms an apex level with the surface of the fluidised bed, as shown in Fig. A3.1.

In this case the depth of the sphere is of the form

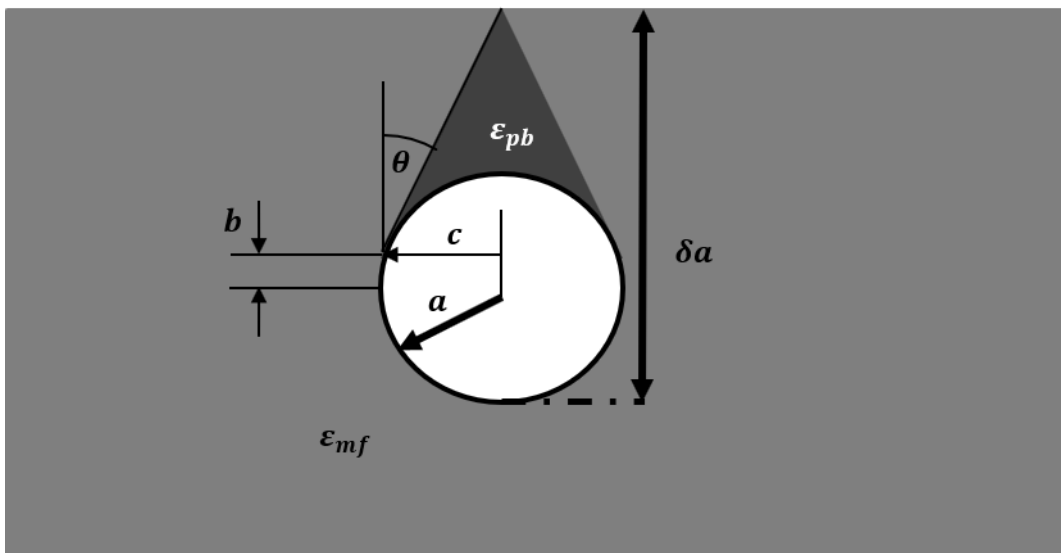


Fig. A3.1. The maximum height of a defluidised hood above a sphere of radius a of side angle θ with the apex level with the surface of the fluidised bed.

$$\delta a = a + b + \frac{c}{\tan \theta} \quad (\text{A3.1})$$

The height b is the distance from the centre of the sphere to the point at which the side defluidised hood meets the surface of the sphere tangentially at angle θ and thus

$$b = a \sin \theta \quad (\text{A3.2})$$

And

$$c = a \cos \theta \quad (\text{A3.3})$$

So

$$\delta = 1 + \sin \theta + \frac{\cos \theta}{\tan \theta} \quad (\text{A3.4})$$

A 3.2 Ratio between the volume of a conical pile of bed material above a sphere and the sphere itself.

The volume of a conical pile of bed material sitting on top of a sphere is found by finding the volume of a cone, side angle β , whose sides are tangential to the surface of the sphere as shown in Fig. A3.2, given by given by Eq. (A3.5)

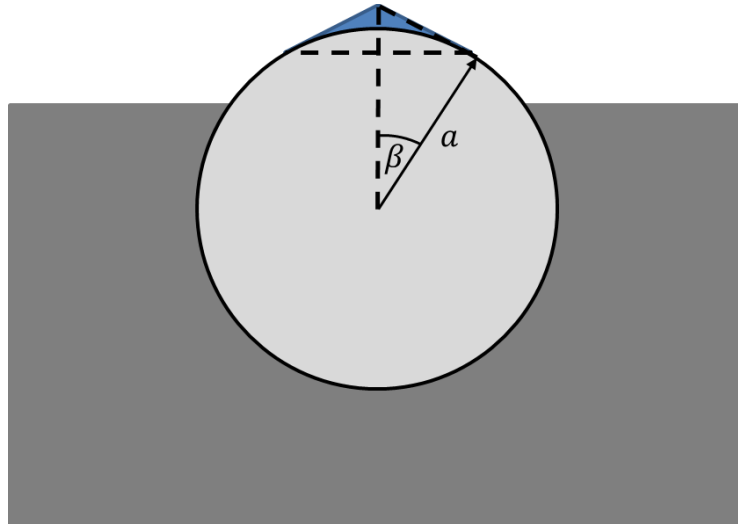


Fig. A3.2 Schematic representation of the form of a conical pile (blue) of particles above a sphere of radius a .

$$V_{cone} = \frac{1}{3} \pi a \sin^3 \beta \tan \beta \quad (\text{A3.5})$$

From the volume of a cone the volume of a spherical cap must be subtracted to give the volume of the pile:

$$V_{pile} = \frac{1}{3} \pi a \sin^3 \beta \tan \beta - \frac{1}{3} \pi a^3 ((1 - \cos \beta)^2 (2 - \cos \beta)) \quad (\text{A3.6})$$

therefore

$$\frac{V_{pile}}{V_{sphere}} = \frac{\{\sin^3(\beta) \tan(\beta) - (1 - \cos(\beta))^2(2 + \cos(\beta))\}}{4} \quad (A3.7)$$

A 3.3 Volume of the fluidised cap.

A 3.3.1 Cylindrical Geometry

The salient dimensions and form of the fluidised hood, as taken from the images shown in Fig. 3.18 a) – d) are shown in Fig A3.3.

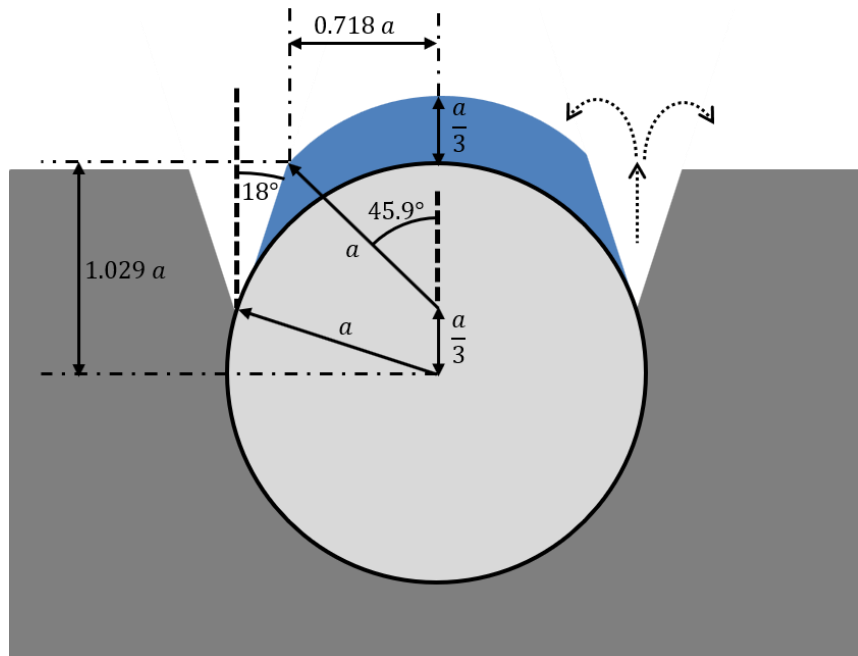


Fig. A3.3. Schematic representation of the form of the fluidised cap (blue) of particles above a cylinder or sphere of radius a .

The cap is represented by a trapezoidal prism with a cylindrical segment on top, minus a further cylindrical segment from underneath. The side angle of 18° was measured from the photographs shown in Fig. 3.18 a) – d). The height, $1.029 a$, and width, $0.718 a$, of the trapezoidal part were found by determining the intersection point between the equation for the angled side (taking the origin to be the centre of the cylinder

$$y = \frac{x}{\tan(18)} + a \left(\sin(18) + \frac{\cos^2(18)}{\sin(18)} \right) \quad (\text{A3.8})$$

and the equation which describes the upper boundary of the cap:

$$x^2 + \left(y - \frac{a}{3} \right)^2 = a^2 \quad (\text{A3.9})$$

The factor of $\frac{a}{3}$ and the side angle 18° can be altered if found necessary for different bed materials.

Working in radians this gives:

$$\begin{aligned} V_{cap} = la^2 & \left[\left\{ (1.029 - \sin\left(18 \frac{\pi}{180}\right)) \left(\cos\left(18 \frac{\pi}{180}\right) + 0.718 \right) \right\} \right. \\ & + \left\{ \frac{1}{2} \left(2 * 45.9 \frac{\pi}{180} - \sin\left(2 * 45.9 \frac{\pi}{180}\right) \right) \right\} \\ & \left. - \left\{ \frac{1}{2} \left(144 \frac{\pi}{180} - \sin\left(144 \frac{\pi}{180}\right) \right) \right\} \right] \quad (\text{A3.10}) \end{aligned}$$

Simplifying:

$$V_{cap} = la^2 [\{1.202\} + \{0.3016\} - \{0.9627\}] \quad (\text{A3.11})$$

$$V_{cap} = 0.5409la^2 \quad (\text{A3.12})$$

Now, resolving the vertical forces on the sphere, taking into account the weight of the fluidised cap:

$$\begin{aligned} \pi a^2 \rho_s g l + 0.5409 a^2 l g \rho_p (1 - \varepsilon_{mf}) & \quad (\text{A3.13}) \\ = 2a^2 l \rho_p (1 - \varepsilon_{mf}) g \int_{\frac{\pi}{2}}^{\pi} (\cos(\theta) + 1 - \delta) \cos(\theta) d\theta & \end{aligned}$$

Evaluating the integral:

$$\pi a^2 \rho_s g l + 0.5407 a^2 l g \rho_p (1 - \varepsilon_{mf}) = 2a^2 l \rho_p (1 - \varepsilon_{mf}) g \left(\delta + \frac{\pi}{4} - 1 \right) \quad (\text{A3.14})$$

Which gives the following expression for the density ratio.

$$\frac{\rho_s}{\rho_p (1 - \varepsilon_{mf})} = \frac{1}{\pi} (2\delta - 2 - 0.5407) + \frac{1}{2} \quad (\text{A3.15})$$

A 3.3.2 Spherical Geometry

The solid of revolution of the blue profile shown in Fig. S3.2 was used to represent the fluidised cap. This comprised a conical frustum, plus a spherical cap on top, minus a spherical cap from beneath. The volume of the cap was thus:

$$V_{cap} = \frac{\pi a^3}{3} \left[\{(1.029 - \sin(18))(\cos^2(18) + 0.718\cos(18) + 0.718^2)\} \right. \\ \left. + \left\{ \left(1 + \frac{1}{3} - 1.029\right)^2 \left(3 - 1 - \frac{1}{3} + 1.029\right) \right\} \right. \\ \left. - \{(1 - \sin(18))^2(3 - 1 + \sin(18))\} \right] \quad (\text{A3.16})$$

Simplifying:

$$V_{cap} = \frac{\pi a^3}{3} [1.514 + 0.2496 - 1.1025] \quad (\text{A3.16})$$

$$V_{cap} = 0.6923a^3 \quad (\text{A3.17})$$

Now, resolving the vertical forces on the sphere, taking into account the weight of the fluidised cap:

$$\frac{4}{3}\pi a^3 \rho_s g + 0.6923a^3 g \rho_p (1 - \varepsilon_{mf}) \quad (\text{A3.18}) \\ = a^3 \pi 2 \rho_p (1 - \varepsilon_{mf}) g \int_{\frac{\pi}{2}}^{\pi} (\cos(\theta) + 1 - \delta) \cos(\theta) \sin(\theta) d\theta$$

Evaluating the integral and rearranging for the density ratio yields:

$$\frac{\rho_s}{\rho_p (1 - \varepsilon_{mf})} = \frac{3}{4} \left(\delta - \frac{1}{3} - \frac{0.6923}{\pi} \right) \quad (\text{A3.19})$$

Appendix 4: A Model for a Floating Particle Assuming a Leidenfrost Mechanism

A 4.1. Derivation of cylindrical stream function solution for $\delta = 1$

The following derivation follows the same set of assumptions as set out in Section 3.2 with the following specific to the 2D cylindrical geometry.

- a) For the initial case, the floating particle was taken as cylindrical, uniform radius, a , and long in comparison with its radial measurement so that the problem could be treated in two dimensions.
- b) On arrival at the surface, the picture is of a cylinder half-submerged in the particulate phase of a fluidised bed, as shown in Fig. 4.1. This is the limiting case for flotation.

The following largely follows the treatment of interstitial gas flows in the particulate phase undertaken by Davidson & Harrison (1963). The particulate phase is considered to be incompressible therefore the continuity equation for particle motion is:

$$\frac{\partial v_r}{\partial r} + \frac{1}{r} \frac{\partial v_\theta}{\partial \theta} = 0 \quad (\text{A4.1})$$

where r is the radial co-ordinate, θ is the angle as shown in Fig. 4.1 and v_r and v_θ are particle velocities in the radial and tangential directions respectively. The relative velocity between the particles and the fluidising fluid is proportional to the pressure gradient within the fluidising fluid giving, for the absolute components for the interstitial fluid flow:

$$u_r = v_r - K \frac{\partial p_f}{\partial r} \quad (\text{A4.2})$$

$$u_\theta = v_\theta - \frac{K}{r} \frac{\partial p_f}{\partial \theta} \quad (\text{A4.3})$$

where p_f is the pressure in the fluidising fluid and K is the permeability constant. Here, u_r and u_θ are the interstitial velocity of the fluid in the radial and tangential directions. Assuming that the fluidising fluid is incompressible, then continuity gives:

$$\frac{\partial u_r}{\partial r} + \frac{1}{r} \frac{\partial u_\theta}{\partial \theta} = 0 \quad (\text{A4.4})$$

and so, eliminating the velocities in eqs. (S4.1), (S4.2), and (S4.3) leaves Laplace's equation

$$\frac{\partial p_f^2}{\partial^2 r} + \frac{1}{r} \frac{\partial p_f^2}{\partial^2 \theta} = 0 \quad (\text{A4.5})$$

Equation (4.5) is the same result for a fixed bed of particles so one arrives at the important conclusion that the fluid pressure distribution is unaffected by the motion of the particles. The fluid has been assumed to be inviscid, hence there can be no shear forces within the system and the flow can be considered irrotational by ensuring the sum of angular momentum around a fluid element is zero:

$$\frac{\partial}{\partial r}(ru_\theta) - \frac{\partial u_r}{\partial \theta} = 0 \quad (\text{A4.6})$$

This defines the velocity potential Φ

$$u_r = \frac{\partial \Phi}{\partial r} \text{ and } u_\theta = \frac{1}{r} \frac{\partial \Phi}{\partial \theta} \quad (\text{A4.7})$$

From D'Arcy's law, when the fluid flow is independent of particle motion as arrived at above

$$u_r = -K \frac{\partial p_f}{\partial r} \text{ and } u_\theta = \frac{-K}{r} \frac{\partial p_f}{\partial \theta} \quad (\text{A4.8})$$

So a direct comparison can be made such that

$$\Phi = -K p_f \quad (\text{A4.9})$$

for axially symmetric, inviscid, irrotational percolation. This allows a pressure distribution to be directly obtained from the velocity potential. Thus, in order to investigate the flotation phenomenon, a velocity potential model was generated starting from the general solution to Laplace's equation in 2D polar co-ordinates to describe the motion of the fluid, namely:

$$p_f(r, \theta) = -\frac{1}{K} \left[a_0 \ln(r) + b_0 + \sum_{n=1}^{\infty} (A_n \cos(n\theta) + B_n \sin(n\theta)) \left(C_n r^n + \frac{D_n}{r^n} \right) \right] \quad (\text{A4.10})$$

where r is the radial co-ordinate, θ is the angle as shown in Fig. A4.1 and a_0, b_0, A_n, B_n, C_n and D_n are constants defined by the boundary conditions for the problem. Consider the boundary conditions shown in Fig. A4.1 for the blowing particle at the surface of an infinite stagnant medium, as $r \rightarrow \infty, \Phi(r, \theta) \rightarrow 0$ so a_0 and $C_n = 0$. The surface of the bed is represented by a plane of zero potential so $\Phi(r, \theta) = 0$ at $\theta = \frac{\pi}{2}$ and $\theta = \frac{3\pi}{2}$ which gives the conclusion that $A_n = 0$ and $b_0 = 0$. This leaves:

$$\Phi(r, \theta) = \sum_{n=1}^{\infty} \frac{1}{r^n} B_n \cos(n\theta)$$

The boundary condition for the surface of the particle is now considered. It is assumed that the velocity of gas, generated within the particle, passes radially out of the particle at the surface. Initially it is assumed that the gas is produced at a uniform velocity, U_b . As the model is inspecting the onset of floating behaviour it is assumed that the fluidised medium is still just in contact with the particle so:

$$\frac{\partial \Phi}{\partial r} \Big|_{r=a} = U_b \text{ for } \frac{\pi}{2} < \theta < \frac{3\pi}{2}$$

$$\frac{\partial \Phi}{\partial r} \Big|_{r=a} = -U_b \text{ For } \frac{-\pi}{2} < \theta < \frac{\pi}{2}$$

To satisfy the symmetry of the situation and impose vertical streamlines through the bed surface, and therefore the line of zero potential, the blowing velocity over the top of the particle must be $-U_b$ by the method of images as shown in Figure A4.1.

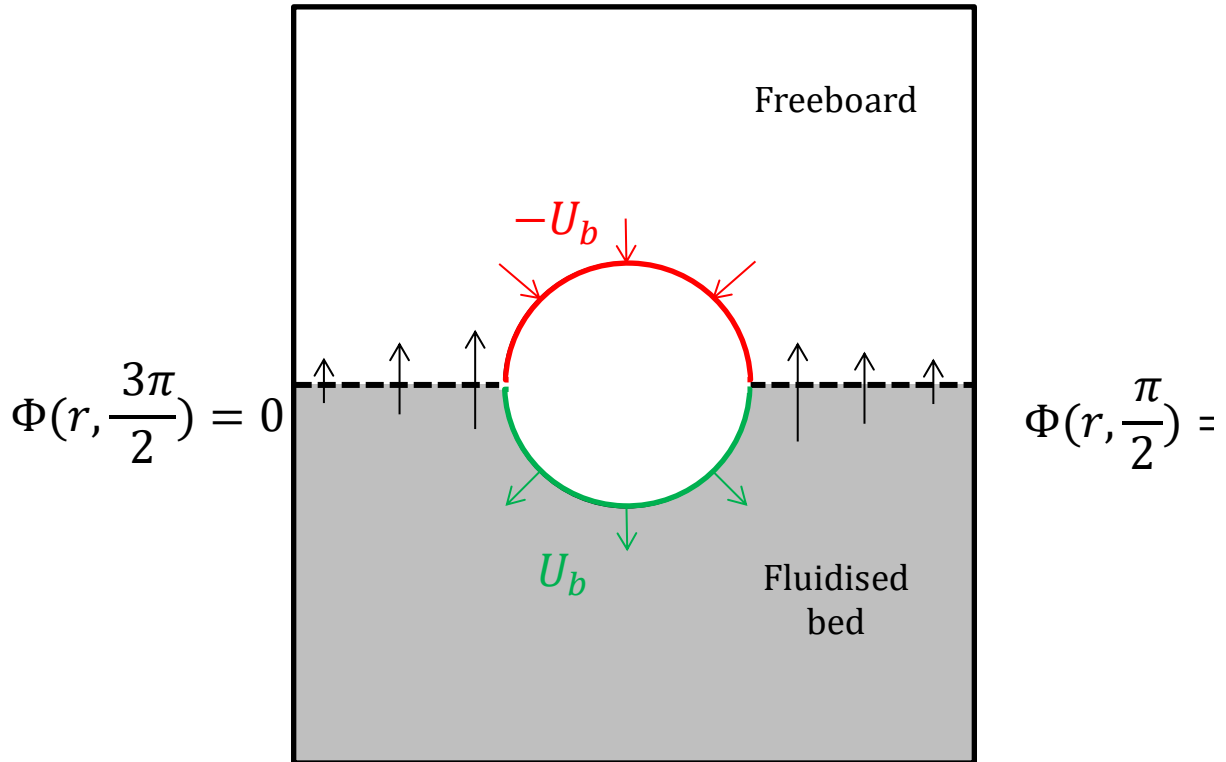


Figure A4.1 The symmetry condition satisfied by a positive potential at the cylinder's underside and an equal and negative potential at the cylinder's upper side.

Consequently the solution for $-\frac{\pi}{2} < \theta < \frac{\pi}{2}$ is unphysical, for this domain, the freeboard, there is no fluidised behaviour to consider and it is assumed that there is nothing in this region affecting flotation.

By using orthogonality:

$$B_m = \frac{4U_b a^{m+1}}{m^2 \pi} \quad \text{for all } m \text{ odd}$$

hence,

$$\Phi(r, \theta) = \sum_{m=1}^{\infty} \frac{4U_b a^{m+1}}{m^2 \pi r^m} \cos(m\theta) \tag{A4.12}$$

The series quickly converges for $r > a$ and yields the vector field shown in Fig. A4.2 a).

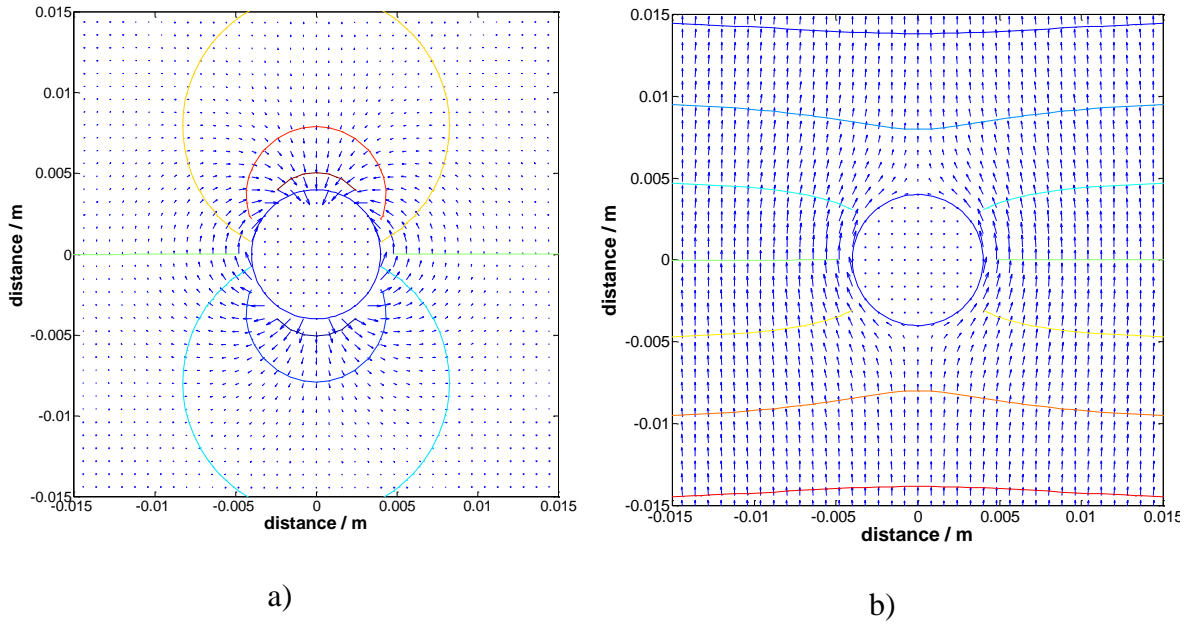


Figure A4.2. Vector plot showing the gas velocities (arrows) around cylinder of radius 0.004 m for a) a blowing particle in a stagnant medium where $U_d = 0.04 \text{ m s}^{-1}$ and b) an inert particle in a uniform flow where $U_\infty = 0.1 \text{ m s}^{-1}$. The coloured lines are lines of constant potential

Now the property of superposition of velocity potentials is utilised to add the fluidised behaviour of the medium below the particle to the solution. The velocity potential for linear flow around a cylinder is readily shown to be obtained from the combination of a doublet and a uniform stream, as:

$$\Phi(r, \theta) = -U_\infty r \left(1 + \frac{a^2}{r^2} \right) \cos(\theta) \quad (\text{A4.13})$$

and yields the velocity vector plot shown in Figure A4.2 b). The higher order terms of equation (A4.12) are curtailed at $m = 3$ such that the velocity potential is given by (A4.12) + (A4.13):

$$\Phi(r, \theta) = \frac{4U_b}{\pi} \left(\frac{a^2}{r} \cos(\theta) + \frac{a^4}{9r^3} \cos(3\theta) \right) - U_{mf} r \left(1 + \frac{a^2}{r^2} \right) \cos(\theta) \quad (\text{A4.14})$$

This is shown in Fig. A4.2. Now using equation (9) for irrotational, incompressible percolation flow where the motion of the fluidising gas is assumed to be independent of the motion of the particles:

$$p_f(r, \theta) = -\frac{U_\infty r}{K} \left(1 + \frac{a^2}{r^2}\right) \cos(\theta) + \frac{4U_d}{\varepsilon_{mf} K \pi} \left(\frac{a^2}{r} \cos(\theta) + \frac{a^4}{9r^3} \cos(3\theta)\right) \quad (\text{A4.15})$$

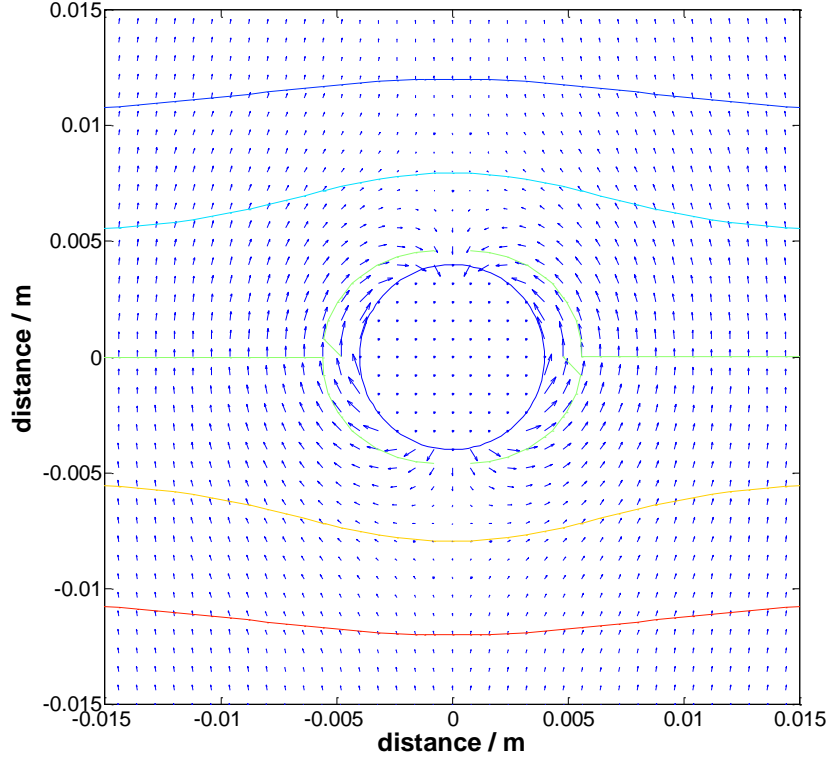


Figure A4.3 Vector plot showing the gas velocities (arrows) around cylinder of radius 0.004 m for a blowing particle, $U_d = 0.04 \text{ m s}^{-1}$, in a submersed within a uniform stream where $U_\infty = 0.1 \text{ m s}^{-1}$. The coloured lined are lines of constant potential

We know, given the model captures the incipient floating behaviour for a particle that the pressure distribution integrated around the particle must just support the weight of the particle. Integrating the pressure distribution at $r = a$ for the submerged portion of the cylinder for $\frac{\pi}{2} < \theta < 3\pi/3$:

$$\int_{\pi}^{2\pi} p_f(a, \theta) a \cos(\theta) d\theta = \frac{U_\infty a^3 \pi}{K} + \frac{U_d a}{K} \quad (\text{A4.16})$$

The pressure distribution around the top of the particle, within the freeboard, is assumed to vary little away from the pressure at the bed surface. Now a force balance is performed on the particle, just supported by the pressure beneath it.

$$\pi a^2 \rho_{bp} = \frac{U_\infty a^3 \pi}{Kg} + \frac{U_d a}{Kg} \quad (\text{A4.17})$$

where ρ_{bp} is the density of the blowing particle and g is the acceleration due to gravity. According to two phase theory (Davidson & Harrison, 1963) for gas fluidised beds $U_\infty = U_{mf}$ and:

$$\frac{\Delta p_f}{L} = (\rho_p - \rho_f)g(1 - \varepsilon_{mf}) \quad (\text{A4.18})$$

As used before $U = -K\nabla p_f$ and, assuming the density of the gas is negligible compared to the density of the bed particles, the interstitial velocity at incipient fluidisation is, therefore:

$$U_{mf} = K\rho_p(1 - \varepsilon_{mf})\varepsilon_{mf}g \quad (\text{A4.19})$$

Substituting (3.18) into (3.16):

$$0 = a^2 \rho_p (1 - \varepsilon_{mf}) \varepsilon_{mf} \pi - a \pi \rho_{bp} + \rho_p (1 - \varepsilon_{mf}) \varepsilon_{mf} \frac{U_d}{U_{mf}} \quad (\text{A4.20})$$

A 4.2. Parameters used for analysis of a gas-emitting sphere in a porous medium in Comsol

Comsol “porous flow” coupled with non-porous flow was used. The same geometry as the experimental fluidised bed described in Section 2.5.1 was simulated with a 6 mm diameter solid sphere located axially. The sphere was set to emit gas from its surface uniformly and radially. The particle’s height relative to the surface of the bed could be altered. A surface integration over the complete surface of the simulated fuel particle was carried out to find, for each combination of δ and U_d/U_{mf} investigated, the density of a sphere whose weight would give a net vertical force of 0 on the sphere. The boundary conditions between the porous and non-porous regions in the simulation was “continuity”. The permeability of the material was

arrived at numerically by finding a value of permeability which gave a pressure drop across the porous region which was equal to that measured experimentally for the equivalent fluidised bed at a superficial flow velocity equal to the experimentally determined U_{mf} . Table A4.1 lists the conditions used to set up the simulation.

Table A4.1. Values and properties used in the Comsol simulation for a particle of 0.003 m diameter at $\delta = 1$

Temperature / °C	800
Nominal bed particle size / μm	512
Permeability of porous medium / $\text{m}^3 \text{s}^{-1}$	1.604×10^{-10}
Voidage of porous medium	0.403
Bed height /m	0.0445
Pressure Drop across the bed / Pa	691
Minimum fluidisation velocity / m s^{-1}	0.0598

The depth of the simulated fluidised bed material, H_{mf} , was estimated using the method described by Dennis (2013).

Appendix 5: A Model for Heat transfer to a Particle Emitting Gas

A 5.1 Modified Agarwal (1991) heat transfer model

The model of Agarwal (1991) for heat transfer from a mobile sphere to a bubbling fluidised bed uses two particle convective terms, one for the portion of time that a circulating particle spent rising through the bed, $h_{pc,a}$, and one for when the circulating particle fell through the bed, $h_{pc,d}$ as well as the gas convective heat transfer coefficient h_{gc} . Additionally, a heat transfer coefficient for the proportion of time that the particle was in the bubble phase, h_{bub} was described. The 5 different heat transfer coefficients were combined into a single effective heat transfer coefficient according to Eq. (A5.1).

$$h_{eff} = P'h_{pc,a} + (P - P')h_{pc,d} + ph_{gc} + (1 - P)h_{bub} \quad (A5.1)$$

Where P is the probability that the mobile sphere is in the emulsion phase rather than in a bubble and, P' is the probability that the mobile sphere is in the emulsion phase while ascending to the surface of the bed. Expressions for P , and P' are given in Section A5.1.4. The modifications made, in this dissertation, include the addition of two radiative heat transfer coefficients, h_{rad} , and $h_{rad,bub}$, a modified gas convective heat transfer coefficient to account for the emission of gas from the mobile sphere, \dot{h}_{gc} , and the inclusion of the proportion of the surface of the mobile sphere, which is in contact with the bed material, f_c , to give:

$$h_{eff} = f_c P' h_{pc,a} + f_c (P - P') h_{pc,d} + P \dot{h}_{gc} + (1 - P) h_{bub} + P h_{rad} + (1 - P) h_{rad,bub} \quad (A5.2)$$

A 5.1.1 Particle convective heat transfer coefficients.

The particle convective heat transfer coefficient describes the heat transfer to the surface of the gas-emitting sphere from the bed particles. The surface renewal theory of Mickley and Fairbanks (1955) assumed that packets of bed particles are brought into contact with the heat-transfer surface by the mixing action of bubbles within the bed. Transient heat transfer occurs

to, or from, these packets before they move away after a given residence time, assumed constant for all packets. Agarwal (1991) used two particle convective heat transfer coefficients to describe a sphere ascending or descending in the bed. Each particle convective heat transfer describes two resistances in series, one across a packet of particles and the other across a thin gas film next to the mobile sphere. The expressions are given in Eq. A5.3 and A5.4 respectively.

$$\frac{1}{h_{pc,a}} = \left(\frac{d_p}{\phi k_f} + 0.5 \sqrt{\frac{\pi t_2}{k_e \rho_p (1 - \varepsilon_{mf}) C_p}} \right) \quad (\text{A5.3})$$

$$\frac{1}{h_{pc,d}} = \left(\frac{d_p}{\phi k_f} + 0.5 \sqrt{\frac{\pi H_d}{U_D k_e \rho_p (1 - \varepsilon_{mf}) C_p}} \right) \quad (\text{A5.4})$$

where $\frac{d_p}{\phi}$ represents the thickness of the gas film around the heat transfer surface and ϕ is the ratio between the bed particle diameter and the thickness of the gas film surrounding the sphere (given by Eq. (A5.5)), d_p is the mean diameter of the bed particles, k_f is the thermal conductivity of the fluidising gas, t_2 is the contact time between each packet of bed particles and the heat transfer surface (given by Eq. (A5.10)), k_e is the effective thermal conductivity of the particulate phase (given by Eq. (A5.17)) and ρ_p is the density of the bed particles (2680 kg m⁻³ for silica sand) and C_p is the heat capacity of the bed particles taken to be 0.798 × 10³ J kg⁻¹ K⁻¹ (Agarwal, 1991). H_d is the depth to which the gas-emitting spheres penetrate the bed, (given by Eq.(A5.12) and U_D is the velocity of a mobile sphere, descending through the bed (given by Eq. (A5.16)) and ε_{mf} is the voidage of the bed at incipient fluidisation conditions.

The ratio between the bed particles' mean diameter and the thickness of the gas film surrounding the heat transfer surface, ϕ , was left as a fitting parameter in the original model. Parmar and Hayhurst (2002) used Eq. (A5.5) to find an estimate of it.

$$\phi = 4\Phi \left\{ \left(1 + \frac{2\lambda_m}{d_p} \right) \ln \left(1 + \frac{d_p}{2\lambda_m} \right) - 1 \right\} + 2 \left(\frac{1 - \Phi}{\sqrt{2} + \frac{2\lambda_m}{d_p}} \right) \quad (\text{A5.5})$$

where Φ is defined as the fraction of the heat transfer surface covered by particles in the bed by Schlünder (1982) (given by Eq. (A5.6), λ_m is the modified free path of the gas molecules as defined by Schlünder (1982) (given by Eq. (A5.7).

$$\Phi = (1 - \varepsilon_{mf})^{\frac{2}{3}} \quad (\text{A5.6})$$

$$\lambda_m = 2\lambda\left(\frac{2}{\gamma} - 1\right) \quad (\text{A5.7})$$

where λ is the mean free path of gas molecules (given by Eq. (A5.8)) and γ is the accommodation coefficient (given by Eq. (A5.9)) from Schlünder (1982).

$$\lambda = \frac{1}{\sqrt{2}n\sigma_d^2} \quad (\text{A5.8})$$

where n is the number of molecules per m^{-3} and σ_d is the molecular collision diameter of the gas, taken to be 364×10^{-12} m (Ismail *et al.*, 2015) for nitrogen gas.

$$\log_{10}\left(\frac{1}{\gamma} - 1\right) = 0.243 - \frac{357}{T_{bed}} \quad (\text{A5.9})$$

The contact time between the packets of bed particles and the mobile sphere during the upwards journey of the mobile sphere through the bed material, t_2 , was given by Agarwal (1991) as Eq. (A5.10).

$$t_2 = \frac{f_1^{-\frac{1}{3}} U_{bub}^{-\frac{2}{3}} (U_{bub} - U_R)}{U_D + U_R} \quad (\text{A5.10})$$

Where f_1 is the frequency of coalescence of bubble per cross sectional area of the bed (given by Eq. (A5.11)), U_{bub} is the velocity of the bubbles rising through the bed (given by Eq. (A5.13)), U_R is the rise velocity of the mobile sphere in the wake of a bubble (given by Eq. (A5.15)) and U_D is the velocity of the mobile sphere falling through the emulsion phase of the bed (given by Eq. (A5.16)).

$$f_1 = \left\{ \frac{0.0195(2H - H_d) + 0.57}{(0.039H + 0.57)^2 + [0.039(H - H_d) + 0.57]^2} \right\} 10^4 \quad (\text{A5.11})$$

Where H is the height of the fluidised bed calculated using the iterative method described by Dennis (2013) and H_d is the depth to which the mobile sphere penetrates the fluidised bed given by Eq. (A5.12) (Nienow *et al.* (1978)).

$$H_d = 1.2(U - U_{mf})^{\frac{1}{2}} \quad (\text{A5.12})$$

where U is the fluidisation velocity and U_{mf} is the incipient fluidisation velocity.

The average velocity of the bubbles comes from Davidson and Harrison (1963), given by Eq. (A5.13).

$$U_{bub} = (U - U_{mf}) + 0.711\sqrt{gd_{bub}} \quad (\text{A5.13})$$

where g is the acceleration due to gravity and d_{bub} is the average diameter of the bubbles in the bed given by Eq. (A5.14) (Agarwal (1991)).

$$d_{bub} = \frac{0.3(U - U_{mf})^{0.4}}{g^{\frac{1}{5}}H_d} \left((H + 4\sqrt{A_0})^{1.8} - (H - H_d + 4\sqrt{A_0})^{1.8} \right) \quad (\text{A5.14})$$

The area of the bed per orifice in the distributor A_0 , was taken to be zero as a porous frit distributor was used in the experiments in Chapter 5. The rise velocity of the mobile sphere in the wake of a bubble, U_R , is given by Eq. (A5.15) from Agarwal (1991).

$$U_R = 0.19(U - U_{mf})^{\frac{1}{2}} \quad (\text{A5.15})$$

The velocity at which the mobile sphere sinks through the emulsion phase of the bed is given by Eq. (A5.16) and comes from Kunii and Levenspiel, (1969).

$$U_D = \frac{\alpha\varepsilon_{bub}U_{bub}}{1 - \varepsilon_{bub} - 0.3\varepsilon_{bub}} \quad (\text{A5.16})$$

where α is the wake fraction associated with bubbles, taken to be 0.3 (Agarwal, 1991), ε_{bub} is the bubble void fraction given by Eq. (A5.17) (Agarwal, 1991).

$$\varepsilon_{bub} = \frac{U - U_{mf}}{U_{bub} + 2U_{mf}} \quad (\text{A5.16})$$

The effective thermal conductivity of the particulate phase is given by Eq. (A5.17) from Gelperin and Einstein (1971)

$$k_e = k_e^o + 0.1\rho_f C_p d_p U_{mf} \quad (\text{A5.17})$$

where k_e^o is the effective thermal conductivity of a packed bed of static fluid given by Eq. (A5.18) from Xavier and Davidson (1981), ρ_f is the density of the fluidising gas found using the ideal gas law.

$$k_e^o = k_f \left(1 + (1 - \varepsilon_{mf}) \left(1 - \left(\frac{k_f}{k_p} \right) \right) \left(\left(\frac{k_f}{k_p} \right) + 0.28 \varepsilon_{mf}^\beta \right) \right) \quad (\text{A5.18})$$

Here k_p is the thermal conductivity of the bed particles, taken to be 0.3288 for silica sand $\text{W m}^{-1} \text{K}^{-1}$ (Agarwal, 1991) and the parameter β is taken from Flemmer and Banks (1986) and given by Eq. (A5.19)

$$\beta = 0.261 Re_p^{0.369} - 0.105 Re_p^{0.431} - 0.124 [1 + (\log_{10} Re_p)^2]^{-1} \quad (\text{A5.19})$$

where Re_p is the particulate phase Reynolds number defined by Eq. (A5.20)

$$Re_p = \frac{\rho_f u_e 2a}{\mu_f} \quad (\text{A5.20})$$

where U_e is the velocity of the gas passing through the particulate phase (given by Eq. (A5.21)), a is the radius of the mobile sphere and μ_f is the viscosity of the fluidising gas for which Sutherland's formula was used.

$$u_e = \frac{U_{mf}}{\varepsilon_{mf}} \quad (\text{A5.21})$$

A 5.1.2 Gas convective heat transfer coefficient

Agarwal's (1991) expression for the coefficient of gas convective heat transfer for the case where the active particle is within a bubble was used as the starting estimate of h_{gc} , thus

$$h_{gc} = \frac{k_f}{2a} \left[2 \frac{k_e}{k_f} + 0.693 \left((1 + Re_p Pr)^{\frac{1}{3}} - 1 \right) \left(\frac{C_{D\varepsilon a} Re_p}{8} \right)^{\frac{1}{3}} \left(\frac{q}{\varepsilon_{mf}} \right)^{\frac{2}{3}} \right] \quad (\text{A5.22})$$

where $C_{D\varepsilon a}$ is the porosity dependent drag coefficient, given by Agarwal and O'Neil (1988) correlation in Eq. (A5.22), Pr is the Prandtl number of the fluidising gas and q is the tortuosity given by Eq. (A5.23) (Agarwal & O'Neill, 1988).

$$C_{D\epsilon a} = \left(\frac{24}{Re_p} \right) \left(\frac{(2z(1 - \epsilon_{mf}))}{q} + (10^{(0.261Re_p^{0.369} - 0.105Re_p^{0.431} - 0.124[1 + (\log_{10} Re_p)^2]^{-1})} - 1) \right) \quad (A5.22)$$

$$q = \frac{1}{1 - 0.9(1 - \epsilon_{mf})^{\frac{2}{3}}(\epsilon_{mf} - 0.25)^{\frac{1}{3}}} \quad (A5.23)$$

where z is the cross-section factor, given by Eq. (A5.24) (Agarwal & O'Neill, 1988).

$$z = \frac{5.3}{q^2} \left(\frac{\epsilon_{mf}}{1 - \epsilon_{mf}} \right)^{0.3} \quad (A5.24)$$

Subsequently h_{gc} was corrected to account for the large quantity of gas emitted from the surface of the source particle using the technique described by Bird *et al.* (2002), the corrected term is denoted by \dot{h}_{gc} . As the volumetric flux of gas emitted from the surface of the particle depended upon the total heat transfer coefficient, the contributions from $h_{pc,a}$, $h_{pc,d}$, \dot{h}_{gc} , h_{bub} , h_{rad} and $h_{rad,bub}$ were calculated iteratively to find updated values for the flux of gas away from the sphere and therefore, \dot{h}_{gc} .

An alternative gas convective hat transfer coefficient was used for the times when the mobile sphere was lifted to the surface of the bed by a bubble.

$$h_{bub} = \frac{k_f}{2a} \left[2 + 0.693 \left((1 + Re_{bub} Pr)^{\frac{1}{3}} - 1 \right) \left(\frac{C_{Da} Re_{bub}}{8} \right)^{\frac{1}{3}} \right] \quad (A5.25)$$

where C_{Da} is the drag coefficient for the sphere inside the bubble defined by Eq. (A5.26) by Agarwal and O'Neill (1988)

$$C_{Da} = \frac{24}{Re_{bub}} 10^{(0.261Re_{bub}^{0.369} - 0.105Re_{bub}^{0.431} - 0.124[1 + (\log_{10} Re_{bub})^2]^{-1})} \quad (A5.26)$$

and Re_{bub} is the Reynolds number for the gas passing around the mobile sphere inside a bubble defined by Eq. (A5.27).

$$Re_{bub} = \frac{\rho_f U_{tf} 2a}{\mu_f} \quad (A5.27)$$

where U_{tf} is the velocity of gas passing up into the bubble, estimated at $U_{tf} = 3U_{mf}$ from Valenzuela and Glicksman, (1985).

A 5.1.3 Radiative heat transfer

The radiative portion of the overall heat transfer becomes significant in fluidised beds at bed temperatures exceeding 800 K according to Flamant *et al.* (1993). The radiative heat transfer changes depending on if the circulating sphere is inside a bubble or in close contact with the bed material so two separate radiative heat transfer coefficients were calculated, one for the time that the sphere was in a bubble, $h_{rad,bub}$ and the other for the time that the sphere was in close contact with the bed, h_{rad}

To estimate the radiative heat transfer coefficient from the bed particles to the source particle it was assumed that the view factor, F, was unity and that the source particle and bed particles behaved as an opaque, grey medium. Radiative heat transfer, h_{rad} and $h_{rad,bub}$ were calculated as:

$$h_{rad} = \frac{\sigma(T_{mean}^4 - T_{particle}^4)}{(T_{bed} - T_{particle}) \times \left\{ \frac{1 - \epsilon_d}{\epsilon_d} + 1 + \left(4 \times \frac{1 - \epsilon_{bed}}{\epsilon_{bed}} \right) \right\}} \quad (A5.28)$$

$$h_{rad,bub} = \frac{\sigma(T_{bed}^4 - T_{particle}^4)}{(T_{bed} - T_{particle}) \times \left\{ \frac{1 - \epsilon_d}{\epsilon_d} + 1 + \left(\frac{4 \times r_s^2}{d_{bub}^2} \times \frac{1 - \epsilon_{bed}}{\epsilon_{bed}} \right) \right\}} \quad (A5.28)$$

where ϵ_{bed} and ϵ_d are the emissivities of the bed and devolatilising particles respectively. The bed emissivity is estimated to be 0.85 (Botterill, 1975). The emissivity of dry ice was found using the infrared spectral reflectance given by Keegan and Weidner (1966). It was assumed that the emissivity was equal to (1 – reflectance), the emissivity of the gas inside the bubble or gas film was neglected. The relationship between the emissivity of dry ice and the bed temperature was found and, as shown by Fig. A5.1, the emissivity varies considerably within the temperature range utilised in the experiments in Chapter 5.

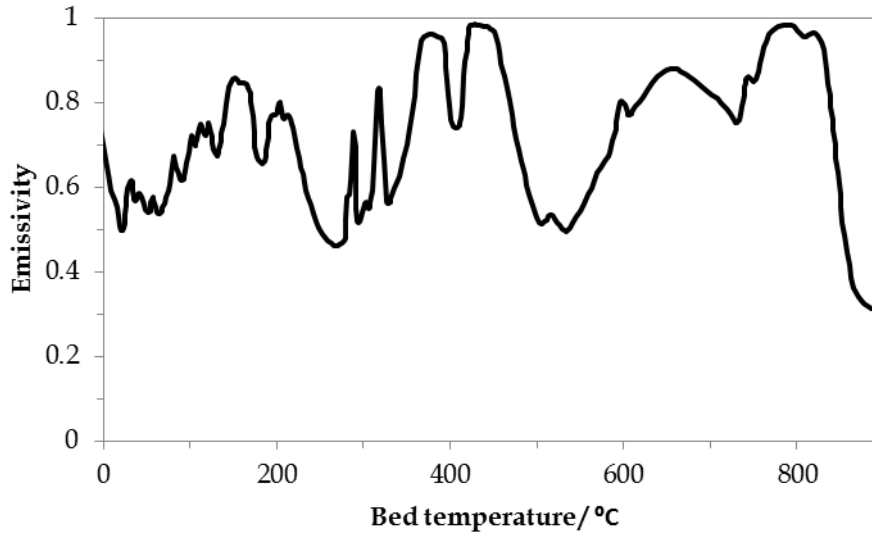


Fig. A5.1. Infrared spectral emissivity of crushed commercial carbon dioxide “dry ice” at sublimation temperature varying with bed temperature. Keegan and Weidner (1966).

To obtain a single value of emissivity of dry ice when subjected to beds for each temperature it was assumed that thermal radiation was emitted by the bed material at a distribution of intensity of radiation at different wavelengths according to Planck’s law. This distribution of intensities at each bed temperature was used to determine a weighted mean value of emissivity. The emissivity of the dry ice, ϵ_d , was found using T_{bed} for $h_{rad,bub}$ and T_{mean} for h_{rad} to allow for the cooling of the bed particles in close proximity to the sphere.

A 5.1.4 Weighting

To recap, the overall effective heat transfer coefficient is a weighted sum of size individual heat transfer coefficients. The weighting coefficients are P the probability that a mobile sphere is in the emulsion phase (Agarwal, 1987) and P' , the probability that a mobile sphere is in the emulsion phase during the upwards part of its circulation (Agarwal, 1991) are given by Eqs. (A5.29) and (A5.30) respectively.

$$P = \frac{U_{bub}}{U_{bub} + U_D} \quad (4.29)$$

$$P' = \frac{(U_{bub} - U_R)U_D}{(U_{bub} + U_D)(U_R + U_D)} \quad (4.30)$$

The coverage fraction, f_c , was found empirically in Section 4.4.2 to be Eq. (A5.31)

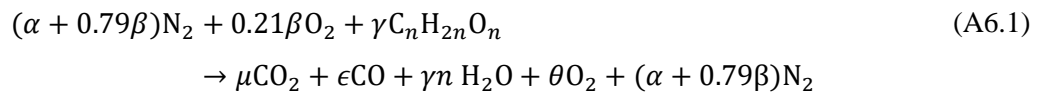
$$f_c = 1 - m \frac{U_d}{U_{mf}} - c \quad (4.30)$$

where $m = 0.031 \pm 0.022$ and $c = 0.50 \pm 0.05$ and U_d is the velocity at which gas is emitted by the mobile sphere.

Appendix 6: Combustion

A 6.1 Stoichiometric flowrate calculations for combustion of volatile matter for section 6.1.1

Hence, the overall combustion reaction is arrived at:



where the Greek letters describe the molar flowrate of: α , N_2 fed to the distributor of the reactor, β , air fed above the baffle, γ , evolved volatile matter (VM), μ , CO_2 in the freeboard, ϵ , CO in the freeboard, θ , O_2 in the freeboard. The assumption that the composition of the VM does not change through the devolatilisation process is examined in Section 6.1.2.

By performing an oxygen balance

$$0.42\beta + n\gamma = 2\mu + \epsilon + n\gamma + 2\theta \quad (A6.2)$$

θ can be determined, being the molar flowrate of O_2 in the freeboard

$$\theta = 0.21\beta - \mu - \frac{\epsilon}{2} \quad (A6.3)$$

In the experiments, the off gas was dried before it was directed to the CO_2 and CO analysers. Hence, the concentration of CO_2 and CO in the sampling line can be calculated on a dry basis according to Eqs. (A6.4) and (A6.5):

$$[CO_2] = \frac{\mu}{\mu + \epsilon + \theta + \alpha + 0.79\beta} \quad (A6.4)$$

$$[CO] = \frac{\epsilon}{\mu + \epsilon + \theta + \alpha + 0.79\beta} \quad (A6.5)$$

Equations 6.4 and 6.5 simplify after substituting for θ using Eq. (A6.3):

$$[CO_2] = \frac{\mu}{\beta + \alpha + \frac{\epsilon}{2}} \quad (A6.6)$$

$$[CO] = \frac{\epsilon}{\beta + \alpha + \frac{\epsilon}{2}} \quad (A6.7)$$

Rearranging gives ϵ , the molar flowrate of CO, and μ , the molar flowrate of CO_2 :

$$\epsilon = \frac{[CO] \times (\beta + \alpha)}{1 - \frac{[CO]}{2}} \quad (\text{A6.8})$$

$$\mu = [CO_2] \times \left(\beta + \alpha + \frac{\frac{[CO] \times (\beta + \alpha)}{1 - \frac{[CO]}{2}}}{2} \right) \quad (\text{A6.9})$$

From the carbon balance:

$$\gamma n = \mu + \epsilon \quad (\text{A6.10})$$

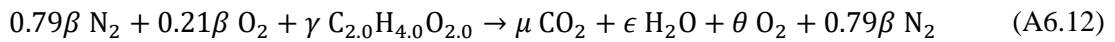
and, assuming the n remains constant throughout devolatilisation:

$$n = \frac{\mu + \epsilon}{\gamma} \quad (\text{A6.11})$$

Hence, by comparing the molar flowrate of the VM, γ , with the combined flowrates of CO₂ and CO, ϵ and μ , which arise owing to the combustion of the VM, n can be evaluated, yielding an average value for the molar mass of the species comprising the VM.

A 6.2 Stoichiometric flowrate calculations for Section 6.2.1

The combustion of the VM emitted by each sphere of beech was assumed to take place according to the following instantaneous steady state equation:



Here, β is the molar flowrate of air through the reactor, γ is the molar flowrate of volatiles produced by the wood, μ is the molar flowrate of CO₂ in the exhaust gas, ϵ is the molar flowrate of H₂O in the exhaust gas, and θ is the molar flowrate of O₂ in the exhaust gas. It should be noted that Eq. (A6.12) differs from Eq. (A6.1) because, here, the bed is fluidised by air rather than by N₂, with air introduced separately as described in Section 6.1. Hence the oxygen balance is now given by:

$$\theta = 0.21\beta + \frac{2.0\gamma}{2} - \mu - \frac{\epsilon}{2} \quad (\text{A6.13})$$

A hydrogen balance gives:

$$2.0\gamma = \epsilon \quad (\text{A6.14})$$

with a carbon balance giving:

$$2.0\gamma = \mu \quad (\text{A6.15})$$

By substituting Eqs. (A6.14) and (A6.15) into (A6.13) to eliminate the flow of H₂O and VM, the expression for the molar flowrate of oxygen, θ , can be simplified:

$$\theta = 0.20\beta - \mu \quad (\text{A6.16})$$

The concentration of CO₂ in the exhaust gas from the reactor, [CO₂] is now given by:

$$[\text{CO}_2] = \frac{\mu}{\theta + \mu + 0.79\beta + \epsilon} \quad (\text{A6.17})$$

Substituting Eq. (6.16) into Eq (6.17) to eliminate θ gives:

$$[\text{CO}_2] = \frac{\mu}{\beta + \epsilon} \quad (\text{A6.18})$$

Noting from Eq. (6.14) and (6.15) that $\epsilon = \mu$, then

$$[\text{CO}_2] = \frac{\mu}{\beta + \mu} \quad (\text{A6.19})$$

Rearranging for the molar flowrate of CO₂ gives:

$$\mu = \frac{[\text{CO}_2]\beta}{(1 - [\text{CO}_2])} \quad (\text{A6.20})$$

The (1-[CO₂]) term in Eq. 6.20 accounts for the water from combustion as there was no CaCl₂ trap used on this sample line. Hence, the molar flowrate of CO₂ in the exhaust gases from the reactor was found from the CO₂ concentration and the known molar flowrate of air into the reactor, β .

Appendix 7: Poem

Hi Gran, how've you been? I know it's been a while I'm sorry,
but I've been busy working in the laboratory.
"What do I do again"? It's hard to explain I must confess,
But broadly speaking I'm working on Bio-CCS.

With carbon dioxide emissions ever on the rise,
despite the Paris Agreement (not to anyone's surprise).
Now to cap the temperature rise to 2 degrees or less,
It's likely we'll have to employ Bio-CCS.

In growing, reaping, burning trees and other vegetation.
Then burying the exhaust gas (that posh word "sequestration"),
carbon dioxide's taken out of the air in the process.
Climate damage could be limited by Bio-CCS.

There's a long way to go before all our energy is clean,
and there are other CO₂ emitters which often go unseen,
such as concrete, steel and meat production also fertilisers
And no ones willing to make any lifestyle compromises...

So while we all agree that something really should be done.
We blythly go on with our lives emitting by the giga-tonne.
So to reconcile the climate and our thirst for excess,
I'm working on the combustion bit of Bio-CCS.

